Fabio Santanni

Molecular approaches for quantum technologies

Optimization of electron spin-based quantum bits and quantum logic gates

FIRENZE
UNIVERSITY
PRESS

Premio Tesi di Dottorato
Città di Firenze 2023

PREMIO TESI DI DOTTORATO CITTÀ DI FIRENZE

– 1 –

PREMIO TESI DI DOTTORATO CITTÀ DI FIRENZE

Commissione giudicatrice, anno 2023

Stefano Grassi, Presidente della commissione

Aldo Bompani, Area Scienze Sociali
Franco Cambi, Area Umanistica
Roberto Casalbuoni, Area Scientifica
Fabrizio Desideri, Area Umanistica e della Formazione
Anna Dolfi, Area Umanistica e della Formazione
Andrea Novelli, Area Biomedica
Raffaele Paloscia, Area Tecnologica
Orlando Roselli, Area Scienze Sociali
Vincenzo Schettino, Area Scientifica
Marco Tarchi, Area Scienze Sociali
Maria Chiara Torricelli, Area Tecnologica
Luca Uzielli, Area Tecnologica
Marcello Verga, Area Umanistica e della Formazione

Fabio Santanni

Molecular approaches for quantum technologies

Optimization of electron spin-based quantum bits and quantum logic gates

FIRENZE UNIVERSITY PRESS
2025

Molecular approaches for quantum technologies : optimization of electron spin-based quantum bits and quantum logic gates / Fabio Santanni. - Firenze : Firenze University Press, 2025.
(Premio Tesi di Dottorato Città di Firenze ; 1)

https://books.fupress.com/isbn/9791221506709

ISBN 979-12-215-0669-3 (Print)
ISBN 979-12-215-0670-9 (PDF)
ISBN 979-12-215-0671-6 (XML)
DOI 10.36253/979-12-215-0670-9

Graphic design: Alberto Pizarro Fernández, Lettera Meccanica SRLs
Front cover image: © glebdesign159|123rf.com

This work is part of the FETOPEN project FATMOLS (GA862893)

Peer Review Policy
Peer-review is the cornerstone of the scientific evaluation of a book. All FUP's publications undergo a peer-review process by external experts under the responsibility of the Editorial Board and the Scientific Boards of each series (DOI 10.36253/fup_best_practice.3).

Referee List
In order to strengthen the network of researchers supporting FUP's evaluation process, and to recognise the valuable contribution of referees, a Referee List is published and constantly updated on FUP's website (DOI 10.36253/fup_referee_list).

Firenze University Press Editorial Board
M. Garzaniti (Editor-in-Chief), M.E. Alberti, F. Vittorio Arrigoni, E. Castellani, F. Ciampi, D. D'Andrea, A. Dolfi, R. Ferrise, A. Lambertini, R. Lanfredini, D. Lippi, G. Mari, A. Mariani, P.M. Mariano, S. Marinai, R. Minuti, P. Nanni, A. Orlandi, I. Palchetti, A. Perulli, G. Pratesi, S. Scaramuzzi, I. Stolzi.

FUP Best Practice in Scholarly Publishing (DOI 10.36253/fup_best_practice)

The online digital edition is published in Open Access on www.fupress.com.

Content license: except where otherwise noted, the present work is released under Creative Commons Attribution 4.0 International license (CC BY 4.0: http://creativecommons.org/licenses/by/4.0/legalcode). This license allows you to share any part of the work by any means and format, modify it for any purpose, including commercial, as long as appropriate credit is given to the author, any changes made to the work are indicated and a URL link is provided to the license.

Metadata license: all the metadata are released under the Public Domain Dedication license (CC0 1.0 Universal: https://creativecommons.org/publicdomain/zero/1.0/legalcode).

© 2025 Author(s)

Published by Firenze University Press
Firenze University Press
Università degli Studi di Firenze
via Cittadella, 7, 50144 Firenze, Italy
www.fupress.com

This book is printed on acid-free paper
Printed in Italy

Table of contents

FUP Best Practice in Scholarly Publishing (DOI 10.36253/fup_best_practice)

Fabio Santanni, *Molecular approaches for quantum technologies. Optimization of electron spin-based quantum bits and quantum logic gates*, © 2025 Author(s), CC BY 4.0, published by Firenze University Press, ISBN 979-12-215-0670-9, DOI 10.36253/979-12-215-0670-9

Preface

The general idea of quantum computing was born in the late 20th century thanks to the works of outstanding scientists like R. Feynman, C. H. Bennett, D. Deutsch, and many others. The idea of overcoming the limitations of classic computation in understanding nature's laws by adopting a universal machine capable of "speaking" the same language of the microscopic quantum world appeared absolutely sensible. Seminal results were initially obtained by physicists, mathematicians, and even philosophers, who laid the groundwork of this interdisciplinary subject, i.e., the quantum information science. Nowadays, the scientific community rides the wave of the second quantum revolution, thus presenting formidable examples of quantum architectures for implementing a new kind of computation. For instance, leading groups such as IBM and Google have already presented superconductive circuits for quantum processors operating with 65 (Falcon processor) and 53 (Sycamore processor) quantum bits, respectively. Companies provide online and cloud platforms, thus giving them the possibility to access such powerful quantum computers to solve different problems.

Although their calculation power was proven to be incredibly high, these architectures present practical limitations that must be overcome to reach a fast, fault-tolerant, and universal computation.

Among the proposed strategies, electron spin-based molecular qubits aroused a specific interest in the community because of the tunability properties of molecules. In this respect, chemistry can give the chance of getting various and tailored molecular systems that might be adopted for different purposes, e.g., for implementing qubits and quantum logic gates, encoding quantum error correction algorithms, for quantum sensing applications, and so on. Nevertheless, combining the need for a specific molecular design and target quantum properties is not trivial. Efforts are still needed to reach essential objectives and overcome common

FUP Best Practice in Scholarly Publishing (DOI 10.36253/fup_best_practice)

Fabio Santanni, *Molecular approaches for quantum technologies. Optimization of electron spin-based quantum bits and quantum logic gates*, © 2025 Author(s), CC BY 4.0, published by Firenze University Press, ISBN 979-12-215-0670-9, DOI 10.36253/979-12-215-0670-9

problems in different physical and chemical systems. For example, a crucial parameter for qubits is the so-called coherence time, roughly the time in which a certain state of the system can store the encoded information, and it is strictly correlated to the spin dynamics of the system. This specific parameter is not easily controllable since a blend of contributions (magnetic coupling interactions, spin-phonon interactions, etc.) may cause its reduction. Up to now, the effect of various contributions on this parameter is still unclear, and more investigations are mandatory to untangle further the different phenomena originating in its loss.

The author of this thesis mainly worked as a synthetic and inorganic chemist. He synthesized and probed different molecular systems based on transition metal complexes, principally of Cu^{II} and V^{IV} ions, for reaching more performant spin qubits and quantum logic gates. Consequently, this thesis work aims mainly to give a complete overview of the different molecular strategies proposed during these three years as a PhD student at the University of Florence and to show important results and limitations of the employed systems.

The thesis will start with an extensive introduction to the subject of quantum computing, mainly presenting the logic and working principles of quantum computers' fundamental units (Chap.1). Then, different chemical and physical strategies for the obtaining of qubits will be presented in Chap.2, focusing on those based on nuclear and electron spins. In the same chapter, the electron spin relaxation subject will also be treated. An overview of the most promising molecular systems proposed so far is then reported in Chap.3. The general introduction given within these three chapters provides the theoretical bases of quantum information science necessary for understanding the following chapters.

The first principal subject of the thesis will be presented in Chap.4, where different examples of molecular qubits synthesized and characterized by the author will be discussed. Here, we will focus on phenomena originating from the spin-spin and spin-lattice relaxation processes in molecular qubits and the proposed molecular strategy for overcoming the present limitations. In particular, this chapter is mainly devoted to presenting those systems fulfilling three main requirements for the optimization of molecular qubits: i.e., i) a multilevel structure of electronic or nuclear states; ii) a nuclear spin-depleted environment; iii) neutral charge and appreciable thermal stability so that they can be employed for surface deposition experiments. Two examples of hydrogen-free neutral copper(II) molecular qubits will be presented. In particular, the syntheses and magnetic investigations of two complexes of porphyrazine- and dithiolene-like ligands are reported in Sec.4.1 and Sec.4.2, respectively. This section will also focus on the rationalization of the systems' spin dynamics, followed by the experimental and theoretical approaches employed. Furthermore, the treatment of the spin-lattice relaxation phenomenon and its investigation will be extended to the case of lanthanide-based single-molecule magnets. In Sec.4.3, it is reported a comparative experimental and *ab initio* study conducted on an archetypical SMM, i.e., the dysprosium(III) complex of acetylacetonate ligand, aimed at unveiling the role of phonons in the relaxation of this class of compounds.

A relevant part of this thesis work is also related to the application of molecular qubits for advanced EPR experiments. In this respect, there will be presented two studies conducted on the archetypical oxovanadium(IV) qubit with the tetraphenyl porphyrin ligand, i.e., [VO(TPP)]. In Sec.5.1, we will show some intriguing results obtained from the collaboration with the University of Modena and Reggio Emilia (Prof M. Affronte's Group). In that work, single crystals and polycrystalline samples of [VO(TPP)] are coupled with superconductive coplanar resonators and employed for the storage and retrieval of the information in a molecular spin ensemble, i.e., for implementing "quantum memories". In Sec.5.2, we will further show some preliminary results on the investigation of coherence properties of a [VO(TPP)] single crystal by working at the so-called atomic clock transitions, thus exploiting the multilevel nature of the vanadium element. This work was conducted in collaboration with Prof J. R Friedman's group (Amherst University). Additionally, we report a short treatment on the purification procedure employed for obtaining iron(III)-free porphyrins (Sec.5.3). The main objective of the author here was that of removing iron(III) contaminants found in [VO(TPP)].

In the end, the last part of the work will focus on the molecular approaches employed for the realization of two molecular spin-based quantum logic gates. In Chap.6, two examples of porphyrin-based oxovanadium(IV) complexes suitable for the encoding of two- or multi-qubit gates will be presented. On the one hand, the chapter aims to discuss how porphyrins could be sensibly employed to get target multi-qubit architectures, thus allowing the possibility of scaling up the system dimension effectively. On the other hand, the chapter stresses how difficult rationalizing such a complex system's magnetic and coherence properties could be. An example of a multi-qubit system characterized by a switchable interaction is presented in Sec.6.1. This work was realized in collaboration with the University of Manchester, where the author spent three months as a visiting student under the supervision of Prof R. E. P. Winpenny and Dr G. Timco. The work will focus on preparing and synthesizing a vanadyl qubit with the tetrapyridyl porphyrin complex [VO(TPyP)]. The central qubit is linked through coordination bonds to four more purple-Cr_7Ni rings qubits. Furthermore, we will show our results obtained on a two-qubit logic gate based on a vanadyl dimer obtained by condensing two A3B triphenyl porphyrin complexes (Sec.6.2). The dimer is characterized by two distinguishable and exchange-coupled vanadyl units suitable for the implementation of logical operations.

Chapter 1
Logical units of quantum computers

The aim of this thesis is to show different molecular approaches for the optimization of electron spin-based quantum bits and *quantum logic gates*. These words, however, could be unfamiliar to those who have never had to deal with the subject of quantum information. In this respect, a minimum theoretical background must be recalled before starting the discussion of the results. Figuring out how a quantum computer works is not trivial. It requires the introduction of several basic notions from quantum physics, subsequently relying on a drastic change of the logic behind the fundamental units and operations involved. This chapter aims to provide a theoretical overview of the physics and mathematics behind the quantum computers' basic units, i.e., quantum bits and quantum logic gates. Indeed, a profound understanding of these general aspects is paramount to getting close to this thesis's focus. A more detailed introduction to the approaches adopted will be presented in the following chapters (Chap.2 - 3), where further insights into exploiting different spin systems for quantum computing will be given.

1.1 The quantum bit

We have already introduced some fundamental concepts as *quantum computing* or *quantum bits* regardless of their working procedures and properties. The quantum bit, or *qubit*, represents the fundamental unit of a quantum computer. As the qu-"bit" word recalls, there are several analogies with the classical bit. Indeed, in classic information science, we conceive a bit as a two-state logical unit where only two values are possible: the state 0 = *false*, and the state 1 = *true*, congruently with the Boolean logic behind it. The physical object works precisely as a switch, so just these two values are possible. In general, the qubit, conceived as a physical

Fabio Santanni, University of Florence, Italy, santannifabio@gmail.com, 0000-0002-0506-8333

Referee List (DOI 10.36253/fup_referee_list)
FUP Best Practice in Scholarly Publishing (DOI 10.36253/fup_best_practice)

Fabio Santanni, *Molecular approaches for quantum technologies. Optimization of electron spin-based quantum bits and quantum logic gates*, © 2025 Author(s), CC BY 4.0, published by Firenze University Press, ISBN 979-12-215-0670-9, DOI 10.36253/979-12-215-0670-9

object, works roughly in the same way. Its working principle is based on two well-defined basis states that would be conveniently referred to as $|0\rangle$ and $|1\rangle$. Each time we measure the state of a qubit, we read the state $|\psi\rangle = |0\rangle$ or $|1\rangle$ with an associated probability $p(\psi)$.

Nevertheless, such a general description is simplistic, and it does not exalt the real potential of the qubit as technological innovation. Following the exceptional explanation given by *Nielsen* and *Chuang* in [1], the qubit may be more conveniently considered as an abstract object or a mathematical one. The natural operation of a qubit can be unveiled only by exploiting its quantum properties. The following treatment of the qubit will be a personal interpretation and adaptation of what is extensively described in three main textbooks from *Nielsen and Chuang* [1], *Le Bellac* [2] and *Holevo* [3].

As stated before, the enormous difference between qubits and classical bits relies on the possibility of encoding the information by taking advantage of the infinite set of states $|\psi\rangle$ obtained as *superposition* of two basis states $|0\rangle$ and $|1\rangle$. Indeed, each state of a system in a Hilbert space can be described by a unit state vector (or unit wavefunction) $|\psi\rangle$ due to the first postulate of quantum mechanics. In the case of a qubit of finite two-dimensional complex Hilbert space (Eq. 1.1) [1], each state vector might be obtained as a linear combination of the orthogonal basis states $|0\rangle$ and $|1\rangle$. Remember that the Hilbert space to whom the generic state vector belongs is a normed space. Moreover, because the vector is a unit one, the *normalization conditions* expressed in the Eq. 1.1 must be respected.

$$|\psi\rangle = \alpha|0\rangle + \beta|1\rangle, \qquad \langle\psi|\psi\rangle = \|\psi\|^2 = |\alpha|^2 + |\beta|^2 = 1 \tag{1.1}$$

Now, if the two scalars α and β are expressed as sine and cosine functions, following the normalization condition stated above, the whole equation may be rewritten as:

$$|\psi\rangle = cos\frac{\theta}{2}|0\rangle + e^{i\phi}sin\frac{\theta}{2}|1\rangle \tag{1.2}$$

Where the two angles θ and ϕ represent the zenith and azimuthal ones, respectively. As a result, the qubit state is projected from an abstract complex state to a bidimensional complex one. The latter is called the Bloch-Majorana or Poincaré sphere (Fig.1.1). In this way, depicting a qubit results much easier. Here, the two basis states are commonly fixed in correspondence with the two sphere poles, thus recalling the general idea of the ground and excited states. In addition, the whole set of points individuating the geometrical space of the sphere's surface are the other infinite possible states $|\psi\rangle$ defined by linear combinations of $|0\rangle$ and $|1\rangle$. All of them are unit vectors originating at the centre of the Bloch sphere, and their

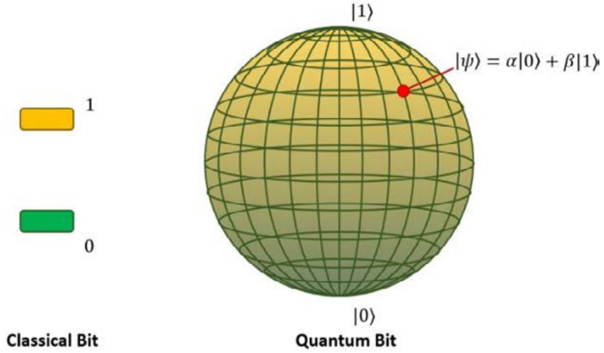

Figure 1.1. Cartoons of a classical (left) and quantum bits (right). The qubit is represented as a Bloch sphere, in which the two basis states are pinned at the poles.

modulus coincides with the sphere radius. Hereafter, we will refer to this complex space simply as the Bloch sphere.

Let us suppose that once we have generated a specific state $|\psi\rangle$, we make it free to evolve. It is known from the second postulate of quantum mechanics that the evolution of each state in a closed quantum system can be described by a unitary operator $\widehat{U}^{*} = \widehat{U}^{-1}$. We will focus on this point in the section dedicated to the multi-qubits systems, namely *quantum logic gates* (Sec. 1.2). In particular, the time evolution of the system is described by the Schrödinger equation (1.3).

$$i\hbar\frac{d}{dt}|\psi(t)\rangle = \widehat{\mathcal{H}}(t)|\psi(t)\rangle \tag{1.3}$$

Quantum mechanics is fully deterministic at this level. Indeed, the qubit can be initialized in a well-defined state (or variously manipulated) and then let free to evolve without losing the tracking of its state. Recalling a practical example reported by *Le Bellac* [2], we can present experimental proof of qubit's manipulability, i.e., the *Rabi oscillations*.

Let us consider a generic spin S = 1/2 placed in a static magnetic field $\vec{B}_0$, free to evolve under the effect of an oscillating field $\vec{B}_1$. We assume that $\vec{B}_0$ and $\vec{B}_1$ are orthogonal vectors. The expression of the magnetic field $\vec{B}$ is thus conveniently defined as:

$$\vec{B} = B_0\boldsymbol{z} + B_1(cos(\omega t)\boldsymbol{x} - sin(\omega t)\boldsymbol{y}) \tag{1.4}$$

Where ω is the angular frequency of the oscillating field, B_0 and B_1 the amplitudes, and [$\boldsymbol{x}$ $\boldsymbol{y}$ $\boldsymbol{z}$] the three unit-vectors of the reference frame. Such an expression is usually adopted in Electron Spin and Nuclear Magnetic Resonances (EPR and

NMR) to introduce the _field-effect onto electron or nuclear spins (see Appendix A). We are referring to this specific example because magnetic resonance techniques have been extensively employed in this thesis, and it could help in understanding what follows in Chap. 4, 5, and 6. If we switch to matrix notation, it is then possible to define a Hamiltonian describing the time evolution of the system of the form reported in Eq.1.5.

$$\hat{\mathcal{H}}(t) = -\frac{\hbar}{2}\begin{bmatrix} \omega_0 & \omega_1 e^{i\omega t} \\ \omega_1 e^{i\omega t} & \omega_0 \end{bmatrix} \tag{1.5}$$

Here, ω_0 is the spins precession frequency (in radians) due to the application of the static field along the *z* axis (namely the Larmor frequency), and ω_1 is the Rabi frequency proportional to B_1. As an example, we shall now consider a generic qubit initialized into the $|0\rangle$ state at *t* = 0. The probability of observing the qubit in the state $|1\rangle$ at the generic time *t* is:

$$p_{0\rightarrow 1}(t) = \left(\frac{\omega_1}{\Omega}\right)^2 sin^2\left(\frac{\Omega t}{2}\right) \tag{1.6}$$

Where $\Omega = \sqrt{(\omega - \omega_0)^2 + \omega_1^2}$, with $\omega - \omega_0$ taken as the offset between the Larmor and the working frequency. In particular, when $\omega = \omega_0$, we fulfill the resonance condition, thus maximizing the oscillation amplitude between $|0\rangle$ and $|1\rangle$. It follows that the probability $p_{0\rightarrow 1}$(t) is proportional to $sin^2\left(\frac{\omega_1 t}{2}\right)$. Now, if we want to go from $|0\rangle$ to $|1\rangle$, we need to tune the time in which B_1 acts. In magnetic resonance spectroscopy, it is usually defined as a π pulse. By tuning the time *t*, it is even possible to put the system in one of the other states $|\psi\rangle$. Nevertheless, once the system is measured, we can read only the state $|0\rangle$ or $|1\rangle$ depending on the associated probability. Furthermore, because the probability is a periodic function of time, we can plot its behavior as a function of t as it is reported on the left side plot in Fig.1.2. The oscillating function reported here represents the Rabi oscillations mentioned before. A pictorial representation of the overall manipulation and reading process is reported on the right side of Fig.1.2. In the figure, the initial $|0\rangle$ and generic $|\psi\rangle$ quantum states of the qubits are represented as red vectors.

It is now clear that introducing a measurement system requires incorporating a probabilistic treatment axiomatically. Furthermore, while all the unitary operations proposed before are reversible (this concept will be of paramount importance in the next section), the quantum measurement (QM) results in a switch of the system state due to an irreversible evolution. Such a phenomenon is a consequence of the third postulate of quantum mechanics, which gives rise to many considerations about the QM process all over the textbooks proposed so far. Here, we will summarize the treatment, going through the key points.

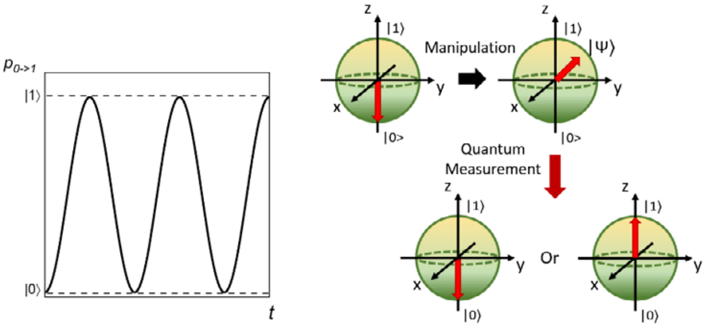

Figure 1.2. On the left, plot of simulated Rabi oscillations on a generic two-level system. On the right, pictorial representation of the overall process of manipulation and reading out of the qubit.

Let us suppose to have a qubit prepared in a generic state $|\psi\rangle = \sum_{\gamma} c_{\gamma}|\gamma\rangle$ by a unitary transformation, where γ is chosen as its computational basis. When we introduce the measurement apparatus into the system and let it act on $|\psi\rangle$, we can physically represent the process with a generic measurement operator $\widehat{M}$ acting on the state $|\psi\rangle$. Recalling what the third postulate states, we obtain a set of measurement's outcomes $\{M_{\gamma}\}$ upon the measurement process. It follows that the probability of finding the system in the generic state is expressed by the equation:

$$p(\gamma) = \langle\psi|\widehat{\mathrm{M}}_{\gamma}^{\dagger}\widehat{M}_{\gamma}|\psi\rangle \tag{1.7}$$

And the final quantum state is:

$$|\gamma\rangle = \frac{M_{\gamma}\ |\psi\rangle}{\sqrt{\langle\psi|\widehat{M}_{\gamma}^{\dagger}\widehat{M}_{\gamma}|\psi\rangle}}, \qquad p(\gamma) > 0\ \rangle \tag{1.7}$$

Which must fulfil the completeness condition $\langle\psi|\widehat{M}_{\gamma}^{\dagger}\widehat{M}_{\gamma}|\psi\rangle = \hat{I}$, because the probabilities must sum to one.

Now, if the projector $|\gamma\rangle\langle\gamma|$ is chosen as the measurement operator, all the equations reported above can be conveniently rewritten by adopting the operator $\hat{E}_{\gamma}$. Here, we are formally introducing the POVM (Positive Operator-Valued Measure) formalism. The operators $\hat{E}_{\gamma}$ are known as the POVM elements associated with the measurement onto the basis. The complete set $\{\hat{E}_{\gamma}\}$ g is instead known as a POVM. Because we have initially chosen two orthogonal states $|0\rangle$ and

$|1\rangle$ as the computational basis, the probability of observing the system in the state $|0\rangle$ is:

$$p(0) = \langle \psi | \widehat{\mathrm{E}}_0 | \psi \rangle = \alpha^* \langle 0|0\rangle\langle 0|0\rangle \alpha = |\alpha|^2 \tag{1.9}$$

And subsequently, the probability of finding it in the state $|1\rangle$ is $p(1) = \beta^2$. Such a result is of paramount importance in this treatment of the physical object. Indeed, at the end of the measurement process, we can obtain one of these two orthogonal, and thus distinguishable, states with an associated probability p. The probability depends on the coefficient of the linear combination resulting from the initial unitary transformation.

What might appear complex to understand from the overall treatment introduced before is the quantity of information storable into the qubit because, in the end, only $|0\rangle$ or $|1\rangle$ will result from the QM process. Notwithstanding, the groundbreaking novelty of the qubit is that this system properly keeps track of the superimposition state, which was generated before the measurement through the unitary transformation.

The overall process can be schematized as reported in Fig.1.3. When starting, we initialize the system in a state $|0\rangle$. Then, we operate on the qubit by exploiting a unitary transformation, thus preparing the qubit in a generic state $|\psi\rangle$. Until this point, we are applying the first and second postulates. Then, we measure the qubit state going through the QM process, and, at this step, we need to introduce the third postulate.

However, during the measurement processes, two more phenomena occur. Let us figure out the two distinct objects involved in the process, namely the qubit and the measurement system.

These objects are characterized by an initial state $|\psi\rangle$ and $|\Xi\rangle$, respectively (where $|\Xi\rangle$ is a dummy state of the measurement system). Following the von Neumann theory of measurement, we must select a process generating an entanglement condition between the qubit and the measurement system so that:

$$|\psi\rangle \otimes |\Xi\rangle \longrightarrow \sum\nolimits_{\gamma} c_\gamma |\gamma\rangle \otimes |\Xi\rangle \tag{1.10}$$

Where $|\Xi^\gamma\rangle$ is a generic output state of the measurement apparatus labelled according to the basis. It means that we must have a one-to-one correspondence between the QM apparatus states and those of the system. Here, the entanglement condition is set because of the correlation between parties. For the moment, we can introduce the concept of entanglement based on the fourth postulate of quantum mechanics. It is postulated that the state space of a composite physical

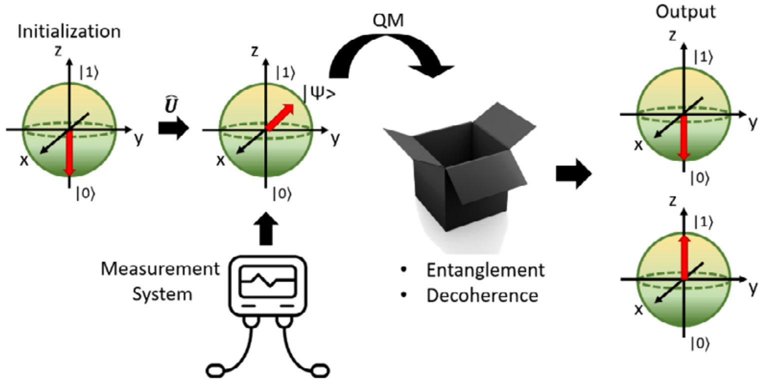

Figure 1.3. Representative scheme of the overall process described in the text. The QM process leads to two physical phenomena (listed below the black box) when the measurement system is introduced. At the end of the process, we read out two possible states because of the wavefunction collapsing.

system is the tensorial product of the state spaces of the components ($|\psi_i\rangle$). In this way, the final state of the joint system ($|\psi\rangle_{Tot}$) can be written as $|\psi\rangle_{Tot} = |\psi_1\rangle \otimes |\psi_2\rangle \dots \otimes |\psi_N\rangle = |\psi_1 \psi_2 \dots \psi_N\rangle$. The final state of the joined system is thus defined by a new orthogonal basis as expressed above. If the parties are in an entanglement condition, the new state is no more separable. As an example, we can think to a pair of generic states $|\psi\rangle = \alpha(|01\rangle + |00\rangle)$ and $|\psi\rangle = \alpha(|11\rangle + |00\rangle)$, where α is a generic scalar. The first one can be rewritten as $|\psi\rangle = \alpha|0\rangle(|1\rangle + |0\rangle)$, so it is a separable state. On the counter hand, the second one cannot be rewritten as the direct product of the initial basis states, and it is defined as an entangled state. More insights on the importance and applications of entanglement within qubits will be provided in the next section.

Going back to the QM process, we generated a set of distinguishable states $|\Xi^{\gamma}\rangle$. We recall that the necessary condition for two or more states to be distinguishable is to form an orthonormal set of states. Thus, we can introduce a new theorem without getting more insights on that (because it is a deviation from the main focus of this thesis, and it will not be treated here): *if a pair of states of the system of interest becomes correlated with mutually orthogonal states of another system, then all the phase coherence between the orthogonal states of the first is lost*. The introduction of this theorem is straightforward to demonstrate that the decoherence phenomenon listed in Fig.1.3 firstly generates during the QM.

After the two mentioned processes (entanglement and decoherence), the system's wave function collapses onto one of the computational basis states due to the third postulate, i.e., the QM process.

Now, we have not extended the treatment of the decoherence phenomenon occurring during the QM. Nonetheless, the decoherence process plays a paramount role in quantum information theory, and it must be deeply understood before the following chapters. The decoherence phenomenon arising from the QM process described above is generally defined as an *adiabatic decoherence* process of the system. Indeed, as long as we can keep control over the system variables, the coherence of qubits within the probed ensemble can be locally or temporarily lost, while it can be recovered during other physical measurement processes. This can be a property of the system only if qubits are well-isolated (i.e., in an ideal case), so they cannot interact with the environment. In a real case, when losing control over one or more of the experimental variables (e.g., temperature, homogeneity or intensity of the magnetic field, statistic thermic noise, etc.), the *true decoherence* process occurs. This latter process results in an irreversible loss of information from the system. To better understand such a concept, we will refer to a more practical example in which an ensemble of magnetic dipoles is considered. The switching from a single qubit case to a qubit ensemble would result in a more accessible and intelligible explanation of the decoherence process, also related to the molecular systems presented in the following chapters. Furthermore, we will refer to some basic concepts of magnetic resonance in the following example, e.g., the rotating frame notation. This notation is usually employed to explain the resonance phenomenon for a spin ensemble (see the section dedicated to the EPR spectroscopy reported in Appendix A).

Let us think of an ensemble of isolated electrons with a spin quantum number $S = 1/2$ that are placed into a pulsed EPR spectrometer. The experimental apparatus is taken as an ideal one so that we can set a homogenous static field $\vec{B}_0$, a stable temperature *T*, and we can perfectly control the oscillating field $\vec{B}_1(t)$. Once the static field is on, the two projections of the spin along the *z* quantization axis, $m_S = 1/2$, split in energy because of the Zeeman interaction between the spin and the magnetic field (see the section dedicated to the spin Hamiltonian in Appendix A). The basis of the $|S, m_S\rangle = |1/2, \pm 1/2\rangle$ is thus taken as the computational basis of the ensemble. At the beginning of the experiment, being $\vec{B}_0 = +B_z\boldsymbol{z}$, most of the spin population is aligned with the magnetic field direction, and the associated magnetic dipoles precess along the *z* axis (Fig.1.4). The net magnetization of the ensemble given as the sum of the *z* components of magnetic moments within the ensemble (i.e., $\vec{M_z}$) is thus aligned along +*z*. This state is the ground-state of our system, and we will refer to this state (i.e., $|1/2, -1/2\rangle$), as the initialisation $|0\rangle$ one (we use a different notation here with respect to figures showed before since it is more convenient for visualizing the magnetization evolution in the laboratory framework). It follows that the other possible state, characterized by a $m_S = 1/2$, will be the computational state $|1\rangle$.

When $t = 0$, the precession dynamics differ from one spin to another, so we do not know the spins' position on the circular trajectory and their phase. It follows that the total component of the magnetization onto the *xy* plane is null. If we let $\vec{B}_1(t) \parallel x$ acting for a time t sufficiently long (a $(\pi/2)_x$ pulse) to ensure the generation of the superposition state:

$$|\psi\rangle = \frac{1}{\sqrt{2}}(|0\rangle + |1\rangle) \tag{1.11}$$

All the spins start to process coherently with a frequency equal to the Larmor frequency ω_0 and, before any relaxation phenomenon occurs, the population equalises in the two states. The magnetization is thus projected in the *xy* plane and oscillates with a frequency $\omega = \omega_0$. In the rotating frame (i.e., in an arbitrary reference frame oscillating with the same frequency ω_0), the net magnetisation of the ensemble is aligned with the *-y* axis as it is reported in Fig.1.4. Now, if we consider a random perturbation arising from a field inhomogeneity, one spin may start to precess with a different phase, losing its coherence with respect to the other spins. Following what was stated above, the qubit undergoes an entanglement condition with a pair of the environment orthogonal states that we cannot control. Since we cannot access those states, we permanently lose the information on the spin phase. For clarity, the process can propagate to the other spins of the ensemble, causing the total loss of coherence and, subsequently, the magnetization will disappear from the plane. In addition, the spins in the excited state also return to the ground state with different relaxation dynamics called longitudinal relaxation. In this way, the initial condition is recovered. These relaxation processes will be treated in detail in Chap.2.

Since the decoherence process led to an irreversible loss of information, it must be restrained as much as possible. Because of this, a deep understanding of the

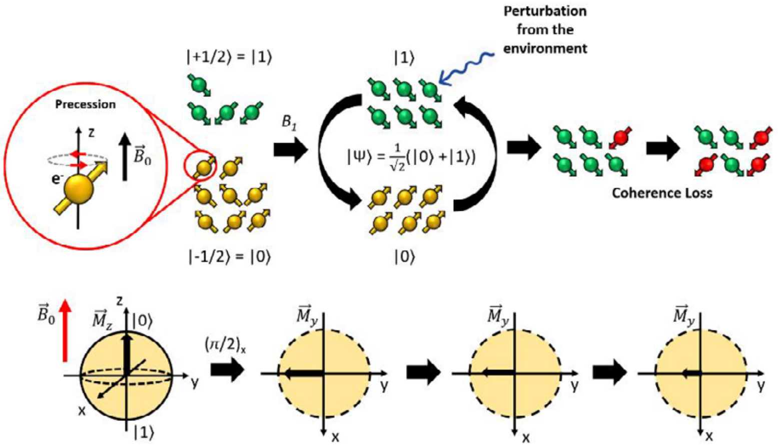

Figure 1.4. On top, pictorial representation of the changing in spin states' population occurring after a $(\pi/2)_x$ pulse. The decoherence phenomenon occurs after the state ψ is generated. At the bottom, the same process is represented by adopting magnetization and rotating frame notations.

decoherence process and related phenomena is of utmost importance to overcome the current limitations in practical devices. Referring to the case of molecular qubits, which are the central subject of this thesis, the decoherence phenomenon in molecular spin-based devices can result from a wide variety of system's variables. Among them, we can recall: i) the insurgence of fluctuant fields due to the dipolar interaction with other spins; ii) the interaction with lattice vibrations; iii) the effect of the magnetic field inhomogeneity related to the experimental setup. Emerging approaches aimed at reducing the mentioned effects and enhancing the so-called coherence time (i.e., the time in which the information is stored within the spin ensemble) are those resulting from i) a rational design of the employed molecules, or from ii) the development of different experimental and measurement strategies. Since the study of the coherence properties in molecular qubits was a large part of this thesis, several molecular and instrumental approaches will be presented during the following chapters (Chap.4 - 5).

1.2 Quantum logic gates

The transition from classical to quantum computing requires developing a novel set of apparatuses that can replace the classical analogues. Due to the second and fourth postulates, operations must be reversible, and an entanglement condition can be set among systems. These two requirements pave the way for realizing a new set of logical operators, thus expanding the horizons to a more powerful computation. At first, we must recall some of the basic concepts expressed in the previous section. The bit represents the minimum amount of information of a classical computer, following the binary logic. All the system's variables satisfy the same Boolean algebra, and they can only assume two finite values 0 and 1, namely *true* and *false* [4]. Similarly, all the operations between the computational variables are expressed by different logic gates, e.g., YES, NOT, AND, OR, NAND, NOR, XOR and many others (Fig.1.5). Each of these gates requires at least 1 bit to be employed, and they operate following the specific table reported below the symbols in the figure. Implementing a series of digital circuits, it is thus possible to carry all the operations out.

The irreversibility of such processes is not compatible with the definition of quantum operation. Indeed, as stated in the previous section, all the implemented operations aimed at manipulating the qubit's state or a collection of entangled ones must be performed through a unitary transformation that is reversible by definition. If we take as an example the AND gate, there exist three distinct combinations of the two input values resulting in a "0" output, i.e., (00), (01), and (10). Once the value 0 is obtained, there is no chance to recover the information on the composition of the initial state.

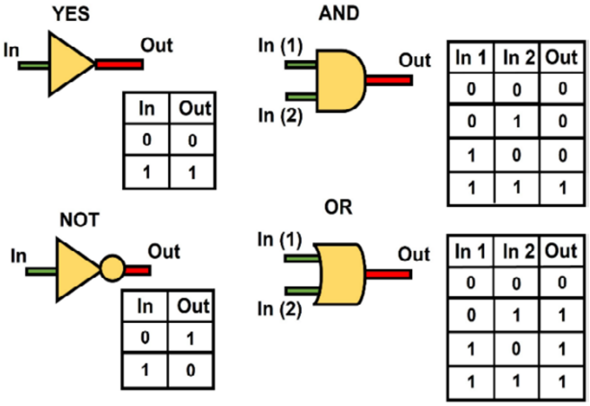

Figure 1.5. Representative sketch of some classical gates which may be adopted to implement logical operations within classical algorithms by digital circuits.

Because only unitary transformations agree with quantum mechanics' laws, we must define a new series of reversible logical operations which may be implemented within quantum algorithms (Fig.1.6). Among them, it is strictly necessary to introduce those operating at the single qubit level. For example, the well-known Pauli matrices (usually denoted as σ_x, σ_y, and σ_z in quantum mechanics) are largely employed. In the quantum information scenario, they are usually named as $\hat{X}$, $\hat{Y}$, or $\hat{X}$ gates. As an example, the $\hat{X}$ gate is the very first employed gate in Grover's algorithm [5] reported in Fig.1.6 [6].

Even the Hadamard gate ($\hat{H}$) gains a relevant role in quantum computing science. Indeed, if implemented on a qubit initialized as $|0\rangle$, it gives the state $|+\rangle$ (top in Eq.1.12), while, if applied to $|1\rangle$, it gives $|-\rangle$ as a result (bottom in Eq1.12).

$$\begin{aligned} \hat{H}|0\rangle &= \frac{1}{\sqrt{2}}\begin{bmatrix} 1 & 1 \\ 1 & -1 \end{bmatrix}\begin{bmatrix} 1 \\ 0 \end{bmatrix} = \frac{|0\rangle + |1\rangle}{\sqrt{2}} = |+\rangle \\ \hat{H}|1\rangle &= \frac{1}{\sqrt{2}}\begin{bmatrix} 1 & 1 \\ 1 & -1 \end{bmatrix}\begin{bmatrix} 0 \\ 1 \end{bmatrix} = \frac{|0\rangle - |1\rangle}{\sqrt{2}} = |-\rangle \end{aligned} \tag{1.12}$$

The mentioned operations represent rotations or reflections concerning the Bloch sphere’s framework and are widely used to operate on the single-qubit state. While these operations may be easily introduced by the ”quantization” of their classical analogues, we still need to define the quantum analogues of multi-bit operations, e.g., AND or NAND. Obtaining these gates with classical bits is straightforward (e.g., the communication within two physical bits can be obtained by connecting them with an electrical contact), but expanding the computational basis of quantum systems is quite challenging and often requires an entanglement condition to be imposed between qubits.

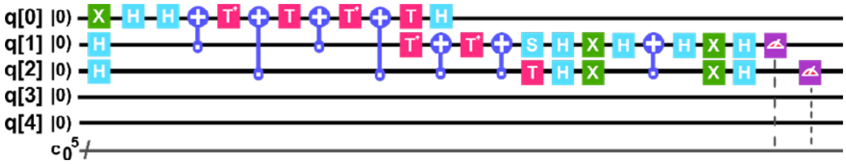

Figure 1.6. Grover's algorithm implemented on the IBM's 5-qubit quantum circuit [6].

Recalling what stated in the previous section, the possibility of getting two states entangled arises from the fourth postulate of quantum mechanics (Sec.1.1). If two qubits states are expressed as $|\psi\rangle = \alpha|0\rangle + \beta|1\rangle$ and $|\psi'\rangle = \alpha'|0\rangle + \beta'|1\rangle$, thus the joint system $|\psi\psi'\rangle$ is represented by

$$\hat{H}|\psi\psi'\rangle = \alpha\alpha'|00\rangle + \alpha\beta'|01\rangle + \beta\alpha'|10\rangle + \beta\beta'|11\rangle \tag{1.13}$$

Where the states $|00\rangle$, $|01\rangle$, $|10\rangle$, and $|11\rangle$ represent the new computational basis. For clarity, the obtained state is not necessarily an entangled one. Indeed, the entanglement condition emerges when the states are no more separable, and it depends on the value of the scalar products $\alpha\alpha'$, $\alpha\beta'$, $\beta\alpha'$, and $\beta\beta'$.

Before entanglement is further discussed, an introduction to the *Controlled*-NOT (CNOT) quantum gate is foremost. The scheme of the CNOT gate is reported in Fig.1.7 together with the associated matrix representation. This gate is the quantum analogue of the XOR classical one, and it is suitable for implementing the reversible analogue of the function COPY. It means that given two different qubits A and B, respectively defined as control and target qubits, when the qubit A is in the state $|0\rangle$ the qubit B is copied ($|00\rangle \rightarrow |00\rangle$). On the contrary, when the state of the control bit is $|1\rangle$, the quantum NOT operation is performed on the target qubit ($|10\rangle \rightarrow |11\rangle$). The computational basis here is taken as $|AB\rangle$, which is not equivalent to $|BA\rangle$. In Fig.1.7, the "*plus*" symbol is placed in correspondence of the target qubit, while the circle represents the control one.

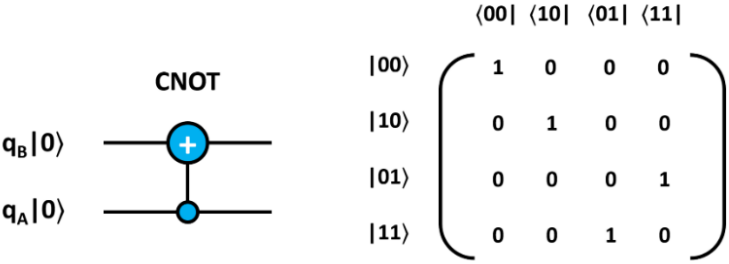

Figure 1.7. Scheme of a CNOT gate applied to a two-qubit quantum register (left side) and the associated matrix representation (right side).

It must be stressed that the CNOT gate is capable of implementing plenty of logical operators, e.g., AND, NOT, and many others. Indeed, the CNOT gate is *universal* in the sense that any other complex operation would be implemented by letting it act a finite number of times [7]. Furthermore, as stated by Lloyd [8], almost any quantum logic gate is universal, too, such as the well-known Toffoli gate [9].

One of the most useful properties of the CNOT gate is its capability of generating an entanglement condition between two qubits when coupled to the Hadamard gate operation. Let us take two qubits (A and B) as the basis of our quantum register initialized in a $|0\rangle$ state (Fig.1.8). The joint quantum basis will be $|00\rangle$. When the Hadamard gate (Eq.1.12) acts on the control qubit (A) the final state is thus transformed as reported in Fig.1.8. The so obtained state is not an entangled one because it can be still written as a tensorial product of the two individual states (see Sec.1.1):

$$|00\rangle \rightarrow \hat{H}|0\rangle \otimes |0\rangle = \frac{1}{\sqrt{2}}(|0\rangle + |1\rangle) \otimes |0\rangle = \frac{1}{\sqrt{2}}(|00\rangle + |10\rangle) \qquad (1.14)$$

At this point, the CNOT gate plays a fundamental role within the algorithm. The control qubit contemporarily exists in the state $|0\rangle$ and $|1\rangle$ after the Hadamard operation. It follows that the state $|00\rangle$ is copied while the quantum NOT operation ($\hat{X}$) is implemented on the state $|10\rangle \rightarrow |11\rangle$. The algorithm produces one of the four Bell's states as the output (Eq.1.15). The Bell's state arising from the register

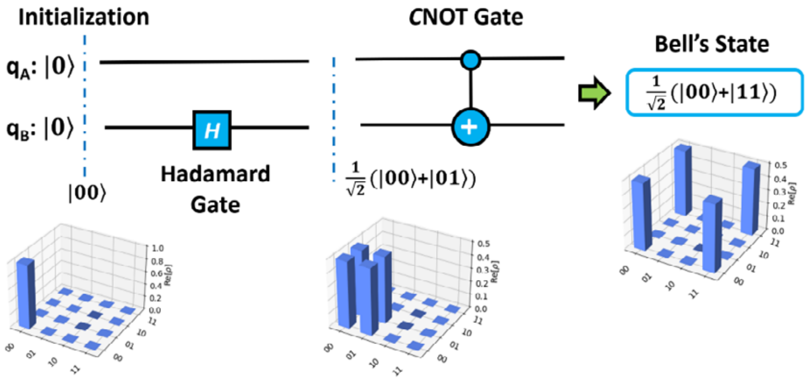

Figure 1.8. Quantum register that can be adopted for obtaining the entanglement condition between a couple of qubits A and B. 3D-bar plots (obtained with the open-source software *Qiskit* [10]) report the probability of finding the qubits in a specific state ψ when it is initialized or after each quantum operation.

is no more separable, thus it is maximally entangled. Depending on the initial value of the two qubits, four different states may be obtained from the same process.

$$|\psi\rangle = \tfrac{1}{\sqrt{2}}(|00\rangle + |11\rangle) \tag{1.15}$$

The four states reported in Eq1.16 represent Bell's basis.

$$\begin{aligned} |\psi_1\rangle &= \frac{1}{\sqrt{2}}(|00\rangle + |11\rangle) \\ |\psi_2\rangle &= \frac{1}{\sqrt{2}}(|00\rangle - |11\rangle) \\ |\psi_3\rangle &= \frac{1}{\sqrt{2}}(|10\rangle + |01\rangle) \\ |\psi_4\rangle &= \frac{1}{\sqrt{2}}(|01\rangle - |10\rangle) \end{aligned} \tag{1.16}$$

Quantum logic gates have practically infinite applications and can be adopted to implement many quantum algorithms. To shed light on their potential, we might introduce the concepts of *superdense coding* and *quantum parallelism* here.

Let us think about two general interlocutors A and B (from the conventional names adopted: *Alice* and *Bob*) who need to share two bits of information from A to B with just one chance of sending a single qubit. Consider that A and B share two different qubits on which the entanglement condition had been generated before from another party, namely *Eve* or E. The entangled state is obtained through the process described in Fig.1.8, and it has the form of Eq.1.15. At this point, A may perform one of the unitary transformations $\hat{I}$, $\hat{X}$, $\hat{Y}$, or $\hat{Z}$ on her qubit to obtain one of the Bell's states reported in Eq.1.16. For instance, neglecting the trivial application of the identity operator, if A performs the $\hat{Z}$ transformation, thus the system's state is changed as:

$$|\psi\rangle = \hat{I} \otimes \hat{Z} \frac{1}{\sqrt{2}}(|00\rangle + |11\rangle) = \frac{1}{\sqrt{2}}(|00\rangle - |11\rangle) \tag{1.17}$$

Adopting a matrix notation, the outcome can be calculated as:

$$\begin{bmatrix} 1 & 0 & 0 & 0 \\ 0 & 1 & 0 & 0 \\ 0 & 0 & -1 & 0 \\ 0 & 0 & 0 & -1 \end{bmatrix} \tfrac{1}{\sqrt{2}} \begin{bmatrix} 1 \\ 0 \\ 0 \\ 1 \end{bmatrix} = \tfrac{1}{\sqrt{2}} \begin{bmatrix} 1 \\ 0 \\ 0 \\ -1 \end{bmatrix} = \tfrac{1}{\sqrt{2}}(|00\rangle - |11\rangle) \tag{1.18}$$

We must employ the tensorial product $\hat{Z} \otimes \hat{I}$ because of the system's dimension gained after that E generated the first Bell's state. The information is sent to B through the quantum channel, and B processes the information by applying a CNOT and a Hadamard gate in sequence. Depending on which state A had prepared, party B may read one of the four strings 00, 01, 10, and 11. In the end, Alice has sent a string of two reliable bits to Bob just by operating at the single qubit level. Although the overall process requires two qubits to be employed, A does not directly interact with the second qubit. A scheme of the overall process is reported in Fig.1.9 [11, 12]. This process is what results from *superdense coding*, and it is arguably the channel that launched the field of quantum communication [13]. In principle, if we could increase the number of qubits employed, it would be possible to ”dense” encode a larger number of strings within a ”small” number of qubits, thus reducing the time and the memory required by classical computers to perform analogous protocols. A seminal contribution to this field can be found in [13], where superdense coding has been successfully employed for encoding quantum communication within optical qubits.

We now pass to the concept of quantum parallelism. It can be efficiently presented by starting from a practical example. Suppose a situation where, given a certain x, calculating a function value $f(x)$ is the final task. As an example, we might think to calculate the solution of an easy problem, such as that one reported in [14]. Starting from two possible values of $x = [0\,,1]$, we want to

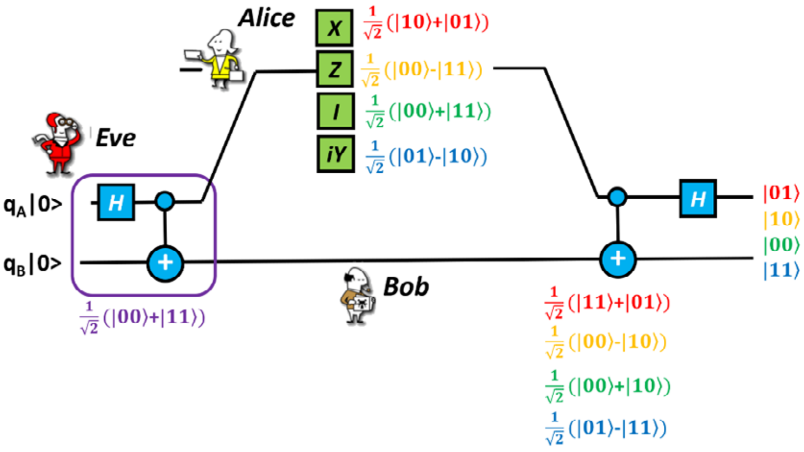

Figure 1.9. Representation of the superdense coding protocol [12]. Depending on Alice's choice, one of the four colored Bell's states can be obtained. The string of bits read by Bob are mapped with the same color code adopted for Alice's operations to highlight the dependence from the unitary transformation adopted by Alice.

define a generic function that gives $f(0) = 1$ or $f(1) = 0$ upon the calculation. From a classic point of view, we need to calculate the two functions and then compare them to know the result. By adopting qubits, we may adopt a two-qubit register where one of the qubits stores the value of x and the other accounts for $f(x)$. Performing a series of logical operations, it could be possible to define a unitary transformation $\hat{U}_f$ which transforms the "function"-qubit into $f(x)$ (Eq.1.19).

$$\hat{U}_f|\mathrm{x} \otimes 0\rangle = \left|\mathrm{x} \otimes \hat{U}_f 0\right\rangle = |\mathrm{x} \otimes f(\mathrm{x})\rangle \tag{1.19}$$

Such an operation can be performed by adopting the quantum algorithm reported in the quantum circuit of Fig.1.10. Here, we started considering the generic state $|00\rangle$ ($|0\rangle \otimes |0\rangle = |x\rangle \otimes |0\rangle$), on which we performed a CNOT and an $\hat{X}$ gates. At the end, the algorithm's output will be the state $|01\rangle = |x\rangle|f(x)\rangle$. If we start from the usual $|00\rangle$ initial state, and then we perform a $\hat{H}$ gate onto the x-qubit, thus when $\hat{U}_f$ is applied the final state will be:

$$|\psi\rangle = \hat{U}_f\left|\hat{H}0 \otimes 0\right\rangle = \frac{1}{\sqrt{2}}\left(\left|0 \otimes \hat{U}_f 0\right\rangle + \left|1 \otimes \hat{U}_f 0\right\rangle\right) \tag{1.20}$$

and thus:

$$|\psi\rangle = \frac{1}{\sqrt{2}}(|0 \otimes f(0)\rangle + |1 \otimes f(1)\rangle) \tag{1.21}$$

The state $|\psi\rangle$ now accounts for $f(0)$ and $f(1)$ simultaneously. This equation illustrates a striking property of quantum computing, which distinguishes it from its classic counterpart. Indeed, we are correctly running the machine in "parallel"

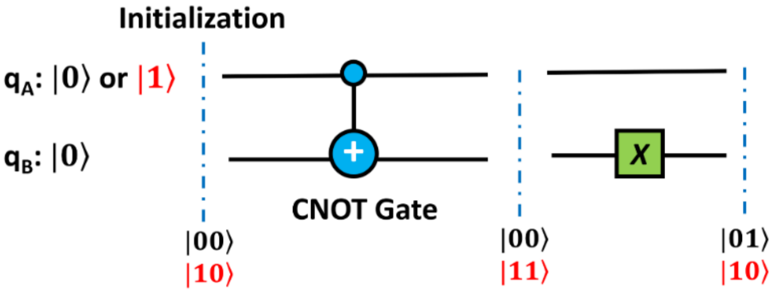

Figure 1.10. Schematic representation of the quantum circuit operating the function $f(x)$ on the quantum register $|00\rangle$, for which $f(0) = 1$ and $f(1) = 0$.

by exploiting the superimposition properties of inputs, and, as Harcoche and Raimond stated [14]:" *making it compute all the values of a function simultaneously and keeping its state before any final bit detection is performed, suspended in a coherent superposition of all the possible outcomes*". Furthermore, when extending this procedure to a set of *n* qubits, we can obtain $2n$ values of the function $f(x)$ simultaneously. However, the quantum measurement results in only one of these values.

Nevertheless, the calculation of $f(x)$ for each value of *x* is unnecessary because all of them can be obtained in a single shot, thus theoretically speeding up the whole process. Although this protocol can only be considered a proof of concept of quantum computing because of its limitations [14], nowadays, different strategies have been proposed to overcome such limits. However, their treatment is a deviation from the scope of this thesis, and we refer to [14] for further details on this subject.

These two reported cases are great examples of the enhanced calculation power of quantum computers, which overwhelms that of classical computers. For this reason, the research aimed at discovering new materials for more performing quantum logical units will be at the basis of quantum computers breakout in the next few years.

Chapter 2
Spin qubits and relaxation processes

Some basic concepts of quantum information were introduced in the previous chapter by adopting a mathematical and physical language. Such a procedure is often employed when explaining the fundamental requirements for quantum computing. In this chapter, we will continue to provide an overview of the implementation of quantum computers but, on the other hand, by employing several practical examples. Starting briefly with a recap of the tasks necessary to implement a performing quantum computing, we then rapidly move to present how to adopt different approaches to integrate spins within quantum architectures. Furthermore, we will introduce some basic notions of electron spin relaxation, mainly referring to molecular spin qubits. Indeed, understanding the relaxation dynamics of electron spins is a central task for engineering more performing molecular spin qubits.

2.1 Tasks for quantum computing

Recalling what has been stated in Chap.1, the overall quantum computational process is efficiently resumed in Fig.1.3. Once the qubit is initialized, the information can be manipulated by implementing different unitary transformations on the qubit state. Then, as the information is adequately prepared, the system undergoes the quantum measurement process, thus resulting in an output that still needs interpretation.

Fabio Santanni, University of Florence, Italy, santannifabio@gmail.com, 0000-0002-0506-8333

Referee List (DOI 10.36253/fup_referee_list)
FUP Best Practice in Scholarly Publishing (DOI 10.36253/fup_best_practice)

Fabio Santanni, *Molecular approaches for quantum technologies. Optimization of electron spin-based quantum bits and quantum logic gates*, © 2025 Author(s), CC BY 4.0, published by Firenze University Press, ISBN 979-12-215-0670-9, DOI 10.36253/979-12-215-0670-9

The process is full of critical aspects. Their understanding is the starting point for improving quantum computers. Recalling what was stated by Nielsen and Chuang in [1], there are four crucial requirements to fulfil:

- Robustly represent quantum information
- Perform a universal family of unitary transformations
- Prepare a fiducial initial state
- Measure the output result

While the last three points might appear straightforward to a reader after the basic working procedures of quantum computers' logical units were presented, the first point derives from the nature of qubits. Indeed, quantum computing is based on the manipulation of qubit states. Even if the characteristic two-state nature of qubits characterizes plenty of systems, e.g., nuclei, electrons, or polarized photons, it is also required that the two states can be precisely manipulated and superimposed to get one of the states on the Bloch sphere. Furthermore, the lifetime of the state must be long enough to allow the implementation of an algorithm.

Let us suppose an ideal case of a $S = 1/2$ system free of any contribution to the spin Hamiltonian except for the electron Zeeman interaction term (Appendix A). The spin experiences a static magnetic field B parallel to its quantization axis z. As the field strength increases, the two levels $m_S = \pm 1/2$ lose their degeneracy and split in energy. Therefore, we can define a computational basis $|\pm 1/2\rangle = |0\rangle$ or $|1\rangle$. Adopting a sequence of microwave pulses (see Appendix A), we can hence manipulate the system state to reach any possible superposition state. Such an example represents a robust way to reproduce an ideal qubit since only the two states $m_S = \pm 1/2$ can be selectively probed, and no other chances to involve different levels are included. However, finding such an ideal system in a real case is uncommon, and multilevel structures are usually involved. Because of the presence of these boundary states, it is tough to manipulate a single couple of states selectively, and decoherence can arise from interference with other states of the system [1]. Moreover, decoherence is introduced because of the interaction between the qubit and the environment (e.g., the thermal bath or other spins). In this sense, isolating a qubit might still reduce the decoherence.

It is also important to stress the importance of performing a universal family of unitary transformations. Indeed, single and multi-qubit operations, e.g., $\widehat{H}$ or CNOT gates, are fundamental to perform universal quantum computing. All these operations require both a single qubit and a multi-qubit architecture and an efficient control of external stimuli to manipulate the qubits' states.

Plenty of different systems have been presented as candidates for qubit implementation. Among the various strategies proposed so far, significant results have been obtained by employing physical and chemical systems, e.g., superconducting circuits [15−18], nitrogen vacancies in diamonds [19−22], optical cavities [23,24], defects in insulators [25,26] or semiconductors [27−29], molecular systems [30−33], and many others [34,35] (Fig.2.1).

The following chapter will focus on the latter type of qubits, thus showing their potential for competing with other quantum systems.

2.2 The spin qubit

In the previous section, some fundamental tasks for the quantum computing were introduced. The first requirement asserts that quantum information can be efficiently represented if and only if quantum states are well-defined and selectively manipulable. The research aimed at probing different candidates for implementing qubits must focus on those systems that satisfy this prerequisite.

Following what has been reported by D. P. DiVincenzo in 2000 [39], five essential prerequisites must be contemporarily satisfied for a qubit to be practically employable in a quantum computer. An operable qubit must be: i) easily initialized in a well-defined state; ii) individually measurable, even when well-isolated from other qubits (here, there exist differences in sensitivity requirements for detecting a well-defined signal from a single qubit or an ensemble); iii) sensibly engineered to scale up the system dimension for getting multi-qubits architectures; and iv) employable within algorithms so that a universal set of unitary transformation can be implemented (on single or multiqubit gates). Moreover, one of the most critical parameters of qubits is the coherence time typical of the physical system chosen.

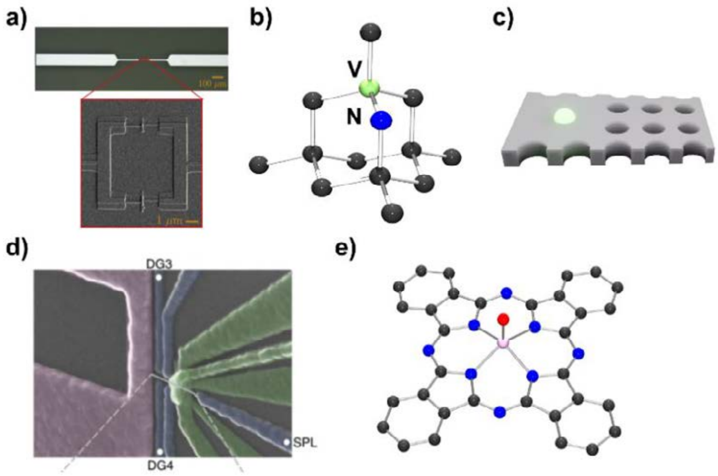

Figure 2.1. a) micrograph of superconductive qubit [36]; b) representative structure of a diamond nuclear spin-qubit where a nitrogen defect is highlighted (blue and green); c) representation of a quantum dot spin-qubit (green dot) within a photonic cavity; d) electron scanning micrograph of a nano-circuit for the read-out of an electron spin-qubit made by a single phosphorus atom in silicon [37]; e) molecular structure of an electron-based molecular spin-qubit obtained as a phthalocyanine-vanadyl complex [38]. Color code: C = black, N = blue, V = pink, O = red.

The more significant the coherence time, the wider the possibilities of storing information and transforming it within quantum algorithms. The practical limit of application of the qubit critically depends on the gate operation time, i.e., the time required for a single logical operation to be performed with the employed physical apparatus. In particular, such a time should be $10^4 - 10^5$ times longer than a single gate operation (the clock-time of the object) to allow quantum error correction to be actuated [39]. Indeed, employing quantum error correction through specific algorithms would result in highly fault-tolerant quantum operations.

Try now to consider the case of two coupled electron qubits forming a two-qubit gate, for which the generic joint state $|00\rangle$ can be defined. If we want to perform a CNOT operation by exploiting their electronic states through a series of EPR pulses, we will need 19 pulses to complete the protocol [40]. The time required for the gate implementation is not lower than 200 ns. Therefore, the system must be coherently stacked in the superimposed state for a sufficiently long time larger than 1 μs.

Among systems proposed for obtaining qubits, spin-based technologies represent one of the most promising classes for developing performing quantum processors. Indeed, nuclear and electron spin-based qubits constitute an intriguing playground for scientists as they can be obtained by employing different strategies (i.e., by working both with solid-state or molecular systems) and manipulated through already available and well-developed magnetic resonance techniques, i.e., EPR and NMR.

Nuclear spin-based qubits were among the first proposed systems for quantum computing. They were successfully employed by Chuang and coworkers in [41]. In this work, a simple quantum algorithm was performed by adopting NMR pulse sequences to manipulate nuclear states of ^{13}C nuclei in an isotopically enriched chloroform solution. Nuclear spin-based qubits benefit from a very long coherence time due to the low energy scale at which they work. Such a feature is the key to disentangle the spin states from the environment, thus reducing the decoherence effects due to external perturbations [42]. However, molecules are not eligible for implementing employable nuclear spin qubits because of several problems: i) the difficulties encountered in rationalizing possible scale-up processes. Indeed, final multi-qubit adducts should contain nuclear units still distinguishable based on their identity (i.e., based on different orientations or chemical/magnetic environment); ii) the need for fast initialization of the qubits within algorithms (not a trivial aspect for nuclear states, in which the recovery time of the initial state can span a time window of several minutes); iii) the experimental requirements correlated both to the low energy involved and the low signals' intensities. The last one is due to the smaller strength of nuclear magnetic dipoles than that of electron ones [42]. Nowadays, groundbreaking results have been obtained by exploiting other strategies based on more promising solid-state devices. Among them, a figure of merit is the exploitation of the nuclear level of a single ^{31}P atom in solid-state devices reported in [43,44]. Moreover, nuclear qubits have been reintroduced in the field of quantum technologies as emerging systems for developing quantum memories (see Chap.5) or for implementing quantum error correction in hybrid coupled nuclear-electron spin qubits [45−48].

Working with energy levels of electron spins would result in a faster and precise manipulation of information through selective microwave pulses. Furthermore, a scale-up process can be carried out by employing *ad hoc* designed molecular systems. Furthermore, molecular adducts have more chances to maintain the desired addressability of distinct units and overcome the problems correlated to the very low coupling with the environment usually observed in nuclear spins. On the other hand, we must consider that electronic levels are generally less ”protected” from external perturbations. It follows that different strategies must be employed to enhance coherence times and obtain efficient qubits.

Among the proposed strategies, diamond-based qubits represent one incontrovertible example of performing solid-state electron spin qubits. Using electron energy levels of a nitrogen atom implanted into the carbon framework of an artificial diamond (a so-called nitrogen-vacancy), it is possible to perform single-qubit operations [19−22]. On the one hand, these systems show appreciable coherence times over a wide temperature range [20]. On the other hand, implanting more vacancies to get multiqubit architectures is challenging. Indeed, it might be tricky to introduce more than one qubit center in specific positions of the diamond’s framework. Because vacancies are randomly generated within the carbon structure, it is impossible to gain the spatial resolution needed for obtaining a precise scheme of ”connected” qubits for which entangled states might be determined [49]. Moreover, the coherence properties of spin centers in diamond strictly depend on the disposition of the vacancies within the carbon framework; the nearer the external surface is, the shorter the coherence time is because of the interaction with the surroundings. Notwithstanding these peculiarities, such systems may be employed for different purposes, such as quantum sensing [50].

Solid-state spin qubits can be obtained by employing defects implanted in a semiconductor framework, such as silicon [27,51]. These devices might be realized with the desired level of spatial control for achieving multi-qubit architectures [29] and probed by microwave pulses. Moreover, they can be introduced in solid-state devices without trapping them with magnetic or electric fields [52]. However, working with them is still challenging in terms of operational requirements due to the high sensitivity required to probe a single spin or realize physical hardware.

In this respect, molecular systems presenting magnetic properties started to arouse a particular interest due to their tunability. Indeed, the chemical and physical properties of molecules could be widely tuned to fulfil specific requirements [52, 53]. Potential molecular qubits are metal complexes [30] or organic molecules containing stable or photogenerated organic radicals. Here, organic ligands and molecules can be tailored and variously functionalized through synthetic approaches to tune the relaxation properties of the spin center (thus enhancing the coherence time) [30,31] and get multi-qubit architectures [54−59]. Furthermore, depending on the molecular system employed (e.g., the nature of paramagnetic centers), it is possible to exploit different energy levels of nuclei and electrons to embed quantum error correction in a single object [60]. This last application is particularly appealing since, in this way, quantum error correction can be performed without employing other states of surrounding nuclei.

The theoretical knowledge of the mentioned properties and the experimental techniques to probe them have been deeply developed and are readily available. However, the route for obtaining performing qubits and multi-qubit architectures is full of pitfalls. For instance, the coherence time of most performing molecular qubits has been enhanced up to several microseconds [61], but we do not have sufficient information on multi-qubit systems. It is not trivial to foresee the coherence properties of systems containing two or more qubits placed in an entangled state since the system's fragility usually increases as the number of energy levels involved increases. A more detailed analysis of these features is given in Chap.3.

Since the coherence properties of spin-based qubits rely on spin relaxation processes, we must introduce the fundamental concepts of spin dynamics. We will be focusing our attention on electron spin relaxation in molecular compounds since they represent the argument of interest of this thesis. Understanding the relaxation phenomena is of utmost importance to appreciate how a tailored molecular approach can open the way for obtaining more performing qubits and quantum logic gates.

2.3 Electron relaxation phenomena

The starting point of a quantum algorithm is the initialization of a qubit in a well-defined state, e.g., $|0\rangle$. Let us consider a single electron spin $S = 1/2$ immersed in a static magnetic field aligned with the quantisation axis z. The ground state of the qubit, i.e., $|S, m_S\rangle = |1/2, +1/2\rangle$ (Appendix A), can be conveniently chosen as the initialization state $|0\rangle$ (See Chap.1, Sec.1.1). The treatment is now extended to an ensemble of identical spins. All of them are initialized as $|0\rangle$ and are coherently manipulable. Once the initial state of this spin ensemble is perturbed from its equilibrium, the recovery of the initial condition follows a well-defined spin dynamic through specific relaxation pathways (See also Sec.A.3).

In general, the spin dynamics is characterized by two distinct relaxation channels [62]. The first one depends on the energy exchange with the environment and is dominated by the interaction with the lattice, namely the longitudinal or spin-lattice relaxation mechanism characterized by the time constant T_1. The second one is due to spin-spin interactions, i.e., the transverse relaxation mechanism characterized by a time constant T_2 (Fig.2.2). However, in the case of an isolated spin, the decoherence is correlated to a blend of different channels, e.g., thermal noise, field fluctuations, field inhomogeneities, and other features. Many of them can also hamper the coherence properties of a spin ensemble.

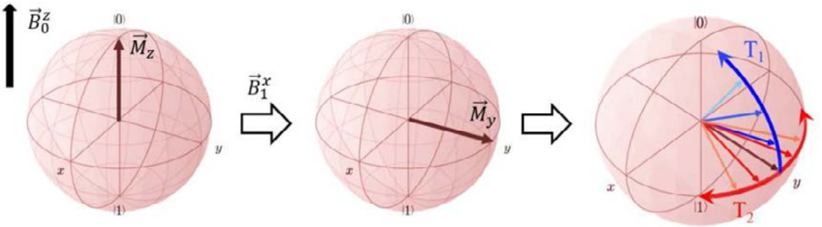

Figure 2.2. Pictorial representation of the manipulation and relaxation processes occurring in a molecular spin qubit. Bloch spheres are obtained by the QuTIP software [65].

The time constants are usually defined as the spin-lattice relaxation time (T_1) and the system's coherence time (T_2). Moreover, T_1 and T_2 are profoundly interconnected in the sense that T_1 sets the upper bound of T_2. Nevertheless, these two quantities could differ up to two or three orders of magnitude depending on the temperature of the investigated systems. For clarity, we will refer to the lower experimental limit of T_2, i.e., the *phase memory time* (T_m). Such an approximation is necessary when adopting pulsed EPR to investigate qubits' coherence properties since contributions from instantaneous diffusion or dipolar coupling critically affect the measurement outcomes [62].

Molecular spin dynamics is thus dramatically affected by several of the system's properties [63]. As a general rule, the spin relaxation is always conditioned by spin-spin interactions between different paramagnetic centers (through dipolar-like interactions), i.e., electron spins and active nuclei of the surrounding [64].

The principal investigation techniques adopted to probe these quantities are pulsed electron paramagnetic resonance (EPR) spectroscopy, both for T_1 and T_m, and alternate current (AC) susceptometry (see Appendix A), which practically gives access to the characteristic relaxation time constant of the magnetization dynamics (τ) due to spin-lattice relaxation process in the investigated sample. However, spin and magnetization dynamics may not be directly correlated, and T_1 and τ may differ by several orders of magnitude for the same sample. Indeed, these two techniques have different limits of applications, both in terms of physical properties' accessibility and spin concentration. Indeed, while pulsed EPR is more sensitive and can be adopted even for a very low concentration of electron spins [38,66,67], AC susceptometry requires large quantities of moderately concentrated samples.

2.4 Spin-lattice relaxation

The spin-lattice relaxation phenomenon occurs because of the energy exchange between the spin system and the environment. Therefore, the main contributions to longitudinal relaxation rates of molecular magnets arise: i) from the energy separation of electronic states; ii) from the magnetic anisotropy; iii) from molecular lattice vibrations (namely phonon modes) and their efficiency of coupling with the spin [63].

For instance, when the qubit is a molecule and the environment is the crystal lattice, the spin-lattice interaction strictly depends on the distribution of lattice phonons, i.e., intra- or intermolecular harmonic modes of atoms or molecules being readily accessible at the same energy scale of the electron spin relaxation phenomenon. When the spin couples to one or more phonons, the spin-lattice relaxation process takes place. To understand this, let us consider the example of a magnetic ion with a total spin S embedded by a certain number of donor atoms, namely a generic metal complex, experiencing a static magnetic field B. The fundamental electronic structure of the complex can be well represented by the spin Hamiltonian of Eq.A.1 (See Appendix A). As the magnetic system undergoes a spin transition $|m_S^a\rangle \rightarrow |m_S^b\rangle$, the initial state $|m_S^a\rangle$ can be recovered thanks to the emission/absorption of one or several phonons depending on the multiplicity of the spin state. For simplicity, the phonon can be considered a molecular vibration that perturbs the coordination sphere of the metal ion. The modification of the overlap between the ion's magnetic orbitals (e.g., the d orbitals for transition metal ions) and those of the surrounding ligands produces a perturbation of the spin Hamiltonian. In particular, the perturbation modulates those terms depending on $\hat{L}$, e.g., the Zeeman or the crystal field ones (see Appendix A, Sec.A.1). We recall that the difference between the principal components of the g-tensor and the Landé g_e factor comes from the admixing of the ground state with excited states through the spin-orbit coupling [68]. Because of this modulation, the equilibrium is perturbed, and the spin relaxes back to the initial state. The spin-phonon coupling efficiency is thus directly correlated to the order of magnitude of the spin-orbit coupling interaction. The stronger the spin-orbit coupling interaction, the stronger the effects on the spin dynamics due to the modulation of Hamiltonian terms depending on $\hat{L}$.

However, phonons do not equally induce relaxation, and some of them may present a stronger coupling with the spin. For instance, we can define a first-order spin-phonon Hamiltonian for considering the energy variation of the system as [69]:

$$\hat{\mathcal{H}}_{s-ph} = \sum_k \left(\frac{\partial \hat{\mathcal{H}}_s}{\partial q_k}\right)_0 \hat{q}_k \tag{2.1}$$

Where $\hat{q}_k = 1/\sqrt{2}(\hat{a}_k^\dagger + \hat{a}_k)$. Here, $\hat{a}_k^\dagger$ and $\hat{a}_k$ are the creation and annihilation operators for a phonon with frequency ω_k calculated at the Γ point of the Brillouin zone. We refer to a *Spin-Phonon Coupling* constant (SPC) as an indicator of the interaction between the spin and the specific vibration. Therefore, the SPC values can be extracted from first-principles calculations by evaluating the partial derivatives of anisotropic terms of the spin Hamiltonian with respect to the generic distortion q_α. In Eq.2.2 (extracted from [69], but also employed in [70, 71]), the second-order SPC distributions are evaluated for each of the vibrational modes calculated for a $S = 1/2$ system as:

$$SPC_k = \sum_{jr} \left| \frac{\partial g_{jr}}{\partial q_k} \right|^2 \tag{2.2}$$

Where *j* and *r* fix the nine components of the g-tensor. Additional parameters to be considered are the phonons thermal population and the density of states (DOS). We refer to Chap.3, Sec.4.1 and 4.3 for a detailed treatment of these aspects.

2.4.1 Relaxation pathways

There exist three main relaxation pathways contributing to the spin-lattice relaxation of molecular magnets (Fig.2.3): i) a direct relaxation process involving a single phonon whose energy matches that of the two levels of interest; ii) a multi-step one-phonon relaxation process, namely the Orbach-relaxation mechanism [72], where the transitions from the initial to the final state requires the absorption/emission of several phonons; iii) a two-phonon relaxation process called the Raman-relaxation mechanism where two phonons are involved (see Sec.4.3).

Referring to Fig2.3, the direct relaxation process is characterized by the absorption or emission of a single phonon of the same energy of the ΔE between the initial ($|\alpha\rangle$) and final ($|\beta\rangle$) states.

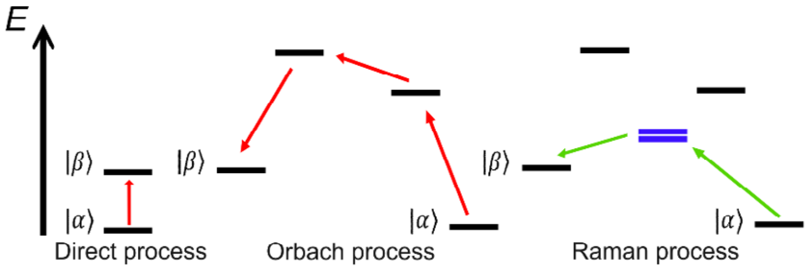

Figure 2.3. Representative scheme of the three different relaxation pathways for electron spins in a generic static magnetic field $B \neq 0$. From the left to the right: 1) Direct relaxation process; 2) Orbach relaxation process; 3) Raman relaxation process for a $S > 1/2$. In the picture, electronic levels (solid black lines) are reported as a function of energy. Red and green arrows represent the spin transition due to the absorption or emission of a phonon. Solid blue lines represent virtual states accessible during the Raman process.

This phenomenon results in a spin transition occurring with a rate constant R_1, which is correlated to the spin-lattice relaxation times constant by the relation: $R_1 \propto T_1^{-1}$. In general, the relation between the relaxation time and the relative energy of the system follows the equation [73]:

$$\frac{1}{T_1} = \frac{3}{2\pi}\left(\frac{\Delta E_{\alpha\beta}}{\hbar}\right)^3 \frac{coth\left(\frac{\Delta E_{\alpha\beta}}{2k_BT}\right)}{\rho\hbar v^5}\left|\langle\beta|\hat{V}|\alpha\rangle\right|^2 = \lambda coth\left(\frac{\Delta E_{\alpha\beta}}{2k_BT}\right) \tag{2.3}$$

In this equation, $\Delta E_{\alpha\beta}$ is the difference in energy between the initial and final states, ρ is the crystal density, v is the velocity of the sound in the crystal, and $\hat{V}$ is the operator accounting for the interaction of the spin with the lattice.

Whereas the whole set of systems presented in this thesis are of Kramers' type, the treatment we are going to face is sensibly restricted to this specific case. For a Kramers' ion, the eigenstate β is defined as the conjugate of the state α. It follows that a two-manifold degeneration of the associated eigenvalue is given. The most general formulation of Kramers' theorem states: *for a generic system with a semi-integer value of S, symmetric with respect to the time reversal operator $\hat{\theta}$, at least two distinct and orthogonal degenerate states can be obtained for each value of M_S* [74]. In the lzero-field limit, the transition between the orthogonal states is not allowed, either by quantum tunnelling or direct relaxation process. The latter consideration is trivial since $\Delta E = 0$, and phonons that match the difference in energy between the states are those of zero energy.

Such a limit can be overcome when a static magnetic field is applied to the spin system. Indeed, the degeneracy is lost because of the Zeeman interaction, and the spin transition is allowed. Once a magnetic field of strength *H* is applied, the two levels α and β are split in energy by $\Delta E_{\alpha\beta} = g\mu\beta H$ (where $g = \sqrt{lg_x + mg_y + ng_z}$, being *l*, *m*, and *n* the opportune direction cosine). in the limit of $\Delta E_{\alpha\beta} < k_BT$ (that is generally true in our case), the Eq.2.3 can be opportunely simplified as reported in [73]. The direct relaxation process hence follows a relaxation dynamics of the type [73,75,76]:

$$\frac{1}{T_1^{Direct}} \propto H^4T \tag{2.4}$$

Where T is the temperature of the thermal bath containing the system. This equation is purely phenomenological and emerges from an empirical treatment of the relaxation mechanism. As observed in Eq.2.4, the relaxation dynamic depends on the fourth power of the magnetic field. It follows that the higher the applied field, the faster the spin's relaxation rate. There are some cases in which such a field-dependence has been found to be reduced to the third power of H [77]. Nevertheless, second-order interactions (e.g., the hyperfine interaction in a system with $S = 1/2$ and $I \neq 0$) may cause the admixing of ground and excited states, thus removing the degeneracy and allowing spin relaxation processes at the zero-field limit. In the following chapters, we will focus on a more physical explanation of this process by employing a combined theoretical and experimental approach for investigating qubits (Chap.4).

In general, when the magnetic field strength is below 100 mT, the relaxation dynamics of molecular spin qubits of the first row's transition ions can be severely affected by dipolar and hyperfine coupling interactions. These contributions have been commonly observed in vanadium- or copper-based molecular complexes employing the AC spectrometry technique as a probe [30,38,78]. In those cases, the field dependence of the magnetization relaxation time (τ) has been rationalized through the semi-empirical model by Brons-van Vleck [79].

$$\tau^{-1} = cH^4 + d\frac{(1+eH^2)}{(1+fH^2)} \tag{2.5}$$

In Eq.2.5, the first term accounts for the effect of the direct relaxation process weighted by a constant value *c*. The second term accounts for the effect of internal fields due to spin-spin or nucleus-spin hyperfine coupling interactions. The other constant parameters d, e, and *f* represent the relaxation coefficient at zero-field, the weight of the magnetic field on spin-spin and spin-nucleus induced relaxation, and the efficiency of suppressing this kind of contributions when enhancing the magnetic field strength, respectively. As it has been observed, the *d* parameter shows an exponential *T* dependence analogously to what is usually observed for Arrhenius-like dynamics [80].

As stated above, two more processes may be competitive with this first-order relaxation mechanism, i.e., the Orbach and the Raman ones. When the Orbach relaxation process occurs, spins must overcome an energy barrier U_{eff} to reach the final state $|\beta\rangle$. Such a process requires the absorption/emission of several phonons to jump from a generic spin-state to the successive one. The overall process thus follows a relaxation dynamic of the form:

$$\frac{1}{T_1^{Orbach}} \propto exp\left(\frac{-U_{eff}}{k_B T}\right) \tag{2.6}$$

In this case, adsorbed and emitted phonons must match the difference in energy between the two states. Because of its nature, the Orbach model is commonly employed to reproduce the relaxation behavior of systems with larger spin states than $S = 1/2$ and presenting an Ising-type anisotropy (i.e., presenting an easy-axis anisotropy; see Appendix A). This model cannot be employed for pure $S = 1/2$ systems (i.e., those systems having no magnetically active excited states) or for systems presenting an easy-plane anisotropy.

The Raman relaxation process resembles what is usually observed for Raman optical spectroscopies. We may refer to such a process as a scattering-like relaxation mechanism where a lattice phonon couples to the spin, facilitating its relaxation. As an example, in a two-level system like a $S = 1/2$, the spin transition from a state $|\alpha\rangle$ to a state $|\beta\rangle$ is promoted by the simultaneous adsorption/emission of two phonons (Fig.2.4). For clarity, the process characterized by the absorption of a first phonon and the emission of a second one is equivalent to the inverse case. The first absorbed or emitted phonon causes the spin to transit from the $|\alpha\rangle$ ground state to a virtual metastable state. Thus, the excited spin relaxes to the final state $|\beta\rangle$ by the emission or absorption of a second phonon. Depending on the system and on the magnetic field strength, the second phonon can be of the same energy (see Sec.4.3) or, as it is reported in the figure, higher in energy with respect to the first one adsorbed. We need to mention that these two phenomena co-occur since the lifetime of metastable states is practically null [81]. Indeed, the system only virtually reaches such states while a partial admixing of ground and excited magnetic states occurs during the process, hence causing relaxation.

To understand the last consideration, let us consider the case of the dysprosium(III) complex shown in Chap.4 Sec.4.3. This peculiar case exemplifies how the Raman relaxation process contributes to spin relaxation. In that case, the relaxation process that drives the spin relaxation involves the spin transition between the two fundamental states of the Kramers' doublet $m_J = \pm 15/2$ even in zero-field (Fig.2.5). We can state that the spin experiences a transition from the initial to the final state through a virtual metastable state. Indeed, even if the transition is forbidden (see the Kramers' theorem above), it is here allowed because of the admixing with excited states that led to a new set of non-pure m_J states.

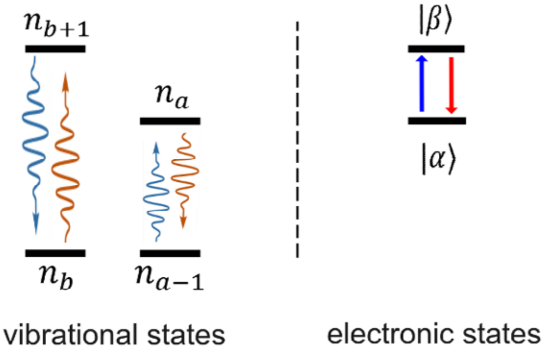

Figure 2.4. Pictorial representation of possible two-phonon processes that may occur during the Raman relaxation process causing a spin transition from $|\alpha\rangle$ to $|\beta\rangle$ or *vice versa*. Curly arrows represent phonon transitions, while solid arrows account for electronic ones (cyan + blue = emission/absorption process, orange + red = absorption/emission process).

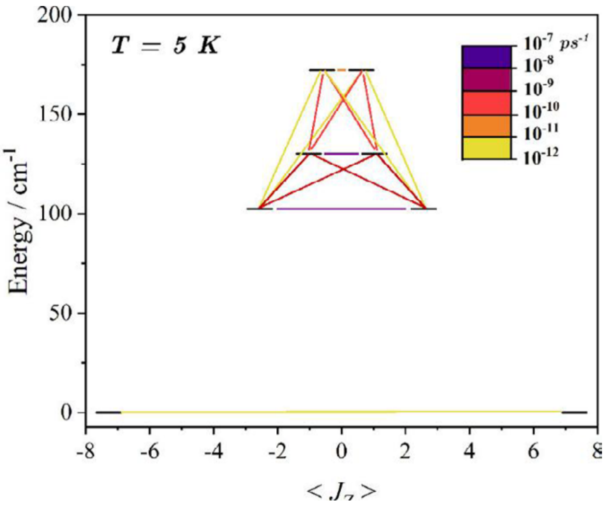

Figure 2.5. Plot of computed relaxation rates due to the Raman relaxation process for the **Dyacac** complex reported in Chap.4. Adapted from [81].

The process presented in Fig.2.4 is that one for a $S > 1/2$ under the effect of a static field, and the difference in energy between adsorbed phonons is represented by adopting blue arrows of different lengths. It follows that if higher- or lower-energy phonons are available at the thermal energy of the system (i.e., the ΔE between states is not matched), the relaxation could still take place. Usually, such a process follows a temperature dependence of the type:

$$\frac{1}{T_1^{Raman}} \propto T^n \quad n = 3, 7, 8, 9 \tag{2.7}$$

Like Eq.2.4, Eq.2.7 derives from phenomenological considerations. The exponent may, in fact, vary depending on the investigated system. While larger values are usually employed to reproduce the relaxation behaviors of single-molecule magnets [82], an exponent $n = 3$ is often employed for the molecular spin system of $S = 1/2$ species [38, 77, 83]. As a consequence, no microscopic physical interpretation can be provided with this model. Many efforts have been directed toward the investigation of the microscopic origin of such phenomena, both in molecular qubits and lanthanide-based single-molecule magnets [69, 84, 85, 86, 87]. Supporting experimental results by employing *ab initio* calculations has been abundantly stressed here; more details will be provided in the following chapters.

Magnetic resonance communities often refer to a different relaxation path described as *Local Modes Relaxation*. This mechanism occurs when localized lattice modes contribute to spin-lattice relaxation [88]. Such a relaxation process is the dominant one in molecular and covalently linked crystals, and many studies aimed at investigating the origin of relaxation in SMMs and molecular qubits revealed that this might be appropriately identified as the first source of Raman-like relaxation [84]. The correlated temperature-dependent relaxation process follows the phenomenological model:

$$\frac{1}{T_1^{LM}} = A_{loc}\frac{e^{\frac{\Delta_{loc}}{k_B T}}}{\left(e^{\frac{\Delta_{loc}}{k_B T}} - 1\right)^2} \tag{2.8}$$

Where A_{loc} is the weighting coefficient for a given local mode and Δ_{loc} its energy. Moreover, more than one local mode can be introduced by expanding the expression as a sum over the whole set of involved modes.

Since the presented contributions strictly depend on temperature, the weight of each term is correlated to the thermal energy of the spin bath. Indeed, if we consider a single spin $S = 1/2$, the direct process dominates the low-temperature regime, while the Raman relaxation process is the most active in the high-temperature one. At low temperature, e.g., from 2 K to 20 K, only few low-energy phonons (1 cm^{-1} up to 20 cm^{-1}) are active, and they could match exactly the difference in energy between the two states $|\alpha\rangle$ and $|\beta\rangle$. Plenty of phononic modes become instead available as the temperature increases, causing the spin to relax through virtual state pathways.

On the other hand, when a spin with higher multiplicity is the probed one (such as an SMM), the Raman process dominates at low temperature while the Orbach one drives the relaxation in the high-temperature range (see Chap.4, Sec.4.3). This fact results from the different energy levels scheme observed for highly anisotropic lanthanide-based systems with respect to molecular qubits based on transition metal ions. Indeed, it would be possible that specific phonons favor the spin to undergo an under-barrier relaxation process through metastable states. At higher temperatures, the spin system can couple with different phonon modes to overcome the energy barrier and reach the final state following a multi-step process.

2.5 Spin-Spin Relaxation and Related Phenomena

The spin-spin relaxation process is related to the coherence loss in spin qubits. Let us take an ensemble of molecular spin qubits as an example. The decoherence phenomenon takes place when losing the phase of the oscillatory precession of the magnetization in the *xy* plane according to the rotating framework convention (see Appendix A and Chap.1). This results in a loss of information on the state $|\psi\rangle$ obtained as the superimposition of the two basis states $|0\rangle$ and $|1\rangle$.

As previously stated, the spin-spin relaxation process follows relaxation dynamics depending on constant T_2. Longitudinal relaxation and flip-flop transitions of neighboring spins contribute to the dephasing phenomenon. For clarity, the flip-flop phenomenon for a pair of spins could be visualized as $|\uparrow\downarrow\rangle \rightarrow |\downarrow\uparrow\rangle$, i.e., a zero-quantum transition. It follows that T_2 is a function both of T_1 (i.e., the time in which the initial state $|0\rangle$ is recovered) and of a second contribution T_2' correlated to the zero-quantum transitions [62]. In particular:

$$\frac{1}{T_2} = \frac{1}{2T_1} + \frac{1}{T_2'} \tag{2.9}$$

However, as stated in Sec.2.3, T_2 is a meaningful parameter when we are considering the decoherence properties of a spin ensemble in solids. As stated in [62]: *it is also impossible to make a clear cut between a finite spin system that behaves coherently and its environment. It depends very much on the actual experiment how many mutually coupled spins exhibit coherent and reversible dynamics*. We thus refer to the empirical parameter T_m taken as the lower experimental limit of T_2, which includes other contributions arising from a wide variety of phenomena. Among them, we can recall instantaneous diffusion and other relaxation mechanisms due to dipolar interactions. The constant T_m is correlated to the decay of the primary echo of the spin system and can be collected by the Hahn echo technique (see Appendix A.3 pp.).

In general, there are two classes of contributions to the molecular spin qubits' decoherence, i.e., the dipolar interaction with other electron spins and with active nuclei of the surrounding. We can consider two distinct regions of temperature when rationalizing the coherence of a molecular spin ensemble. The spin relaxation in the high-temperature regime (usually above 20/30 K) is generally driven by the longitudinal relaxation process, which practically limits T_m. When the temperature is lowered below 20 K (low-temperature regime), T_1 and T_m can differ up to two or three orders of magnitude [38,83]. As an example, T_1 can reach values from 1 to 100 ms at 5 K, while T_m is far shorter than 100 μs. It follows that the transverse relaxation process is the primary source of relaxation at these temperatures. For clarity, the definition of low- and high-temperature regimes must be restricted to the considered case because it depends on the Hamiltonian of the system.

Several contributions can be evidenced as a source of decoherence [89]. At first, the most straightforward source of decoherence can be correlated to a dipolar-like interaction of the spin center with active nuclei of the ensemble (namely, a hyperfine coupling interaction). Another source of decoherence can be correlated to the molecular motion of functional groups within the ligand, e.g., methyl group rotation around the R-CH_3 axis [88]. Furthermore, electron spins and nuclei can interact through spin diffusion mechanisms. We will thus analyze all the presented cases.

While the dipolar spin-spin contribution can be easily lowered by diluting the spin centers, adopting both solid- or liquid-phase dilutions (See Chap.4, 5, and 6), the reduction of spin-nucleus interactions is instead not trivial. This particular task has represented one of the central subjects of this thesis.

The nature of the electron-nuclear coupling interaction depends mainly on the distance between the two spins. The electron spin can interact with the nuclear momentum of the same paramagnetic center through the hyperfine coupling interaction that practically limits T_1 and, subsequently, T_m. Furthermore, the paramagnetic ion may interact with directly bonded active nuclei through a superhyperfine coupling interaction. This latter type of interaction has been demonstrated to set the limit of T_m when the electron spin-spin interactions are removed or largely reduced [90]. Whereas this latter type of contribution is similar to a dipolar interaction, it can spread through the space to other active nuclei such as ^1H or ^{14}N and decrease with the distance from the spin center as $1/r^3$.

Another source of decoherence arises from active nuclei placed beyond a well-defined distance called the *spin diffusion barrier*. This process is called spin diffusion, and in molecular qubits, it is mostly due to protons placed at 4 - 6 Å from the electron spin. Here, the decoherence efficiency is not a monotonic function of the electron-nuclear distance. In a nutshell, magnetic moments within the barrier cannot relax due to external stochastic oscillating fields since they are too strongly coupled with the magnetic moment of the paramagnetic center. The magnetic interaction with the paramagnetic center is lost as the distance reaches a critical radius. Then, nuclear moments can undergo zero-quantum transitions such as the *flip-flop* relaxation process mentioned above (Fig.2.6). This behavior is more marked for spins lying on the border of the diffusion sphere. At the same time, it decreases as the distance from the spin center increases [91].

Contrary to what has been reported for longitudinal relaxation mechanisms in Sec.2.4, the rationalization of the coherence time behavior as a function of T is not trivial, and it does not follow a general rule. In many cases, it is instead possible to adopt a model for reproducing the trend of T_m vs T for paramagnetic centers dipole-coupled with surrounding nuclei. For instance, we consider a $S = 1/2$ system where the T_m behavior can be rationalized by considering only the dipolar-like

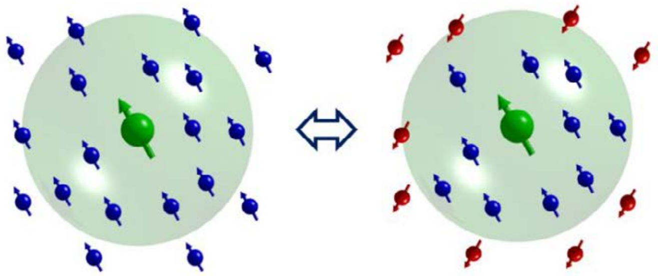

Figure 2.6. Pictorial representation of the flip-flop transition of nuclear spins (red and blue nuclei and arrows) coupled with a generic spin (green nucleus and arrow). The spin diffusion barrier is represented as a transparent green sphere.

interactions between electron and nuclear spin, neglecting those correlated to spin diffusion mechanisms. In the limit of low spin-spin dipolar interaction, the nuclear contribution to T_m can be computed by adopting the model [92]:

$$T_m = \frac{\hbar\Delta}{E_n^2} \tag{2.10}$$

Where E_n is the nuclear contribution to the echo linewidth, and Δ is the energy gap between the two spin states (e.g., at the operation frequency of Q-band EPR $\nu \approx 33$ GHz, the Δ is of ≈ 1 cm^{-1}). In accordance with [92], the E_n values can thus be computed as: $E_n^2 = \sum_k \left(\omega_k^{||}\right)^2 I_k(I_k + 1)/3$. Here $\omega_{\cdot k}$ is the difference between the interaction energies of the electron spin with the k-th active nucleus when the spin is in the state $|m_s\rangle = |+1/2\rangle$ or $|m_s\rangle = |-1/2\rangle$. Extended formula for the computation of E_n values are also reported in [66,90], that inspired the authors of [92].

The presented treatment is introductory to the following chapter, in which we will discuss the different molecular strategies proposed so far for obtaining the best-performing molecular spin qubits.

Chapter 3
Magnetic molecules for quantum information science

In the previous chapter, we discussed many proposed systems for implementing quantum computing. Furthermore, we presented a detailed analysis of relaxation properties in electron spin qubits, particularly molecular-based systems. These systems have been widely investigated in this thesis since they guarantee readily tunable properties as a function of the structure and magnetic properties involved. Upon these observations, chemists proposed plenty of examples showing how different molecular approaches can give the chance to tune the relaxation properties of qubits finely. In this chapter, we present an overview of different molecular strategies proposed so far. We will also show a few examples of how to couple a rational molecular design with advanced EPR strategies to get a specific enhancement of the qubits' coherence properties. Ultimately, we will show many currently proposed examples of *ad hoc* designed multifunctional molecules successfully employed as molecular quantum logic gates.

3.1 Molecular Spin Qubits

As stated in Chap.2, molecular magnets represent an outstanding playground for scientists interested in developing quantum technologies. We could say that molecules are tunable platforms from chemical (molecular design) and physical (engineering of spin Hamiltonian) points of view. Indeed, compared to solid-state systems, molecules are characterized by various properties that strictly depend on their chemical, structural, electronic, and magnetic properties. Among these advantages, we may recall those reported in [52]: i) it would be possible to address

Fabio Santanni, University of Florence, Italy, santannifabio@gmail.com, 0000-0002-0506-8333

Referee List (DOI 10.36253/fup_referee_list)
FUP Best Practice in Scholarly Publishing (DOI 10.36253/fup_best_practice)

Fabio Santanni, *Molecular approaches for quantum technologies. Optimization of electron spin-based quantum bits and quantum logic gates*, © 2025 Author(s), CC BY 4.0, published by Firenze University Press, ISBN 979-12-215-0670-9, DOI 10.36253/979-12-215-0670-9

individual qubits with microwave pulses; ii) it would be possible to tune (chemically) and control (e.g., optically) the qubit-qubit interaction; iii) they can be characterized by a multilevel structure (nuclear or electronic), with which is thus possible to perform different kind of quantum operations (i.e., quantum logical operations and quantum error correction algorithms); iv) they offer the possibility of encoding qubits in chiral structures (indeed, chirality can protect qubits from decoherence properties) [93]; v) their magnetic properties, and subsequently the encoded computational states, can be manipulated through electric field modulation, which is more selective and gives the chance of a better targeted addressing of qubits [94]; vi) in many cases, their optical properties can be tuned in order to achieve hybrid spin-photon devices [95, 96], whose manipulation with light sources as lasers can offer several advantages in terms of time (i.e., manipulation time, but also coherence time), and selectivity; vii) physical hardware can be obtained by exploiting surface deposition techniques and taking advantage from the organization properties of molecular systems on surface. Moreover, they can be investigated and singularly addressed on surfaces, thanks to scanning probe microscopy techniques (e.g., STM, STS) [97]. However, it is still challenging to selectively probe magnetic levels or investigate the relaxation properties of these systems at the single-molecule level. Nevertheless, several works have recently reported intriguing examples of manipulations and investigation of coherence properties [98− 100].

The general idea of using magnetic molecules as potential candidates for quantum computing emerged in the first decade of this century. Indeed, while polynuclear compounds with high-spin states such as Mn_{12} and Fe_8 had been widely investigated as single-molecule magnets [101,102], the same systems started to arouse interest in the quantum information scenario because of the large set of perfectly characterized magnetic levels [103]. Following this idea, the first set of measurements aimed at exploring the coherence properties of a molecular magnet for quantum information applications were performed on Fe_8 [104]. A different appealing platform to encode qubits is represented by the $\{Cr_7Ni\}$ cluster [105, 106] (Fig.3.1). First obtained by the Molecular Magnetism Group in Manchester, this compound is among the first examples of metal clusters presenting a giant $S = 1/2$ ground state, for which Rabi oscillations (Chap.1) can be recorded at the liquid helium temperature. Such a compound and its derivatives are still being investigated to obtain multi-qubit architectures suitable for quantum logical gates operations [108−110].

However, the close dependence on spin-lattice relaxation leads these systems to undergo quite fast decoherence dynamics. Here, appreciable coherence properties can be observed below 10 K, where the fully populated state is with $S = 1/2$. As the temperature goes beyond the 4−5 K limit, excited states characterized by a higher spin multiplicity (e.g., the first excited state $S = 3/2$) become populated, and the Orbach process contributes to the dynamics increasing the spin-lattice relaxation rate. As shown in Fig.3.2, the Orbach process becomes

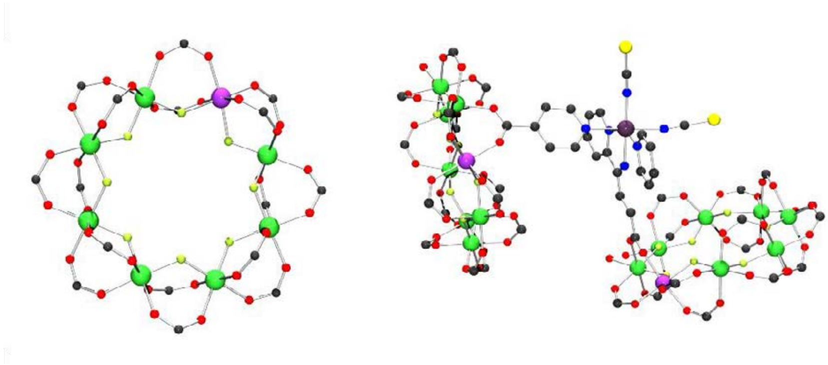

Figure 3.1. On the left, molecular structure of the complex $[Cr_7NiF_8(O_2CCMe_3)_{16}]$ [107]. On the right side, molecular structure of the $\{Cr_7Ni\}$-Co^{II}-$\{Cr_7Ni\}$ proposed as a candidate for implementing CNOT operation [108]. Color code: C = black, N = blue, O = red, F = lime green, S = yellow, Cr = green, Ni = purple, Co = violet.

the principal source of relaxation above 4 K. At 6 K, when T_1 reaches the same order of magnitude of the coherence time, the T_2 values dramatically collapse [106]. However, a T_2 enhancement has been observed in the analogue structure containing deuterated ligands, in which dipolar interactions with hydrogens have been removed efficiently.

Based on these observations, later works were directed toward the investigation of magnetic molecules containing a single ion with a total $S = 1/2$ (e.g., a coordination compound containing a copper(II) ion or a mono-radical system), thus avoiding possible contributions to the relaxation process arising from excited spin states. Let us recall the energy levels scheme for a $S = 1/2$ system in the absence of any other contributions to its spin Hamiltonian except the Zeeman one. Under the effect of a static magnetic field oriented along the z quantization axis, the levels' scheme is simply described by a two-level model where the ground and excited states $|S, m_S\rangle = |1/2, \pm 1/2\rangle$ are split in energy proportionally to the strength of the field. Because they are perfectly addressable and manipulable to implement quantum operations [40,52], thus fulfilling the fundamental requirement previously presented in Chap.2, it is sensible to choose them as the $|0\rangle$ and $|1\rangle$ computational states. In this respect, the well-known copper(II) ($S = 1/2$) complex with the phthalocyanine ligand, [Cu(Pc)], has been investigated for this purpose because of its electronic structure [66].

The study of its coherence properties was conducted on a diluted sample by employing pulsed EPR technique as a probe. In this example, coherence times of several microseconds have been observed up to 80 K.

Following this example, other macrocyclic-based complexes have been investigated so far, e.g., vanadyl and copper complexes of porphyrins and porphyrazines [38,77,84,111,112]. All these works show how these compounds may present different appealing features as potential qubits, such as coherence of

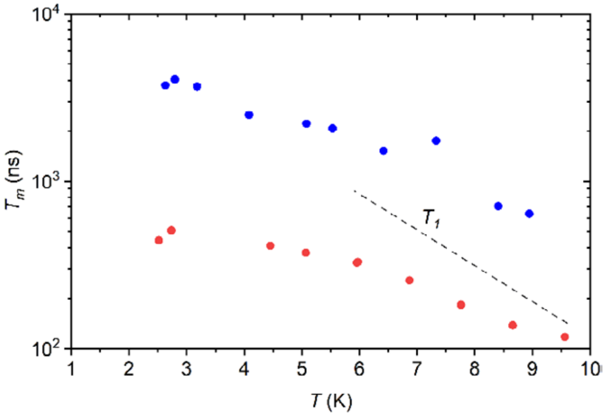

Figure 3.2. Plot of T_m as a function of temperature obtained by pulsed EPR measurements at X-band (9.5 GHz) on Cr_7Ni (red circles) and Cr_7Ni-d_8 (blue circles). The dashed line approximatively indicates the trend of T_1 and its values above 6 K for the Cr_7Ni system. Data are extracted from [106].

about 1 - 2 μs up to room temperature and the possibility of depositing them on surfaces [97,111,113].

Furthermore, macrocycle-based molecules containing porphyrins have been employed to get multi-dimensional arrays of qubits such as 2D or 3D-MOFs (Metal-Organic Frameworks), where units might be anchored to each other to implement systems suitable for quantum sensing and quantum information science [111112]. However, these examples show relatively low coherence times due to the decoherence induced by the nuclei in the molecular structures, i.e., bonded nitrogen and peripheral hydrogen atoms (see Chap.4, Sec.4.1 for more insight on this subject).

Nowadays, coherence times have been so enhanced that hundreds of μs have been reached (Fig.3.3). Important examples of molecular spin qubits obtained employing first row's transition metal ions are certainly those containing copper(II), vanadium(IV), and oxovanadium(IV) (namely vanadyl) cations embedded in rigid [38,114] or nuclear-spin free environment [61,67,83].

Adopting vanadium(IV) ions results in a general T_1 enhancement because of the lower spin-orbit contribution than copper(II) ions. Indeed, it has been demonstrated that a general increase of T_1 can be obtained by reducing the spin-orbit coupling interaction or the total angular momentum contributions, including target ions such as vanadium(IV), titanium(III), or scandium(II) [38,92,115]. It has also been observed that molecular complexes containing the vanadyl moiety can show an appreciable coherence time enhancement above 30 K with respect to those containing vanadium(IV) ion [80,83]. Here, the abrupt decrease of T_1 limits the coherence properties of the system, reducing T_m.

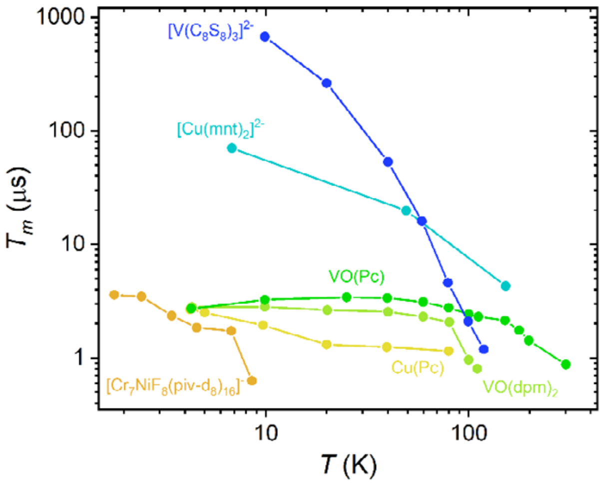

Figure 3.3. Plot of coherence time values (T_m) as a function of the temperature for some of the aforementioned molecular systems. Data have been extracted from [38,61,66,67,78, 106].

This latter observation can be explained as follows. Vanadyl complexes generally show a square pyramidal coordination geometry composed of the four bonding atoms of ligands on the plane of vanadium and the apical oxygen atom (V=O). In this coordination geometry, the unpaired electron of vanadium(IV) (d^1) resides in the low-lying magnetic orbital d_{xy}, which is well-isolated from higher energy orbitals. On the other hand, vanadium(IV) complexes prefer a trigonal coordination geometry. The low-lying orbital, in this case, is the d_{z^2} one. Here, d_{z^2} is less separated in energy from other excited d orbitals with respect to the case of d_{xy} in vanadyl. It follows that the orbital contribution is not efficaciously quenched, and the energetic contribution due to the spin-orbit coupling is larger. Consequently, vanadium(IV) tris-chelated compounds undergo faster spin-lattice relaxation at high temperatures due to the stronger effect of the spin-phonon coupling interaction. However, the abrupt decrease of T_1 in tris-chelated vanadium(IV) complexes is also correlated to the smaller rigidity of their coordination environment than that of bis-chelated vanadyl complexes.

Adopting rigid ligands and rigid coordination environments is thus of extreme importance for enhancing the longitudinal relaxation time of molecules. Such a molecular strategy gives the chance of reducing the number of available phonons within the crystal lattice, thus generally leading to a T_1 enhancement. The decrease of the spin-lattice relaxation rate is observed, especially at higher temperatures where the Raman process drives the spin relaxation (Chap.2, Sec.2.4). Many examples are reported in [69,77,80,114]. Furthermore, the adoption of nonsubstituted ligands, such as catechol or tetraphenyl porphyrins, removes alkyl groups that hamper the spin relaxation dynamics of molecular qubits. For instance, several studies of the spin dynamics of acetylacetonate ($CH_3COCHCOCH_3^-$) or diethyldithiocarbamate ($(CH_3CH_2)_2NCS_2^-$) complexes of vanadium(IV) and copper(II) highlighted the effect of ethyl- or methyl groups in reducing the T_m of molecular complexes as soon as the temperature is sufficiently high to allow rotational motions [78,80,116].

All the mentioned examples highlight the effect of various contributions to T_1. Indeed, enhancing T_1 is also of utmost importance to guaranteeing longer coherence times in molecular systems. However, many other molecular strategies can be adopted to enhance the coherence time of molecular qubits directly. As discussed in Chap.2, the effect of nuclei (within the ligand or surrounding) on the coherence properties of spins is detrimental. Different contributions can arise from hyperfine interactions and spin-diffusion mechanisms (see also Fig.3.2). While removing nuclear spins from the coordination sphere can be sensibly gained by adopting oxygen or sulfur atoms, removing those hydrogen atoms commonly present in organic ligands can be challenging. It has been already mentioned in Chap.2 that protons can strongly interact with the spin through dipolar interactions or spin diffusion mechanisms. Evidence of the latter phenomenon can be found in these papers [117,118], in which organic radicals and vanadium(IV) metal complexes have been extensively investigated. In particular, the role of spin diffusion processes on the coherence time of molecular spin qubits is well-argued by D. Freedman and coworkers in [118,119]. They employed an extensive synthetic approach, pulsed EPR, and Dynamic Nuclear Polarization (DNP) experiments. As soon as the distance between hydrogen atoms within peripheral positions of sulfur-rich ligands and the central magnetic ion increases to a critical value, the coherence time of those potential molecular qubits decreases dramatically. A representative picture of such a phenomenon extracted from this work is reported in Fig.3.4.

In this respect, there are two main works reporting a coherence time enhancement in molecular qubits where nuclear spins have been successfully removed from both the coordination sphere of the central ion and the environment [61,67]. In both cases, hydrogen atoms have been removed by employing hydrogen-free ligand and counterions (e.g., the deuterated PPh_4^+ anion), and by replacing coordinating atoms with virtually non-active nuclei, such as sulfur (^{32}S, natural abundance (NA) = 94.99%, $I = 0$).

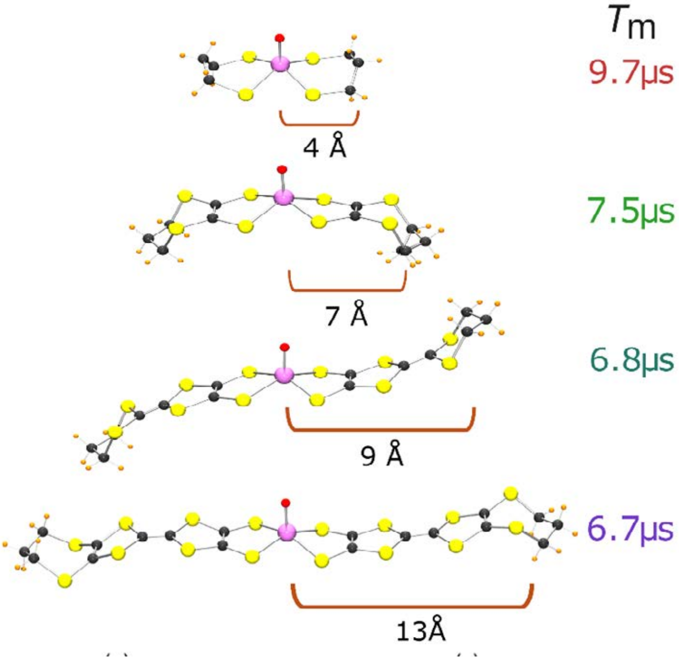

Figure 3.4. Molecular structures of compounds probed in [118]. The T_m values collected by Hahn echo experiments at 40 K evidence that coherence decreases dramatically when the distance from hydrogens and vanadium overcomes 6 Å, i.e., the limit of the diffusion barrier. Color code: C = black, H = orange, O = red, S = yellow, V = pink.

The dithiolene-based system proposed by Freedman and coworkers in [61] represents state of the art in this scenario. Here, the authors observed a T_m of 1 ms at low temperature adopting a diluted sample of $[V(C_8S_8)]^{2-}$ (six S atoms of the ligand coordinate the V^{IV} ion) in CS_2 solution.

The effect of active nuclei on coherence can also be correlated to their position within the ligand. As observed in this work by Zadrozny *et al.* [120], it is possible to tune the coherence time of qubits by chemically addressing the different relative positions of hydrogen and bromine atoms (^{79}Br, NA = 50.69 %, $I = 3/2$; ^{81}Br, NA = 49.31 %, $I = 3/2$) on catechol derivatives. They demonstrated that different dephasing phenomena, principally due to spin-diffusion mechanisms, may arise depending on the protons and bromine positions more than their relative distances from the spin center. Indeed, minimal variation in H···H distances does not affect T_m significantly. At the same time, a dramatic T_m decrease has been observed for 4,5-dibromocatechol. The hydrogen atoms in positions 3 and 6 present the same NMR transition resonance, i.e., the same chemical shift, because of the symmetry of the molecule and the weak nuclear coupling interaction. This additional feature contributes to enhancing the decoherence firstly induced by the spin-diffusion mechanism.

As stated before, adopting a molecular system characterized by a total $S = 1/2$ is advantageous in terms of the coherence properties of molecular qubits. However, adopting systems with multilevel nuclear or electronic structure (e.g., with a total $S > 1/2$ or $I \neq 0$) would be advantageous as well for operating logical operations at the single-molecule level. Recent works aimed at understanding how such architectures, namely *qudits* or ”logical qubits”, may be employed in quantum information science showed that quantum error correction could be embedded in a single object thanks to this multi-levels nature of molecular qubits [33,45,46,110,115,121,122], thus increasing the interest on such devices. Lanthanide ions also started to arouse interest as potential qudits. As an example, the Grover’s algorithm has been successfully implemented by exploiting the multilevel structure of terbium(III) single-qubit [123]. The algorithm implementation was accomplished by exploiting the four nuclear levels of a single $Tb(Pc)_2$ molecule ($I = 3/2$) when frozen in its fundamental state characterized by a total angular moment $J = 6$. Each of the three possible transitions among the four nuclear states can be selectively probed since the quadrupolar contribution to the hyperfine coupling makes them different in energy, i.e., $\nu_{1-3} = 2.45, 5.58,$ and 9.39 GHz. In this case, the system successfully encodes a four-state qudit, which can be probed through microwave pulses. Then, using the apparatus schematized in Fig.3.5, the authors were able to read out the nuclear spin state of the manipulated qudit by using transport measurements at the single-molecule level.

Reducing the number of active nuclei is an arduous task, especially if combined with the need for neutral compounds suitable for surface deposition experiments (e.g., porphyrin- and phthalocyanine-based compounds) that guarantee the control of deposited molecules at the monolayer level (e.g., physical vapor deposition: PVD). Indeed, investigating the properties of molecules deposited on surfaces is extremely important in the view of the realization of prototypical hardware employable in quantum computers. In Chap.4, we will present two possible molecular systems developed during these years. These systems have been selected since they are hydrogen-free and neutral compounds, thus fulfilling both the requirements of reducing nuclear contributions to coherence properties and being suitable for PVD experiments. The principal objective of the reported works is to extend the knowledge on the nuclear contribution to the decoherence processes of molecular qubits. Moreover, we will focus on understanding the relaxation properties of both transition metal and lanthanide complexes, giving many insights into the different contributions affecting the spin dynamics of potential qubits. Indeed, both transition metals and lanthanide complexes are appealing platforms for implementing performing qubits.

Many other strategies aimed at enhancing the coherence time of a qubit involve the implementation of specific pulse sequences or the exploitation of some specific resonance frequencies, i.e., the atomic clock transitions observed in lanthanide and

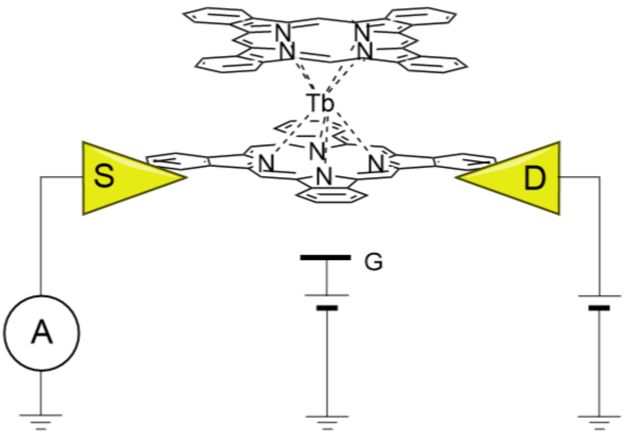

Figure 3.5. Representative scheme of the setup employed in [123]. The apparatus contains a single $TbPc_2$ molecule contacted to source (S) and drain (D) electrodes through the electromigration technique. The third electrode is the gate (G). The whole system forms a single-molecule transistor.

cluster-like molecular systems [124, 125]. Indeed, by adopting clock transitions as working resonances, it is possible to reduce the effect of the environment on the electron spin coherence.

In Chap.5, we will present two examples of how to employ EPR approaches to gain a coherence time enhancement or encode quantum memories in a $S = 1/2$ ensemble constituted of vanadyl complexes of the tetraphenyl porphyrin ligand

3.2 Molecular Quantum Logic Gates

The coherence time of qubits is a significant parameter, and the strategies to enhance it are still central tasks for chemists. Nevertheless, many other parameters must be considered to fulfill the requirements presented in Sec.2.1. Among them, obtaining multi-qubit architectures is one of the central tasks. It follows that even achieving an entanglement condition between parties is fundamental. Moreover, the coupling interaction should be tuned to fulfil an efficient addressability of distinct qubits instead of getting a system characterized by a giant total spin like in the case of metal clusters previously mentioned (e.g., Cr_7Ni, Fe_8, *etc.*).

There exist two main strategies for obtaining molecular quantum logical gates [108]: i) adopting systems where the interaction between parties can be switched by employing different processes (e.g., electromagnetic radiation, conformational transitions, *etc.*); ii) employing direct coupled units, i.e., non-switchable systems where the communication between different qubits is always on because of exchange interaction. It is essential to mention that the exchange coupling interaction should not be literally translated with an entanglement condition, but it may help obtain an entangled state [53].

Realizing molecular systems of the first type is sensibly preferable because the interaction between parties can be selectively switched on, for example, by adopting specific EPR pulse sequences. In this sense, rationalizing a possible scale-up procedure, which may lead to the realization of a complex multi-qubit architecture, is of easier deduction. However, two additional factors must be considered. At first, realizing such extended architectures is challenging from a synthetic point of view, especially if different metal ions have to be introduced within a single structure. Furthermore, it is tough to reconcile the necessity of obtaining scalable architectures with keeping control over the quantum properties of the systems. Many factors (e.g., dipolar or exchange interactions among spins) may also seriously hamper the coherence properties of such systems (see Chap.6, Sec.6.1).

As an example of a switchable gate, let us consider the CNOT gate obtained by employing the Cr_7Ni architectures presented in Fig.3.1 [108]. Two Cr_7Ni rings form the quantum gate, respectively functionalized with pyridyl and terpyridine units, linked to a central Co^{2+} ion whose coordination sphere is completed by two SCN^- ligands. The fundamental state of the Co^{2+} ion (d^7), according to the octahedral symmetry imposed by the ligands, is the $^4T_{1g}$ characterized by the high-spin electronic configuration $S = 3/2$. Because of the *Zero-Field Splitting* effect (see Appendix A), the ground spin state is the doublet represented by a giant $S = 1/2$ at $T = 5$ K. In this limit, the ground state is well isolated from the excited state. The overall architecture is then subject to a very weak exchange coupling between metal centers, i.e., the contribution of the exchange coupling is negligible with respect to the Zeeman interaction. The total spin system is that of an ABX one so that the exchange interaction between A (Cr_7Ni-O_2C-py) and B ($Co(SCN)_2$) is larger than that between B and X (terpy-CO_2-Cr_7Ni). This feature is due to the small anisotropic exchange interactions between Cr_7Ni rings and Co^{2+} ion. In this limit, a correlation condition between the eigenstates of the two sub-units Cr_7Ni is introduced because of the mentioned low exchange coupling interaction. Thus, we may refer to a total computational basis of the system expressed as it is reported in Eq.1.13.

Once the system is optimally engineered and practically obtained, we need to force it in a specific condition. Indeed, the Co^{2+} must be frozen down in its fundamental state of a $S = 1/2$, for example by lowering the temperature of the system. After that, we can enhance the strength of the external magnetic field up to 5 T to induce a large splitting between the two projection $M_S = \pm 1/2$ of the Co^{2+} central unit. The so obtained levels' scheme is that reported in Fig.3.6a.

The CNOT gate operation can be performed by employing a series of EPR pulses (Fig.3.6b) in order to: i) opportunely define an initial state for the two-qubit (e.g., the state $1/\sqrt{2}(|00\rangle + |10\rangle)$); ii) implement, in sequence, $R_y(\pi/2)$-C_Z-$R_y(-\pi/2)$ operations (see Chap.1) to implement the gate operation and reach the final entangled state $1/\sqrt{2}(|00\rangle + |11\rangle)$. The two R_y rotations (grey pulses in Fig.3.6b) are single qubit operations implemented in the computational space and

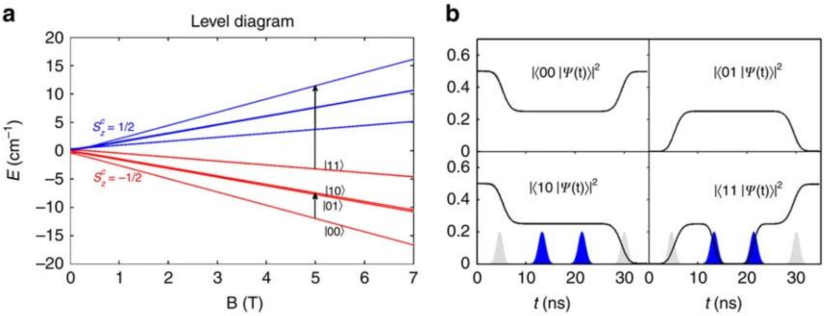

Figure 3.6. a) Energy Levels' scheme of the adduct {Cr_7Ni-O_2C-py} → [$Co(SCN)_2$] ← {terpy-CO_2Cr_7Ni}. b) Simulated plots of a CNOT gate operation for the mentioned system. Reproduced from [108].

do not alter the spin state of the cobalt ion. On the other hand, the C_Z operation (two consecutive pulses highlighted in blue in Fig.3.6b) involves the spin transition of the central Co^{2+} ion and, subsequently, the leaving of the computational space.

A molecular approach built for obtaining non-switchable two-qubit architectures may instead result in better control of the quantum properties of the system. Furthermore, synthesizing this latter type of system might be easier (see Chap.6, Sec.6.2).

A different example of interacting spins suitable for implementing non-switchable molecular quantum gates is reported in [126]. The exceptional molecular design employed resulted in a molecular complex containing two different lanthanide ions, namely an Er^{3+} and a Ce^{3+} ion (Fig.3.7a), which has been proven to be an appealing system for encoding the CNOT quantum gate. Because of the weak exchange interaction, the scheme of low-lying magnetic states of the system ($\Delta/k_B = 0.21$ K) is of the form reported in Fig.3.7b, where each state is one of the four Bell's states (Chap.1).

In the limit of the low-temperature regime, the two units behave as pseudo $S = 1/2$ coupled through an antiferromagnetic interaction. It follows that the low-lying state at zero-field is that made by the composition of $|01\rangle$ and $|10\rangle$ states, while excited states are those resulting from a ferromagnetic exchange interaction (i.e., $|11\rangle$ and $|00\rangle$). As the magnetic field strength rises, the energy levels split due to the Zeeman effect. Since the energy distance between the states is never the same, it is hence possible to selectively implement a CNOT gate operation on the ground state by employing a selective X-band pulse at 470 mT. As shown in Fig.3.7c, where states are labelled as $|00\rangle$, $|01\rangle$, $|10\rangle$ and $|11\rangle$ for simplicity, just one transition is resonant with the employed microwave pulse of 9.5 GHz. Hence, just the $|00\rangle \rightarrow |01\rangle$ transition is allowed. Here, contrarily to what was reported in Chap.2, the control bit operates on the target one when set on $|0\rangle$.

Adopting lanthanide or transition metal complexes, e.g., hetero or homonuclear lanthanide metal complexes [126,127], vanadyl complexes [54,128], metal clusters [108, 129], photogenerated molecular spin-qubits [59] or porphyrin-based metal complexes [130], the community has thus shown straightforward examples of promising molecular systems (based both on static and switchable qubits) for quantum logic gates implementation. The mentioned systems are great examples evidencing the massive potential of organic/inorganic synthesis as a tool for getting multi-qubit architectures. However, most of them show practical limitations for quantum computing. Referring to the previous example on the {Cr_7Ni} adduct, it might be difficult to employ different pulses to probe the two states |10⟩ |10⟩ with the appropriate selectivity grade. Indeed, an appealing molecular quantum logic gate should be composed of selectively addressable qubits, a condition emerging from fully addressable spin transitions observed as sharp bands on the EPR spectrum of the system.

In view of the preceding, Chap.6 of this thesis will treat two different systems investigated during these years. The former (Sec.6.1) was realized to be a first-type quantum gate, and the latter (Sec.6.2) to be a second-type quantum gate. Moreover, we will show these systems' advantages and practical limitations, giving insights on the targeted molecular approach employed to overcome them.

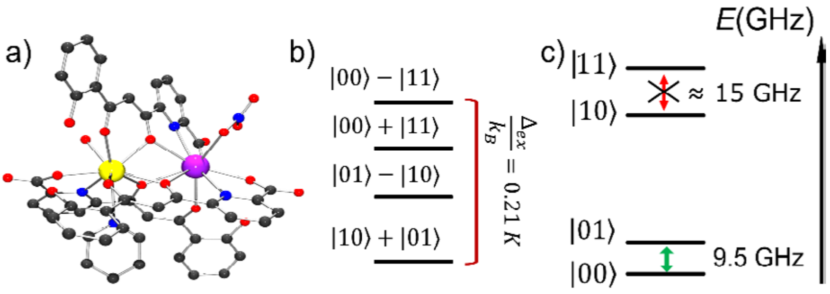

Figure 3.7.a) Molecular structure of the {ErCe} complex from [126]. Color code: C = black, N = blue, O = red, Ce = purple, Er = yellow; b) Energy scheme of the low-lying magnetic levels in zero-field; c) Energy scheme for the low-lying magnetic fields at 470 mT. In the figure, the 9.5 GHz transition allowing the CNOT gate implementation is highlighted in green. Crystal structure and energy levels scheme data are extracted from [126].

Chapter 4
Investigating the relaxation properties of molecular qubits

In the previous chapters, we outlined some of the fundamental properties of quantum bits. We discussed the importance of developing this research field on magnetic molecular systems, i.e., lanthanide and first-row transition ions coordination compounds. Indeed, several literature reports (see Chap.3) evidenced that, in addition to the tunability properties provided by their molecular nature, they guarantee an appreciable coherence time (T_m or T_2) over a wide range of temperatures [30]. As discussed in the introductory chapter, this is the first property of a qubit to be controlled, and we may safely state that the longer the coherence time, the better the qubit. Indeed, as T_m increases, the superposition state of two well-defined basis states is more stable and can be used for further logical operations [39]. As shown in Chap.2, several studies demonstrate how a T_1 and T_m enhancement can be achieved by *ad-hoc* engineering of metal complexes [61,67,83,114,131]. Furthermore, all these experimental results can be rationalized by theoretical calculations, which improve the understanding of the microscopic origin of relaxation mechanisms. Theoretical results can sensibly help synthetic chemists outline new guidelines for obtaining more performant molecular spin qubits [69, 132].

This chapter will directly face the importance of combining synthetic, experimental, and theoretical approaches to investigate relaxation phenomena in molecular complexes, particularly regarding potential molecular qubits. However, it will focus on obtaining long coherence times and controlling other relevant

Fabio Santanni, University of Florence, Italy, santannifabio@gmail.com, 0000-0002-0506-8333

Referee List (DOI 10.36253/fup_referee_list)
FUP Best Practice in Scholarly Publishing (DOI 10.36253/fup_best_practice)

Fabio Santanni, *Molecular approaches for quantum technologies. Optimization of electron spin-based quantum bits and quantum logic gates*, © 2025 Author(s), CC BY 4.0, published by Firenze University Press, ISBN 979-12-215-0670-9, DOI 10.36253/979-12-215-0670-9

parameters. As an example, the employing of a multilevel system would result in better exploitation of molecular qubits [45] both for quantum algorithms implementation [123], and quantum error correction (QEC) procedures [110]. In addition, integrating molecular qubits into solid-state devices, such as resonating circuits or superconductive devices, will be of utmost importance because it would afford a physical hardware adaptable for different quantum applications, e.g., quantum memories [133,134]. Using thermally stable and neutrally charged molecules would facilitate their integration into circuits through controllable methods such as thermal sublimation techniques. An example of this may be found in [135], where a single qubit readout was conducted on $[Tb(Pc)_2]$ molecular units sublimed on a solid-state device composed of source, drain, and gate electrodes.

The following sections will present many of our recent studies aimed at disentangling different contributions to the spin relaxation in molecular compounds that partially, or even wholly, fulfill the requirements listed below:

- A multilevel structure of electronic or nuclear states (Sec.4.1, Sec.4.2, Sec.4.3). As an example, Cu^{2+} accounts for a multilevel structure of nuclear states (^{63}Cu,^{65}Cu: I=3/2, isotopic abundance: 69.15% and 30.85%, respectively), while lanthanide ions account for multilevel structure of both electron and nuclear states.

- A nuclear spin-depleted environment so that T_m enhancement can be achieved (Sec.4.1, Sec.4.2).

- Neutral charge and appreciable thermal stability so that they can be employed for surface deposition experiments (Sec.4.1, Sec.4.2). In this respect, we employed aromatic or pseudo-aromatic ligands as charge-rich scaffolds to enhance interaction with surfaces.

4.1. [Cu(TTDPz)] as an hydrogen-free molecular qubit

As mentioned in Chap.2, the [Cu(Pc)] complex was among the first proposed single-ion qubits [66]. Similar molecular complexes containing analogous ligands (e.g., porphyrin and phthalocyanine derivatives [77,111,135]) have attracted further specific interest in the quantum information scenario because of their excellent features in terms of thermal stability [136] and surface adsorption [97,113,137]. At the same time, all these compounds present a short coherence time ($T_m \simeq 1-2\ \mu s$) within a wide temperature range [38,66]. The origin of such limited coherence times is twofold.

On the one hand, the effect of directly bonded nuclear nitrogen through superhyperfine coupling interaction drives the loss of coherence [66,124]. On the other hand, those hydrogen nuclei placed at 6 Å may affect the relaxation process because of spin-diffusion mechanisms [91,118]. Moreover, [Cu(Pc)] shows a dramatic loss of coherence above 100 K correlated to the abrupt decrease of T_1.

Since T_1 is mainly affected by spin-phonon coupling (SPC) (i.e., by the vibrational properties of single-molecule and crystal lattice), a detailed investigation in this sense is mandatory to disentangle different contributions to the spin relaxation.

We employed a combined experimental and theoretical approach to investigate the relaxation properties of porphyrazine-based molecular qubits and shed light on the effect of hydrogen nuclei on the coherence of the bonded ion in this class of compounds. In particular, we compared the relaxation and vibrational properties of two compounds: i) [Cu(TTDPz)] (**CuPz**), where TTDPz = tetrakis(thiadiazole)porphyrazine is the hydrogen-free analogue of H_2Pc (Fig.4.1); ii) the archetypical [Cu(Pc)] (**CuPc**). Although the coherence properties of these compounds were not comparable to those of dithiolene-base systems presented in Chap.3, the exceptional thermal stability usually observed in these systems makes them particularly appealing for surface deposition experiments. For instance, compounds H_2TTDPz, [Co(TTDPz)], and [VO(TTDPz)] have been successfully deposited on metal substrates and investigated through the STM/STS techniques [138−140].

Since [Cu(Pc)] is a common chemical, it can be conveniently purchased and purified before use. On the other hand, the **Pz** class of compounds must be specifically synthesized. The synthesis of **CuPz** can pursue two principal strategies (Fig.4.2): i) by employing the multi-step procedure reported in [143] (the strategy was adapted from the well-known Linstead method [144]); ii) by adopting a one-pot synthesis procedure, as it was reported in [145]. In the first case, the porphyrazine unit is obtained as magnesium complex by templating the macrocyclization of four 1,2,5-thiadiazole-3,4-dicarbonitrile (tdadc) molecules around an Mg^{2+} ion using a strong base. Therefore, the reaction is conducted in n-propanol by employing $Mg(PrO)_2$ formed in-situ.

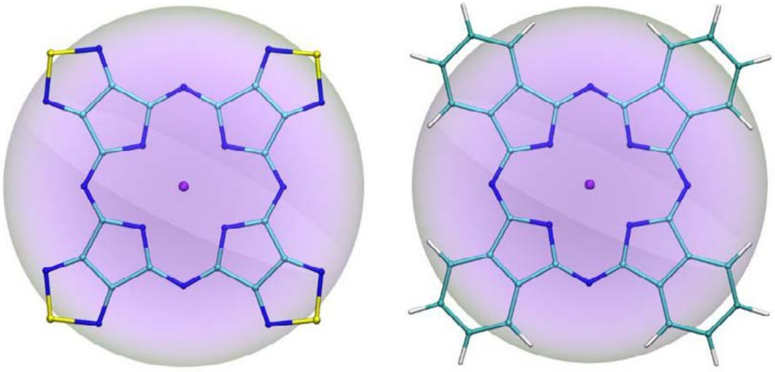

Figure 4.1. Molecular structures of [Cu(TTDPz)] (left) [141] and [Cu(Pc)] (right) [142]. Purple spheres behind structures represent a plausible spin-diffusion barrier of 6 Å. Color code: C = cyan, H = white, N = blue, S = yellow, Cu = violet. Reproduced from [84].

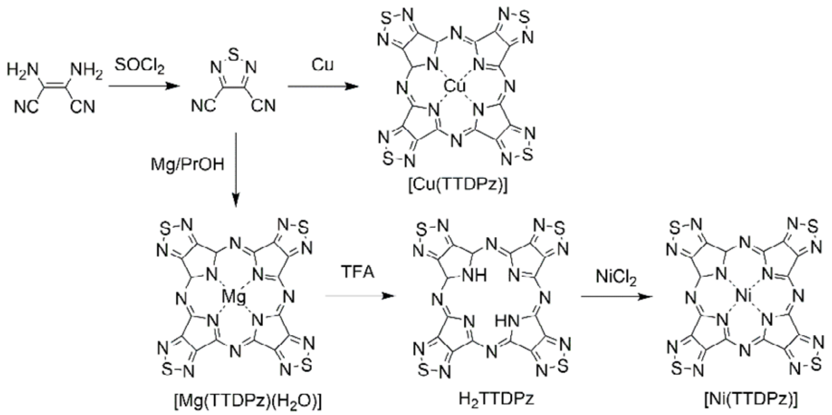

Figure 4.2. Synthetic steps employed for the obtaining of [Cu(TTDPz)] and related compounds. TFA = trifluoroacetic acid.

Such a step is crucial since several factors, e.g., the high moisture sensitivity of $Mg(PrO)_2$ (that is not a trivial aspect when working in alcohols) or the removal of Mg oxides and hydroxides impurities, may reduce the final yield or affect the product's purity. The isolation of the final product is particularly challenging. [Mg(TTDPz)(H_2O)] crushes out the solution as a nanocrystalline, or even amorphous, solid, which is stacked within a mixture of residual Mg salts, triazine impurities, and unreacted tdatc. Its isolation thus required several centrifugations and washing cycles adopting different solvent mixtures (e.g., MeOH, acetone, CH_2Cl_2, acetic acid, and water). This made it difficult to obtain both high yields and a sufficiently pure product at this step. However, the complete removal of Mg byproducts was fundamental. Indeed, the ligand H_2TTDPz is obtained by decomplexation of [Mg(TTDPz)(H_2O)] with strong acids, e.g., CF_3COOH (trifluoroacetic acid = TFA), and the presence of $Mg(OH)_2$ impurities may significantly reduce the yield of target ligand's synthesis. Once the ligand is obtained, various metal complexes can be synthesized by heterogeneous-phase reactions involving the respective metal salt precursor and dispersion of ligand in DMSO, pyridine, or DMF

Because this strategy did not guarantee good yields, especially at the first step involved, we preferred to adopt the second one-pot strategy proposed in [145]. In this case, **CuPz** is directly obtained by templating the macrocyclization of tdadc units with metallic Cu and adopting tdadc as the solvent for the reaction. Indeed, **CuPz** is synthesized at 180 °C under N_2 static pressure in a well-sealed Schlenk tube. Thus, tdadc rapidly undergoes a liquid-phase transition at these temperatures and reacts with metallic copper powder, forming the target product. At the end of the reaction, **CuPz** was obtained in satisfactory yields (up to 40%) as a polycrystalline solid (Fig.B.1). Furthermore, the only three identified contaminants were the initial dicyano-dithiazole, residual copper, and a triazine [145]. Both triazine and the organic precursor were quickly removed by washing with CH_2Cl_2, while residual Cu powder was washed away with a concentrated ammonia solution.

Strong spin-spin dipolar interactions usually characterize pure paramagnetic compounds. These effects are generally more marked for compounds presenting flat structures and characterized by strong stacking interaction between molecular units. These properties make molecular units largely packed within the crystal lattice, thus reducing the mean distance among spin centers. For example, the minimum distance between copper centers can range from 4 Å for **CuPc** to 8 Å for **CuPz**. It follows that a magnetic dilution is mandatory to reduce such interactions and enhance the coherence properties of molecular qubits (see Chaps.2 and 3). A common way to mitigate spin-spin interactions is to dilute molecular compounds with solvents or solid diamagnetic (and possibly isostructural) hosts. In this case, we initially decided to adopt the diamagnetic analog [Ni(TTDPz)] (**NiPz**) as a solid diluent. The Ni^{2+} ion is indeed diamagnetic when coordinated in the square planar geometry guaranteed by the employed ligand [141]. Furthermore, the isotopic abundance of ^{58}Ni, ^{60}Ni, and ^{62}Ni ($I = 0$), covers 98.9% of the entire isotopic distribution of the Ni element, thus guaranteeing a very low spin-nuclear contribution to the spin dynamics of **CuPz**. The diamagnetic compound **NiPz** was synthesized according to the first-mentioned strategy (Fig.4.2) and obtained as microcrystalline powder presenting a slightly different crystalline phase with respect to the α one reported in the literature (Fig.B.1). Diluted compounds were thus obtained by the coprecipitation of paramagnetic and diamagnetic species from a solution.

The compounds mentioned are not soluble in organic solvents or water, so their purification through standard techniques was impossible. This behavior could be strictly correlated to the strong interactions within molecules in the crystal. The absence of hydrogen atoms (hydrogens naturally keep molecules away from each other thanks to the steric hindrance) and the presence of diffuse sulfur atoms or electron-rich N atoms may be at the basis of stronger interactions (i.e., stacking and van der Waals ones). For this reason, all the obtained systems were purified by thermal treatment at ≈ 400 °C in vacuum (10^{-2} mbar). Moreover, the lack of solubility seriously complicated most of the necessary steps for obtaining diluted compounds, and strong acids were employed to get target solutions of paramagnetic and diamagnetic species. A magnetically diluted sample **Cu$_{20\%}$Pz** was obtained by the coprecipitation of Cu^{2+} and Ni^{2+} analogs from CH_3SO_3H (methanesulfonic acid = MSA) solutions at 0 °C (to avoid decomposition of dissolved compounds) by the addition of i-PrOH. However, we found a percentage of about 0.25 % of paramagnetic Ni centers characterized by an $S = 1$ within the pure **NiPz** sample (Fig.B.2) after its treatment with MSA. Such a phenomenon was probably due to the formation of a small amount of octahedral Ni centers after exposure to such harsh conditions.

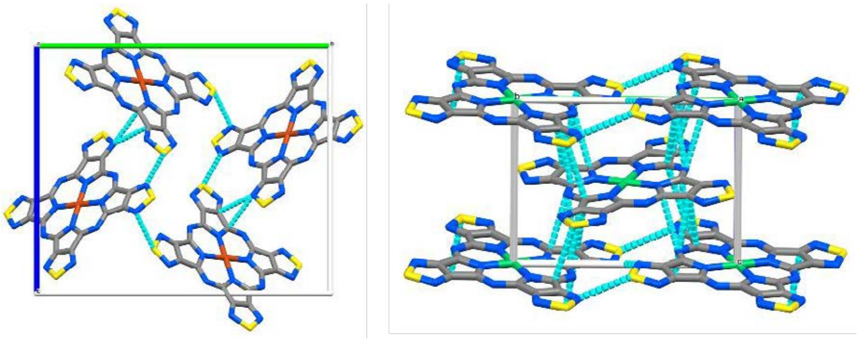

Figure 4.3. View along the *a* crystallographic axis of **CuPz** (left) and **NiPz** (right) crystal structures extracted from [141]. The short contacts are highlighted as cyan rods. Color code: C = grey; N = blue; S = yellow; Ni = green; Cu = bronze.

As shown in Fig.4.3 [141], crystal structures of these compounds are characterized by several short-contact interactions localized on charge-rich S and N atoms. Some domains may contain octahedral Ni^{2+} centers formed upon the precipitation of amorphous fractions in solids. For instance, the crystal structure of the analog (**ZnPz**) shows Zn^{2+} centers octahedrally coordinated by the four N atoms of the ligand and two additional N atoms from neighboring thiadiazol units. Furthermore, powders of doped samples obtained through the employed strategy were amorphous or less crystalline than pure compounds. Therefore, we decided to use the free ligand as the diamagnetic host for gaining highly diluted samples of both **CuPz** and **CuPc**, i.e., **Cu$_{2\%}$Pz**, **Cu$_{0.1\%}$Pz**, **Cu$_{20\%}$Pc**, **Cu$_{2\%}$Pc**, and **Cu$_{0.1\%}$Pc**.

Based on what was stated above, the PXRD technique could not give us any information about the homogeneity of the samples. Segregation phenomena could occur during the precipitation of products from MSA solutions. Thus, we employed X-band cw-EPR (9.4 GHz) to validate diluted species homogeneity and probe the static magnetic properties of obtained compounds. A qualitative interpretation of the spectra can prove the homogeneity of these species. Indeed, dipolar interactions are reduced if the spins are homogeneously distributed within the sample and well isolated. Consequently, the characteristic line width of EPR transitions reduces since the electron relaxation is enhanced. Narrower EPR transitions were observed when lowering the percentage of the paramagnetic fraction (see spectra reported in Figs.B.3 and B.4). Such a phenomenon can be correlated to a homogeneous distribution of paramagnetic centers within the diamagnetic framework. When the dilution is pushed to 0.1%, no appreciable line width variations are observed compared to the 2% doped sample, suggesting that complete homogeneity is somehow lost below this limit.

The analysis of cw-EPR and EDFS (Echo Detected Field Sweep) spectra on amorphous powders of 2% and 0.1% doped **CuPz** samples collected at the X-band (≈ 9.4 GHz) and Q-band (≈ 33.8 GHz) frequencies provided accurate estimates of the spin Hamiltonian parameters. Because of the spectral complexity, we found it convenient to simulate the best-resolved Q-band spectra first and then use the parameters obtained to simulate X-band data. The experimental Q-band spectra (cw and EDFS ones) of **Cu**$\mathbf{Cu_{2\%}Pz}$ and $\mathbf{Cu_{0.1\%}Pz}$ are reported in Fig.4.4 together with their simulation obtained with the script *Easyspin* [146]. All the other cw-EPR spectra at X-band frequency can be found in Appendix B (Figs.B.3 - B.5). Spectra were thus simulated by employing the spin Hamiltonian:

$$\hat{\mathcal{H}}_S = \mu_B \mathbf{g} \cdot \vec{B} \cdot \hat{S} + \hat{S} \cdot \mathbf{A}^{\mathbf{Cu}} \cdot \hat{I} + \sum_{i=1}^{4} \hat{S} \cdot \mathbf{A}^{\mathbf{N_i}} \cdot \hat{I} \tag{4.1}$$

The whole set of spin Hamiltonian parameters employed for simulation is listed in Table 4.1, and it is consistent with that of **CuPc** [147].

The simulation of **CuPz** spectra confirmed the general structure observed in **CuPc** samples [147]. As expected, the spectrum reflects the axial symmetry of the g tensor (i.e., $g_z > g_x = g_y$) usually observed for Cu^{II} ions in square-planar geometries. Each signal is thus split due to: i) the hyperfine coupling interaction of the $S = 1/2$ with nuclear spins of ^{63}Cu ($I = 3/2$, natural abundance (NA) = 69.17%) and ^{65}Cu ($I = 3/2$, NA = 30.83%); ii) a superhyperfine coupling interaction of the Cu^{2+} ion spin $S = 1/2$ with the nuclear spins of four bonded N atoms (^{14}N, $I = 1$, NA = 99.64%). Moreover, experimental SH parameters extracted from cw-EPR spectra validate calculation outcomes obtained by periodic DFT optimization.

Table 4.1. Comparison between best simulation parameters (*a*), DFT outcomes (*b*), and experimental parameters extracted from [147] (*c*). The local reference frame for nitrogen atoms (*x′y′z′*) was chosen with the *z′* direction along with the Cu-N bond.

	$Cu_{2\%}Pz^{a}$	$Cu_{0.1\%}Pz^{a}$	$CuPz^{b}$	$CuPc^{b}$	$CuPc^{c}$
g_x	2.043(1)	2.043(1)	2.044	2.042	2.0390(5)
g_y	2.043(1)	2.043(1)	2.044	2.042	2.0390(5)
g_z	2.172(1)	2.172(1)	2.146	2.134	2.1577(5)
(MHz)	69(2)	69(2)	30	31	83(3)
(MHz)	69(2)	69(2)	30	31	83(3)
(MHz)	630(1)	630(1)	663	671	648(3)
(MHz)	45(2)	45(2)	44	45.2	44.7(2)
(MHz)	45(2)	45(2)	44	45.2	44.7(2)
(MHz)	51(2)	51(2)	57	57.7	56.5(2)

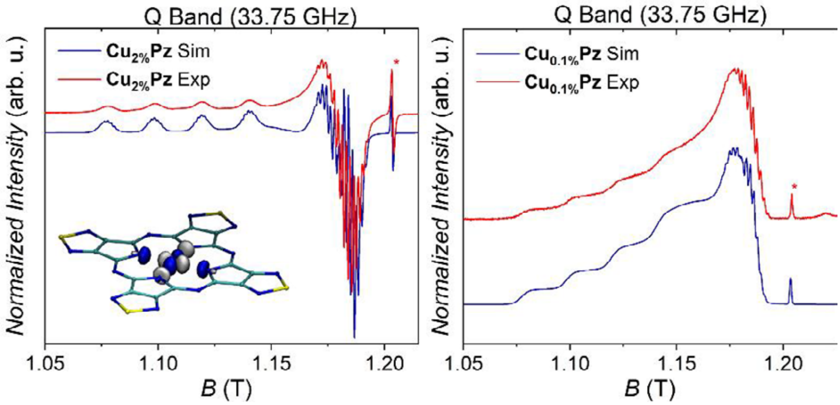

Figure 4.4. On the left, Q-band cw-EPR spectrum of compound **Cu2%Pz** collected at 30 K. The asterisk highlights a signal arising from radical impurity, whose concentration is estimated around the 0.01% of the Cu^{2+} one. A representative sketch of the DFT calculated magnetic SOMO UNO orbital (blue and white lobes) on the molecular structure of **CuPz** is reported in the inset. On the right, Q-band EDFS spectra collected on a powder sample of **Cu0.1%Pz** collected at 30 K.

After this first step aimed at rationalizing the static properties of the two investigated samples, doped species were employed to further explore the relaxation dynamics at two distinct regimes. The first occurs at the 20% doping percentage, in which electron-electron dipolar interactions drive the spin relaxation. The second regime arises at 0.1% doping percentage of paramagnetic species, where spin-spin interactions are reduced, and electron-nuclear dipolar interactions drive the coherence properties of both samples. We adopted a multi-technique approach for investigating the relaxation properties of **CuPz** and **CuPc**, employing both AC susceptometry for 20% doped samples (left side in Fig.4.6), and pulsed EPR spectroscopy at the Q-band frequency for 0.1% doped samples. Furthermore, we performed pulsed EPR experiments to highlight the presence of Rabi oscillations in **Cu0.1%Pz**. The observation of Rabi oscillations up to 50 K (Fig.4.5) guarantees the coherent spin manipulation of this system and, according to what was previously stated in Chap.1, its employability as a molecular spin qubit.

The spin dynamics of the two species presented several differences in 0.1% doped samples. We observed a moderate but appreciable T_m enhancement for the hydrogen-free complex **CuPz** within the whole investigated temperature range (Fig.4.6). Indeed, the T_m values extracted from Hahn echo experiments on **Cu0.1%Pz** span from 2.4 μs to 0.8 μs in the 5 - 110 K range, while those of **Cu0.1%Pc** span from 0.9 μs to 0.2 μs. We tried to validate our observations by measuring both compounds in a diluted solution of D_2SO_4, where larger T_m values have been previously observed for **CuPc** [131].

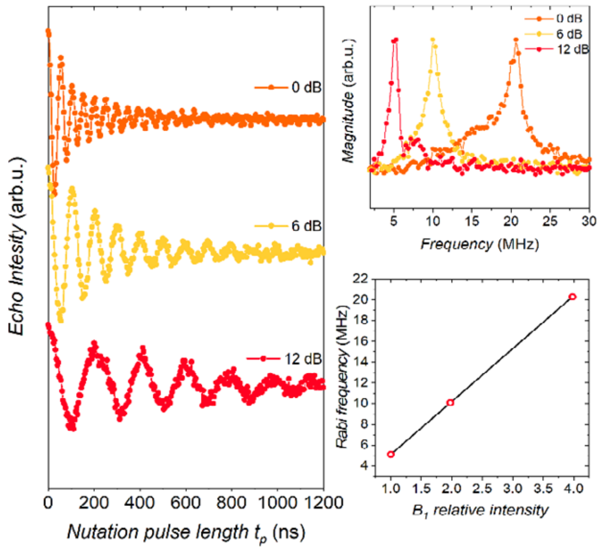

Figure 4.5. Rabi oscillations observed for **Cu0.1%Pz** at 50 K for three different attenuation values of 0, 6, and 12 dB. On the right side, the Fourier transform of the echo intensities (top) and the linear dependence of the Rabi frequencies with respect to the B_1 relative strength are reported.

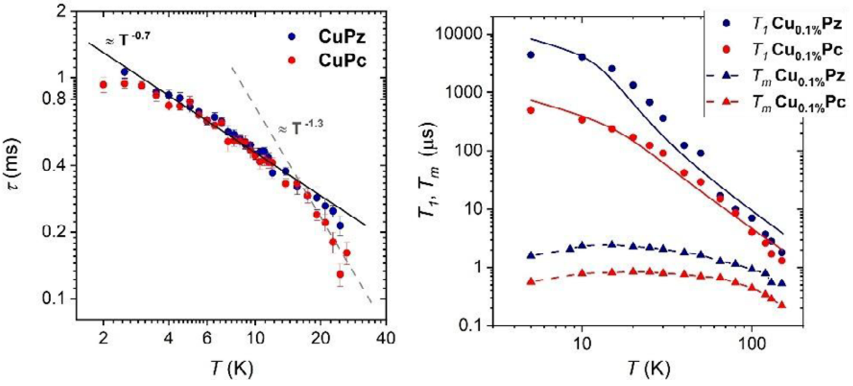

Figure 4.6. On the left side, plot of τ values extracted from AC susceptometry measurements. The lines in the plot indicate the different dependence by temperature in direct or Raman relaxation regimes. On the right side, plot of T_1 (circle) and T_m (triangle) values extracted from pulsed EPR measurements conducted on **Cu0.1%Pz** and **Cu0.1%Pc**. Solid lines on T_1 represent best fits obtained by employing Eq.4.2.

Unfortunately, **CuPz** showed a marked variation of EDFS spectrum upon dilution, and it was not possible to perform a comparative measurement with the same experimental conditions (Fig.B.6).

We analyzed the spin-lattice relaxation data and compared the obtained T_1 and τ in the two molecular systems. From our analysis, conducted by a multi-technique approach and rationalized thanks to the performed *ab initio* study of molecular vibrations, several features emerged depending on the temperature at which T_1 value was extracted. Our calculation results were directly employed within the fitting function reported in Eq.4.2 [86].

$$T^{-1} = a_{dir}\frac{exp(\Delta E/k_BT)}{\exp(\Delta E/k_BT)-1} + a_{Ram}\frac{\exp\,(\hbar\omega_i/k_BT)}{(\exp\,(\hbar\omega_i/k_BT)-1)^2} \qquad (4.2)$$

The first term resembles the direct relaxation process, with a_{dir} and ΔE being a constant weight term, and the difference in energy between the two m_S states of the $S = 1/2$ ion (for Q band experiment, such energy was fixed at 1 cm^{-1}), respectively. The second term in the equation accounts for the Raman relaxation process driven by the coupling with available molecular vibrational modes. Here, V_i^{s-ph} and ω_i are the SPC constant and the vibrational frequency of the i-th mode extracted from *ab initio* calculations, respectively (see Appendix B). The sum runs over all the calculated vibrational modes, and it is thus rescaled by the constant term a_{Ram}. In this model, the fitted parameters are a_{dir} and a_{Ram}, while all the others were kept fixed.

The extracted values for best-fit parameters are reported in Table 4.2. The best fit of T_1 trends obtained through the mentioned model are reported as solid lines in the right plot of Fig.4.6. We need to mention that, even if those fits do not perfectly reproduce the behavior of T_1 at high T, they rely on a more physical description of the process compared to commonly employed methods [88]. Moreover, the adopted *ab initio* outcomes account only for single-molecule vibration. A complete description of the process could be instead obtained by considering lattice vibrations too, as reported for other systems in [69] and Sec.4.3. Above 40 K, where electron-nucleus interactions are less contributing to the spin dynamic of the system, T_1 trends of **Cu$_{0.1\%}$Pz** and **Cu$_{0.1\%}$Pc** are similar. This fact is highlighted by the fit outcome reported in Table 4.2, where a similar weight of Raman contribution is evident for the different samples.

Table 4.2. Experimental parameters extracted from best fits of T_1 vs T data employing Eq.4.1.

	Cu$_{0.1\%}$Pz	**Cu$_{0.1\%}$Pc**
$a_{dir}(ms^{-1})$	$(3.32\pm1.47)\times10^{-2}$	$(3.87\pm0.64)\times10^{-1}$
$a_{Ram}(ms^{-1})$	$(1.99\pm0.41)\times10^{6}$	$(4.20\pm0.55)\times10^{6}$

Further analysis of the single-mode contribution to the relaxation rate indicated that the most effective modes are those with SPC coefficients higher than 10^{-7} and energies lower than 500 cm^{-1}. Among them, the first two *gerade* optical modes placed at 58.16 and 58.47 cm^{-1} (**Cu$_{0.1\%}$Pz**) and 57.78 and 58.05 cm^{-1}(**Cu$_{0.1\%}$Pc**) have the most influence on the relaxation (a plot of all the contributions is reported in Fig.B.7). Here, it must be stressed that the thermal population is not the only ingredient determining the spin relaxation rate. Indeed, the vibrational density of states (DOS) and the magnitude of SPC are additional quantities that must be carefully considered because they largely compensate for the difference in thermal populations. Both these quantities are much more significant for optical phonons than acoustic ones.

A plot of SPC intensity (obtained as the sum of calculated SPC constants of the exact symmetry and similar energy) as a function of the energy of calculated normal modes is reported on the left side in Fig.4.7. In the figure, SPC constants are only reported for those modes affecting the spin-relaxation process above 40 K. As can be observed in the figure, those optical modes that are characterized by an *ungerade* (u) symmetry do not significantly interact with the spin. While for g modes, the larger SPC constants reach a magnitude of 10^{-5}, u modes do not overcome the limit of 10^{-7}. The striking dependence of relaxation processes from the symmetry properties of optical modes can be explained as follows. For a copper(II) ion in a square-planar coordination geometry, the magnetic SOMO orbital ($d_{x^2-y^2}$) points toward the N bonding atoms' orbitals. As a result, the larger modulation on the g-tensor (due to SPC and practically causing spin relaxation) arises from the efficient distortion due to symmetric modes that mainly activate the spin-orbit-induced perturbation. On the other hand, asymmetric distortions lead to a net null variation of the overlap, thus giving rise to small contributions to the total relaxation. A representative sketch is reported on the right side of Fig.4.7.

As soon as the temperature was lowered, we observed a T_1 divergence in the two compounds. We observed a different weight of the direct relaxation process for the two species, as it is well reflected by the fitted value of a_{dir} parameter reported in Table 4.2. By comparing this observation with AC susceptometry results, we hypothesized that at 20 % doping percentage, the contribution arising from spin-spin interactions primarily drive the direct process, and no differences between **CuPz** and **CuPc** (where similar Cu-Cu distance can be found) were observed. On the contrary, when the spin concentration is lowered to 0.1%, the spin-lattice relaxation process appears less active for the porphyrazine-based compound. Such a behavior could be related to the presence of the highly polarizable sulfur atoms within the ligand scaffold of **CuPz**. In theory, the role of these can be relevant for van der Waals interactions affecting the acoustic phonon dispersion, but more calculations are still needed to confirm such a hypothesis.

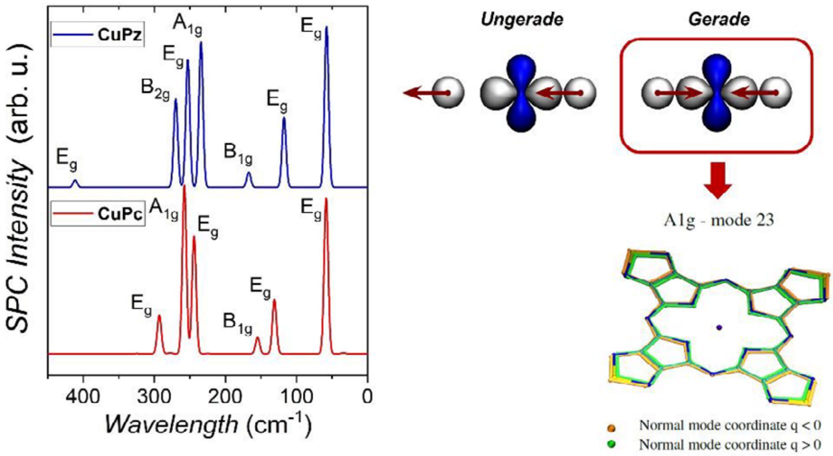

Figure 4.7. On the left, plot of SPC intensities extracted from ab initio calculations as a function of optical modes energy. On the right, representative sketch of the overlap variation between the two nitrogen σ orbitals interacting with the copper $d_{x^2-y^2}$ orbital in response to asymmetric (left) and symmetric (right) displacements. A pictorial representation of the most active A_{1g} mode for **CuPz** is reported below the associated orbital variation scheme.

In conclusion, we reported a complete characterization of the relaxation properties of benchmark **CuPz** and its hydrogen-free analogue **CuPz**. We observed a moderate T_m enhancement for **CuPz** and highlighted several differences in T_1 trends for the two species. By employing a combined theoretical and experimental approach, we were able to disentangle different contributions to the direct and Raman relaxation processes arising from intrinsic molecular properties of the presented class of potential molecular qubits.

AUTHOR'S CONTRIBUTIONS. The author of this thesis synthesized all the mentioned compounds and solid dilutions, except for purchasable [Cu(Pc)] and H_2Pc. Furthermore, he performed AC susceptometry measurements and treated the resulting data. The author (together with Dr A. Albino) also performed cw-EPR measurements at X band, simulated cw-EPR and EDFS spectra, and rationalized the T_1 data trend by employing the model reported in the text.

4.2. Further reducing the number of active nuclei: [Cu(dttt)$_2$]

In the previous section, we outlined some advantages gained by exploiting the macrocyclic ligand H_2TTDPz rather than its hydrogen-rich analogue H_2Pc. However, our observations partially confirmed what was specified in previous works [66, 124]. The interaction with four bonded nitrogen atoms of porphyrazine ligands could still drive the decoherence phenomenon in this class of copper complexes, thus setting the limit of T_m to $\approx 2\ \mu$s. Here, we present a different strategy to obtain a potential molecular qubit based on a hydrogen-free copper(II) complex where the coordination sphere does not imply any N nucleus. Notwithstanding the stringent prerequisites imposed, we found the ligand 1,3,2-Dithiazole-4-thione-5-thiolate (dttt$^-$) to be the perfect candidate for our purposes. Indeed, the choice of this ligand is threefold: i) it guarantees the metal coordination with non-active nuclei like S atoms; ii) it shows a hydrogen-free structure, where just C, N, and S atoms (i.e., less active nuclei) are included (Fig.4.8); iii) it is mononegatively charged, therefore giving the possibility of obtaining neutral coordination complexes, free of nuclear-rich counterions, and suitable for surface deposition experiments. The molecular structure of dttt$^-$ is indeed similar to that of dithiolene ligands shown in Fig.3.4 (Chap.3), with the difference that it is mononegative rather than binegative.

The 1,3,2-dithiazole-4-thione-5-thiolate ligand was obtained as a TBA$^+$ salt (TBA = tetrabutylammonium), following a one-pot synthesis described in the literature [148]. This procedure involves the fusion of two 1,3,2-dithiazolium cations in CH_2Cl_2 by adding NEt_3. The synthesis scheme is here reported in Fig.4.8.

However, obtaining the precursor 1,3,2-dithiazolium chloride was not trivial. While this precursor had been previously obtained through the reaction of 1-chloroethane-1,2-bis(sulfenyl chloride) [148, 149], in our case, we preferred to use the simpler ethane-1,2-bis(sulfenyl chloride) [150, 151] as reported in [152], whose synthesis did not require the use of Cl_2 as chlorinating agent [153]. It is important to mention that the outlined strategy does not guarantee a substantial yield, and it

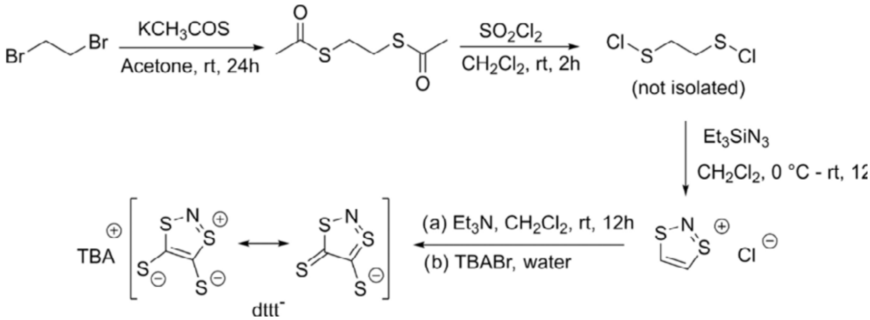

Figure 4.8. Synthesis scheme reporting the synthetic steps adopted in this work for obtaining the ligand TBAdttt.

demands long procedural times. The final product, TBAdttt, was finally isolated as a crystalline purple solid (see Appendix C) in a good yield of about 13 - 15 %. This result agrees well with that reported in [148], where authors started from the 1-chloroethane-1,2-bis(sulfenyl chloride) precursor.

The obtained ligand was thus employed for the synthesis of the paramagnetic copper(II) complex and its diamagnetic analogue of nickel(II), namely [Cu(dttt)$_2$] (**Cudttt**) and [Ni(dttt)$_2$] (**Nidttt**). The synthesis scheme is reported in Fig.4.9, while the detailed procedure and the characterization of compounds are reported in Appendix C. To our knowledge, this is the first proposed synthesis of [M^{II}(dttt)$_2$] complexes. Target products were obtained as polycrystalline, pure, black powders (see the PXRD pattern reported in Appendix C).

Both Ni^{2+} and Cu^{2+} complexes showed complete insolubility in all common (and not common) organic solvents and acids, even when refluxed. Furthermore, H_2SO_4 or methanesulfonic acid (used for solubilizing **CuPz**, see Sec.4.1) readily decompose the molecular complexes after a few minutes. Because of these properties, it was impossible to obtain single crystals of X-ray quality suitable for structure determination with standard techniques. We also tried to obtain crystalline powder samples by employing different strategies, e.g., by slow diffusion of the precursor and ligand solutions in a U-shaped tube through viscous media like glycol or diethylene glycol or by crystallization in agarose gels (from 1% to 0.1% $w_{agarose}/w_{Water}$). However, all these fractions were not enough crystalline to collect sufficiently sharp and intense PXRD patterns for structure determination. As, on the one hand, such compounds were obtained as polycrystalline solids, on the other hand, it was impossible to get a structure from PXRD patterns. However, these compounds showed marked thermal stability (see the TGA analysis in Fig.C.3 and the following XPS analysis). We plan new experiments to get microcrystalline powders or single crystals by thermal sublimation of target compounds in a high vacuum apparatus. Appealing results were indeed obtained with similar methods in the case of **Pz**-based compounds in [141].

For the same reason, the magnetically diluted compound [Cu$_{0.2\%}$Ni$_{99.8\%}$(dttt)$_2$] (**Cu$_{0.2\%}$dttt**) was not obtained by recrystallization, but following the same strategy

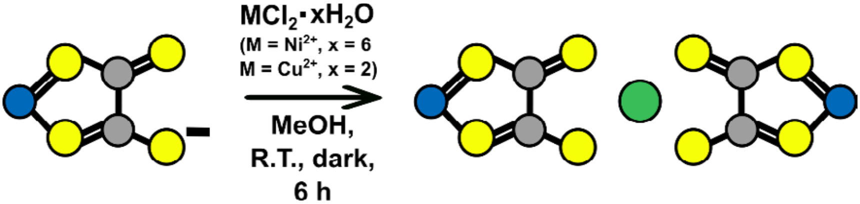

Figure 4.9. Synthesis scheme reporting the synthetic strategy adopted for obtaining the metal complexes **Cudttt**, **Nidttt**, and their dilution **Cu$_{0.2\%}$dttt**.

reported in Fig.4.9. Stoichiometric amounts of the two metal chloride precursors were added together to a ligand solution, causing the precipitation of the doped sample.

We attributed the large insolubility of these two compounds to the presence of strong stacking and van der Waals interactions. The latter interaction may arise because of the presence of nitrogen and sulfur atoms within the molecular scaffold. Similar behavior was indeed observed also for **CuPz** (see Sec.4.1). Our hypothesis is supported by the experimental results obtained from the investigation of static magnetic properties of pure crystalline **Cudttt** by cw-EPR spectroscopy and DC magnetometry.

The EPR spectra collected on **Cudttt** at 30 K and 300 K are shown in Fig.4.10a. We recorded an abrupt decrease of the signal intensity when lowering T and for constant values of the modulation amplitude and $\vec{B}_1$ power (attenuation = 40 dB). The observed behavior suggests the presence of antiferromagnetic interactions extended through the molecular framework within the crystal [154]. A similar antiferromagnetic behavior was indeed observed in dithiolene-based complexes [155, 156], and in [Cr(dttt)$_3$] [148]. The DC magnetometry outcomes reported in Fig.4.10b further mark a trend of M vs B/T characteristic of antiferromagnetically coupled systems. The M vs B/T trend is due to increased magnetic susceptibility as the temperature increases. Furthermore, the M value extracted from the DC measurement is far below that of 1 μ_B expected for a paramagnet, thus highlighting an antiferromagnetic behavior of this compound. A plot of magnetic susceptibility as a function of the temperature is reported in the inset of Fig.4.10b as χT vs T. Adopting the Curie-Weiss model to approximatively fit the linear region of $1/\chi = (T - \Theta)/C$ (where Θ and C are the Weiss and the Curie constants, respectively), we can roughly estimate an indicative value of $J/k_B \approx \Theta = -184\,K$.

Due to the lack of a reliable structure for investigated compounds, a possible molecular structure was rationalized using an extensive spectroscopic characterization of doped **Cu$_{0.2\%}$dttt**. The rationalization of a square planar coordination geometry follows from the SH parameters obtained from the simulations of both Q-band and X-band EPR spectra. The obtained spectra, which are obviously narrower than for pure **Cudttt**, show the typical pattern expected for a CuS_4 system (Fig.4.11a and b) [157]. Moreover, the signal-to-noise ratio (S/N) increases as the temperature is lowered to 30 K, indicating that, contrarily to the case of pure **Cudttt**, the observed EPR spectrum is likely to be correlated to isolated paramagnetic centers. Here, it is possible to observe two peaks at 293 mT and 311 mT due to the splitting of the g_z component upon the effect of the hyperfine coupling interaction between the spin and Cu nucleus (the splitting is of 17 mT in the X-band spectrum). Additionally, these parallel transitions clearly show a secondary splitting of ≈ 1 mT due to the difference in the g_n of the two Cu isotopes in accordance with their natural abundance. The other parallel and perpendicular transitions are convoluted within the 320 - 350 mT region of fields. A weak superhyperfine structure was also observed. It is due to the coupling between the spin and the two distal nitrogen nuclei within the ligand. Furthermore, the presented spectra show a weak signal from a possible radical impurity (highlighted with an asterisk in Fig.4.11) that we attributed to a radical byproduct fraction formed during the synthesis. A similar contamination source was indeed found even for porphyrazine- or porphyrin-based complexes [77, 84].

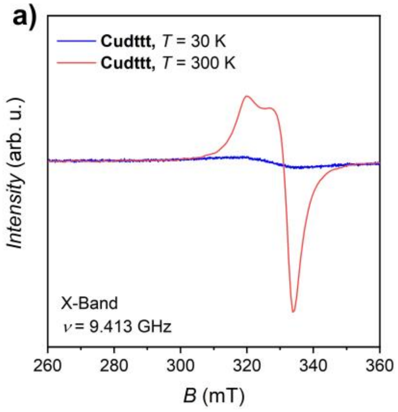

Figure 4.10. a) Experimental X-band EPR spectra collected on a polycrystalline powder sample of **Cudttt** at 30 K and 300 K. b) Magnetization curves reported as *M* vs. *B/T* obtained from DC magnetometry measurements. The plot of χT as a function of *T* for $B = 100$ mT is reported in the inset.

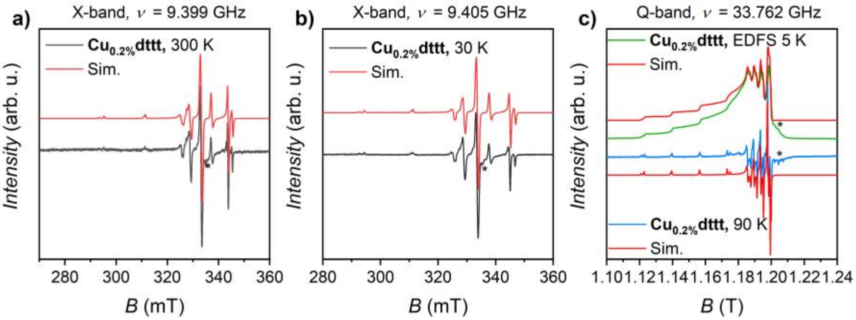

Figure 4.11. a) Experimental X-band EPR spectrum collected on a polycrystalline powder sample of **Cu$_{0.2\%}$dttt** at 300 K. b) Experimental X-band EPR spectrum collected on a polycrystalline powder sample of **Cu$_{0.2\%}$dttt** at 30 K. c) Experimental Q-band cw-EPR (90 K) and EDFS (5 K) spectra collected on a polycrystalline powder sample of **Cu$_{0.2\%}$dttt**.

All spectra were simulated adopting the SH of the form:

$$\hat{\mathcal{H}}_S = \mu_B \boldsymbol{g} \cdot \vec{B} \cdot \hat{S} + \hat{S} \cdot \boldsymbol{A}^{\boldsymbol{Cu}} \cdot \hat{I} + \sum_{i=1}^{2} \hat{S} \cdot \boldsymbol{A}^{\boldsymbol{N_i}} \cdot \hat{I} \tag{4.3}$$

The best simulation parameters were extracted from the best-resolved Q-band spectrum and adopted as starting parameters for simulating X-band data. We also collected an EDFS spectrum at the Q-band frequency (simulated with the same SH parameters of cw-EPR spectrum), demonstrating that echo can be observed within the whole experimental field range (Fig.4.11c). The best parameters for the Cu^{2+} ion are listed in Table 4.3. The adopted values of A^{N_i} are not reported in the table since it was tricky to extract reliable values from cw spectra because of the order of magnitudes of these splitting frequencies (less than 3 MHz).

Table 4.3. Best SH parameters for the Cu ion extracted from the simulations of X-band, and Q-band cw-EPR and EDFS spectra.

Freq.	*T* (K)	g_x	g_y	g_z
X	300	2.0216(1)	2.0257(1)	2.1017(1)
		A_x^{Cu} (MHz)	A_y^{Cu} (MHz)	A_z^{Cu} (MHz)
		103(1)	109(1)	476(1)
X	30	2.0214(1)	2.0251(1)	2.1015(1)
		A_x^{Cu} (MHz)	A_y^{Cu} (MHz)	A_z^{Cu} (MHz)
		112(1)	115(1)	496(1)
Q	90	2.0211(1)	2.0242(1)	2.1015(1)
		A_x^{Cu} (MHz)	A_y^{Cu} (MHz)	A_z^{Cu} (MHz)
		110(1)	113(1)	496(1)

However, they were extracted from simulations of X-band HYSCORE measurements data obtained by our collaborators at the University of Turin (see Fig.C.7). The HYSCORE spectra collected on three different field positions of the EDFS spectrum show a characteristic fine structure that confirms a superhyperfine coupling interaction of the copper ion with two symmetrical nitrogen atoms placed on distal positions. Furthermore, it is also possible to observe two ^{14}N combination peaks due to two equivalent N atoms. This evidence perfectly resembles the predicted structure. No other characteristic signals due to strong coupling with other nuclei are observed within the sample.

The values of $\mathbf{A}^{\mathrm{N}}$ components extracted from simulations are: $A_x^{N_{1,2}}$= 2.6 MHz, $A_y^{N_{1,2}}$ = 2.6 MHz, and $A_z^{N_{1,2}}$ = 3.2 MHz. Furthermore, simulations highlighted a tilt of 90° between the $\mathbf{A}^{\mathrm{N}}$ and **g** frames, with A_z lying on the plane of $g_\perp$. If we compare the obtained values for superhyperfine components with those of ≈ 50 MHz observed for **CuPz** (see Sec.4.1), we can say that they reasonably agree with a Cu-N distance of ≈ 5 Å estimated for **Cudttt**.

Another evidence corroborating the hypothesized coordination geometry of the **Cudttt** complex is that extracted by evaluating the ratio between the axial components of **g** and **A**. To do this, we reported the experimental A_z values for **Cudttt** as a function of the correspondent g_z value in the so-called Peisach-Blumberg plot (Fig.4.12) [158]. We compared our results with those obtained for structurally characterized CuS_4 species reported in the literature [67, 157, 159, 160]. The graph analysis showed good agreement between **Cudttt** parameters and those extracted for planar systems. Furthermore, the **Cudttt** compound might also undergo a distortion of the coordination environment as soon as the temperature decreases from 300 K to 30 K, as evidenced in the plot.

Since the data collected until this moment showed a good agreement with the predicted structure of the **Cudttt** compound, we investigated its relaxation properties. The spin dynamics and manipulability properties of **Cudttt** were investigated by pulsed EPR spectroscopy working at Q-band. Here, we compared these results with those extracted on a hydrogen-rich copper(II) complex synthesized by D. Ranieri as the object of his thesis.

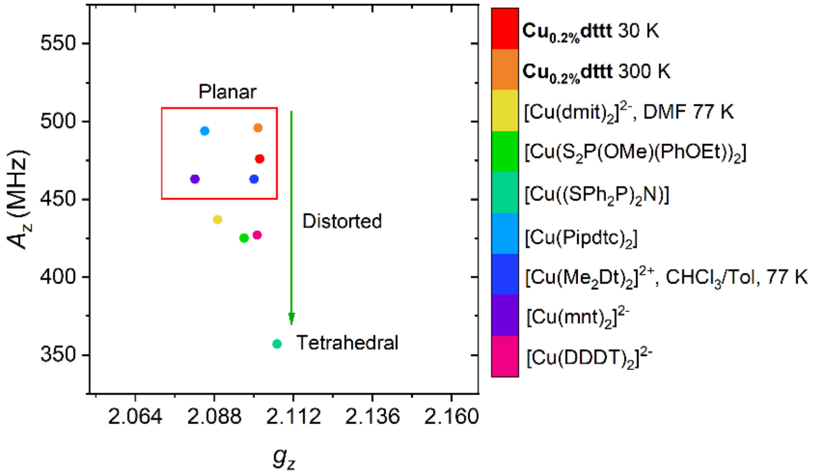

Figure 4.12. Peisach-Blumberg plot reporting the comparison between our SH parameters and those extracted from [67, 157, 159, 160]. dmit = 1,3-dithiole-2-thione-4,5-dithiolate; Pipdtc = piperidinedithiocarbamate; Me_2Dt = N,N-dimethyl piperazine 2,3-dithione; mnt = maleonitriledithiolate; DDDT = 1,2-dithiolene-5,6-dihydro-1,4-dithiin-2,3-dithiolate.

The investigated compound is the square planar complex of copper(II) with the ligand 2-mercaptopyridine-1-oxide (mpo$^-$), i.e., [Cu(mpo)$_2$] (**Cumpo**, Fig.C.6a). This compound presents several analogies with **Cudttt**: i) the ligand is mononegative, and its complexes are neutral; ii) the coordinating atoms are S and O atoms, so the first-coordination sphere is nuclear-free; iii) the molecular structure is planar; iv) the copper complex shows a similar EPR spectrum to that of **Cudttt** (Fig.C.6b). Furthermore, **Cumpo** is characterized by more marked solubility in different solvents (e.g., DMSO, CH_2Cl_2, DMF, chloroform, etc.) with respect to **Cudttt**. Indeed, a 0.3% doped sample of **Cumpo** in [Ni(mpo)$_2$] was obtained by coprecipitating the two species from a mixture of dichloromethane and ethanol.

Let us recall that all potential molecular qubits must present manipulability properties that the observation of Rabi oscillations can evidence. Nutation experiments conducted on **Cu$_{0.2\%}$dttt** and **Cu$_{0.3\%}$mpo** successfully unveiled Rabi oscillations, proving their employability as potential qubits (Fig.4.13a and b).

Once the manipulability properties were probed, we investigated the spin dynamics within the two systems by employing inversion recovery and Hahn Echo experiments (see Appendix A, Sec.A.3). T_1 and T_m values were determined for both compounds in the 5 K- 110 K temperature range (Fig.4.13) by fitting the resulted echo traces with a stretched exponential law: $I = I_0 + k_1 exp((\tau_\rho/T_1)^{\beta_1})$ and $I = I_0 + k_m exp((\tau_\rho/T_m)^{\beta_m}$, with τ_p = delay time and $\beta_{1,m}$ = stretching factors for T_1 and T_m traces, respectively. The plot of T_1 and T_m values as a function of T is reported in Fig.4.14. We superimposed the experimental data previously obtained for **CuPz** to compare the whole systems set.

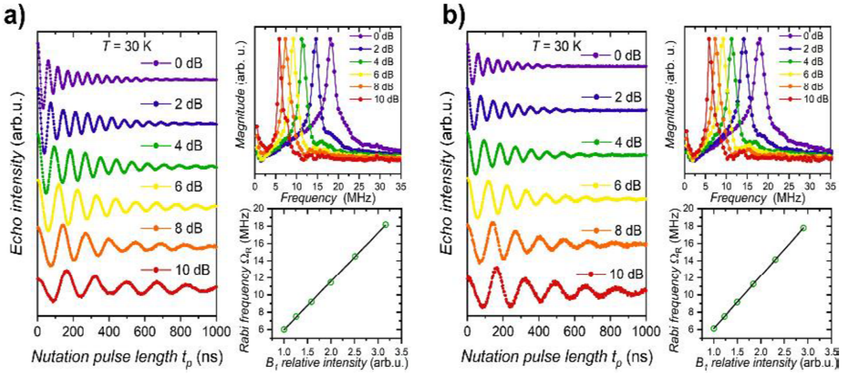

Figure 4.13. a) Plots of Rabi oscillations, their Fourier transforms, and B_1 relative intensity vs Rabi frequency, obtained by the nutation experiments conducted on **Cu$_{0.2\%}$dttt** at different attenuation values of the oscillating field B_1. The same plots are reported for **Cu$_{0.3\%}$mpo** in (b).

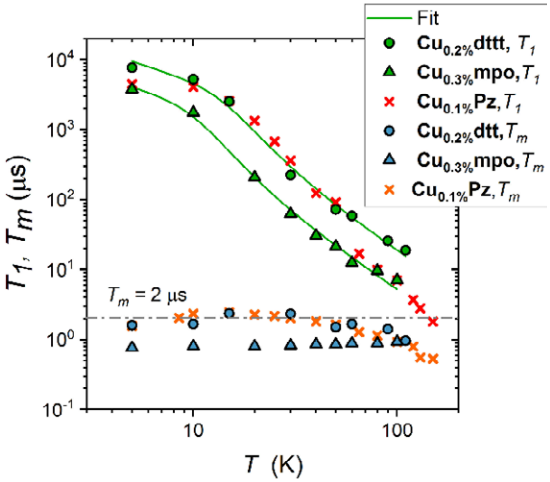

Figure 4.14. Comparison between the experimental T_1 and T_m trends as a function of T observed for **$Cu_{0.2\%}$dttt**, **$Cu_{0.3\%}$mpo**, and **CuPz**.

We rationalized the spin-lattice relaxation dynamics of these two compounds by readapting the model reported in Eq.4.2 to a more phenomenological description of the relaxation process like that in Eq.4.4 since no calculations were employed at this step. In this case, the Raman term accounts just for one phonon mode of energy $\hbar\omega$, and we did not introduce a SPC constant, which is, in practice, included in the a_{Ram} term.

$$\frac{1}{T_1} = a_{dir}T + a_{Ram}\frac{e^{(\hbar\omega/k_BT)}}{(e^{(\hbar\omega/k_BT)}-1)^2} \tag{4.4}$$

The best-fit parameters are: **$Cu_{0.2\%}$dttt)** $a_{dir}^{dttt} = (2.1 \pm 0.4)\,10^{-5} MHz\,K^{-1}$, $a_{Ram}^{dttt} = (0.034 \pm 0.018)\,MHz$, $\hbar\omega^{dttt} = 55 \pm 12$ cm^{-1}; **$Cu_{0.3\%}$mpo)** $a_{dir}^{dttt} = (4.9 \pm 0.9)\,10^{-5} MHz\,K^{-1}$, $a_{Ram}^{dttt} = (0.070 \pm 0.029)\,MHz$, $\hbar\omega^{mpo} = 42 \pm 7$ cm^{-1}. As expected from the similar experimental behavior, the parameters describing both direct and Raman processes are similar for the two complexes. In particular, the energies of involved vibrational modes are similar in these complexes.

In a second step, we compared the experimental T_1 vs T trends of **$Cu_{0.2\%}$dttt** and **$Cu_{0.3\%}$mpo** with those obtained for **CuPz**. The high-temperature behavior is quite different in **CuPz** above 70 K since, in that case, the T_1 trend abruptly decreases above this limit following a more pronounced temperature dependence with respect to **Cudttt** and **Cumpo**. There are two possible explanations for this behavior: i) It could be possible that smaller molecules such as **Cudttt** and **Cumpo** may present a larger rigidity with respect to the **CuPz** system. Such an enhanced rigidity may lead to a general decrease in the number of higher energy phonon modes; ii) in CuS_4 systems, the SOMO molecular orbital is mainly localized on the Cu^{2+} ion [157]. On the contrary, **CuPz** shows a SOMO orbital partially delocalized over the four donating N atoms of the porphyrazine ligand (see Fig.4.6 in Sec.4.1). It follows that a lower effect due to the distortion of the first coordination sphere is expected. However, DFT calculations corroborating these hypotheses are still needed, and a more detailed treatment is mandatory to validate these assumptions further.

As for the decoherence properties, the T_m values extracted for **$Cu_{0.2\%}$dttt** span from 2.36 μs to 0.96 μs within the experimental T range, while those of $Cu_{0.3\%}$mpo span from 0.81 μs to 0.56 μs within the same T interval. Such evidence highlights the effect of hydrogen nuclei on the coherence properties of the copper(II) ion. Indeed, even if the concentration of paramagnetic species in the two samples is slightly different, this significant difference in the observed coherence cannot be correlated only to the effect of spin-spin interactions [66, 90]. In particular, the T_m values of the two complexes differ in the low-temperature regime (5 − 40 K) and become similar as soon as T reaches 100 K. This behavior well agrees with what has been previously observed on **CuPz** and **CuPc** in Sec.4.1. At the low-temperature regime, the coherence properties of the two compounds are mainly affected by the effect of spin-nuclei interactions, which are expected to be largely different in the two systems. On the other hand, T_1 becomes the dominating term in the high-temperature regime, thus setting the limit of T_m. Based on the similar T_1 behavior in the two complexes in this regime, coherence properties of **Cumpo** and **Cudttt** are naturally similar within this temperature range.

Notwithstanding the appreciable coherence properties of these two compounds, which are perfectly comparable with those commonly observed in porphyrin- and porphyrazine-based copper(II) complexes [84, 112], we did not reach any T_m enhancement with respect to the **$Cu_{0.2\%}$Pz** case. In our opinion, this phenomenon cannot be attributed to the effect of the superhyperfine coupling with the distal N atoms. Indeed, the estimated N-Cu distance in **Cudtt**t (≈ 5 Å) is comparable to that observed in the $[Cu(mnt)_2]^{2-}$ system reported in [67], for which coherence times up to 4 μs have been observed on a 1 % doped sample. We initially hypothesized that the limiting factor here could be the presence of a paramagnetic fraction of **Nidttt** gaining an octahedral coordination geometry within the crystal framework ($Ni^{II}L_6$, $S = 1$). Indeed, DC magnetometry measurements conducted on pure samples of **Nidttt** unveiled the presence of a paramagnetic fraction of about 0.7 % of the total weight (see Fig.C.5). Some domains of less crystalline fractions may exist, where short-contact interactions between two neighboring molecules might lead to the formation of octahedral nickel centers. This could be related to bulky donor S atoms within the ligand (which may influence the ligand field interaction even for longer distances) or the presence of distal and donor N atoms. Indeed, similar behavior has been previously observed in the case of **NiPz** (See Fig. Appendix B). However, we think that the effect of $S = 1$ species, especially in the limit of estimated concentrations, should not be the limiting factor for T_m, which is significantly lower than that observed in [67]. Indeed, the $S = 1$ concentration is comparable to that of copper within the sample, and their distribution within the solid matrix should be similar.

An alternative explanation of such low T_m values could be related to the synthetic procedure used to obtain **Cu$_{0.2\%}$dttt**. The investigated compound was obtained by coprecipitating stoichiometric amounts of Ni^{II} and Cu^{II} species while reacting with the ligand. This strategy does not allow to have sufficient control over the homogeneity of the products. Indeed, when reacting, Ni^{II} and Cu^{II} complexes suddenly precipitate from the solution, and it would be possible that segregation phenomena may occur during this step. Although we think that these two ions would react similarly with the employed ligand, it might be possible that the formation kinetics of **Cudttt** or **Nidttt** would be non-identical. Furthermore, the two systems are not perfectly isostructural (see PXRD patterns in Fig.C.1), and it could be hard to determine the homogeneity grade based on standard PXRD. Furthermore, cw-EPR analysis might not discriminate from different dilution grades at such low concentrations of the paramagnetic fraction. This last hypothesis mostly agrees with the low T_m observed. We are now working on a more diluted species, i.e., **Cu$_{0.01\%}$dttt**, to validate this hypothesis since a higher dilution should disadvantage the formation of more concentrated domains.

An alternative strategy to get diluted samples and enhance the distance between spin centers could be co-depositing the paramagnetic and diamagnetic systems on surfaces. We started by probing the sublimation properties of pure compounds. The deposition of the pure **Cudttt** on surfaces was studied by thermal sublimation in ultra-high vacuum conditions ($P \approx 10^{-10}$ mbar). The compound was successfully sublimed on a HOPG surface (HOPG = Highly Oriented Pyrolytic Graphite) at 200 °C for about 15 h. By monitoring the sublimation rate (of about 2 Å/h) using a quartz-crystal microbalance (QCM), the deposition time was chosen to get a thickness of the deposited molecular layer of about 3 nm. The chemical properties of the molecular film deposited by sublimation were studied by X-ray photoelectron spectroscopy (XPS) and compared with those of a bulk molecular sample used as a reference. The latter was fabricated by scratching an Al substrate to accommodate **Cudttt** powders that report the core-level XPS of the Cu 2*p*, S 2*p,* and N 1*s* regions. The main components observed in each XPS region qualitatively indicate the molecule's expected elemental composition. The XPS characterization of the bulk sample is shown in Fig.C.4. The core-level XPS spectra of the molecule after thermal sublimation in UHV are reported in Fig.4.15. The Cu2p region presents two prominent peaks due to the spin-orbit coupling, i.e., Cu $2p_{1/2}$ (953.2 eV) and Cu $2p_{3/2}$ (933.4 eV) signals. The binding energy of the Cu $2p_{3/2}$ component indicates the presence of Cu^{II} species [161,162]. Further evidence of the presence of Cu^{II} species is the satellite peaks at 962.9 eV, 944.2 eV, and 941.7 eV [163,164]. We notice that the presence of XPS components ascribed to Cu atoms in a different oxidation state (violet components for Cu^{I}) could be attributed to contaminations, and it can be observed either in the bulk sample or on the sublimated one.

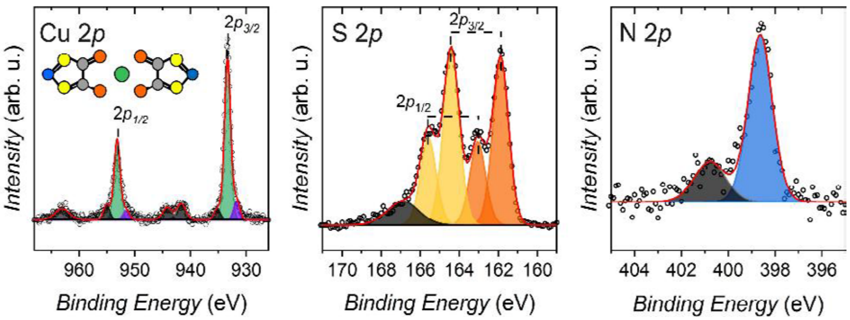

Figure 4.15. From the left to the right: Cu 2*p*, S 2*p*, and N 1*s* core-level XPS regions of **Cudttt** deposited by sublimation on HOPG surface. The color code of the XPS components ascribed to specific molecular sites follows that of the molecular sketch reported in the inset.

However, their presence is less than 5% of the main signal. All the other components are due to minor contaminations or to other phenomena such as shake-up processes (grey components). The N 1s region in Figure 4.15 shows a single component at 398.6 eV, attributable to the S−N−S moiety of the ligand [165]. The small peak at 400.8 eV is instead attributed to an N 1*s* shake-up process commonly observed in conjugated systems containing N atoms, such as porphyrins and phthalocyanines [113]. Besides, in the S 2*p* core-level spectrum of Fig.4.15, we observed two distinct signals of equal intensity at 164.4 eV and 161.8 eV, due to the S $2p_{3/2}$ components with their relative spin-orbit components, S $2p_{1/2}$, at 165.6 eV and 163.0 eV. The presence of two components in the S 2*p* spectrum aligns with the molecular structure having two non-equivalent S species within the ligand [166]. The comparison between XPS regions acquired on the bulk and the sample obtained by sublimation does not reveal significant differences and indicates that molecules can be successfully sublimed. The semi-quantitative elemental analysis of the XPS spectra gives a more detailed indication of the stoichiometry of the molecular deposit (see Tables 4.4 and 4.5).

Table 4.4. Semi-quantitative elemental analysis of the XPS spectra collected on **Cudttt**@HOPG.

Conc%	Theo	Exp	Ratio	Theo	Exp
Cu	9.1	7.0 ± 0.4	Cu/N	0.50	0.36 ± 0.02
N	18.0	19.0 ± 1.8	N/S	0.25	0.27 ± 0.01
S	72.7	73.7 ± 3.7	Cu/S	0.125	0.095 ± 0.031

Table 4.5. Semi-quantitative elemental analysis of the XPS spectra collected on bulk **Cudttt**@Al.

Conc%	Theo	Exp	Ratio	Theo	Exp
Cu	9.1	11.1 ± 0.6	Cu/N	0.50	0.52 ± 0.03
N	18.0	21.2 ± 0.8	N/S	0.25	0.23 ± 0.01
S	72.7	67.7± 3.7	Cu/S	0.125	0.164 ± 0.026

The relative concentration of elements was estimated by considering the area of fitted components and considering the cross-sections characteristic of each element from [167]. The extracted stoichiometry for the sublimated film aligns with the bulk (Table 4.5) and the theoretical one. The analysis did not consider carbon percentage, mainly because of the overlap between the C 1*s* signals of the molecule and HOPG substrate.

We are still managing the deposition of pure **Nidttt** as a possible diamagnetic diluent for **Cudttt**. Moreover, we are currently investigating both systems with the STM technique to highlight possible organization features and preferential orientations of molecules once on a surface. However, based on the magnetic characterization shown before, **Nidttt** could not be the best choice for removing spin interactions since we do not know how molecules are packed on the surface. Different strategies for diluting paramagnetic centers could involve different organic molecules, e.g., deuterated benzo[a]pyrene or C_{60}, that may serve as spacers among paramagnetic units.

AUTHOR'S CONTRIBUTIONS. The author of this thesis performed the whole set of syntheses to get the ligand **dttt**$^{-}$, **Cudtt**, **Nidttt**, and **Cu$_{0.2\%}$dttt** and their magnetic and chemical characterization. Furthermore, he performed X-band cw-EPR characterization on these compounds and implemented their simulations. The author also simulated the Q-band cw and EDFS spectra and rationalized the T_1 data trends. These data were extracted from the measurements conducted at the University of Turin by S. F. Russi, Dr. E. Salvadori, and Prof. M. Chiesa.

4.3 Beyond Transition Metals: [Dy(acac)$_3$(H$_2$O)$_2$]

In the previous sections, we outlined the fundamental role of low-energy vibrations in the spin dynamics of transition metal-based molecular qubits. The spin can undergo a faster spin-lattice relaxation process when an efficient coupling with crystal and molecular phonons (of appropriate energy and symmetry) is set. It has been widely stressed that fast spin-lattice relaxation processes can seriously limit the coherence properties of electron spin-based qubits above 20/30 K. For this reason, a profound comprehension of the role of phonons in this process is mandatory for reducing their effects through the specific design of molecular units. While this aspect has been here treated for transition ions, it has not been presented for lanthanide-based complexes yet, but it can be relevant as well. Because of their electronic and nuclear structure, lanthanide ions are appealing systems for encoding logical qubits and several quantum logic operations in single- or multi-qubit architectures (see also Chap.3). In this respect, the comprehension of the relaxation properties of lanthanide-based molecular magnets is of paramount importance. Intuitively, phonons' effect may be detrimental for lanthanide systems, for which the spin-orbit coupling interaction is usually larger than for the first-row transition metal ions. Up to now, exciting achievements in simulating the magnetic two-phonon (Raman process) relaxation of lanthanide ions through theoretical approaches were gained by including phenomenological parameters [168], or they were limited to systems in gas-phase (at the single-molecule level) [87,169,170]. However, we already observed in Sec.4.1 that calculations on molecules in the gas-phase lead to results partially representative of the true spin relaxation process, and crystal phonons should be included for a more accurate and complete description.

In this work, we provided an accurate fully *ab initio* description of one- and two-phonon processes involved in the magnetization dynamics of lanthanide ions. Indeed, this is the first example where the lower part of the phonon spectrum (lattice vibrations) is introduced within the computational model.

For our purposes, we selected [Dy(acac)$_3$(H$_2$O)$_2$]·H$_2$O·EtOH (acac$^-$ = acetylacetonate) as the archetypical system on which perform our study (from now we will refer to **Dyacac** for simplicity). Indeed, this compound was among the very first investigated single-ion magnets [171] and simple enough to allow a full *ab initio* analysis without prohibitive computational costs (the asymmetric unit contains just sixty atoms). The molecular unit is composed of a central dysprosium(III) ion embedded by six O donor atoms of acac$^-$ ligands and two O atoms from donor water molecules, thus resulting in point-group symmetry D_{2d} (Fig.4.16). The extended framework created by hydrogen bonds and forming the crystal structure is reported on the right side of the same figure.

While our collaborators supported the theoretical calculations, we principally faced the compounds synthesis and their magnetic characterization. **Dyacac** and its diamagnetic isostructural analogue **Yacac** were synthesized according to the reported procedure [171].

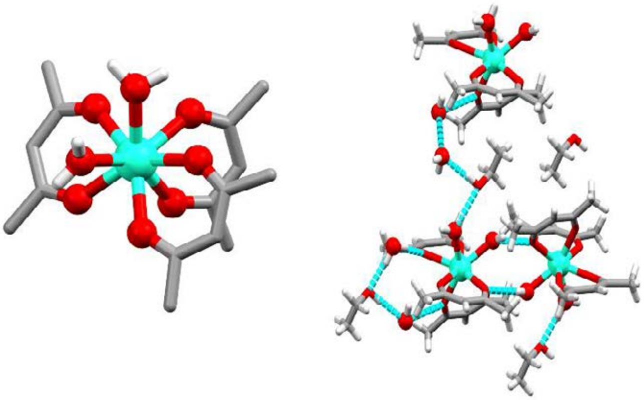

Figure 4.16. On the left, top view of the **Dyacac** molecular structure extracted from [171]. On the right side, it is reported the view on the molecular assembly that forms the crystal structure. Hydrogen bonds between different complexes and crystallization molecules are highlighted as cyan rods. Oxygen atoms of water molecules are represented as spheres for clarity. Color code: Dy = cyan, O = red, C = grey, H = white.

The 1:10 magnetic dilution of **Dyacac** in **Yacac** was prepared by reacting stoichiometric amounts of precursors' salt. X-ray quality crystals and crystalline powders of the title compounds were obtained by slow evaporation of mother liqueurs (H_2O/EtOH solution) for several weeks and employed for further experimental investigations. Notwithstanding the easy synthetic procedure involved, obtaining and manipulating target compounds presented several complications that were initially not expected based on the previous work. Indeed, we observed a change in crystallinity of both **Dyacac** and **Dy$_{0.1}$acac** upon solvent loss when extracted from crystallization solutions. As it is possible to observe in Fig.4.17, the PXRD pattern of **Dy$_{0.1}$acac** crystals well resembles the simulated one within the first minute of air exposure (i.e., until crystals are still wet). Repeating the PXRD analysis as a function of the time, thus leading to residual solution evaporating and crystals drying, it is possible to follow the mentioned change in crystallinity attributed to the loss of ethanol. Furthermore, the change in crystallinity can also be followed by observing the change in crystalline fractions' transparency. Crystals become white and opaque upon solvent loss.

The ethanol crystallization molecule is bridged through a hydrogen bond network to one of the coordinating water molecules and others within the crystal framework. It follows that the magnetic properties can sensibly change upon the loss of EtOH because of a possible rearrangement of the coordination sphere of the dysprosium(III) ion. This behavior was not previously reported, so we performed a complete AC susceptometry characterization of freshly prepared **Dy$_{0.1}$acac** to confirm previous observations (Fig.B.8).

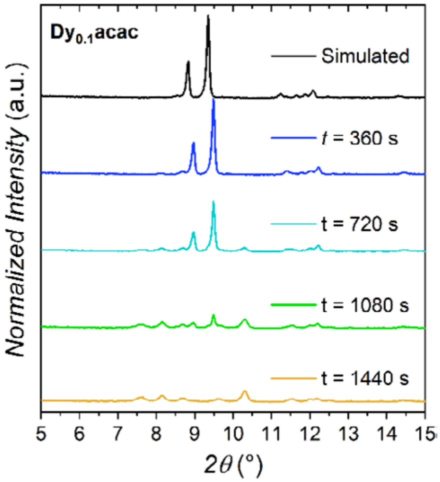

Figure 4.17. Experimental PXRD patterns collected on a freshly prepared crystalline sample of **Dy0.1acac** collected at different times. For preparing the sample, crystals were smashed in a minimum amount of crystallization solvent and then suddenly dropped onto a zero-background sample holder by using a pipette. In this way, crystals are initially protected by the residual solvent.

Due to the hard manipulability of crystals observed once they were extracted from crystallization solution, we faced two main challenges: i) outlining an efficient samples' preparation procedure and ii) interpreting extracted magnetic data. We found it convenient to filter the crystals and rapidly put them into a capsule without further washing or pressing them. Thus, freshly filtered samples were immediately introduced within the susceptometer at 200 K. Such a non-standard procedure caused the measured samples to be poorly homogeneous, and AC signals were naturally broadened by the distribution of particles with different crystallinity grades. Indeed, while the most crystalline fraction grew slowly during crystallization, the product fraction still dissolved in the residual solvent could have gained an amorphous structure when frozen in the susceptometer. As shown in Fig.B.8, the imaginary component of AC susceptibility presents two distinct contributions characterized by two relaxation time constants (τ). We thus fitted AC data with the semi-empirical model reported in Eq.A.17 extended for two contributions. Comparing our experimental results with those reported in [171], we found the faster contribution to be the characteristic one for the compound of interest (Fig.B.9). However, the rationalization of the observed τ vs T trend with empirical models (see Chap.2) was not trivial. Indeed, the accessible temperature interval was precisely where the Raman mechanism gives way to the Orbach one, and it was hard to get a univocal estimation of the empirical parameters characterizing the two regimes. However, we obtained an estimation of the U_{eff}

barrier of 139 ± 8 cm^{-1} (Fig.4.18), which compares well with the outcomes of our calculations (see below).

Many insights on spin relaxation processes given within the paper followed from the theoretical calculations employed. Starting from the electronic structure, we will thus discuss the key points of our observations. Our calculations individuated a $m_J = \pm 15/2$ ground state characterized by an axial symmetry of the associated g-tensor (g_x = 0.045, g_y = 0.089, g_z = 19.371), as commonly observed for Dy^{3+} complexes [132]. In the computed electronic structure, the gap (ΔE) between the ground and first/second excited states is of 101 cm^{-1} and 129 cm^{-1}, while the total ${}^6H_{\frac{15}{2}}$ multiplet energy spans a 450 cm^{-1} interval [82]. The ground state easy axis' direction is roughly parallel to that of the two oxygen atoms (one per $acac^-$ unit) with the shortest distance from the metal center [172]. The hard plane of magnetization lies on the plane individuated by the two water molecules having the larger distance from the Dy^{3+} core.

The computed outcomes were thus validated by cantilever torque magnetometry (CTM) experiments conducted on a freshly prepared single crystal of **Dyacac**. Because of the problems above relative to the solvent loss, a **Dyacac** single crystal was rapidly submerged into grease, indexed at 100 K, and suddenly mounted onto the cantilever probe. Such a technique detects the torque momentum $\vec{t}$ of the sample magnetization by rotating the crystal in a static magnetic field $\vec{B}$ as: $t_Y = M_z B_x - M_x B_z$, where *XYZ* is the laboratory reference framework.

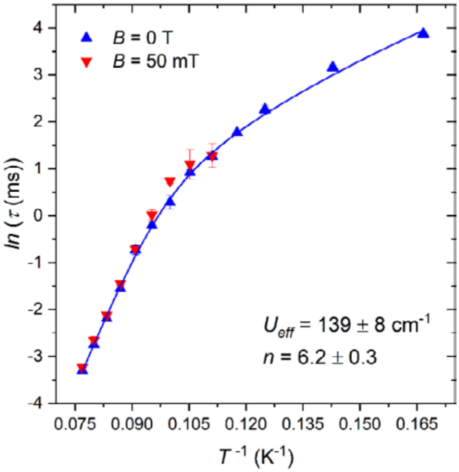

Figure 4.18. Plot of τ values extracted from fits of AC data collected at 0 mT (Blue triangles) and 50 mT (red triangle), reported as ln(τ) vs T^{-1}. The continuous blue line represents the fit obtained by adopting the model: $\tau^{-1} = C_{Ram}T^n + \tau_0^{-1}exp\left(\frac{U_{eff}}{k_BT}\right)$. $\tau_0^{-1} = (8.0 \pm 7.8) \cdot 10^{-9}\ ms^{-1}$; U_{eff} = (139 ± 8) cm^{-1}, $C = (3 \pm 2) \cdot 10^{-7}\ ms^{-1}K^{-n}$; n = (6.2 ± 0.3).

Thus, the absolute orientation of the magnetic anisotropy axes in the xyz molecular reference framework can be extracted by applying opportune Euler's transformations to project *XYZ* into the orthogonal crystal reference framework $ab'c^*$ and subsequently into the *xyz* one [173,174]. Furthermore, such a technique is a very sensitive tool allowing measurements over a wide temperature range, thus probing also excited spin states [175]. The torque curves obtained at the lowest and highest values of temperature and magnetic field strength for two orthogonal rotations of the crystal (Rot1 and Rot2) are reported in Fig.4.19. Rot1 was performed around a generic crystallographic axis on the ac^* plane. We found the rotation axis for Rot1 to lay on the bc^* plane and to form a 25° angle with the *b* crystallographic axis. On the other hand, Rot2 coincides with the c^* crystallographic axis, and the *ab* plane is the probed one. The simulations were implemented by exploiting the whole set of crystal field (CF) parameters (B_m^l in Eq.4.5) extracted from *ab initio* calculations, in accordance with the CF spin Hamiltonian:

$$\hat{\mathcal{H}}_{CF} = \sum_{l=2}^{6}\sum_{m=-l}^{l} B_m^l \hat{O}_m^l(\bar{\boldsymbol{J}}) \tag{4.5}$$

WhereB_m^l are anisotropy terms, and $\hat{O}_m^l(\bar{\boldsymbol{J}})$ are tesseral operators [176]. In the equation, *m* and *l* indexes are related to the spherical harmonic's order ($l \leq m$, and m = even integer). Our simulations are in fair agreement with experimental results, despite a marked offset of ca. 14° for Rot1 data. The best agreement between simulations and experimental results was obtained by fixing the CF parameters and fitting the Euler's matrix; the latter correlates the crystal field with the crystallographic reference frameworks.

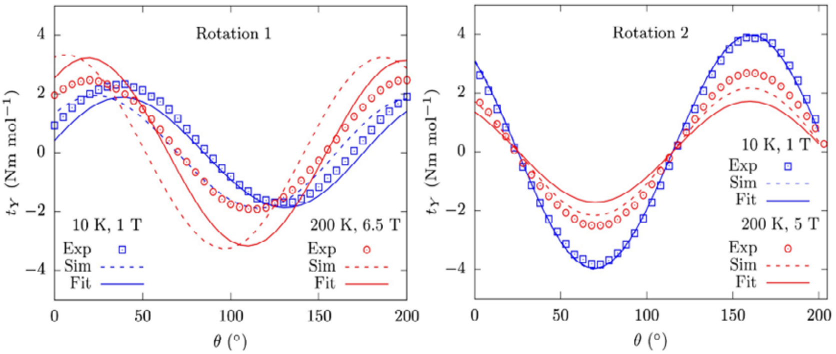

Figure 4.19. Plots of the Y component of the experimental torque momentum for two orthogonal directions of a **Dyacac** single crystal reported as a function of the rotation angle θ. Reproduced from [81].

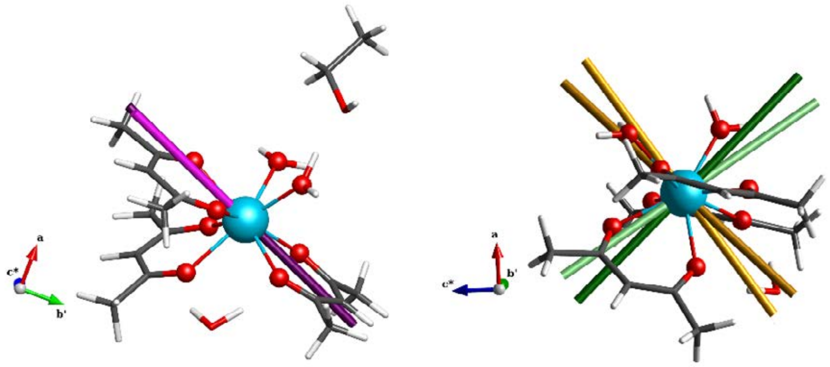

Figure 4.20. Pictorial representation of calculated (light colors) and fitted (dark colors) easy (magenta), intermediate (green), and hard (yellow) axes directions on the molecular structure of **Dyacac**. Color code: Dy = cyan, O = red, C = grey, H = white. Reproduced from [81].

Such a procedure resulted in a better agreement of experimental and fitted values of Rot2, while it did not improve Rot1 analysis. However, only minor deviations of the best-fit principal axis directions from theoretical predictions were observed (Fig4.20), especially regarding the easy axis one (magenta axis on the left side in Fig4.20).

Comparing computed CF parameters with experimental CTM results was fundamental for validating the quality of *ab initio* calculations, especially those concerning the different contributions to the magnetic relaxation dynamics. Indeed, the CF Hamiltonian reported in Eq.4.5 describes the electronic structure of the ground multiplet at the equilibrium. Any fluctuation of atoms' positions due to the thermal vibrations at finite temperatures gives rise to the spin-phonon coupling (SPC) phenomenon through the modulation of $\hat{\mathcal{H}}_{CF}$, which subsequently leads to the relaxation of the magnetization. Two principal quantities were considered in this limit, namely the vibrational modes of the lattice (q_α) and the spin-phonon coupling operator ($\hat{V}_\alpha = \sum_{l,m}(\partial B^l_m/\partial q_\alpha)\hat{O}^m_l$) [85,86,177]. Including these quantities in computed relaxation rates for first- and second-order processes (see Appendix B for further details on employed models), i.e., Orbach (W^{1-ph}) and Raman (W^{2-ph}) ones, it was thus possible to extrapolate relaxation time values (τ) characteristic of each mechanism directly as Fourier transform of the computed W^{1-ph} and W^{2-ph} rates (Fig.4.21).

Calculated τ were compared to experimental values extracted from AC susceptometry measurements at zero-field on Dy$_{0.1}$acac (6 K $\leq T \leq$ 13 K). Furthermore, an additional point at 2 K was extracted by treating the hysteresis loop collected at 1500 Oe on the pure **Dyacac** sample and used for the comparison. Here, we observed a discrepancy around two orders of magnitude among calculated and experimental τ values in the whole temperature range.

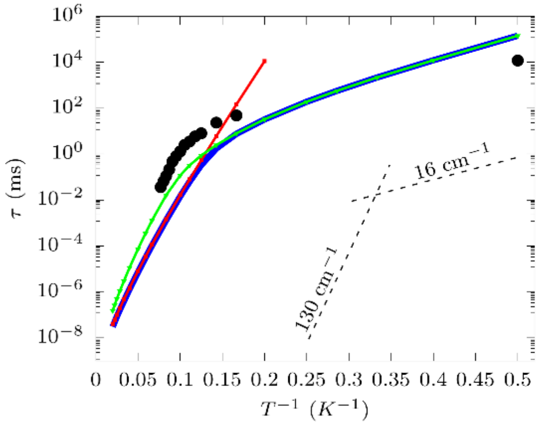

Figure 4.21. Semi-log plot of computed (red = Orbach and green = Raman points) and experimental (black circles) τ values obtained for **Dy0.1acac**. Solid lines on computed points are used as a guide for the eyes. The blue line represents the computed relaxation time due to both Orbach and Raman contributions. Dashed black lines corresponding to $\exp(U_{eff}/k_BT)$, with U_{eff} = 130 cm^{-1} and 16 cm^{-1} are reported in the bottom right part of the plot as a guide to the eye to interpret results. Reproduced from [81].

This evidence can be explained by recalling what was observed from comparing measured and predicted CTM results, which showed only a semi-quantitative agreement between the two data sets. In both cases, the discrepancies observed between calculated and experimental data can be ascribed to our estimation of CF parameters. The accuracy in determining CF parameters must be improved to enhance the agreement between relaxation times. Nonetheless, estimated τ values can also be affected by the accuracy in calculations of phonon modes. Phonon calculations are usually affected by minor inaccuracies due to the lack of anharmonic shifts or deficiencies in describing the lattice's dispersion forces from DFT theory [69,71,178]. These observations clearly show that a more accurate computational procedure will be required in the future to rationalize the relaxation phenomenon best.

However, many other fundamental aspects concerning the relaxation pathways can be deduced from our calculations that still represent a foreground innovation in this field. For instance, we highlighted the relative weight of two different relaxation processes on the overall magnetization dynamics of lanthanide magnets. We confirmed that, while the Orbach relaxation process may dominate the high-temperature regime, a Raman two-phonon process rules low-temperature relaxation (Fig.4.21). In this respect, several aspects should be considered when examining possible contributions to the Raman process. Three requirements must be contemporarily fulfilled: i) phonons should be sufficiently populated. Indeed, the huger the population of the mode, the stronger the effect; ii) their energy should be comparable to that of the virtual spin transition involved, i.e., the transition from a generic state a to any of excited states c; iii) the sum of adsorbed and emitted phonons' energies must match the difference in energy between the initial and final states. In the case of Kramers' ions in zero-field, this implies that phonons must be degenerate.

In the low-temperature regime (below 5 K) at which Raman occurs, only low-energy phonons are significantly populated, and phonons that match the energy between the ground and first excited doublets (100 cm^{-1}) cannot contribute to the Raman process. In this respect, we needed to consider how conditions (i) and (ii) contribute to the computed relaxation rates. Let us consider the expression for $W_{a,b}^{2-ph}$ reported in Appendix B (Sec.B.2), i.e., the computed transition rate associated for a two-phonon relaxation process from the state a to b. It is possible to observe that the thermal population, requirement (i), depends exponentially on the energy of modes. Indeed, $W^{2-ph} \propto [exp(\hbar\omega_\alpha/kBT) - 1] - 1$, where $\hbar\omega_\alpha$ is the energy of the adsorbed or emitted α-th phonon mode involved in the process. On the contrary, condition (ii) is only enforced by a power of two since $W^{2-ph} \propto |[E_c - E_a \pm \hbar\omega_\beta]| - 2$. At the temperature at which the Raman process occurs in lanthanide-based compounds (i.e., below 10 K), condition (i) is thus the most stringent one. Therefore, we found the first couple of degenerate normal modes at 16 cm^{-1} to best agree with these requirements. These modes involve a change in the angles between the Dy ion and the planes containing the acac$^-$ ligands, while the central unit composed by the Dy−O bonds remains almost rigid, and it contributes to τ^{-1} following the relation:

$$\tau^{-1} \propto \frac{e^{\hbar\omega_\alpha/k_BT}}{(e^{\hbar\omega_\alpha/k_BT} - 1)^2} \tag{4.6}$$

This expression is similar to that reported in the Eq.4.2 (presented before for transition metal ions in Sec.4.1), and it replaces the phenomenological model for which the Raman relaxation process depend exponentially on the temperature as $\tau_{Ram}^{-1} \propto T^{\,n}$, $2 \leq n \leq 9$ (see Sec.2.4). Moreover, relation (4.6) reduces to $\tau \propto e^{\hbar\omega_\alpha/k_BT}$ in the limit of $k_BT < \hbar\omega_\alpha$, and, in the present case, to $\tau \propto T^{-2}$when $k_BT > \hbar\omega_\alpha$.

The dependence of $\tau \propto T^{-2}$ has been also obtained for $S = 1/2$ qubits [86]. However, even if such an analogy was effectively found, the different phenomena originating from the SPC in these systems must be considered. Indeed, the principal source of Raman relaxation in a $S = 1/2$ system in zero-field is correlated to the presence of hyperfine and dipolar coupling interactions that break the multiplet symmetry (see Chap.2). Here, the SPC is due to the quadratic dependence of the spin Hamiltonian with respect to atomic displacements [71,86]. On the contrary, in those systems with higher spin multiplicity like SMMs, the Raman relaxation rate depends linearly on SPC (see Eq.B.1) and at the second order on the energy difference between a and c states (i.e., on the time-dependent perturbation theory). The latter dependence is due to the presence of low-lying excited states that can be admixed because of external perturbations like phonons (see also Chap.2). Here, the SPC originates from the modulation of the CF Hamiltonian due to both the first coordination sphere's distortions and the ligands' backbone distortion. The latter is due to the modulation of the coupling between the Dy ion and *sp*^{2} hybridized C atoms of acac$^-$ ligands due to electrostatic polarization effects. This last observation emerged from several considerations on the relation between SPC and the normal modes DOS outlined by *ab initio* calculations. By observing the plot in Fig.4.22, which reports the comparison between SPC and DOS distribution as a function of the wavelength, there is no way to correlate high-density DOS regions (e.g., the region around 1000 cm^{-1}) with strong SPC values. Calculated SPC coefficients are indeed strictly correlated to the nature of the involved vibration. As an example, those vibrations only slightly affecting the first coordination sphere of **Dyacac**, or entirely localized on side functional groups (e.g., methyl groups rotations) and molecules (e.g., EtOH), present non-relevant SPC intensities.

The two vibrational modes characterized by the largest SPC intensities (Vib1 ~ 1500 cm^{-1} and Vib2 ~ 380 cm^{-1}) are represented for clarity in Fig.4.22. Both imply a large distortion of the Dy^{3+} first-coordination sphere, thus resulting in large SPC values. However, the nature of these vibrations presents several differences. At first, Vib1 is mainly affected by the stretching of C=O bonds within ligands (see the two limit Lewis structures reached during the vibration and reported in Fig.4.22), while Vib2 is related to the breathing of the acac$^-$ ligands. Let us consider the effect of charge displacement on the SPC. Adopting an electrostatic model that accounts only for oxygen atoms displacements in acac$^-$, we estimated a set of approximate SPC coefficients that perfectly agree with those extracted with the explicit model adopted before. This result shows that the SPC is largely driven by the modulation of electrostatic interactions of **Dyacac** first coordination sphere.

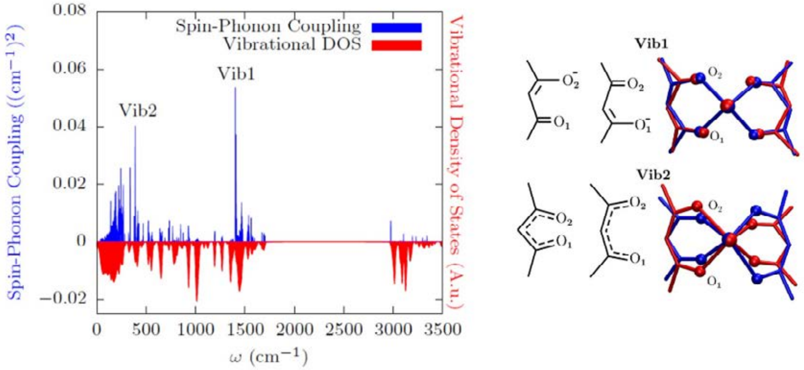

Figure 4.22. Comparative plot of calculated SPC and normal modes DOS as a function of the vibrational wavelengths. A representative sketch of the two vibrations characterized by the highest SPC intensities is reported on the right side of the plot. Reproduced from [81].

However, Vib1 presents a larger SPC than Vib2 despite the smaller distortion of the coordination sphere. It suggested that a second effect would arise from those atoms placed beyond the first coordination sphere. We thus considered the SPC coefficients resolved for each atomic site of the molecule (Fig.B.10a). What interestingly emerged from this analysis was that SPC coefficients are stronger for second and third Dy nearest neighbors (i.e., the carbonyl C atoms, and the C sp^2 atoms in α position to the carbonyl group) than for directly bonded O atoms of water molecules.

Based on this last result and previous outcomes from the electrostatic model employed, we hypothesized that the **acac** backbone could act indirectly through the polarization of the first coordination shell's local charge. For the sake of clarity, the delocalized π system allows the resonance of the double bonds characterizing the structure of ligands. This resonance leads to a natural stretching of carbonyls bonds when switching from C=O to C─O$^-$, that, subsequently, involves the variation of the local charge on the O atoms (Fig.B.10b). How efficient is the capability of the O atoms in donating the charge density to the dysprosium(III) ion is thus strictly correlated to the stretching of the CO bond. This phenomenon is much more significant for Vib1, where the change in the CO bond length gains local charge fluctuation two orders of magnitude greater than those observed for Vib2. The latter brings only small modulations about the charge distribution within the first coordination shell (left side in Fig.4.23). Furthermore, we reproduced the same calculations by changing the acac$^-$ ligand with acetone and 2propoxide molecules to further evidence the role of the conjugated ligand backbone in modulating the oxygen charge (right side in Fig.4.23).

For instance, the absence of conjugated structures in 2-propoxide results in a smaller charge variation upon the stretching of the C─O bond. We thus observed a minor contribution to the SPC of the C atoms for this alcohol with respect to a

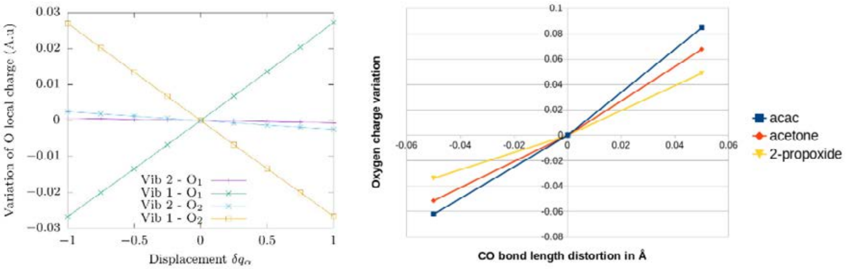

Figure 4.23. On the left, plot of the calculated variation of O total charge as a function of the displacement of two O atoms of one acac$^-$ ligand. On the right, plot of the O charge variation as a function of the C−O bond length distortion for three different ligands. Reproduced from [81]

betadiketonate as the acac$^-$ ligand. At the same time, the acetone molecule shows an intermediate behavior since it does not have a conjugated structure, but the O atom has a significant tendency to distribute the charge over the bonded sp^2 C atoms. From the point of view of a synthetic chemist, such an observation is extremely useful because it can be adopted as an additional guideline for rationalizing new ad-hoc tailored ligands to reduce SPC effects and tune the relaxation process of the embedded spin.

In conclusion, we unveiled the origins of spin-phonon coupling in this class of Dy^{3+}-based molecular magnets, disentangling different contributions to the magnetization dynamics through a coupled experimental/theoretical approach. Indeed, while *ab initio* predictions on Dy^{3+} electronic structure were confirmed by CTM measurements, the extended comparison between experimental and calculated values allowed us to i) rationalize the effect of Orbach and Raman relaxation processes on the magnetic relaxation and ii) to understand limits and opportunities for improvement of *ab initio* methods.

AUTHOR’S CONTRIBUTIONS. The author of this thesis synthesized and characterized all the mentioned compounds and their solid dilutions. Furthermore, he performed AC susceptometry and DC magnetometry measurements and treated the extracted data. He also managed the crystals’ indexing procedures and, together with Dr. L. Tesi, the CTM measurements.

Chapter 5

Exploiting [VO(TPP)] molecular qubit as a platform for advanced EPR experiments

In the previous chapter, it has been shown how a tailored molecular design may lead to a reasonable T_m enhancement and other significant functional properties of potential molecular spin qubits. Moreover, we discussed how a coupled experimental/*ab initio* approach plays a crucial role in comprehending relaxation properties both of first row and lanthanide metal complexes. From an experimental point of view, cw and pulsed EPR spectroscopies provided cardinal tools for investigating and manipulating qubits' quantum properties.

In the present chapter, we present two main works that highlight the potentialities of the EPR technique for precise controlling of quantum properties. In particular, we focused our attention on the study of the prototypical molecular qudit [VO(TPP)] (TPP^{2-} = tetraphenyl porphyrinate) [46,77]. This archetypical qubit was already presented, and its quantum properties were investigated in a previous work [77]. Here, an appreciable coherence time ranging from 1 μs to 0.1 μs was observed within the 5 300 K temperature range.

Moreover, solid dilution of this compound can be obtained by employing the diamagnetic and isostructural analog [TiO(TPP)]. Such a peculiarity is fundamental for investigating and manipulating quantum properties on an oriented crystal, thus allowing the probe of specific electronic transitions selectively as a function of the relative orientation between the instrument's reference framework and that of the molecule. Even if single-spin manipulation is one of the ultimate goals, solid samples containing spin ensembles can be considered test systems for integrating molecular spin qubits in quantum architectures working at microwave frequencies.

Fabio Santanni, University of Florence, Italy, santannifabio@gmail.com, 0000-0002-0506-8333

Referee List (DOI 10.36253/fup_referee_list)
FUP Best Practice in Scholarly Publishing (DOI 10.36253/fup_best_practice)

Fabio Santanni, *Molecular approaches for quantum technologies. Optimization of electron spin-based quantum bits and quantum logic gates*, © 2025 Author(s), CC BY 4.0, published by Firenze University Press, ISBN 979-12-215-0670-9, DOI 10.36253/979-12-215-0670-9

In the end, we will show the results of preliminary purification steps required for the preparation of diluted [VO(TPP)] polycrystalline samples, whose spin dynamics will be investigated by using a particular experimental setup involving both THz-FEL (Free-Electron Laser) radiation and EPR spectroscopy. A high purity grade is indeed required for this peculiar experiment, i.e., the TR-THz-EPR experiment (TR = time-resolved).

5.1 Storage and retrieval of information within a molecular spin ensemble

In the past few years, spin-based quantum memories have attracted considerable interest from the scientific community. In particular, there is a specific interest in combining them with performing superconductive quantum circuits. While superconductive qubits are appealing systems to perform quantum algorithms since they guarantee the fast implementation of single- and two-qubit gates, they usually suffer from short coherence times compared to spin-based devices. Such a feature is detrimental when many information packages must be sent subsequentially to the quantum register for implementing an algorithm. For instance, collections of *n* spins can be adopted as quantum memories integrated within hybrid quantum circuits like the one reported in Fig.5.1. Here, the spin ensemble is coupled to a transmon-based quantum processor through a superconductive planar resonator, namely a *quantum bus*. The complete information is thus cached within the quantum memory (characterized by long T_m values). When needed, an information packet is transferred to a highly efficient quantum processor (a superconductive circuit) for running the algorithm (read step), while the other packets are still stored within the memory. Although different strategies based on the nuclear spin and solid-state electron spin-based qubits have been presented so far [179,180,181], emerging technologies such as molecular spin qubits still need to be investigated for this purpose.

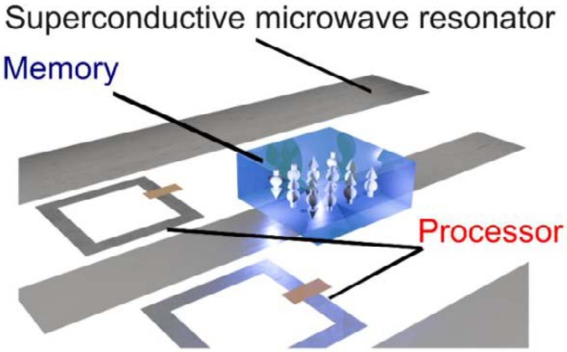

Figure 5.1. Cartoon of a quantum architecture composed by a generic spin-based quantum memory (spin ensemble) coupled to a transmon-based quantum processor.

Indeed, molecular qubits benefit from several features, as already expressed in the previous chapters. For instance, it would be possible to avoid multiple frequency conversion (as in nuclear spin-based qubits), thus working at the same microwave frequency range usually employed for superconducting qubits.

For this reason, we employed the archetypical [VO(TPP)] (**VOTPP**) molecular qubit to couple its spin system with a coplanar superconductive microwave resonator [182]. The latter was made of superconducting YBCO ($YBa_2Cu_3O_7$) film deposited on a Sapphire substrate (Fig.5.2). Some of the authors realized the employed setup [183], which was previously presented in a similar work aimed at investigating a polycrystalline sample of [VO(Pc)] [134]. A sketch of the employed apparatus is reported in Fig.B.11.

We investigated a 2% dilution of **VOTPP** in its diamagnetic isostructural analogue [TiO(TPP)], namely **VO$_{2\%}$TPP**. In particular, we performed a complete cw and pulsed EPR characterization at the X-band frequency, both on a polycrystalline sample and an oriented single crystal. In the following treatment, we will focus on the latter case, while we address the reader to Appendix B for further details on the measurements results obtained in the case of the polycrystalline sample (Figs.B.12-B.14). It must be specified that while our collaborators at the University of Modena and Reggio Emilia conceived the experiments and performed all the measurements using the superconducting resonator, we focused our attention on obtaining the adopted samples. Furthermore, we investigated their structural properties and rationalized their transmission cw-EPR spectra for modelling the transitions' line shapes.

Single crystals of **VO$_{2\%}$TPP** were obtained as reported in [77]. The employed crystal (crystal volume $\approx 0.5 \times 0.5 \times 0.5$ mm^3) was grown by very slow evaporation

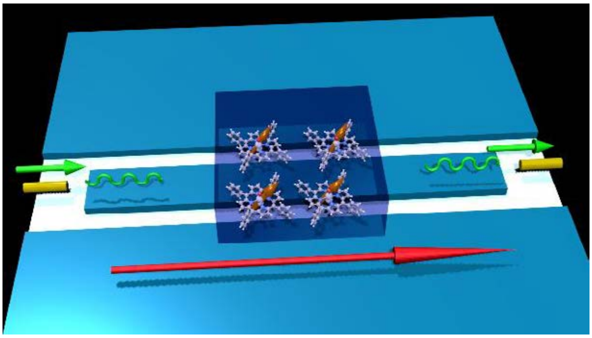

Figure 5.2. Pictorial representation of the experimental setup employed for our experiments on **VOTPP**. The spin ensemble (molecular units within the purple solid) lies in the middle of the coplanar resonator (light-blue area). Yellow cylinders represent the two coupling antennas, while green arrows and sinusoids show the path of the microwave signal. The red arrow represents the externally applied static magnetic field $\vec{B}_0$. Reproduced from [182].

of a CH_2Cl_2 solution, and it was indexed by adopting the X-ray diffraction technique before use.

In this way, we obtained information about the relative orientation between the molecular z axis and the crystallographic planes individuating the crystal's faces. Crystals of **VO$_{2\%}$TPP**, as well as **VOTPP** ones, grow as compressed octahedra, where the most grown faces are those evidenced on the right of Fig.5.3. The figure shows that the triplet of crystallographic axes passes through vertices of obtained octahedral crystals. The molecular magnetic z axis coincides with the V=O bond direction, and it is parallel to the c crystallographic axis of the tetragonal lattice (Space group: $I4$; $a = b = 13.38$ Å; $c = 9.78$ Å; $\alpha = \beta = \gamma = 90°$; $V = 1750$ Å^3). A representation of the molecular structure within the unit cell is reported on the left side of Fig.5.3. Based on these observations, we mounted the crystal on the measurement apparatus with the compressed axis direction normal to the plane of the resonator. In this way, we were able to orient $z \perp B_0$, and $z \mathbin{//} B_1$ (we recall that for perpendicular mode operation $B_1 \perp B_0$; Fig.5.3, right side).

At first, we directed our attention toward the investigation of the magnetic properties of the sample. We collected cw and EDFS transmission spectra and implemented an extensive simulation of the obtained data to i) rationalize the static properties of the sample, ii) confirm the correct orientation of the crystal mounted on the resonator, and iii) highlight different contributions to the line-broadening of EPR transitions. The cw transmission spectrum obtained by measuring a single

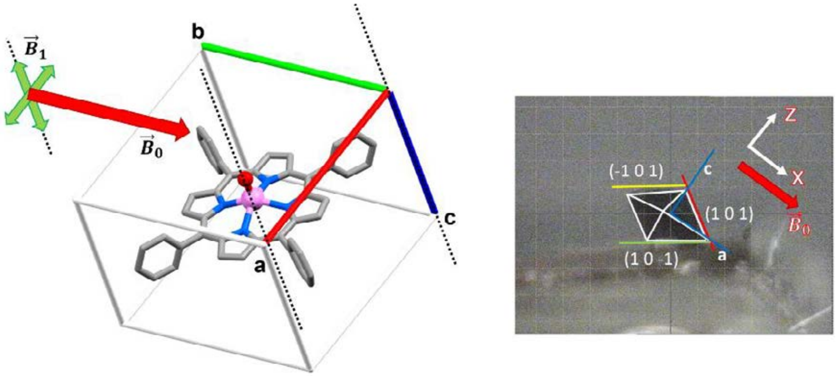

Figure 5.3. On the left, molecular structure of a **VOTPP** unit reported together with the unit cell and crystallographic axes. The directions of the V=O bond (parallel to the blue c axis) and $\vec{B}_1$ (green arrows) component is highlighted by dashed black lines. The red arrow highlights the direction of $\vec{B}_0$. On the right side, a photograph of a **VOTPP** crystal is reported. The relative orientation between the crystallographic axes (blue lines), the crystal's faces (individuated by crystallographic planes reported as yellow, green, and red lines), and the lab's reference framework (X, Y, Z) are highlighted.

crystal of the 2% doped sample is reported in Fig.5.4a. The EDFS spectrum obtained on the same sample is reported in Fig.5.4b.

Here, we observed eight lines due to the hyperfine coupling interaction between the vanadium's electron ($S = 1/2$) and nuclear (^{51}V, N.A. = 99.75%, $I = 7/2$) spins. Furthermore, some of the lines of the EDFS spectrum show additional structure due to a superhyperfine interaction of the spin with the four bonded N of the ligand core (see the zoom reported in the Fig.5.4-c). The best simulations were obtained by adopting the SH parameters reported in [77] ($g_x = g_y = 1.9865(1)$,$g_z = 1.963(1)$, $A_x = A_y = 168(2)$ MHz, $A_z = 477(2)$ MHz). These simulations also highlight that we were probing the perpendicular components of **g** and **A**, hence confirming the correct orientation of the crystal with $z \perp B_0$. The line broadening model for collected spectra considers a Gaussian strain of **A** (≈ 10 MHz in the case of cw-EPR, and ≈ 7 MHz for the EDFS spectrum) acting on a Voigtian line shape. We modelled the line shape by adopting a composition of Gaussian and Lorentzian distributions having $FWHM_{Gaussian} = \Gamma_G \approx 25$ MHz, and $\Gamma_L \approx 11$ MHz for cw-EPR spectrum, and $\Gamma_G \approx 5.5$, $\Gamma_L \approx 2.8$ for EDFS spectrum.

This analysis allowed us to highlight the presence of inhomogeneous broadening contributions affecting the coherence properties of our samples (see also Fig.B.13). The extracted linewidth values for cw-EPR spectra are far beyond the homogeneous linewidth $\gamma_{hom} \approx 1$ MHz expected for the working temperature (2 K) extracted by the relation $\gamma_{hom} \leq 1/T_m$ [74,184], with $T_m = 1\ \mu s$ [77]. This result evidenced that a larger contribution to the line broadening arises from two principal inhomogeneous sources, i.e., intrinsic (due to the sample) and extrinsic (due to the apparatus) ones. The principal sources of intrinsic inhomogeneous broadening are due to dipolar spin-spin interactions, hyperfine interaction and its strain, and unresolved super-hyperfine interactions. The extrinsic broadening is instead mainly related to the inhomogeneity of both B_0 and B_1. The B_0 inhomogeneity is mainly due to the insurgence of non-negligible static magnetic

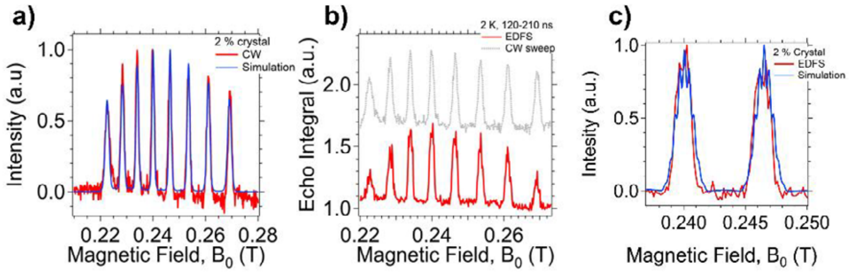

Figure 5.4. (a) Plot of the experimental cw-EPR spectrum (red) obtained on a **VO$_{2\%}$TPP** oriented crystal reported with its simulation (blue). (b) Comparison between the experimental cw-EPR (grey) and EDFS spectra (red). (c) Zoom of the two central lines of the experimental (red) and simulated (blue) EDFS spectra where the superhyperfine transitions are evidenced. Reproduced from [182].

field gradient of ≈ 0.5 T m^{-1} developing along the longitudinal axis of the resonator. Both intrinsic and extrinsic contributions lead to fast spin dephasing, thus reducing the coherence time of the system.

Hence, we employed two distinct dynamical decoupling protocols, i.e., the Carr- Purcell-Meiboom-Gill = CPMG and Uhrig Dynamical Decoupling = DD sequences (where N = number of π pulses sent), to efficiently decouple the spin system from the environment and correct the dephasing effects arising from extrinsic factors [185,186]. The two pulses sequences were implemented working at $B_0 = 0.24$ T, i.e., at the field correspondent to the maximum intensity of the echo signal (Fig.5.4-a). Comparing the value of $T_m = 0.97 \pm 0.10$ μs extracted from our Hahn-echo experiments with those extracted from these dynamical decoupling protocols, it is clear that such procedures resulted in a marked T_m enhancement. The phase memory time of the system increases as the number of the sent π pulses increases (Fig.5.5). We attributed the observed T_m values to our samples' emerging intrinsic spin dynamics as the employed protocols suppress the extrinsic contribution. On the other hand, as T_m increases while increasing the number of π pulses, echo intensities follow an inverse trend. This behavior realistically sets the limits of our experiments to $N = 4$ and $N = 3$ employed pulses for DD and CPMG protocols, respectively.

Once the qubit's coherence properties were successfully characterized, we investigated its storage properties. Recalling what was stated above, the spin ensemble composing the quantum memory must be able to efficiently store the information, which should be retrieved in a second moment. To probe the storage efficiency, we employed a common protocol to highlight the storage capability in other spin systems, e.g., solid-state electron or nuclear spin ensemble [179,187, 188]. The experimental protocol requires several pulses to be adopted within the

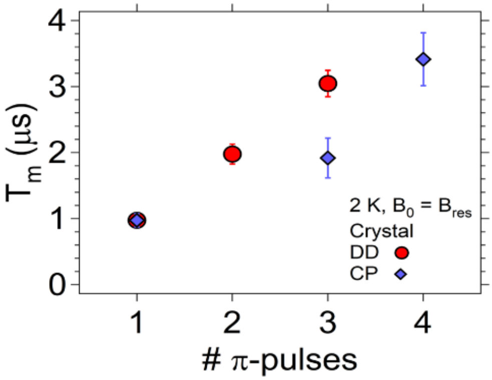

Figure 5.5. Plot of the T_m values extracted from the data analysis of CPMG and DD experiments, which are reported as a function of the number of the employed π pulses. Reproduced from [182].

sequence. At first, the spin system was initialized by employing an initial $\pi/2$ pulse. After a fixed delay τ, a train of shorter "weak" microwave pulses (40 μV output from the arbitrary wave generator: AWG) spaced by a delay $\tau_D = 300$ ns was sent to the sample. Here, the stored string of bits values is generated by switching on (1) or off (0) each pulse (e.g., $1 - \tau_D - 0 - \tau_D - 1 -$ *etc.*). For clarity, each pulse is defined as 1 or 0 depending on the amplitude of the AWG output, i.e., 1 = 40 μV and 0 = 4 μV. During a second delay τ, the spins are left free to diphase until a refocusing π pulse of the same intensity of the $\pi/2$ one is applied. The output was then collected as an echo train retrieving the information stored before. In our case, experimental conditions were $T = 2$ K and $B_0 = 0.24$ T. Because of the reduced crystal dimensions, echo intensities were too low, and we successfully stored and retrieved only three pulses on the **VO$_{2\%}$TPP** single crystal (left side in Fig.5.6).

On the contrary, storage of five pulses was reached in the case of the larger number of spins present in the polycrystalline sample (right side in Fig.5.6; see also Fig.B.14). In the latter case, it was also possible to finely vary the order of 0 and 1 pulses and collect different strings of bits, thus understanding how they are retrieved. Interestingly, the order of outcome echo intensities is reversed with respect to that of the pulse sequence, as expected by the time-reversal (refocusing) of the π pulse (right side of Fig.5.6).

This result compares well with precedent ones reported for NV centers embedded in planar resonator geometries [179,188]. In those cases, up to 6 pulses

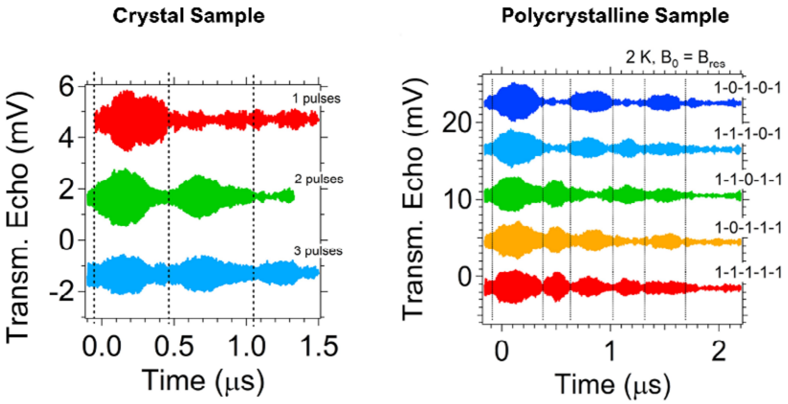

Figure 5.6. On the left, plot of the transmission echo intensities as a function of the time for the [VO(TPP)] single crystal. The number of applied weak pulses increases from the red trace (one pulse) to the light blue trace (three pulses). On the right, plot of the echo traces as a function of time for the polycrystalline sample. Traces were obtained by adopting different sequences of weak pulses. Vertical dashed lines delimit each transmission echo signal. The pulse sequence is reported on the right side of echo traces, and it should be read from the left to the right side. Reproduced from [182].

were successfully stored within the spin ensemble by working at lower temperatures (100−400 mK) and employing a laser apparatus to reset the magnetization, subsequently reducing the delay time between pulses.

In our case, we reached a similar value of 5 pulses by only adopting the pulsed EPR technique and working at higher temperatures. However, we need to consider that the maximum number of storable pulses ($\#M$) strictly depends on the spin dynamics of our system, i.e., $\#M = T_m/T_M^* \approx 1\mu s/120\,ns \approx 8$ (T_M^* = FID limit of the ensemble, taken as the typical decay time of the Rabi oscillations for the crystal).In addition, we compared our experimental results with those observed in an Er^{3+} ions-doped inorganic crystal, in which up to 16 pulses (but with a theoretical $\#M = 56$) were successfully retrieved at 50 mK. We also focused on experimental echo efficiency, defined as the ratio between the energy radiated during the echo related to the energy of incoming pulses. For our system, we estimated a total efficiency $E \approx 4.5 \cdot 10^{-5}$, less than one order of magnitude lower than that of NV centers ($E \approx 2\cdot10^{-4}$) and Er^{3+} ions ($E \approx 1 \cdot 10^{-4}$).

Based on this analysis, we defined possible margins for improvement of our experiments. These could be obtained by cooling our samples down to mK temperature or by upgrading the experimental setup, e.g., by optimizing the pick-up apparatus. Since $\#M$ is a function of the coherence of the employed molecular spin qubits, experiments could be improved by coupling storage and retrieval sequences with a dynamical decoupling protocol.

In conclusion, we integrated a molecular spin ensemble of **VO**$\mathbf{VO_{2\%}TPP}$ units in a coplanar superconductive resonator. We investigated the spin dynamics of our system and rationalized the different contributions to the line broadening of transmission cw-EPR spectra, thus unveiling possible contributions to the decoherence of the spin system. We successfully employed dynamical decoupling protocols to reduce the effect of extrinsic dephasing factors and characterized the T_m of our samples directly correlated to the intrinsic decoherence properties of $\mathbf{VO_{2\%}TPP}$. At last, we obtained seminal results for the storage and retrieval of information within a molecular spin ensemble, thus paving the way toward realizing molecular quantum memories.

AUTHOR'S CONTRIBUTIONS. The author of this thesis and Dr. M. Atzori synthesized all the employed samples and prepared both crystalline and polycrystalline samples. Furthermore, the author carried out the EasySpin simulations of the transmission EDFS- and cw-EPR spectra.

5.2 Enhancing the coherence time by exploiting electronic clock transitions

The previous section showed different strategies for enhancing the coherence time of an ensemble of molecular spin qubits principally based on dynamical decoupling protocols. As a matter of fact, all these protocols rely on removing dephasing contributions correlated to inhomogeneities of the static magnetic field by continuously refocusing the transverse magnetization of the spin system with several π pulses. However, such strategies may suffer from the low signal intensity reached after several pulses in a highly diluted sample. This drawback prompts for the use of other possible strategies to improve T_m. For instance, it is possible to work at specific spin transitions at which the spin dynamics of the system is robustly protected from the magnetic field fluctuations of the environment. These are the so-called clock transitions (Fig.5.7) that occur at specific orientation and intensity of the applied static magnetic field (namely, the clock transition field = B_{CT}) and in correspondence of an avoided level crossing (or anticrossing) between two energy levels of the investigated system. Because of the repulsion between the states $\psi_i = \frac{1}{\sqrt{2}}(|\downarrow\rangle + |\uparrow\rangle))$ and $\psi_i = \frac{1}{\sqrt{2}}(|\downarrow\rangle - |\uparrow\rangle))$, at $B = B_{CT}$, they are separated in energy by a quantity Δ. Interestingly, the energy variation as a function of the applied field $\partial E/\partial B$ approaches to 0 as $B \rightarrow B_{CT}$ (see Fig.5.7). In this limit, small deviations from the resonance field B_{CT} due to field inhomogeneities do not perturb the resonance frequency of the spin, thus not inducing decoherence in the spin dynamics. The wider the curvature of levels (i.e., for lower values of $\partial E/\partial B$), the more marked the effect. In molecular spin qubits, this effect strictly depends on their spin Hamiltonian's parameters.

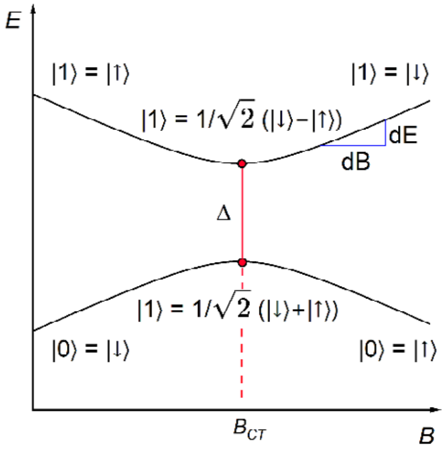

Figure 5.7. Plot of an avoided level crossing occurring in a two-level system. The difference in energy between the two levels (Δ) is here highlighted in red.

Clock transitions have been widely employed for enhancing the coherence time of solid-state, optical, and trapped ion-based quantum devices [189,190−192]. On the other hand, they were investigated for molecular qubits only in the past few years [124,125,193−195]. Even for these systems, coherence time enhancement was reported. Up to now, all the works were focused on anisotropic systems containing lanthanide ions (e.g., polyoxometalates like $Ho(W_5O_{18})^{9-}$ [193]) or transition metal ions with $S > 1/2$ (e.g., magnetic clusters [195] or nickel(II) metal complexes [194]), thus operating on clock transitions between electronic or nuclear spin anticrossing levels.

Inspired by these intriguing results, we employed the archetypical $S = 1/2$ qubit [VO(TPP)] to exploit clock transitions arising between the set of energy levels of its ground multiplet $|m_S,m_I\rangle = |\pm 1/2,\pm 7/2\rangle$. In Fig.5.8, it is reported a simulation of the Zeeman levels diagram for a VOTPP single crystal with the *c* crystallographic axis parallelly aligned with respect the direction of $\vec{B}_0 = \vec{B}_Z$ (i.e., $\theta = 0°$). The simulation was implemented by adopting the set of SH parameters reported in [77] and recalled in the previous section (see Sec.4.1). Here, the clock transitions occurring at avoided level crossings are highlighted in red and labelled as W_1 ($B_Z = 0$ mT, and $\nu = 675$ MHz), W_2 ($B_Z = 17$ mT, and $\nu = 650$ MHz), W_3 ($B_Z = 34$ mT, and $\nu = 582$ MHz), and W_4 ($B_Z = 44$ mT, and $\nu = 444$ MHz).

According to our simulations, clock transitions are allowed only if the direction of the oscillating field $\vec{B}_1$ is parallel to that of $\vec{B}_Z$ (i.e., in the parallel mode). Such behavior can be explained by considering the eigenstates matrix's composition for finite frequency (ν) and B_Z values. For instance, if we consider the spin transition W_2 occurring at $B_Z = 17$ mT and $\nu = 650$ MHz, the clock transition arises

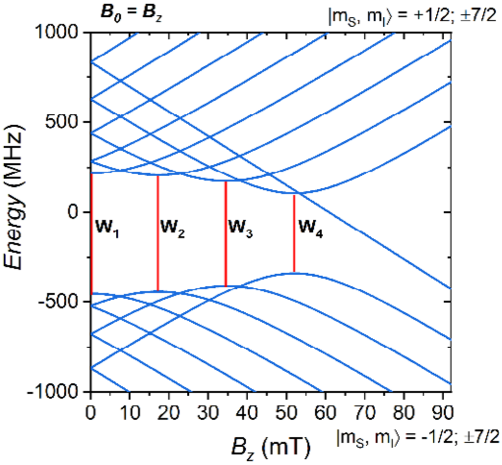

Figure 5.8. Simulation of the Zeeman levels diagram of a **VOTPP** oriented crystal (θ = 0°). The clock transitions occurring at the anti-level crossings are highlighted as vertical red lines.

between the two states $|\psi_7\rangle = -0.710197|1/2,-1/2\rangle + 0.712205|-1/2,-3/2\rangle$ and $|\psi_8\rangle = -0.712205|1/2,-1/2\rangle - 0.710197|-1/2,-3/2\rangle$, that fulfil the transition condition reported in Fig.5.7 (i.e., $\sqrt{2}/2(|0\rangle + |1\rangle) \rightarrow \sqrt{2}//2(|0\rangle - |1\rangle)$). In this limit, clock transitions occur for values of the static magnetic field at which the derivative of the spin transitions' frequencies with respect to B_Z are null, i.e., when $\partial v/\partial B_Z = 0$. In Fig.5.9a, it is reported a plot of some simulated curves showing the dependence of the resonance frequencies W$_n$ from B_Z. The simulations were obtained by using the following equation:

$$v_n = \sqrt{\Delta_n^2 + \gamma_z^2 (B_Z - B_{CT})^2} \tag{5.1}$$

where n = 1,2,3,4, Δ_n is the resonance frequency of the n-th clock transitions, and $\gamma_z = g_z\mu_B/\hbar$ = 27.49 MHz mT^{-1} is the z component of the electron gyromagnetic tensor [193]. In the limit of $B_Z \rightarrow B_{CT}$, this equation can be conveniently approximated as:

$$v_n \approx \Delta_n + \gamma_z^2 (2\Delta_n)^{-1} (B_Z - B_{CT})^2 \tag{5.2}$$

and, in the present case, it is also confirmed by the comparison between the simulated curves reported in Fig.5.9b. However, the approximated Eq.5.2 well resembles the trend obtained by employing the extended formula in Eq.5.1 only around B_{CT}, i.e., in the limit of $\partial v/\partial B_Z \rightarrow 0$.

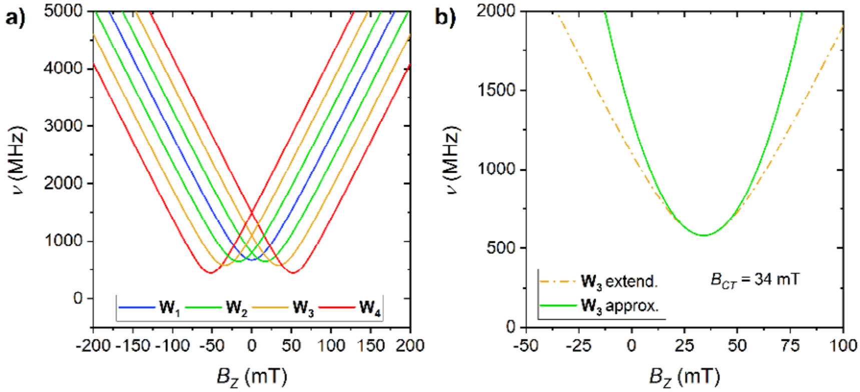

Figure 5.9. (a) Plot of v vs B_Z for each of the four clock transitions obtained by adopting Eq.5.1.(b) Comparison between the extended (Eq.5.1) and approximated model (Eq.5.2) applied on transition W$_3$.

We thus proceeded to the investigation of clock transitions by employing a homemade EPR experimental setup already proposed by Friedman and co-workers in [196] and adopted for previous studies conducted on {Cr_7Ni}-based samples [125,195]. In these previous works, our collaborators worked on single crystals of pure compounds. In this case, we tried to push the coherence time enhancement to the limit by employing single crystals of a 2% doped sample of **VOTPP** in **TiOTPP** (see also Sec.5.1).

Nevertheless, several challenges arose during the experimental investigation of the employed crystals that can be correlated to three principal factors: i) the necessity of developing an *ad hoc* designed resonator capable of working at the low frequencies involved (i.e., hundreds of MHz), and in which the magnetic field is as homogeneous as possible; ii) the necessity of growing larger crystals to increase the signal at the employed magnetic dilution; iii) the necessity of accurately orient the crystal on the adopted loop-gap resonator to get the direction of c crystallographic axis almost parallel to that of both $\vec{B}_Z$ and $\vec{B}_1$ (for clarity, we considered $\vec{B}_Z = \vec{B}_0$ to maintain the convention reported above). While our collaborators at Amherst College fully faced the first challenge, we principally worked on solving tasks (ii) and (iii). Some pictures reporting the grown crystals, and the strategies adopted to mount them on the employed resonator are reported in Fig.5.10.

Obtaining larger crystals for porphyrin-based compounds is not trivial because of their reduced solubility and tendency to twin. Large single crystals of **VO$_{2\%}$TPP** were grown by layering a saturated solution of the target doped compound in CH_2Cl_2 with a small amount of n-heptane. Indeed, n-heptane (which has a higher boiling point with respect to CH_2Cl_2) prevents the fast evaporation of CH_2Cl_2 at the beginning of the crystallization; then, it favors the fast gemination of crystallites that further grow upon CH_2Cl_2 evaporation. The solvent was then left to evaporate from a pinhole for 4/5 weeks, thus obtaining bigger crystals than what usually formed upon the evaporation of dichloromethane (Fig.5.10a).

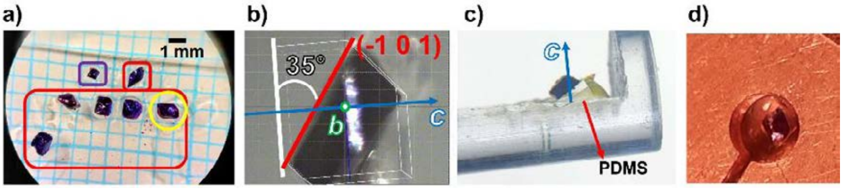

Figure 5.10. (a) Photograph of new (red square) and old (purple square) crystals taken at the microscope. The crystal employed within experiments is the one highlighted in yellow.(b) View along the b crystallographic axis (green) of the ”yellow” crystal mounted on a glass loop for indexing procedures. (c) View of the yellow-circled crystal mounted on a PDMS wedge onto a EPR sample holder. (d) Photograph of the yellow-circled crystal mounted on the loop-gap resonator employed for pulsed EPR experiments at the Amherst College.

Therefore, we extensively investigated the obtained crystal by X-ray diffraction to check for possible twinning and understand how crystals' faces correlated to crystallographic planes. The obtained crystals grew as a quasi-octahedral-shaped prism (see also Fig.5.3), where the larger faces were those growing on planes (-1 0 1) and (1 0 1). Those faces are tilted by 35° with respect to the plane normal to the *c* crystallographic axis, which, in turn, passes through the top vertex of the prism (Fig.5.10b). In order to have the c axis perfectly perpendicular to the plane on which the crystal lies, we prepared a PDMS = poly(dimethylsiloxane) wedge to hold the crystal up in position (Fig.5.10c). To check for the proper orientation of the crystal on the wedge, we recorded cw-EPR spectra for B_Z parallel ($\theta = 0$) and perpendicular ($\theta = 90°$) to c (Fig.5.11). The comparison between experimental and simulated spectra confirmed the correct orientation of the crystal on the PDMS wedge, showing just a small deviation of $\theta \approx 3°$ for $B_Z \perp c$. Finally, the crystal was mounted on the loop-gap resonator as reported in Fig.5.10d and probed by low frequency cw- and pulsed EPR technique in Amherst.

The intensity of EPR signal in the proximity of clock transitions at the radiofrequency regime is lower than at higher frequency because of both transition probabilities and experimental conditions involved, so we started by measuring the crystal at frequencies far above those of the clock transitions, and in perpendicular mode (i.e., $\vec{B}_1 \perp \vec{B}_Z$). This operation allowed us to tune experimental parameters before moving to the EPR experiments conducted at low frequency.

Indeed, our collaborators were largely confident in their apparatus for working at frequencies in the 3 GHz – 5 GHz range [196]. On the contrary, a new setup was necessary for working at frequencies below 1 GHz, i.e., different amplifiers,

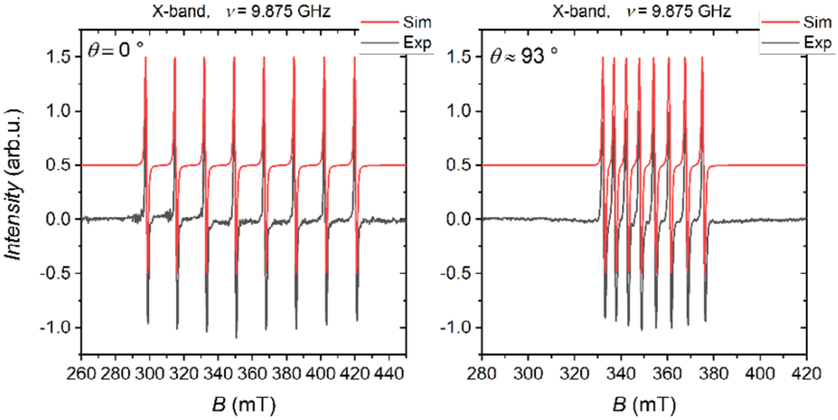

Figure 5.11. Plots of experimental and simulated cw-EPR spectra collected on an oriented crystal of **VO2%TPP** for two distinct orientations of the *c* crystallographic axis with respect to the direction of B_Z.

mixers, filters, and methods to output power from the Arbitrary Waveform Generator (AWG). These parameters were thus optimized on the basis of experimental results collected at a high frequency (above 1 GHz) and then finely tuned when reaching the MHz regime.

Furthermore, we tuned the experimental condition by first measuring a single crystal of pure **VOTPP**. On the one hand, the concentrated sample accounts for more intense EPR transitions. On the other hand, the bands' linewidth is usually broadened by spin-spin dipolar interactions. Experimental results from cw- and pulsed spin nutation experiments on **VOTPP** are reported in Fig.5.12. Here, the EPR transitions occurring

for different values of B_Z (empty circles) are reported with curves simulated for different frequencies employed within the experiments. Experimental and simulated data are in good agreement with each other. In addition, Hahn echo and CPMG (Carr-Purcell-Meiboom-Gill) experiments performed at ν = 4200 MHz, B_Z = 120 mT, and T = 1.8 K provided an estimation of the coherence time: $T_m^{HE} = 0.47 \pm 0.10$ μs, $T_m^{CPMG} = 8.53 \pm 1.06$ μs. Such a T_m observed in **VOTPP** is more than twice time that of ≈ 3.5 μs extracted by CPMG experiment on **VO$_{2\%}$TPP** in Sec.5.1. In the present case, however, we collected the T_m value by employing fifteen π pulses, while in Sec.5.1 it was extracted with just four pulses since the echo signal was lost after that point.

The same strategy was used to investigate clock transitions of a single crystal of [VO$_{2\%}$(TPP)], thus by setting $\vec{B}_1 \parallel \vec{B}_Z \parallel c$. Field sweep results extracted at different working frequencies are reported together with the simulations obtained from SH parameters on the left side plot in Fig.5.13. It is possible to observe that

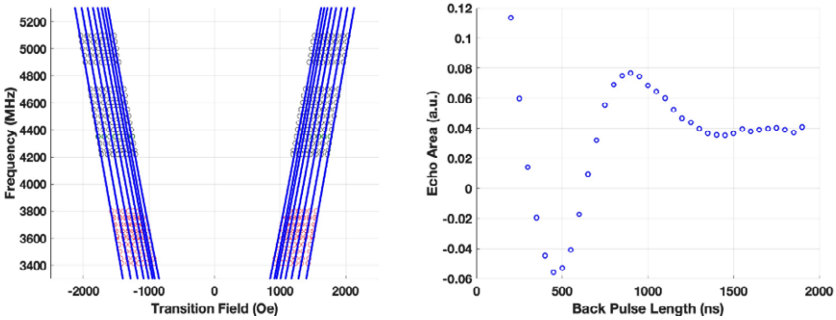

Figure 5.12. On the left side, map of ν vs B_Z of experimental spin transitions (empty circles) extracted from perpendicular mode EPR measurements on a **VOTPP** crystal at T = 1.8 K. Solid lines represent simulations obtained by adopting the SH parameters previously reported in Sec.5.1. On the right side, Rabi oscillations observed at ν = 4200 MHz, B_Z = 120 mT, and T = 1.8 K.

cw-EPR transitions continue to match the theory as the frequency is lowered toward the clock transitions. On the other hand, some outlying points were observed at a higher frequency. Such a phenomenon is well highlighted by the EDFS spectrum obtained at 4192 MHz, and 1.8 K reported on the right-side plot in Fig.5.13. Outlying resonances are here attributed to spin transitions arising in perpendicular mode, i.e., with $B_1 \perp B_Z$. These features are not correlated to a crystal misalignment, but they are due to B_1 inhomogeneity within the resonator. Indeed, mounted crystals may experience stronger field inhomogeneities as soon as the crystal dimension increases, accordingly with the simulation reported in Fig.5.14. On the other hand, smaller crystals show a signal intensity that is too low to be employed.

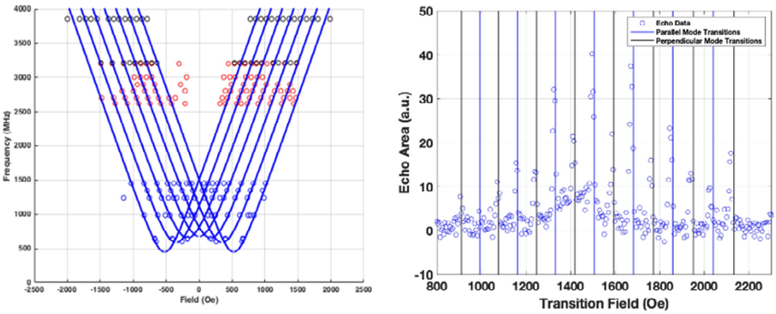

Figure 5.13. On the left, map of ν vs B_Z of experimental spin transitions (empty circles) extracted for parallel mode EPR measurements on a **VO2%TPP** crystal at T = 1.8 K. Solid lines represent simulations obtained by adopting Eq.5.1. On the right, EDFS spectrum collected on the same crystal at ν = 4192 MHz and T = 1.8 K. Parallel and perpendicular mode transitions are highlighted as blue and black vertical lines, respectively.

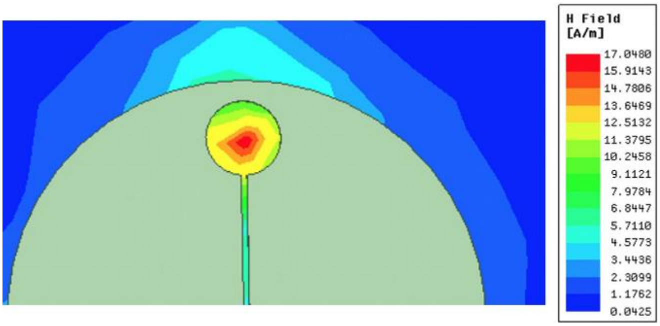

Figure 5.14. Simulation of the radio-frequency field’s intensity within the loop-gap resonator. The colour-code is reported in the colour map on the right side.

In light of these results, we rationalized our inability for collecting T_m values both from Hahn echo or CPMG experiments and attributed the lack of coherence to the effect of such strong inhomogeneity in the radio-frequency field. At the moment, the Amherst group is still improving a new set of resonators sensitive enough to probe smaller samples or provide a more homogeneous field over the employed surface.

AUTHOR'S CONTRIBUTIONS. The author of this thesis synthesized all the employed samples, obtained the crystals, and managed all the operations involving the crystal indexing and orientation on PDMS. The author also performed cw-EPR measurements at X-band on oriented crystal and their simulations. Furthermore, he performed the presented set of preliminary simulations on clock transitions. The whole set of measurements conducted with the loop-gap resonator setup were performed by Prof. J. R. Friedman and his group at the University of Amherst.

5.3 Purification of [VO(TPP)] samples for time-resolved THz-EPR

Working on the purification of chemicals by adopting specific and advanced techniques is of paramount importance when compounds are used for advanced spin dynamics experiments. In this section, we want to stress how different techniques can present different sensitivities for detecting the presence of contaminants. In particular, we present a technical contribution of the author to the experimental investigation of the spin dynamics of **VOTPP** by using time-resolved THz-EPR experiments. The experiments are conducted by the Dr S. Veber's group at the Novosibirsk State University. This peculiar experiment involves THz radiation generated by the NovoFEL facility and sent to the sample introduced in a cw-EPR instrument. The FEL line here can produce a THz macropulse of arbitrary length (up to 400 μs) that is sent on the sample. In this way, it is possible to selectively probe a specific phonon mode of the **VOTPP** molecule and study the correlated spin dynamics. The probe is a cw-EPR instrument working at the X-band frequency in the time-resolved mode [197].

Experiments will be conducted on a polycrystalline sample of **VO$_{2\%}$TPP**. This compound has been chosen as a test system since it has been widely investigated in recent years. Its spin dynamics have been deeply characterized from both experimental and theoretical points of view (a detailed theoretical analysis could be found in the PhD thesis of Dr Andrea Albino). However, the preliminary investigation of some batches of **VO$_{2\%}$TPP** prepared by the author unveiled the presence of a contaminant fraction, firstly highlighted by our collaborators, whose signal interfered with that of vanadyl. In particular, the cw-EPR spectroscopy analysis conducted by Veber and coworkers unveiled the presence of an iron(III) impurity. The most indicative signal of a high-spin iron(III) fraction (S = 5/2) in the EPR spectra reported in Fig.5.15a and b is the one at $g_{eff} \approx 6$ (118 mT) [198]. The iron(III) signal's intensity in the investigated **VO$_{2\%}$TPP** sample increases

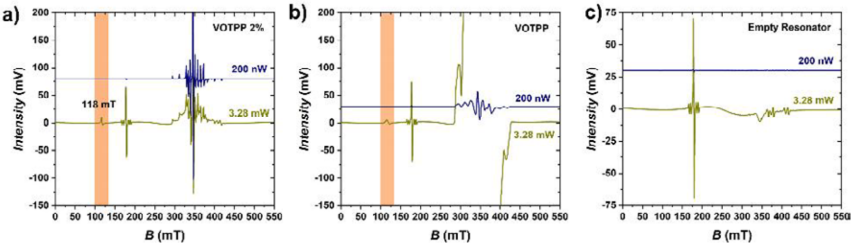

Figure 5.15. (a) Plot of X-band cw-EPR spectra of **VO$_{2\%}$TPP** microcrystalline sample collected at 200 nW and 3.28 mW. The iron(III) impurity at 118 mT is highlighted by the orange region. (b) Plot of X-band cw-EPR spectra of VOTPP microcrystalline sample collected at 200 nW and 3.28 mW. (c) Plot of X-band cw-EPR spectra of the empty resonator collected at 200 nW and 3.28 mW.

when the temperature is lowered to 10 K, the power of the mw radiation is increased to 3.28 mW (18 dB), and the modulation amplitude is set to 2.1 G Based on the estimated g_{eff} value and considering the employed ligand's nature, we mainly correlated the presence of iron(III) impurities to that of a [Fe(TPP)]$^+$ fraction [199, 200]. Such an impurity was not relevant in the case of pulsed EPR studies reported before since the EPR pulses employed for probing the spin dynamics were sufficiently selective for the vanadyl ion. On the other hand, in this particular experiment and within the experimental conditions required, the signal of the impurity arising at low *T* was the principal one detected, thus overcoming the vanadyl one.

While our collaborators carried out the experimental investigation of the THz induced spin dynamics, we principally worked on detecting impurities and their elimination through various techniques. At first, we analyzed the X-band cw-EPR spectra of two different samples of **VO$_{2\%}$TPP**: i) a microcrystalline sample obtained from synthesis; ii) a microcrystalline sample obtained by grounding crystals grown by slow evaporation of a CH_2Cl_2/n-heptane solution. The EPR investigation was conducted using similar experimental conditions to those employed by our collaborators. As it is possible to observe in the two reported plots (Fig.5.16), the iron(III) signal is present for both synthesized (i) and recrystallized (ii) samples. Furthermore, the [Fe(TPP)]$^+$ is more evident in the grounded sample (ii). A possible explanation is that the ionic iron(III) impurity is more prone to precipitate from apolar solvents mixture than vanadyl-porphyrin, and its segregation within crystallites can be favored under these conditions.

Therefore, we also analyzed the whole set of commercial precursors commonly employed for obtaining **VO$_{2\%}$TPP**, i.e., H$_2$TPP, [VO(acac)$_2$,] and [TiO(acac)$_2$]$_2$, by employing cw-EPR technique. No clear signals arising from iron(III) ions were detected in the ligand or in titanyl precursor. However, we observed a wide signal at $g_{eff} \approx 4.3$ (convoluted to that of vanadyl) in the spectrum of commercial

[$VO(acac)_2$] collected at 10 K and 10 dB = 3.28 mW (Fig.5.17). This EPR transition is attributed to a fraction of [$Fe(acac)_3$] within the sample based on previous literature [201, 202].

We thus analyzed HNO_3 solutions of [$VO(acac)_2$] and **VOTPP** samples by ICP measurements for estimating the relative concentration of vanadyl and iron species

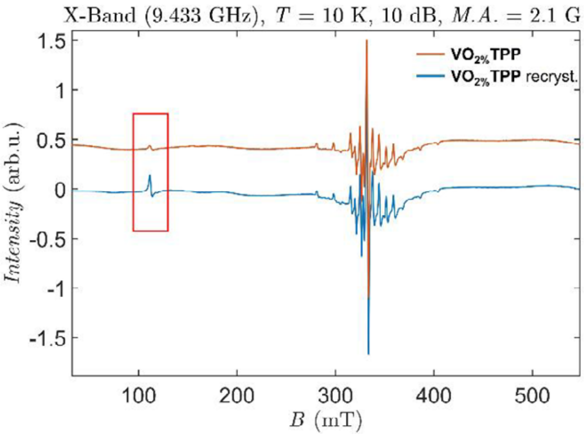

Figure 5.16. Plot of X-band cw-EPR spectra of **$VO_{2\%}$TPP** collected on microcrystalline sample (orange) and grounded crystals (blue) at 10 K.

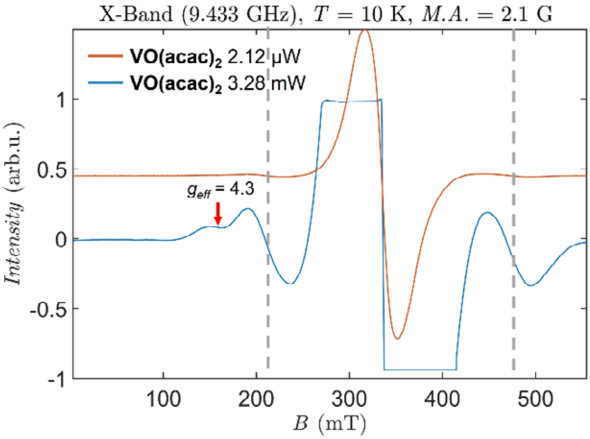

Figure 5.17. Plot of X-band cw-EPR spectra collected on a microcrystalline sample of commercial of [$VO(acac)_2$]. The signal of [$Fe(acac)_3$] impurity is highlighted by the red arrow. Grey dashed lines are placed in correspondence of signals attributed to the vanadyl ion.

in the two compounds. The ICP analysis conducted on a pure sample of VOTPP revealed a Fe^{3+}/V^{4+} molar ratio of about 1.6%. In the case of $[VO(acac)_2]$, we estimated a Fe^{3+}/V^{4+} molar ratio of about 0.7%. Such a result highlights that iron(III) impurities tend to concentrate during the reaction with the porphyrin. This evidence can be sensibly correlated to the more considerable affinity and reactivity of iron(III) species with porphyrin ligands with respect to the more inert vanadyl ion.

At first, we focused our attention on the purification of the vanadyl precursor. We outlined a strategy based on the thermal sublimation of $[VO(acac)_2]$ conducted with a homemade apparatus capable of working in high-vacuum conditions (10^{-6} mbar). Some photographs of the apparatus are reported in Fig.5.18. The system is composed of a central stainless-steel chamber with six openings. The opening at the bottom is closed by a flange, which hosts the crucible and the heating element. The crucible is supported by a metallic holder anchored to the bottom flange. The same holder also supports a tantalum filament (i.e., the heating element), which is soldered to two electrodes (placed on the same flange and external to the chamber) to connect it to an external DC generator. The temperature of the sample, due to the input current, is monitored with a thermocouple. The other openings have a gauge detector, a vacuum outlet, two glass windows, and a blank flange.

The top opening (see Fig.5.18) can also be fitted with a cold finger that serves as a condenser for the sublimed compounds. An aluminum cone is also hosted by the crucible's holder and mounted on the top side of the crucible to focus the molecular ray onto the cold finger and prevent the deposition of compounds on the chamber's walls. When the cold finger is replaced with a glass window, a glass beaker is mounted on the top of the crucible, externally to the aluminum cone, and used to condense the sublimed compounds.

The purification of commercial $[VO(acac)_2]$ was conducted by increasing the input current slowly and monitoring the temperature of the sample. The sublimation started at 50/60 °C (checked by controlling the pressure increase revealed by the gauge) and proceeded overnight at 10^{-6} mbar.

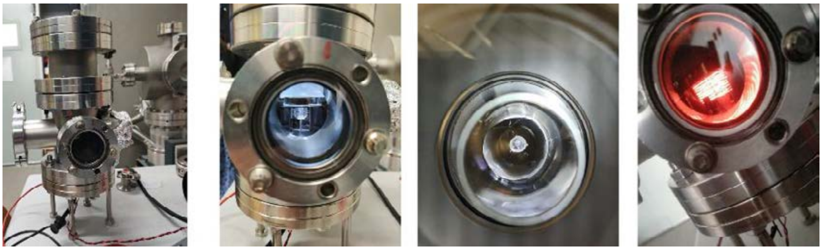

Figure 5.18. From the left to the right: (i) homemade sublimation apparatus, (ii) view of the internal chamber (crucible, heating filament, and thermocouple); (iii) top view of the sublimation chamber; (iv) view of the crucible and filament during the heating procedure.

The sublimed powders and crystals were collected from the cold finger (Fig.5.19) by picking them with a spatula and analyzed at the ICP. However, this strategy did not allow us to remove iron(III) impurities from the precursor completely. ICP analysis showed that the Fe^{3+}/V^{4+} molar ratio within the purified compound was about 0.6%. The observation of an iron(III) fraction after sublimation can be due to the low temperature required for subliming such light molecules, thus not allowing for a selective sublimation of vanadyl compounds.

Because of the behavior observed in the $[VO(acac)_2]$ case, we employed the same strategy for purifying the **VOTPP** directly. In this case, the synthesis product was purified by sublimation at 260 °C and 10^{-6} mbar for 68 h. The product was condensed on the wall of a glass beaker mounted on the top of the crucible (Fig.5.20a), and then recollected by dissolving it in CH_2Cl_2. A microcrystalline powder was obtained by slow evaporation of the solvent. A fraction of this sample was finally investigated by cw-EPR spectroscopy working at the X-band frequency. The EPR spectra collected on the purified sample at 10 K are reported in Fig.5.20b. As evidenced in the figure, the iron(III) impurity's signal is no more present in the EPR spectrum, even for low attenuation values of B_1 (i.e., when the vanadyl's signal is saturated). This evidence provides the proof of the absence of the $[Fe(TPP)]^+$ fraction within the thermally treated sample. We hypothesized that the $[Fe(TPP)]^+$ impurity could not be sublimed because of its ionic nature, and it readily decomposed during the thermal treatment.

After characterization, the so obtained VOTPP sample was used for synthesizing doped sample of **$VO_{2\%}$TPP** and **$VO_{0.5\%}$TPP** necessary for THz-EPR measurements. A comparative plot of EPR spectra collected on non-purified and purified samples with the same experimental conditions are reported in Fig.5.21. As highlighted in the plot, no impurity's signals are observed within the EPR spectra.

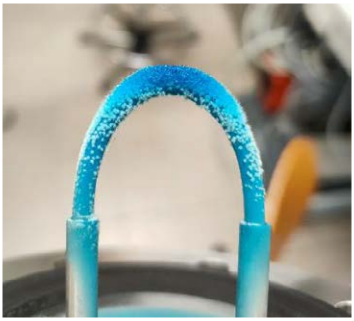

Figure 5.19. Photograph of $[VO(acac)_2]$ crystals formed during condensation of sublimed fraction on the cold finger.

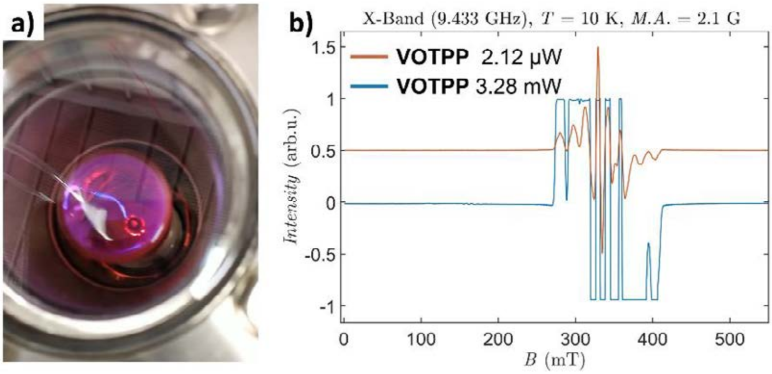

Figure 5.20. (a) Top view of the crucible during the sublimation of **VOTPP**. The sublimed compounds condensed on the glass beaker, thus resulting in the purple color observed in the photograph. (b) Plot of X-band cw-EPR spectra collected at 200 nW and 3.28 mW on the purified **VOTPP** microcrystalline sample. No signals from iron(III) impurities are observed.

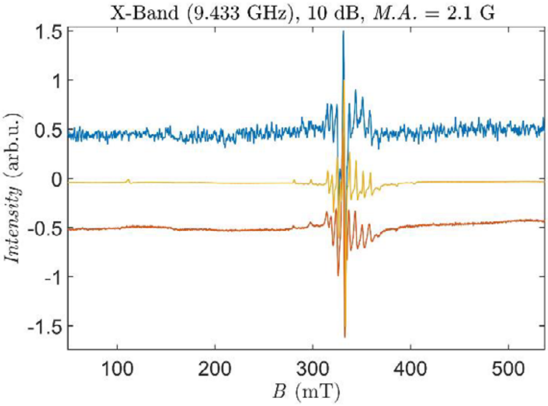

Figure 5.21. Comparative plot of X-band cw-EPR spectra collected at 10 dB on microcrystalline samples of **VO$_{2\%}$TPP** and **VO$_{0.5\%}$TPP** obtained by using purified (orange and blue) or non-purified (yellow) **VOTPP**.

AUTHOR'S CONTRIBUTIONS. The author of this thesis synthesized all the mentioned compounds except for the commercial precursors, and he managed the purification experiments conducted using the apparatus presented in the main text. Furthermore, the author collected all the cw-EPR spectra to detect the iron(III) impurity and to probe the purity of sublimed compounds. B. Cortigiani realized the sublimation apparatus with the assistance of the author.

Chapter 6

From single spins to porphyrin-based multi-qubit architectures

The importance of obtaining multi-qubit architectures in the field of Quantum information processing was extensively discussed in Chaps.1 -3. It has been proven that the encoding of logical quantum gates within molecular and supramolecular structures is central if these systems are to be considered competitive with other quantum-based platforms. Recalling what was stated before, we presented two possible strategies for the design of molecular spin-based quantum logic gates: i) by adopting switchable systems, where the communication and entanglement condition between distinguishable qubits can be selectively turned on or off through electromagnetic pulses; ii) by employing non-switchable architectures, where the interaction within two or more qubits is always set, and the entangled state coincides with the ground state of the system [53]. Recalling what was stated in Chap.3, the interaction involved in the latter case is the exchange coupling interaction, and the possibility of generating entangled states (i.e., non-separable states) is strictly correlated to the coupling properties of exchanged systems [53]. For the sake of clarity, we must specify that the exchange coupling interaction must be finely tuned through the molecular design of coupled systems in order to avoid the strong exchange regime. Indeed, the two individual qubits should still be selectively manipulable and addressable.

In this respect, we present here two molecular strategies based on the adoption of vanadyl-porphyrin complexes. Vanadyl has shown several excellent properties as a spin qubit (see Chap.5), e.g., long coherence time, narrow EPR transitions, and a low spin-orbit coupling contribution to the electronic levels. Furthermore,

Fabio Santanni, University of Florence, Italy, santannifabio@gmail.com, 0000-0002-0506-8333

Referee List (DOI 10.36253/fup_referee_list)
FUP Best Practice in Scholarly Publishing (DOI 10.36253/fup_best_practice)

Fabio Santanni, *Molecular approaches for quantum technologies. Optimization of electron spin-based quantum bits and quantum logic gates*, © 2025 Author(s), CC BY 4.0, published by Firenze University Press, ISBN 979-12-215-0670-9, DOI 10.36253/979-12-215-0670-9

porphyrins are well known as versatile molecules. A wide variety of synthetic strategies aimed at variously functionalizing their periphery are readily available. Adopting oxidative, coupling, or even acid-base reactions makes it possible to realize an enormous set of compounds [203]. As an example, porphyrin might be fused to get multi-porphyrin systems of various dimensions and structures, e.g., 3D materials (MOF, dendrimers, cages, *etc.*) [77,204−206], 2D materials (oligomers, stripes, *etc.*) [207−209], porphyrin-helicene coupled systems [210], and many others (arch-type structure, triangles, *etc.*) [211−213]. Here, we mainly investigated supramolecular and condensation chemistry of A4 (fully symmetric, e.g., tetraphenyl porphyrin) and A3B (asymmetric, e.g., triphenyl porphyrin) vanadyl-porphyrin complexes and explored their quantum properties.

6.1 A multi-qubit system: [VO(TPyP)]{Cr_7Ni}$_4$

Non-trivial quantum logic gates require two or more qubits placed in a superposition state. To obtain multi-qubit structures, the molecular design must be finely and rationally tuned. These structures will be characterized by superposition states arising from the interaction among the spins of the hetero- or homometallic centers.

Possible strategies for obtaining switchable molecular quantum gates (see Chap.C.5) were proposed by the molecular magnetism group in Manchester [108]. The general idea is that of having two or more qubits characterized by a total $S = 1/2$, i.e., {Cr_7Ni} rings (Chap.3), linked through a central metal that works as the interaction switch. The weak exchange interaction among centers thus led to a peculiar energy level's scheme given by the superposition states of different qubits (see Sec.3.2). This kind of strategy might yield quantum gates fully manipulable through microwave pulses, thus removing the challenging requirements of coupling microwave and radiofrequency radiations [114]. In this respect, the most promising strategies involve heterometallic supramolecular structures obtained through tailored ligands containing extra pyridine-like functional groups as linkers between subunits [57,109,129].

However, two critical aspects emerge from the precedent works: i) obtaining such structures is challenging and requires massive synthetic efforts. The resulting structure should show two distinguishable qubits (which may be distinguished based on their different g values, orientation of their anisotropy, etc.). Furthermore, the choice of the central metal ion, and its relative complex, is also fundamental. It must be selected on the basis of specific requirements (Chap.3), e.g., it must form stable complexes leading to a supramolecular arrangement of surrounding units, and it must show electronic spin transitions (possibly sharp ones) well-disentangled from those of the other spin qubits; ii) the magnetic properties of involved ions and clusters might be seriously modified when coupled in multi-quit systems.

On the basis of these requirements, we employed the vanadyl-porphyrin system [VO(TPyP)] (**VOTPyP**), TPyP = tetra-(4-pyridine)porphyrinate, as the building block for getting the target supramolecular complex {[VO-(TPyP)]{Cr_7Ni}$_4$}, hereafter VO{Cr_7Ni}$_4$. The vanadyl complex with porphyrin is very stable and easily characterizable. Moreover, it usually shows very sharp EPR transitions, well- separated from that characteristic of the $S = 1/2$ of {Cr_7Ni} units. Most of the syntheses reported in this paragraph were carried out by the author of this thesis at the University of Manchester under the supervision of Dr G. A. Timco and Prof R. E. P. Winpenny.

The **VOTPyP** unit was synthesized by modifying a general synthetic route commonly employed for synthesizing metal-porphyrin complexes [214]. In particular, the synthesis required the [$VO(acac)_2$] precursor being reacted with H_2TPyP in a DMF/acetic acid 1:1 solution, under N_2 and keeping the reflux overnight (the extended procedure is reported in Chap.C, Sec.C.2). Upon purification and further recrystallisation from a CH_2Cl_2/ CH_3CN solution, compound **VOTPyP** was obtained as a pure crystalline solid. Its structure, reported in Fig.6.1, has been determined by X-ray crystallography and demonstrates that the pyridyl units are available for further coordination. Indeed, short contacts (2.5 Å) among the N atom of the pyridyl unit and the vanadyl of an adjacent molecule are observed. The sketch evidencing short contacts among N and VO units is reported in Fig.6.1c.

We then considered that it was possible to coordinate four {Cr_7Ni} rings around a **VOTPyP** spin center by exploiting the coordinating properties of pyridyl units. Such a strategy led to the obtaining of the supramolecular adduct **VO{Cr_7Ni}$_4$**. In particular, {Cr_7Ni} = [$Cr_7NiF_3(Etglu)(O_2CtBu)_{15}(H_2O)$] purple rings are composed by seven Cr^{3+} ions and a Ni^{2+} ion (Fig.6.2) [215].

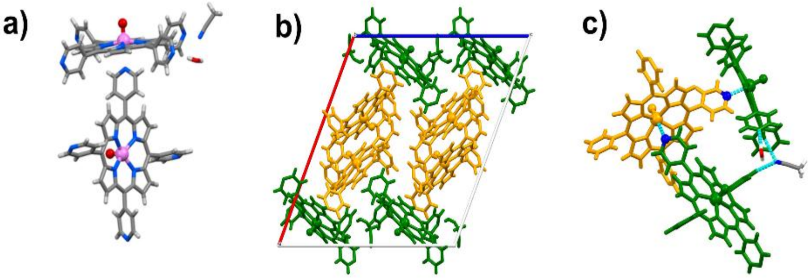

Figure 6.1. a) Molecular structures of two **VOTPyP** units, one H_2O molecule, and an CH_3CN molecule representing the asymmetric unit. Colour code: C = grey, H = white, N = blue, V = pink, O = red. b) Solved crystal structure obtained by X-ray measurements on a **VOTPyP** single crystal. The molecular units are highlighted in green and orange for clarity. Cell parameters: Space group = $P2_1/c$; a (red) = 27.26 Å, b = 12.40 Å, c (blue) = 23.45 Å, $\alpha = 90°$; $\beta = 112°$; $\gamma = 90°$; V = 7370 Å^3. c) Representation of short contacts (cyan rods) between two different units. Colour codes refer to figures a and b.

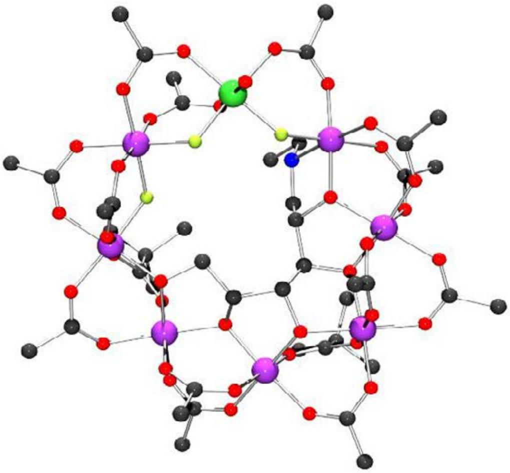

Figure 6.2. Molecular structure of the heterometallic ring $[Cr_7NiF_3(Etglu)(O_2CtBu)_{15}(H_2O)]$ (purple-ring) [215]. Hydrogens and methyl groups of pivalate units are removed for clarity. Colour code: Cr = purple; Ni = green; F = lime; O = red; N = Blue; C = black.

All the ions exhibit an octahedral coordination geometry imposed by bridging pivalate ($tBuCOO^-$), N-ethyl-D-glucamine (Etglu), and by fluorine ions. They compose the ”skeleton” of the heterometallic cluster. A water molecule occupies the sixth coordination position of Ni^{II}. This ligand can be easily displaced by exploiting the different affinity and solubility properties of N-containing ligands. Indeed, large purple rings are highly soluble in apolar, or poorly polar, solvents (e.g., CH_2Cl_2, n-hexane, n-pentane, or diethyl ether), while they are less soluble in acetone and poorly soluble in CH_3CN. Because of the significant solubility of purple rings, their supramolecular adducts with the pyridine-functionalized porphyrin can dissolve in non-common solvents for A4 aryl-porphyrin, like diethyl ether or n-hexane. Indeed, we employed such a strategy to get the target product [215].

Stoichiometric amounts of **VOTPyP** and purple-$\{Cr_7Ni\}$ (1:4) rings were stirred together for three days in CH_2Cl_2 to let the porphyrin substitute the water molecule. After that, CH_2Cl_2 was removed, and the powdered sample was left to stir for two days in acetone to wash it. The target compound was subsequently filtered, extracted in diethyl ether (in which the porphyrin is not soluble), and recrystallized by slow evaporation of a 1:1 acetone/diethyl ether solution. The purity of compound **VO$\{Cr_7Ni\}_4$** was checked via elemental analysis (see Appendix C, Sec.C.2). However, an exemplary structure of this system was obtained by investigating good quality crystals obtained by slow diffusion of acetone vapors into a n-hexane solution (Fig.6.3). It must be stressed here that such a system tends to grow in big hexagonal-shaped crystals of several mm length. However, these crystals are quasi-2D crystals and tend to grow stacked onto each other. Because of their fragility, it was really challenging to separate them to gain a single crystal suitable for X-ray crystallographic measurements.

The supramolecular adduct crystallizes in the $P2_1/c$ space group. The crystallographic unit contains two magnetically non-equivalent vanadyl complexes and their respective {Cr_7Ni} rings. The four rings are distributed around the vanadyl porphyrin, forming the chiral structure reported in the figure, and the main distances from VO and Ni centers range from 9.7 Å to 9.8 Å. Recalling what was reported in Chap.5, the plane of the porphyrin determines the anisotropy of vanadyl **g** and **A**. In this respect, the x and y components of the two collinear tensors lay on the porphyrin plane, while the z component coincides with the V=O direction, perfectly resembling the axial (C_4) symmetry imposed by the ligand. The latter is roughly aligned with the b crystallographic axis. The {Cr_7Ni} cluster is also characterized by the axial anisotropy of $\boldsymbol{g}$ associated with the low-lying spin state $S = 1/2$. In this case, the z component is perpendicular to the plane of the ring, while the x and y components lay on the plane of the ring ($g_\perp = 1.842(2)$, $g_{||} = 1.780(2)$) [216]. Let us think of an EPR experiment conducted on an oriented crystal of the **VO{Cr$_7$Ni}$_4$** system. If we probed the crystal along the direction of the b crystallographic axis (i.e., by aligning B_0 and V=O directions), we would probe the axial component of vanadyl ion and the perpendicular components of the four rings. It follows that they would roughly behave as four equivalent rings since minimal differences in their orientation are present. On the other hand, if we probed the crystal on the ac plane, we would observe the perpendicular component of the vanadyl ion and, at certain orientations, two distinct couple of rings, *i.e.* those having $g_z \parallel B_0$ and those having $g_z \perp B_0$.

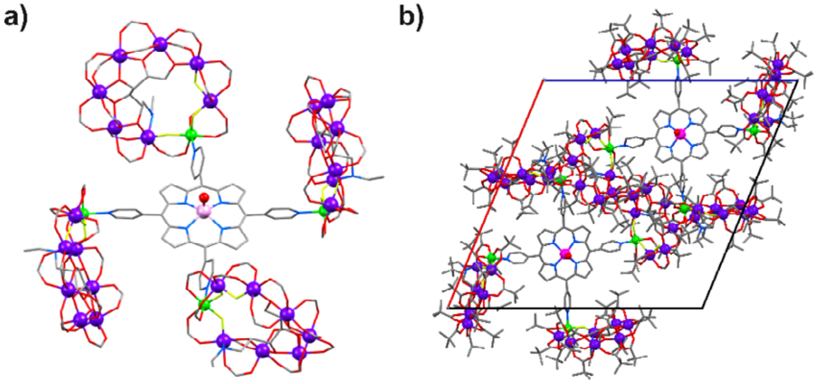

Figure 6.3. a) Molecular structures of **VO{Cr$_7$Ni}$_4$**. b) View along the a crystallographic axis of the solved crystal structure obtained by X-ray measurements on a **VO{Cr$_7$Ni}$_4$** single crystal. Cell parameters: Space group = $P2_1/c$; a (red) = 27.26 Å, b = 12.40 Å, c (blue) = 23.45 Å, α = 90°; β = 112°; γ = 90°.

Although all the rings are non-equivalent, we can roughly say that those lying on planes forming an angle of ≈ 90° are magnetically non-equivalent, while those lying on parallel planes are equivalent. Qubits can thus be distinguished based on their relative orientations when in the crystal phase. Because we could not perform a complete investigation on oriented crystals, the selective manipulability of different qubits within the system is now a hypothesis.

However, we conducted a series of preliminary EPR studies on polycrystalline powders and solutions of **VO{Cr$_7$Ni}$_4$** aimed at investigating the static and dynamic properties of the obtained system. Our collaborators performed the set of EPR experiments at the University of Manchester. As a first check of the dynamic and static properties of this system, we performed a set of cw and pulsed EPR measurements working at the X- and Q-band frequencies on frozen solutions of both **VOTPyP** and VO{Cr$_7$Ni}$_4$. Results of cw and EDFS measurements performed at the X-band frequency and 20 K are reported in Fig.6.4. The cw-EPR spectra collected at the Q-band frequency on **VOTPyP** samples (toluene solution and polycrystalline powder) are instead reported in Fig.C.10.

While compound **VOTPyP** showed similar behavior to the archetypical **VOTPP** system, even showing a characteristic T_m of about 2 μs (see Fig.C.11), results were surprisingly different in the case of VO{Cr$_7$Ni}$_4$. The cw-EPR spectrum collected at the X-band and 20 K (Fig.6.4) shows two distinct signals arising from the **VOTPyP** (centered at 350 mT) and the {Cr$_7$Ni} (centered at 380 mT) units. However, the EDFS spectrum of VO{Cr$_7$Ni}$_4$ does not present any clear fine structure attributable to that of **VOTPyP** and {Cr$_7$Ni} rings, even if a sharp signal at g = 2.0 value (350 mT) is clearly visible. This last EPR transition is likely to be attributable to a radical impurity of the porphyrin system (see also Sec.4.1).

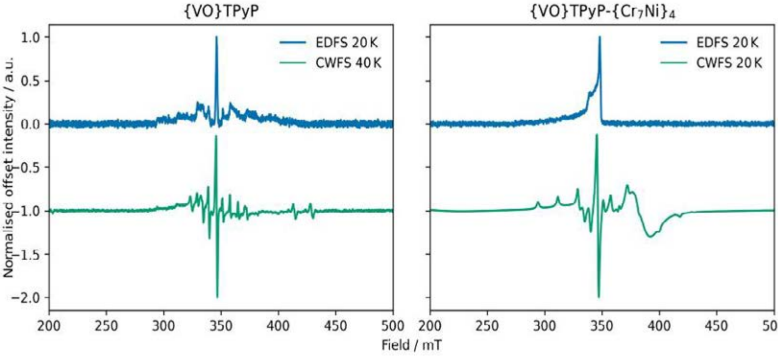

Figure 6.4. Plots of X-band (9.44 GHz) cw- and EDFS EPR spectra of **VOTPyP** (left side) and **VO{Cr$_7$Ni}$_4$** (right side) 1 mM solutions in toluene/CH$_2$Cl$_2$ (1:1) collected at 20 K and 40 K, respectively.

Since the EDFS spectrum is strictly correlated to the coherence properties of the system at a given temperature, we did not expect to collect a coherent signal from the four {Cr$_7$Ni} rings because of their intrinsic coherence properties (see also Chap.3).

Indeed, {Cr$_7$Ni} rings usually show T_m values of 800 ns below 5 K, which drastically decrease above 10 K (see Fig.3.2). On the other hand, we would have expected to observe the echo signal of the **VOTPyP** unit, as in the case reported on the left side of Fig.6.4. We collected a series of cw-EPR spectra at different temperatures on frozen solutions in toluene/CH$_2$Cl$_2$ (1:1) and polycrystalline samples. In Fig.6.5, a plot showing the Q-band EPR signal variation as a function of the working temperature is reported. The vanadyl signal is here well-observable at 100 K, even if convoluted with the $S = 3/2$ signal (≈ 1200 mT) of {Cr$_7$Ni} rings both in polycrystalline and 1 mM solution. As the temperature reaches 20 K, the signal intensities dramatically decrease because of the line broadening of the resonances. At 5 K, the vanadyl signal seems so broad that its hyperfine structure is lost. On the other hand, the intensity of the resonance signal ascribed to the spin transition of the low-lying magnetic state $S = 1/2$ of {Cr$_7$Ni} rings (≈ 1325 mT) increases with the lowering of T.

At first, we hypothesized two main causes for the observed line broadening of the signal pertaining to the vanadyl unit: i) saturation setting in at low temperature due to the slow spin relaxation and ii) dipolar and exchange coupling interactions among the vanadyl's and the rings' spins. The first hypothesis was tested by performing a series of cw-EPR investigations as a function of the attenuation value for the mw field B_1. However, no saturation phenomena were observed at 5 K, even for low attenuation values of 5/10 dB (see Fig.C.12). Therefore, we performed a series of simulations of the spectrum of **VO{Cr$_7$Ni}$_4$** collected at 5 K in order to

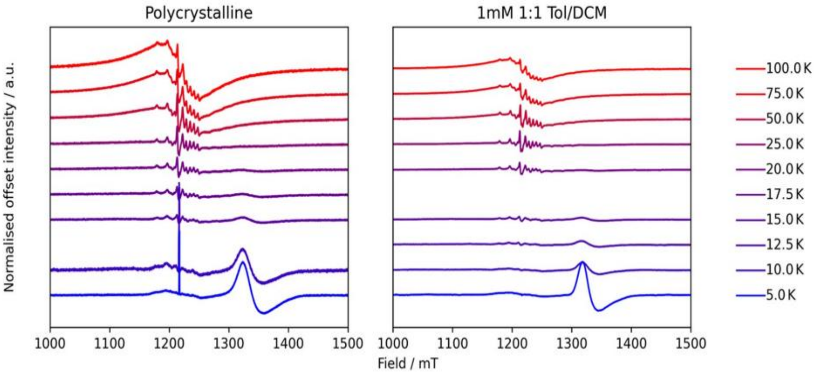

Figure 6.5. Plots of Q-band cw-EPR spectra of polycrystalline sample (left side) and 1 mM solution (right side) of **VO{Cr$_7$Ni}$_4$** collected at different temperatures. The color code follows the temperature map on the right.

validate our second hypothesis. We employed the spin Hamiltonian of Eq.6.1, in which two additional terms are considered. The first term accounts for dipolar interactions among the vanadyl and four surrounding rings, and the second one accounts for the isotropic exchange interaction among spin centers. Interactions among rings were neglected at this step.

$$\begin{aligned}\hat{\mathcal{H}}_S = {} & \mu_B \mathbf{g}^{\mathbf{VO}} \cdot \vec{B} \cdot \hat{S}_1 + \sum_{i=2}^{5} \mu_B \mathbf{g}^{\{\mathbf{Cr7Ni}\}} \cdot \vec{B} \cdot \hat{S}_i + \hat{S}_1 \cdot \mathbf{A}^{\mathbf{VO}} \cdot \hat{I}_1 \\ & + \sum_{i=2}^{5} \hat{S}_1 \cdot \mathbf{d_{1i}} \cdot \hat{S}_i - \sum_{i=2}^{5} J_{1i} \hat{S}_1 \cdot \hat{S}_i \end{aligned} \tag{6.1}$$

The isotropic dipolar interaction term was calculated considering the distance between spin centers extracted from the obtained structure. We estimated main components of dipolar interaction tensors as $d_{12} = d_{13} = d_{14} = d_{15} = 25 - 30$ MHz. The best estimation of isotropic exchange interaction constant J (considering the Heisenberg term $-J_{1i}\hat{S}_1 \cdot \hat{S}_i$) resulted from a series of simulations implemented by varying the J strength and evaluating the broadening of the vanadyl signal (Fig.6.6). We found the best range of J values to be that between $1 \cdot 10^{-3}$ cm^{-1} and $1 \cdot 10^{-2}$ cm^{-1} (Fig.6.6a). In particular, the most representative value could be that comprised between $J = 2.0 \cdot 10^{-3}$ cm^{-1} and $J = 3.0 \cdot 10^{-3}$ cm^{-1}, i.e., ranging between 60 and 90 MHz. Higher values of J are not representative of the current system, indeed, as soon as J reaches 10^{-1} cm^{-1} the spectrum structure around 1300 mT completely differs from the experimental one. Furthermore, the vanadyl signal is completely merged with that of rings, and simulated transitions could be correlated to a strongly coupled system. For the sake of clarity, the estimation of J given along with the treatment is obtained by a visual comparison with the experimental spectra reported in Fig.6.5.

Furthermore, the determination of the sign of J, thus in the type of the interaction involved, was not possible at this step because of the spectra quality and experimental conditions (e.g., temperature). More investigations will be needed to better clarify the nature of the isotropic exchange interaction.

A similar behavior was also observed in the analogous complex made of [Cu(TPyP)] (**CuTPyP**) and {Cr_7Ni}, namely **Cu{Cr_7Ni}$_4$**, synthesized following a procedure analogue to that for **VO{Cr_7Ni}$_4$** (see the generic synthetic strategy in Appendix C). The molecular structure and the obtained EPR spectra are reported in Fig.C.13. These observations suggest that the observed EPR is not likely to be correlated to the central ion but rather to the effect of surrounding wheels.

Interestingly, the coherence properties of {Cr_7Ni} did not change upon the coupling with vanadyl or copper ions. Rabi oscillations, and T_m of 400 ns (Fig.C.14), were indeed observed by pulsed EPR experiments conducted at 5 K and the $S = 1/2$ resonance field (≈ 1320 mT). The signal of {Cr_7Ni} rings in Fig.6.5 is broadened compared to that of purple-{Cr_7Ni} itself [109]. This broadening effect can be correlated to the coupling interaction between rings and a faster relaxation dynamics. To estimate the ring-ring interactions we performed DEER (Double Electron-Electron Resonance, also known as PELDOR) and RIDME (Relaxation-Induced Dipolar Modulation Enhancement) experiments on a **VO{Cr$_7$Ni}$_4$** solution in toluene/CH_2Cl_2 (1:1). Unfortunately, in both cases the data were not of sufficient quality to extract a range of reliable values. However, the DEER experiment allowed us to estimate a two-qubit gate time of 140 ns for a couple of coplanar rings, for which we also estimated the distribution of distances mostly centered on 2.25 nm (Fig.6.7).

The extracted mean distance of 2.25 nm compares well with the Ni-Ni distance between two coplanar rings of 1.95 nm extracted from the crystallographic data,

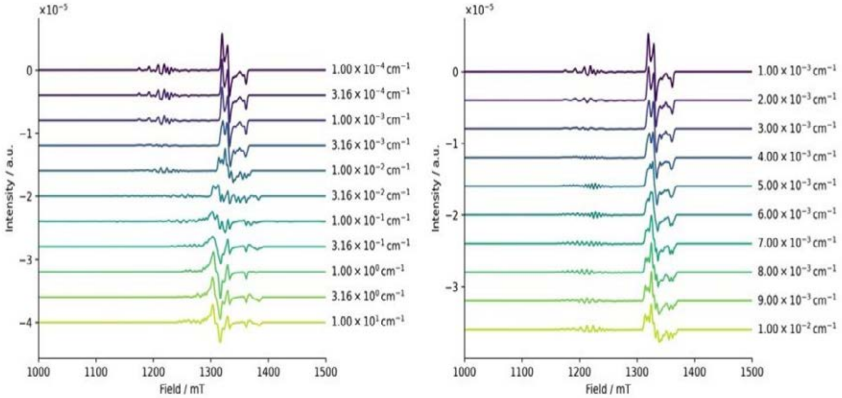

Figure 6.6. Plots of simulated Q-band spectra for **VO{Cr$_7$Ni}$_4$** as a function of the J value.

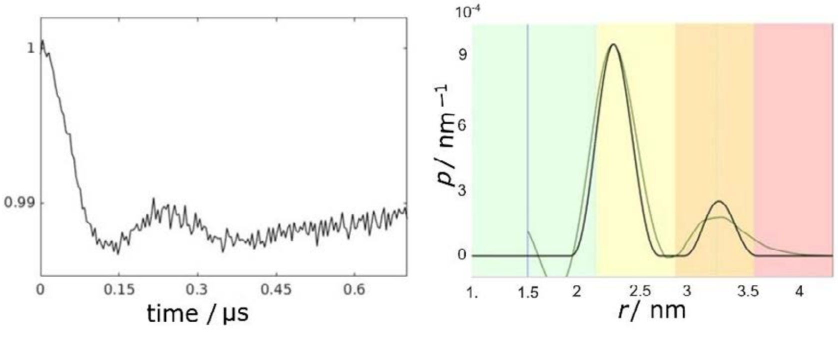

Figure 6.7. On the left, plot of the dipolar oscillation extracted from DEER experiment conducted on a 1 mM solution of **VO{Cr$_7$Ni}$_4$** at 5 K and Q-band frequency. A period of 140 ns can be observed. On the right, plot of the distance distributions obtained by the mathematical analysis (FT and Tikhonov regularization methods) of the dipolar oscillation [217]. The small peak at 3.25 is an artefact due to the mathematical method employed.

thus evidencing the stability of the supramolecular architecture even in solution. We are now trying to perform the same set of analyses on a **Zn{Cr$_7$Ni}$_4$** sample to rule out any possible effects arising from coupling interactions through the spin-active metalloporphyrin.

On the other hand, the EDFS spectra of both copper and vanadyl moiety substantially differ from each other. In Fig.6.8, we reported the comparison between **VO{Cr$_7$Ni}$_4$** and **Cu{Cr$_7$Ni}$_4$** EDFS spectra. It is evident that the hyperfine structure is lost in all of these spectra. However, the broadening effect is more evident in the case of **VO{Cr$_7$Ni}$_4$** rather than in **Cu{Cr$_7$Ni}$_4$**, and a lower temperature of 3 K is necessary to have a less ambiguous echo signal of vanadyl.

These observations mark a different behavior of copper and vanadyl ions. At the moment, no explanation has been found. Nevertheless, in both cases, we successfully recorded coherence times by Hahn echo experiments conducted at different field strength values (Fig.C.14). Large values of $T_m = 2.5$ μs and $T_m = 1.5$ μs were indeed observed when measuring at the field corresponding to resonances of vanadyl and copper ions, respectively. However, Rabi oscillations were not detected within the probed interval both for vanadyl and copper adducts. Such evidence highlights the impossibility of coherently manipulating the central unit at the frequencies involved in the experiment.

We note that while theoretical calculations might provide a clue to explain this nontrivial phenomenon, treating such a complex system might be challenging from a computational point of view. Therefore, we adopted a different molecular approach to overcome this issue. Indeed, we employed the A3B porphyrin 5,10,15(Triphenyl)-20-(4-pyridyl)porphyrin (H$_2$TrPPyP) to target the synthesis of a smaller supramolecular adduct containing just one purple ring ({[VO(TrPPyP)]{Cr$_7$Ni}}).

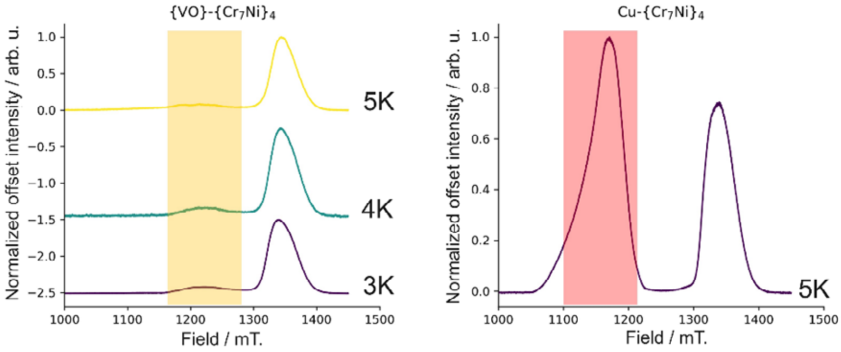

Figure 6.8. Plots of Q-band EDFS spectra of **VO{Cr$_7$Ni}$_4$** (left side) and **Cu{Cr$_7$Ni}$_4$** (right side) collected at different temperatures. Vanadyl and copper signals are highlighted by orange and red boxes, respectively.

The synthesis of the [VO(TrPPyP)] building block has been already performed here in Florence. The synthesis followed the same strategy employed for **VOTPP** and **VOTrPP** (see the following section). Preliminary characterization of the obtained compound is reported together with the detailed synthesis procedure in Appendix C. Our collaborators at the University of Manchester are going to perform the synthesis of the adduct, but it has not yet been achieved. Indeed, it would be convenient to check for the coherence property of vanadyl when just one ring is introduced, thus starting with the rationalization of the dynamic properties of a ”simpler” two-qubit system. However, this additional work is still in progress.

AUTHOR’S CONTRIBUTIONS. The author of this thesis synthesized and characterized **VOTPyP**, **VO{Cr7Ni}4**, **Cu{Cr7Ni}4**, **Zn{Cr7Ni}4**, and [VO(TrPPyP)]. Furthermore, he obtained X-ray quality crystals of **VOTPyP**, and **VO{Cr7Ni}4**.

6.2 $[VO(TrPP)]_2$ as a potential two-qubit gate

The previous section outlined some of the critical issues of adopting porphyrin-based multi-qubit architectures for scale-up perspectives. We highlighted the nontrivial behavior of the $\{[VO(TPyP)]\{Cr_7Ni\}_4\}$ supramolecular adduct, attributing the surprising loss of coherence of VO^{2+} ion to the appreciable coupling interactions with the four surrounding magnetic wheels. However, the non-predictable variation of its quantum properties as a function of the system’s dimension and complexity makes scale-up procedures particularly challenging. Indeed, the system may evolve to a more complex situation in which the environment can severely hamper the coherence properties of the qubits. This suggests that, because of the complex nature of peripheral moieties, simpler chemical systems would be a better solution for encoding quantum logical operations.

Two-qubit architectures known as non-switchable systems can also be of high relevance in this field since they can give the possibility of encoding various types of quantum gates. In this respect, adopting porphyrin ligands to achieve two-qubit architectures would be very advantageous. There exist plenty of examples of possible strategies aimed at coupling two (or even more) porphyrin units starting from various precursors [207−213]. A relevant example in this field is the dimerization reaction of two A3B-type porphyrins, namely the 5,10,15-triphenyl porphyrin (H_2TrPP, 5L), presented by Osuka and coworkers [218].

A *meso-meso* linked copper(II) porphyrin dimer was recently proposed and investigated by EPR and ELDOR spectroscopies. In their work, Wili and coworkers [219] investigated single- and triply-linked $[Cu(TrPP)]_2$ by employing the EDNMR (ELDOR-Detected NMR) spectroscopy (Fig.6.9). What emerged from this work is that the magnetic properties of this class of compounds are correlated to the torsion angle formed by the two units. In particular, they rationalized two distinct exchange coupling regimes for the two configurations: i) when singly-linked (i.e., when the two porphyrin units are free to rotate around the *meso-meso* bond, and the macrocyclic planes form a dihedral angle of about 90°), the two paramagnetic centers only present a very weak exchange coupling interaction (≈ 50 MHz according to EPR measurements); ii) when triply-linked, the antiferromagnetic exchange interaction among the two copper(II) centers is the dominant term of the employed spin Hamiltonian, being much more significant than Zeeman and hyperfine terms ($J \approx -15$ GHz). The system thus behaves like a total $S = 0$ system, with a first excited state characterized by a total $S = 1$ at ≈ 1.35 cm^{-1}. Similar behavior was also highlighted in the β-β bonded copper(II) bisporphyrin system [219]. Indeed, the presence of β bonds extends the conjugation of the molecule and favors a better orbital overlap.

On the one hand, these results demonstrated that the interaction between metal centers could be tuned by varying the torsion angle between the two subunits. On the other hand, it has not been proven if such properties are limited to the case of the copper-based complex. Therefore, we found it interesting to investigate a similar dimer where Cu^{2+} ions are replaced by vanadyl ones to unveil possible differences between the two systems. The magnetic orbital for a vanadyl ion embedded in a square-pyramidal coordination geometry is the d_{xy} atomic orbital of V^{IV}. This feature suggests a weaker coupling interaction mediated by the ligands among the two centers with respect to the copper analogue, in which the magnetic

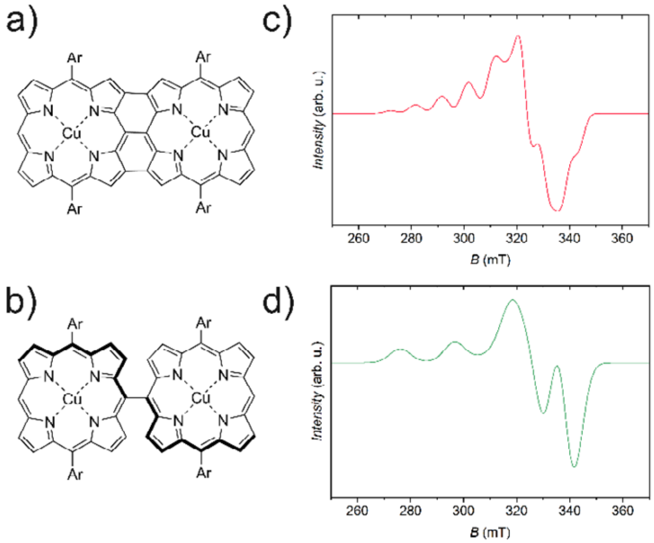

Figure 6.9. a) Sketch of the molecular structure of the triply linked $\{Cu_2\}$ complex: b) molecular structure of the singly linked $\{Cu_2\}$ porphyrin; c, d) Simulated EPR spectra of the triply- (c) and singly linked (d) $\{Cu_2\}$ complexes reported in panels (a) and (b). Simulations were performed using the spin Hamiltonian parameters reported in [219].

orbital of Cu^{II} is the $d_{x^2-y^2}$. As highlighted in Fig.6.10, the four lobes of the d_{xy} orbital of vanadium point toward the meso-positions of the porphyrin's scaffold, thus interacting with the coordinating N atoms through π type interactions. In the case of copper, the interaction between the $d_{x^2-y^2}$ orbital and those of the four N atoms is of the σ type since it points in the direction of coordinating atoms.

However, the d_{xy} lobe of one vanadyl subunit points toward the same lobe of the VO moiety within the linked porphyrin unit for any tilting angle of the two porphyrin rings. It suggests that the interaction among the two spin centers might be relevant for the vanadyl complex, even for the singly linked system (Fig.6.11).

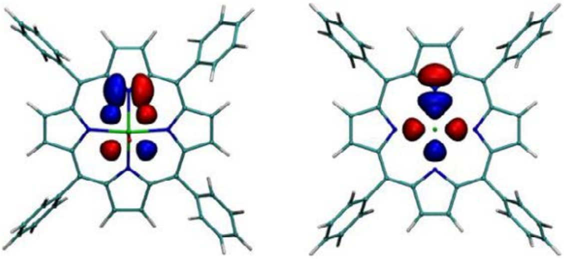

Figure 6.10. On the left, molecular structure of [VO(TPP)] with overlapped the $3d_{xy}$ and nitrogen's $2p_x$ orbitals. On the right, molecular structure of [Cu(TPP)] with overlapped the $3d_{x^2-y^2}$ and nitrogen's $2p_y$ orbitals.

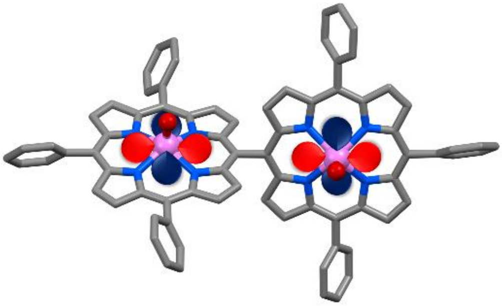

Figure 6.11. Representation of the molecular structure of singly linked vanadyl dimer, in which the d_{xy} lobes of the two VO units are reported to highlight the possible interaction through the space. In this case, the lobes are representative and not extracted from theoretical calculations.

The first step toward realizing the vanadyl-based dimer was the synthesis of the [VO(TrPP)] building block. This complex was never synthesized before, so we employed the common strategy already proposed for the synthesis of [VO(TPP)] [77]. In the practice, the [VO(TrPP)] complex (**VOTrPP**) was here synthesized by reaction of the commercial ligand H_2TrPP and [VO(acac)$_2$] in PhOH at 160 °C under N_2 atmosphere (a more detailed procedure is reported in Appendix C, Sec.C.2). Other synthetic strategies commonly employed and based on different solvents (e.g., DMF, acetic acid, quinoline, and others) were not employed since they usually led to smaller yields. Indeed, the vanadyl ion was relatively inert during reactions, and solvents capable of reaching high temperatures are always preferable to enhance the reaction yield. On the other hand, PhOH is unlikely to be an ideal solvent because of its chemical and physical properties (e.g., PhOH is a solid at RT, and its removal from reaction mixtures is always challenging). A complete description of the used synthesis method is reported in Appendix C.

The reaction product was characterized by UV-Vis spectroscopy. This kind of characterization is mandatory to check the absence of residual ligand fraction. The latter can be easily identified through specific spectral features modified by the interaction with the metal. The two principal indicators are: i) the change of the Soret band position ($S_0 \rightarrow S_2$ transition, 350 - 425 nm); ii) the variation of the relative intensities of the so-called Q bands (i.e., four broad vibronic bands resembling the shape of a hand within the 500 nm - 750 nm range) [220]. The latter property is handy for checking reaction products since Q bands reduce to two broad transitions when the metal forms a stable complex with the porphyrin host. A comparison between the ligand spectrum and those of **VOTPP** and **VOTrPP** is reported in Fig.6.12. The spectrum obtained in CH_2Cl_2 solution presents the

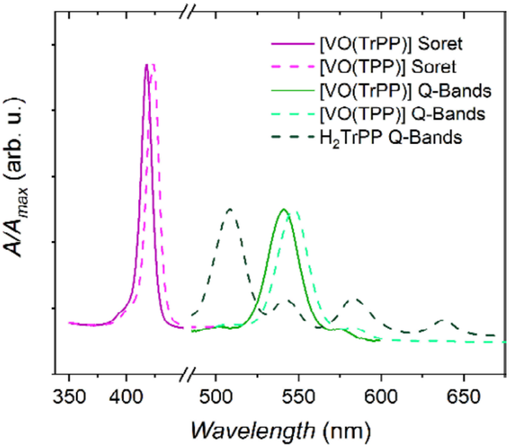

Figure 6.12. Comparison between the experimental UV-Vis spectra collected on CH_2Cl_2 solutions of H_2TrPP, **VOTPP**, and **VOTrPP**.

characteristic intensities distribution of the Q bands expected for a metal-porphyrin complex. Furthermore, the spectrum of **VOTrPP** shows a marked blueshift (≈ 5 nm) of both the Soret and Q peaks compared to that of [VO(TPP)]. Such evidence agrees well with previous experimental observations and DFT calculations [221]. Indeed, redshifts of Soret and Q bands have been identified for the different substituted phenyl-porphyrins when passing from phenyl-free porphine (H_2P) to tetraphenyl porphyrin (H_2TPP). Such a feature is correlated to an energy increase of the porphyrin's HOMO orbital.

Contrary to **VOTPP**, **VOTrPP** showed a marked solubility in various apolar organic solvents (e.g., CH_2Cl_2 and toluene), even in alkanes and cycloalkanes (e.g., pentane, n-hexane, light petroleum ether, and cyclohexane). It resulted insoluble, or very poorly soluble, in polar solvents such as MeOH, EtOH or CH_3CN. The large solubility detected for **VOTrPP** facilitated both the purification and the recrystallisation procedure of the crude compound.

Large needle-shaped crystals up to 7 - 8 mm in length were indeed grown from a wide variety of solvent mixtures (e.g., toluene/MeOH, toluene/CH_3CN, CH_2Cl_2/CH_3CN, *etc.*). Recrystallisation from CH_2Cl_2/CH_3CN mixture was particularly useful for further purification of the reaction product. Acetonitrile was a precipitating agent and helped remove residual PhOH, which commonly contaminates samples. X-ray quality crystals and microcrystalline powders can be obtained by tuning the evaporation rate of CH_2Cl_2, even by controlling the external temperature (for single crystals, the temperature was kept constant to 5 °C during the solvent evaporation).

The molecular structure of **VOTrPP** was obtained by single-crystal X-ray diffraction measurement at 100 K (Fig.6.13). **VOTrPP** crystallizes in the $P2_1/c$ space group, and the unit cell presents four molecular units, see Fig.6.13.

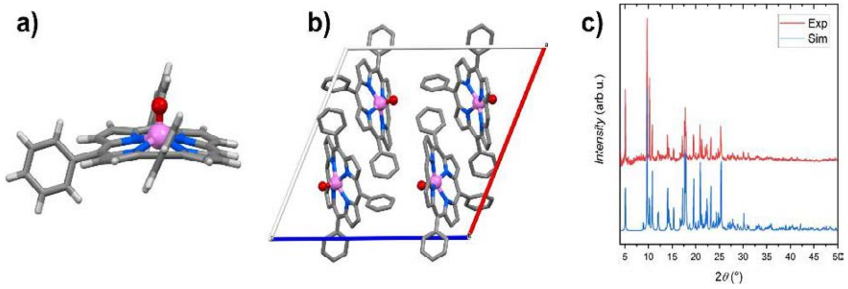

Figure 6.13. a) Molecular structure of **VOTrPP** obtained from single-crystal X-ray diffraction. Color code: C = grey, H = white, N = blue, V = pink, O = red. b) View along the b axis of the unit cell of **VOTrPP**. Hydrogens are omitted for clarity. Cell's parameters: a (red) = 19.05 Å; b =8.16 Å; c (blue) = 19.99 Å; $\alpha = 90°$; $\beta = 114°$; $\gamma = 90°$; V = 2830 $Å^3$. c) Experimental and simulated PXRD patterns of **VOTrPP**.

Each molecular unit is thus composed of a VO^{2+} ion embedded in a distorted square pyramidal coordination geometry given by the four bonded N atoms of the ligand core and completed by the V=O bond. The porphyrin ligand presents a significant distortion with respect to the VOTPP case (Fig.6.13a). Such a distortion may also explain the observed blueshift in the UV-Vis spectrum shown in Fig,6.12. Faster CH_2Cl_2/CH_3CN solution evaporation results in microcrystalline powders. Their PXRD pattern, Fig.6.13c, is in close agreement with that simulated by assuming the single-crystal structure, thus suggesting that the molecular structure and the packing are maintained.

Following what was reported by Osuka about the condensation of two [Zn(TrPP)] units mediated by the Ag^+-assisted oxidative coupling reaction [218], we decided to adopt a similar approach to couple two [VO(TrPP)] units. Compound **VOTrPP** was thus employed for the synthesis of dimer $[VO(TrPP)]_2$ (hereafter **{VO}$_2$**). The employed synthetic strategy partially proved the possibility of obtaining **{VO}$_2$**. However, the final yield was too low (below the 1% of the expected weight), and the purification from residual **VOTrPP** not trivial. We, therefore, decided to adopt a modified strategy as reported in [223,224]. The employment of PIFA = (Bis(trifluoroacetoxy)iodo)benzene (Fig.6.14) as coupling agent (see extended procedure in Sec. C.2) resulted in an improvement of the final yield of **{VO}$_2$** up to 43%. It has been demonstrated that such a reagent can also be conveniently adopted for getting triply-linked $[Zn(TrPP)]_2$ units as well. However, the procedure requires a large excess of PIFA (up to 2.5 eq.). When it was employed for the coupling of **VOTrPP**, reagents/products rapidly decomposed. A possible strategy to get triply linked vanadyl porphyrin would be that of synthesizing a triply linked Zn-porphyrin, demetallizing it, and then adapting it to obtain a VO^{2+} complex [219, 222]. We are indeed considering such a protocol for employing it in the near future.

Compound **{VO}$_2$** was characterized by UV-Vis spectroscopy, MALDI-MS spectrometry, and X-ray diffraction both on single crystals and microcrystalline powders (see Sec.C.2). The UV-Vis spectrum of a CH_2Cl_2 solution of **{VO}$_2$**

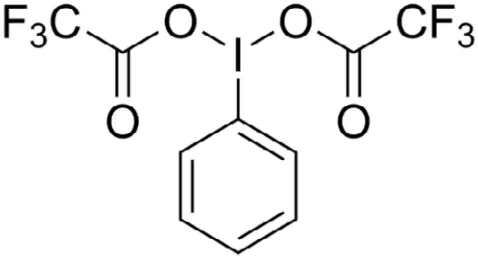

Figure 6.14. Representative sketch of the molecular structure for PIFA reagent.

showed the characteristic bands expected for condensed porphyrins (Fig.6.15). In the figure, the difference in relative absorbances of the two peaks at 422 nm and 457 nm between red and orange lines can be correlated to a difference in purity between **{VO}$_2$** obtained from $AgPF_6$ or PIFA-mediated condensation reactions. Indeed, removal of residual **VOTrPP** after reaction with $AgPF_6$ was not trivial, also because of the low amount of obtained product.

The obtained compound showed a marked solubility in all common organic solvents, from MeOH to n-hexane. In particular, toluene resulted in the ideal solvent for samples' purification and recrystallisation. Microcrystalline powders were indeed obtained by evaporation of the toluene solution. The evaporation rate here is fundamental. A single crystal of **{VO}$_2$** was obtained by very slow evaporation (it was stopped after ≈ 3 months) of a toluene solution dispersed in SEPHADEX gel. Any other crystallization experiment conducted in toluene within a shorter time window (even two months) led to the twinning of crystallites or microcrystalline powders. The molecular structure of **{VO}$_2$** solved from the experimental X-ray data is reported in Fig.6.16a, b, while the unit cell in Fig.6.16c.

{VO}$_2$ crystallizes in the *C*2/c space group with four molecular units per cell and two disordered toluene crystallization molecules per unit. The molecular structure is characterized by two **VOTrPP** units coupled through the C atoms in *meso* positions of the porphyrins' scaffolds. The torsion angle (ϕ) between the two units is 64°. Each molecular unit thus contains two magnetically nonequivalent centers.

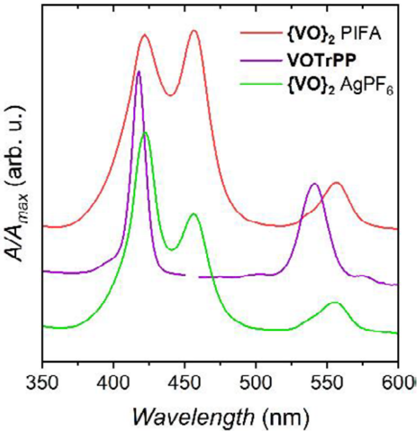

Figure 6.15. Experimental UV-Vis spectra of CH_2Cl_2 solutions of **VOTrPP**, **{VO}$_2$** obtained from condensation reaction with $AgPF_6$, and **{VO}$_2$** obtained from condensation reaction with PIFA.

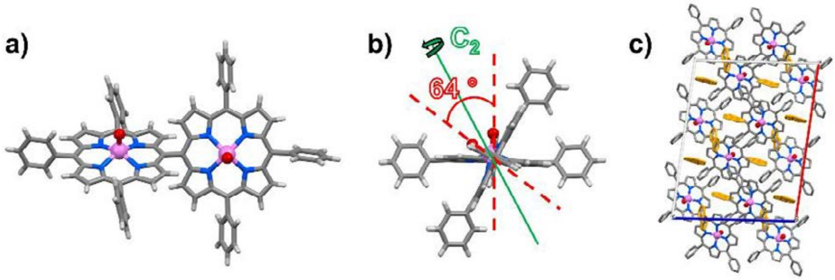

Figure 6.16. a) Molecular structure of **{VO}**$_2$ obtained from toluene in Sephadex gel. b) View along the C─C bond of the **{VO}**$_2$ molecular structure. The torsion angle $\phi = 64^\circ$ is highlighted by red-dashed lines, and the C_2 axis is highlighted by the green solid line. c) View along the *b* axis of the unit cell of **{VO}**$_2$. Hydrogens are omitted for clarity, while disordered solvent molecules are highlighted in orange. Cell parameters: *a* (red) = 29.30 Å; *b* = 11.39 Å; c (blue) = 22.55 Å; α = 90°; β = 97°; γ = 90°; V = 7468 Å^3.

The asymmetric unit is identified as one VO-porphyrin center, while the other half of the molecule is generated by a C_2 rotation around an axis passing through the middle of the POR-C-C-POR bond (Fig.6.16b). In principle, they might be selectively probed by specific EPR pulses when in oriented crystals because of their non-equivalent magnetic nature.

Microcrystalline powders of **{VO}**$_2$ obtained by recrystallisation from toluene solution under vacuum showed the same crystal structure as evidenced in experimental PXRD pattern in FigC.15. However, this particular structure accounts for hydrogen rich solvent molecules within the unit cell. Coherence properties of solid-phase samples might be, therefore, severely hampered by the presence of hydrogen atoms and rotating groups, e.g., the methyl group of toluene molecules. In this respect, we found that slow evaporation of acetone and MeOH solutions of **{VO}**$_2$ can lead to single crystals of solvent-free structures (Fig.6.17). Furthermore, sufficiently large X-ray quality crystals grow in shorter intervals (≈ one month). In this case, the compound **{VO}**$_2$ crystallizes in the orthorhombic *C*cc2 space group. The ϕ between the two **VOTrPP** units is here 72°.

At the moment, we have obtained the titanyl derivative of **VOTrPP** in very low yields because of the scarce reactivity of the titanyl ion. We are now trying to improve this synthetic strategy for enhancing the overall yield. However, we think it will be possible to **{TiO}**$_2$ by adapting the synthetic strategies adopted so far for the vanadyl dimer. Alternatively, the Zn-based analogous dimer might be used for this purpose, but we think the diamagnetic host's isostructural nature could be lost.

In the absence of a solid diluent, we investigated both static and dynamic properties of **{VO}**$_2$ by working in diluted solutions of toluene and toluene-d$_8$ (≈ 10^{-5} M), respectively.

The first set of measurements was performed at 30 K on a glassy solution of **{VO}**$_2$ in toluene by cw-EPR spectroscopy working at X-band frequency. The experimental spectra obtained for monomer and dimer species are reported in Fig.6.18. The non-trivial behavior of **{VO}$_2$** is here well highlighted. If compared to that of the monomer (which is not substantially different from that of **VOTPP**), the EPR spectrum of **{VO}$_2$** shows a larger number of peaks. The very structured spectrum was not simply attributable to two different non-interacting spins. The observed fine structure can be sensibly attributed to the presence of magnetic interactions among the two spins. It follows that the total SH must consider both dipolar and exchange coupling interactions to rationalize the spectrum accurately. Q-band pulsed EPR spectroscopy was thus employed to restrict the parameters space investigation for the spin Hamiltonian of this system.

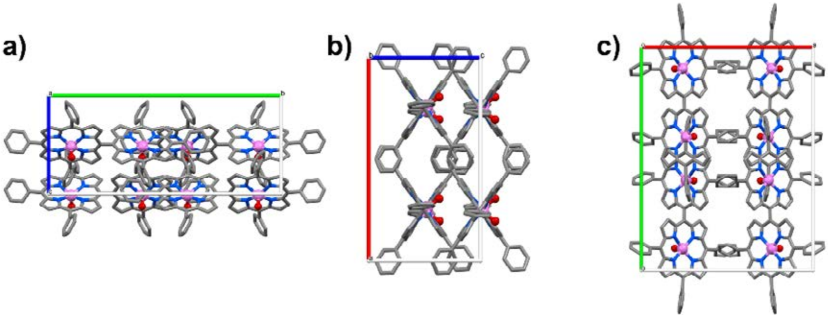

Figure 6.17. Different views of the crystal structure of a **{VO}$_2$** crystal obtained from acetone. Hydrogens are omitted for clarity. Cell parameters: a (red) = 20.86 Å, *b* (green) = 27.17 Å; *c* (blue) = 11.48 Å; $\alpha = 90°$; $\beta = 90°$; $\gamma = 90°$; $V = 6513$ Å^3. a) view along the *a* crystallographic axis; b) view along the *b* crystallographic axis; c) view along the *c* crystallographic axis.

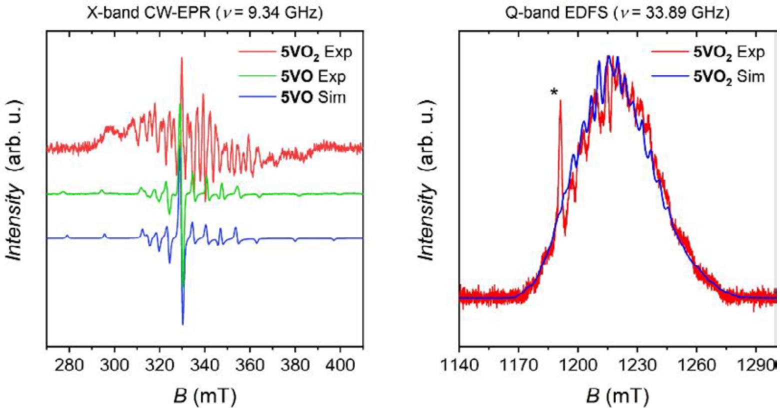

Figure 6.18. Experimental and simulated X-band cw-EPR (left side) and EDFS (right side) spectra collected on toluene solutions of compounds **VOTrPP** and **{VO}$_2$**. An asterisk is placed in correspondence of a residual signal of the cavity.

The simulation of the EDFS spectrum reported in Fig.6.18 was implemented adopting a SH for two interacting spin centers, thus considering both exchange and dipolar coupling interactions (Eq.6.2).

$$\hat{\mathcal{H}}_S = \hat{\mathcal{H}}_{Zeeman} + \hat{\mathcal{H}}_{Hyp} - J_{12}\hat{S}_1 \cdot \hat{S}_2 + \hat{S}_1 \cdot \boldsymbol{d}_{\mathbf{12}} \cdot \hat{S}_2 \tag{6.2}$$

The list of best simulation parameters adopted for **VOTrPP** cw-EPR and **{VO}$_2$** EDFS spectra are reported in Table 6.1. Moreover, the individual **g** and **A** of the two species were considered equal in their principal values but noncollinear, with an angle of 64° between their principal axes. It is known that a distribution of different torsion angles is likely present in solution. For simplicity, we employed the same value of ϕ extracted from the solid-state structure even for the frozen solution. However, it was considered a reasonable mean value for the investigated frozen solution and roughly introduced in our model. As a probable consequence of our approximation, a mismatch between simulated and experimental EDFS spectra is well observable in Fig.6.18. Furthermore, a precise simultaneous estimation of all SH parameters was not possible within our experimental limits. Therefore, we fixed g- and A-tensors components to the values found in **VOTrPP** and calculated the value of the $\mathbf{d_{12}}$ matrix in the approximation of interacting point dipoles. Future experiments on diluted oriented crystals would be the key for accurately determining the magnitude of various contributions to static magnetic properties of the dimer. Indeed, employing a single doped crystal would result in a simplified EPR spectrum, correlated to a fixed ϕ between the two units.

The extracted value of $J_{12} \approx 600$ MHz ($\approx 2 \cdot 10^{-2}$ cm^{-1}) evidences a non-negligible super-exchange interaction within the two vanadyl centers. Indeed, the estimated J value in the case of our singly-linked system differs by one order of magnitude with respect to the representative one of 50 MHz given for the copper(II) derivative in [219]. Nevertheless, it must be stressed that the extracted value of J would result from a distribution of possible structures of the dimer in the solution and that the ϕ angle could be reasonably correlated to the strength of the exchange interaction. Furthermore, the employed cw-EPR technique gave only information on the J absolute value and not on its sign.

In this respect, we performed DFT calculations as support to experimental results for i) evaluating the magnitude of the exchange coupling interaction as a function of the ϕ angle between the two sub-units and ii) for evaluating the sign of J_{12}. To do this, we adopted the broken symmetry model at the DFT level of theory [225] applied on the two limit molecular structures obtained from the single-crystal measurements presented above, i.e., the first structure characterized by a torsion angle of 64°, and the solvent-free one characterized by a torsion angle of 72°. In a nutshell, the calculation starts from the experimental molecular structure (structures were not optimized before calculations) and then computes both low- (Broken-symmetry, s) and high-spin (S_{max}) states of **{VO}$_2$** and their energies.

Table 6.1. Best SH parameters obtained from cw-EPR and EDFS spectra simulations for **VOTrPP** and **{VO}$_2$**.

VOTrPP		**{VO}$_2$**	
$g_{\perp}$	1.9881(1)	$g_{1,2}^{\perp}$	1.9881(1)
$g_{\|\|}$	1.965(1)	$g_{1,2}^{\|\|}$	1.965(1)
$A_{\perp}$	168(2) MHz	$A_{1,2}^{\perp}$	168(2) MHz
$A_{\|\|}$	477(2) MHz	$A_{1,2}^{\|\|}$	477(2) MHz
		J_{12}	599.6(1) MHz
		$d_{1,2}^{x}$	-167.9(2) MHz
		$d_{1,2}^{y,z}$	-83.95(2) MHz

The outcome of the model is the difference in energy between these states defined as [225]:

$$\Delta E(S_{max} - s) = \sum_{i<j} J_{ij}(2|s_i s_j + s_j|)\lambda_{ij} \tag{6.3}$$

Where s_i and s_j are the spin states of coupled units, and $\lambda_{ij} = 0$ if s_i and s_j have the same sign and 1 otherwise. The value of the isotropic exchange interaction term is extracted by the relation $J_{12} = 2\Delta E(S_{max} - s)$. The best estimation of J_{12} for the two limit structures followed the application of the B3LYP functional and the Van der Waals corrective terms (D3) [226]. For the first employed structure (ϕ = 64°) we estimated a ferromagnetic interaction characterized by J_{12} = 48 MHz, while for the second structure (ϕ = 72°) the ferromagnetic interaction is characterized by a J_{12} = 1.167 GHz. These results, in contrast with what has been observed in the case of Cu dimer [219], highlight the strong and counterintuitive dependence of the exchange coupling interaction from the value of ϕ. In our case, such a range of values is well comparable to that validated by our simulations, so we are pretty confident in the estimated value of about 600 MHz for the sample in the toluene solution given within this work.

The value of J estimated by EPR measurements, and confirmed by DFT calculations, is perfectly within the limits of the weak exchange coupling interaction needed for application as a two-qubit gate. In this way, the qubits can ”communicate” while still being distinguishable. In principle, the two qubits could be selectively probed based on their relative orientations with respect to the direction of the employed static field B_0. These properties make the present system particularly appealing for implementing a two-qubit gate. For this reason, we performed a preliminary investigation of the spin dynamics of **{VO}$_2$**. It was possible to determine both T_m and T_1 values at 30 K (Fig.6.19b-c) by performing

Hahn echo and inversion recovery experiments at 1028 mT (Fig.6.19a). We observed a T_m value of 3.6(1) μs for the selected field. Furthermore, we successfully collected Rabi oscillations at the employed field. Such a peculiarity indicates that the probed state is coherently manipulable (Fig.C.16).

The whole set of characterizations employed is just a preliminary step toward the implementation of a *true* quantum gate. Indeed, the tangled structure of the spectrum does not allow to fully and precisely address specific spin transitions on the powder-like sample. It would be tough to determine the effectively probed transition for which the coherence time was determined since plenty of allowed and prohibited resonances are concentrated within a few mT range, even on an oriented crystal (Fig.C.17b). The number of transitions further increase for powder samples because both parallel and perpendicular resonances arise within the same spectral range. Nevertheless, we believe that better exploitation of the quantum properties of such a compound would be possible: i) by working on oriented crystals of diluted species. Indeed, taking advantage of the different orientations of the two V=O moieties within the molecular unit of **{VO}$_2$**, it would be easier to address specific transitions for implementing two-qubit operations. As an example, let us consider the energy levels scheme reported in Fig.6.20. In the high-field region (1250 mT - 1300 mT), there are at least three different transitions (if we do not consider the hyperfine set of transitions hidden below the red lines) that can be selectively probed by changing the frequency; ii) by adopting W-band EPR for better resolving many transitions (Fig.C.17b).

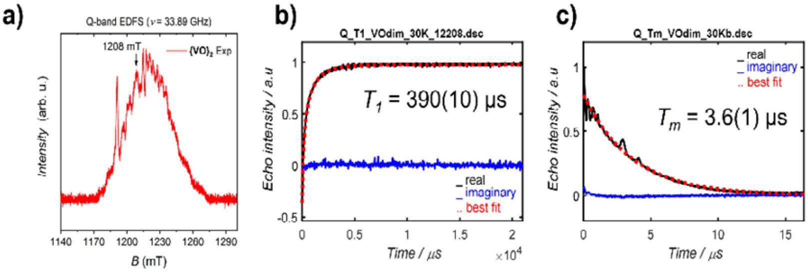

Figure 6.19. a) Experimental EDFS spectrum of **{VO}$_2$** showing the field position adopted for inversion recovery and Hahn echo experiments. The intense signal at ≈ 1190 mT is correlated to a residual impurity signal from the cavity. b) Plot of the echo intensity as a function of time extracted from inversion recovery experiments at 1208 mT and 30 K on **{VO}$_2$**. Data were fitted with a stretched exponential model ($x_{stretch}$ = 0.61). c) Plot of the echo intensity as a function of time from Hahn echo experiment. The best fit was obtained by adopting a monoexponential model.

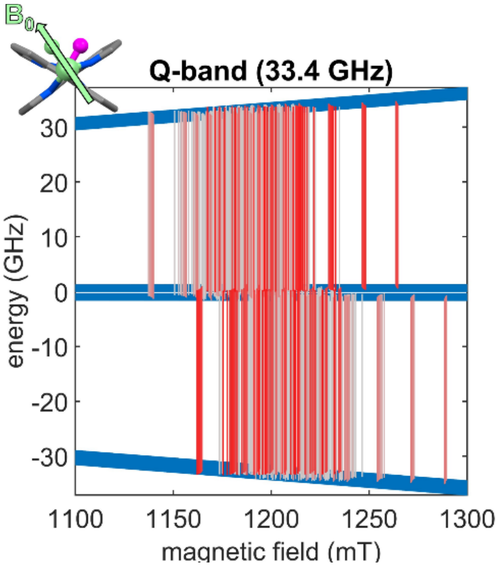

Figure 6.20. Zeeman plot simulated for an oriented **{VO}$_2$** sample in which the direction of the magnetic field B_0 is collinear to the direction of one V=O moiety. Spin transition probabilities are highlighted by red to grey vertical lines (red = larger probability).

AUTHOR'S CONTRIBUTIONS. The author of this thesis synthesized and characterized **VOTrPP**, faced the first synthetic attempt for obtaining **{VO}$_2$** with AgPF$_6$, crystallized **{VO}$_2$** samples, and collected and solved their structures. Furthermore, he actively helped DR in synthesizing and characterizing **{VO}$_2$** obtained through the PIFA strategy.

Chapter 7
Conclusions

Several examples of molecular compounds have been presented in this thesis work, specifically designed to fulfil stringent tasks for quantum technologies. All the presented molecular qubits were rationally introduced within the present work since they fulfil the three main requirements prefixed and presented in Chap.4, i.e., i) a multilevel structure of electronic or nuclear states; ii) a nuclear spin-depleted environment; iii) neutral charge and appreciable thermal stability so that they can be employed for surface deposition experiments. A large part of the project focused on the realization and characterization of the magnetic properties of hydrogen-free compounds suitable for surface deposition experiments, i.e., **CuPz** (Sec.4.1) and **Cudttt** (Sec.4.2). Our results show that the removal of hydrogen atoms resulted in an appreciable coherence time enhancement in **CuPz** with respect to benchmark **CuPc**. However, the coherence properties of the novel set of **dttt** compounds did not reach the expectation, probably because of segregation phenomena occurring during the preparation of the diamagnetically diluted sample. This evidence suggests hydrogen removal as a good strategy for enhancing coherence times. Nonetheless, particular care must be paid to the choice of the ligand's structure since adopting conjugated organic molecules characterized by strong stacking interactions in the crystal phase complicates the handling of products. However, we obtained positive results in the sublimation of **Cudttt**, which combines the need for nuclear-depleted systems and sublimation properties. In this way, we hope to highlight new paths to investigate the properties of this class of molecular qubits on surfaces towards obtaining systems competitive with solid-state electron spin-based devices.

Furthermore, we have widely adopted a combined experimental and theoretical approach for unveiling the different contributions to the spin-lattice relaxation

Fabio Santanni, University of Florence, Italy, santannifabio@gmail.com, 0000-0002-0506-8333

Referee List (DOI 10.36253/fup_referee_list)
FUP Best Practice in Scholarly Publishing (DOI 10.36253/fup_best_practice)

Fabio Santanni, *Molecular approaches for quantum technologies. Optimization of electron spin-based quantum bits and quantum logic gates*, © 2025 Author(s), CC BY 4.0, published by Firenze University Press, ISBN 979-12-215-0670-9, DOI 10.36253/979-12-215-0670-9

process of molecular magnets, extending the treatment from transition metals molecular qubits (**CuPz**) to lanthanide-based SMMs (**Dyacac**). We evidenced that in a symmetrical complex like **CuPz**, the weight of molecular vibrations contributing to the SPC interactions strictly depends on the symmetry of the active optical mode. In particular, *gerade* modes showed a strong interaction with the spin, thus driving its relaxation with the lattice. We also employed a complete model involving crystal phonons to extend the treatment of spin-lattice relaxation in lanthanide-based magnets and presented an innovative strategy. Indeed, our work shows the role of SPC in the Raman relaxation process of lanthanide complexes starting from molecules in the crystal phase. Furthermore, we highlighted the role of the first coordination sphere distortion in inducing relaxation. We evidenced how second-sphere interactions mediated by electrostatic polarization effects may be of prime importance for spin relaxation in the high-temperature regime for betadiketonate complexes. Our results provided a handy set of chemical guidelines for engineering the structure of lanthanide-based magnetic molecules.

Interesting results were also presented in the case of the archetypical molecular qubit **VOTPP**. This system was adopted for advanced EPR experiments aimed at: i) probing the integrability of molecular qubits ensembles within coplanar resonators for evidencing their properties as quantum memories; ii) enhancing the coherence time of molecular qubits by working with atomic clock transitions. In the first case, we obtained satisfactory evidence outlining how such an archetypical system can be employed to store and retrieve information once coupled to the superconductive circuit. In particular, we successfully stored and retrieved up to three π pulses within a single crystal of doped **$VO_{2\%}TPP$**, and up to five pulses in the case of a polycrystalline pellet. In the second case, we obtained preliminary results on the capability of probing atomic clock transition in **VOTPP**. Indeed, the need for sensitive resonators capable of working at the radiofrequency (well in the region of NMR) makes these experiments challenging, and it requires more advanced probes to be developed. However, we demonstrated how working with oriented crystals of this vanadyl-based qubit showing sharp EPR transitions is the key to setting the optimal conditions for an experimental apparatus, thus presenting a series of experiments conducted at the limit of the current instrumental capabilities. In addition, we presented some technical details of the purification process employed for removing iron(III) impurities detected in **VOTPP** powders. In this case, sublimation of **VOTPP** in high vacuum conditions allowed us to efficiently remove this kind of impurities, thus proving that thermal sublimation technique could be a powerful tool even for managing the purity level of this class of thermally stable systems.

The last part of this thesis was mainly focused on multi-qubit architectures. In Chap.6, we presented two examples of multinuclear systems, i.e., **$VO\{Cr_7Ni\}_4$** and **$\{VO\}_2$**, synthesized for gaining switchable or non-switchable molecular quantum logic gates, respectively. In the case of **$VO\{Cr_7Ni\}_4$**, we highlighted how challenging it could be to gain large supramolecular structures whose magnetic properties can still be controllable for implementing multi-qubit logical operations. In particular, an extensive cw- and pulsed EPR investigation evidenced how exchange coupling interactions can seriously hamper the coherence properties of highly coherent ions such as the vanadyl one. However, we are still working on a different molecular approach involving the asymmetric **VOTrPyPP** complex to better understand the origin of such interactions in this class of supramolecular adducts. A sound system could be represented by the **{VO}$_2$** adduct presented in Sec.6.2. We synthesized the system for the first time and obtained different crystal structures on two samples employing different strategies: i) by slow evaporation of toluene from a gel dispersion of the complex; ii) by very slow evaporation of acetone. Our preliminary EPR results obtained by measuring a liquid dilution showed that the exchange interaction among the two dimer's units is in the optimal range for implementing a reliable quantum gate. We also plan to focus our efforts on obtaining doped single crystals of **{VO}$_2$** in **{TiO}$_2$** for better exploiting the addressability properties of the two vanadyl moieties.

In the end, we presented different approaches for the optimization of molecular spin qubits and quantum logic gates. All the presented single-qubit systems have shown interesting features in terms of manipulability and coherence properties. However, while the employed ligands provided an excellent platform for obtaining neutral and thermally stable metal complexes, controlling the relaxation properties of porphyrazine and dithiazole-based complexes to gain more performing molecular qubits was not trivial. Good results were instead obtained in the case of vanadyl-based porphyrin complexes, confirming that they represent a versatile platform for different applications in quantum information science, conciliating the requirement of high coherence time and easy manipulability. In addition, we successfully evidenced the benefits of using porphyrin ligands for obtaining multi-qubit architectures. Nonetheless, the non-trivial character of such complex structures highlighted that much work is still needed to outline a reliable strategy for implementing quantum logical operations.

Appendix A
Theoretical background and experimental techniques

A.1 The spin Hamiltonian

In this text, we use to refer to many physical parameters necessary to understand the magnetic behavior of a spin system. For this reason, such a section wants briefly to recall many aspects of the *spin Hamiltonian* formalism ($\widehat{\mathcal{H}}_S$), i.e., the physical operator describing the spin state of a magnetic molecular system. The following treatment is mainly adapted from [68] and [154].

The general idea of the spin Hamiltonian is that of adopting a spin-only operator to describe the state of an electron when the total angular orbital momentum ($\hat{L}$) can be considered as quenched. Such an approximation is valid only for those systems in which the spin-orbit contribution may be neglected, such as most of the first row's transition metal ions. On the other hand, this approximation should be avoided for heavier metal ions where orbital contribution cannot be neglected, e.g., lanthanide ions.

Let us consider a single electron in an open-shell system. The ground state of the system is thus characterized by a spin quantum number $S = 1/2$. In addition, we may choose a metal ion for which the nuclear momentum is not zero, i.e., with a nuclear ground state characterized by a nuclear spin quantum number $I \neq 0$. The spin Hamiltonian representing the energy state of this system should be written as:

$$\widehat{\mathcal{H}}_S = -\mu_N \mathbf{g}_\mathrm{N} \cdot \vec{B} \cdot \hat{I} + \mu_B \mathbf{g} \cdot \vec{B} \cdot \hat{S} + \hat{S} \cdot \mathbf{A} \cdot \hat{I} \tag{A.1}$$

Fabio Santanni, University of Florence, Italy, santannifabio@gmail.com, 0000-0002-0506-8333

Referee List (DOI 10.36253/fup_referee_list)
FUP Best Practice in Scholarly Publishing (DOI 10.36253/fup_best_practice)

Fabio Santanni, *Molecular approaches for quantum technologies. Optimization of electron spin-based quantum bits and quantum logic gates*, © 2025 Author(s), CC BY 4.0, published by Firenze University Press, ISBN 979-12-215-0670-9, DOI 10.36253/979-12-215-0670-9

Here, μ_N and μ_B are the nuclear and Bohr magneton; $\mathbf{g}_\mathrm{N}$ is the nuclear g-factor, $\mathbf{g}$ is the electron g-tensor, $\mathbf{A}$ is the hyperfine coupling tensor, $\vec{B}$ is the applied magnetic field, and $\hat{I}$ and $\hat{S}$ are the nuclear and electron spin operators. In this equation, the first and the second terms represent the nuclear and electron Zeeman interactions, respectively, that account for the effect of the magnetic field on the spin. The application of a static magnetic field causes the loss of degeneracy of $2S + 1$ electronic level characterized by a different projection along the z magnetic axis (the quantization axis is conventionally chosen as the magnetic field application direction). The resulting splitting of the $S = 1/2$ doublet due to the Zeeman effect is shown in Fig.A.1. The larger the magnetic field (or the spin component along the quantization axes), the larger the energy split between the magnetic levels.

The g-tensor accounts for the electron anisotropy, i.e., the different effect of the magnetic field on the spin with respect to the application direction. Because the g-matrix is usually symmetric (so that off off-diagonal term can be neglected if the system symmetry is sufficiently high) it can be rewritten in its diagonal form:

$$\mathbf{g} = \begin{pmatrix} g_{xx} & 0 & 0 \\ 0 & g_{yy} & 0 \\ 0 & 0 & g_{zz} \end{pmatrix} = \begin{pmatrix} g_x \\ g_y \\ g_z \end{pmatrix} \tag{A.2}$$

We may also refer to an *axial approximation* when the system's properties respect some symmetry conditions, and the g-tensor may be rewritten as $g_x = g_y = g_{||}$ and $g_z = g_\perp$. If the system has a spherical symmetry, i.e., it is isotropic, the g-tensor must fulfil the condition $g_x = g_y = g_z$. On the other hand, the system presents a *rhombic* distortion when all the $\mathbf{g}$ components are different from each other.

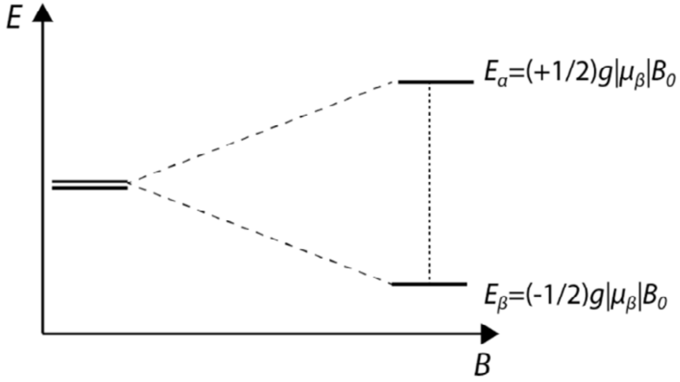

Figure A.1. Representative plot of energy change of an electronic doublet for a S = 1/2 system as a function of the applied magnetic field due to the Zeeman effect.

The g-tensor components are correlated to the Landé g-factor (g_e). Following a perturbation approach, the **g** matrix can be obtained through the relation [68]:

$$\mathbf{g} = g_e\mathbf{I} - 2\lambda\mathbf{\Lambda} \qquad \text{(A.3)}$$

In this equation, $\mathbf{I}$ is the identity matrix, λ is the spin-orbit coupling constant, and $\mathbf{\Lambda}$ is a matrix that accounts for the admixing of the ground state with the excited ones due to the total orbital momentum $\hat{L}$. Because $\mathbf{\Lambda}$ terms always have positive values, the magnitude of g-tensor terms is determined by the sign λ. In particular, for transition metal ions with a number of valence shell electrons $n > 5$, the values of the $\mathbf{g}$ components are higher in value than $g_e \approx 2.003$. On the contrary, for $n < 5$, $\mathbf{g}$ components will be lower than g_e.

The third term in Eq.A.1 considers the electron-nuclear hyperfine coupling interaction, and the **A** term is the hyperfine coupling tensor. As well as the g-tensor, the **A** matrix can be opportunely diagonalized, and its terms values can fulfil the symmetry requirements stated above for **g**. The onset of a hyperfine interaction causes electronic states to split due to the coupling between $\hat{I}$ and $\hat{S}$ momenta, and each M_S splits in $2I + 1$ states. Because the set of M_S and M_I is not a good basis to represent the state of the system after the introduction of the hyperfine term, the new basis of the system can be rewritten as $|M_sM_I\rangle$.

In a nutshell, the hyperfine coupling interaction accounts for three different contributions: i) the Fermi (or *contact*) interaction, which is isotropic and proportional to the electronic density of the unpaired electron on the nucleus; ii) a through-space dipolar interaction between the electron and the nucleus, which is inversely proportional to the third power of the distance; iii) a *pseudo-contact* interaction between the nucleus and the orbital momentum of the electron, which can be usually neglected in the field of molecular magnetism [227]. As a consequence, the **A** tensor can be written as a sum of two terms as reported in Eq.A.4.

$$\mathbf{A} = a\mathbf{I} - \mathbf{T}^{dip} \qquad \text{(A.4)}$$

In this equation, a is the hyperfine coupling constant, and it is proportional to $|\psi(0)|^2$, i.e., the spin density at the nucleus proximity.

The spin Hamiltonian reported in Eq.A.1 is representative of the system when the total spin is $S = 1/2$. When the total spin value is higher than 1/2, an additional term, quadratic concerning the spin operators, is to be introduced. Such a term accounts for the effect of the crystal field on the electron spin and can be added to the total spin Hamiltonian by introducing the term:

$$\hat{\mathcal{H}}_{CF} = \hat{S} \cdot \mathbf{D} \cdot \hat{S} \tag{A.5}$$

Where **D** is the crystal field tensor, that can be opportunely diagonalized when the reference system of *x, y, z* magnetic axes is chosen as collinear to its principal directions. Thus, subtracting a constant term (1/2)(D_{xx}+D_{yy})(S(S+1)), the CF term can be rewritten as:

$$\hat{\mathcal{H}}_{CF} = D\hat{S}_z^2 + E(\hat{S}_x^2 - \hat{S}_y^2) \tag{A.6}$$

$$D = D_{zz} - \frac{1}{2}D_{xx} - \frac{1}{2}D_{yy}; \;\; E = \frac{1}{2}(D_{xx} - D_{yy}) \tag{A.7}$$

The term in Eq.A.6 is often presented as $\hat{\mathcal{H}}_{ZFS}$ where ZFS stands for *Zero-Field Splitting*. Indeed, because this contribution does not depend on the applied magnetic field, electron level splitting always arises at zero-field.

The D parameter in the equation is equal to zero if all the components of **D** are equal (cubic symmetry). When $D_{xx} = D_{yy}$, the system has an axial symmetry and, as a result, the spin doublets having the same absolute value of M_S split in energy because of $D\hat{S}_z^2$. Furthermore, when $D_{xx} \neq D_{yy} \neq D_{zz}$, a rhombic symmetry is present. Therefore, the inclusion of a non-zero E results in a loss of degeneracy of doublets if S is an integer (non-Kramers' ions), while it does not affect degeneracy for half-integer values of S (Kramers' ions) [68].

The effect of the crystal field on the energy scheme of open-shell systems can often be represented by adopting the mentioned formalism. However, in many cases, it is not a good approximation when symmetry requirements are not fulfilled or when spin-orbit coupling cannot be neglected (e.g., for lanthanide ions). Even if this possibility may occur, the latter case will not be presented in this appendix because it is very lowly treated in this thesis work. Specific cases will be treated in detail in the opportune sections.

Just as the electrons systems with higher spin multiplicity require a new term to be introduced, a term like $\hat{\mathcal{H}}_{CF}$ can be introduced within the spin Hamiltonian (Eq.A.8) when the nuclear spin multiplicity is higher than two. The nuclear quadrupole interaction described by **Q** results in a zero-field splitting of nuclear levels in analogy to the electronic states mentioned before.

$$\hat{\mathcal{H}}_{NQ} = \hat{I} \cdot \mathbf{Q} \cdot \hat{I} \tag{A.8}$$

The Q matrix can be thus opportunely diagonalized, and the resulting tensor is a traceless tensor with components: Q_{xx}, Q_{yy}, and Q_{zz} fulfilling the relation $Q_{xx} + Q_{yy} + Q_{zz} = 0$.

At this point, the total spin Hamiltonian operating on the electronic states will be:

$$\hat{\mathcal{H}}_S = -\mu_N \mathbf{g}_\mathrm{N} \cdot \vec{B} \cdot \hat{I} + \mu_B \mathbf{g} \cdot \vec{B} \cdot \hat{S} + \hat{I} \cdot \mathbf{Q} \cdot \hat{I} + \hat{S} \cdot \mathbf{D} \cdot \hat{S} + \hat{S} \cdot \mathbf{A} \cdot \hat{I} \qquad \text{(A.9)}$$

The reported $\hat{\mathcal{H}}_S$ represents well the energy levels scheme of a spin system only if interactions among different electron spins are excluded. Indeed, when a pair of interacting spins is included in the model, such an interaction can be introduced within the spin Hamiltonian by adding a new term (Eq.A.10) [154].

$$\hat{\mathcal{H}}_{Exch} = \hat{S}_1 \cdot \mathbf{J_{12}} \cdot \hat{S}_2 \qquad \text{(A.10)}$$

In this equation, $\hat{S}_1$ and $\hat{S}_2$ are the spin operators for the electrons on centers 1 and 2, respectively. $\mathbf{J_{12}}$ is the electron-electron coupling tensor, which can be conveniently decomposed and rewritten as a sum of three different contributions as follows:

$$\hat{\mathcal{H}}_{Exch} = J_{12}\hat{S}_1 \cdot \hat{S}_2 + \hat{S}_1 \cdot \mathbf{D_{12}} \cdot \hat{S}_2 + \vec{d}_{12}\hat{S}_1 \times \hat{S}_2 \qquad \text{(A.11)}$$

where J_{12} is a scalar, $\mathbf{D_{12}}$ a traceless symmetric tensor, and $\vec{d}_{12}$ a polar vector. The first term is the isotropic, or Heisenberg, exchange interaction term, the second is the anisotropic exchange interaction term, and the third is the antisymmetric exchange interaction term. Briefly, the first interaction tends to align spins, while the second and third ones force the spins to be aligned on a preferred orientation or canted by 90°, respectively. Moreover, we will refer to a *ferromagnetic* exchange interaction when the first term results in a parallel alignment of the two spins or an *antiferromagnetic* exchange interaction when it results in an antiparallel alignment. Therefore, the sign of J_{12} identifies the interaction type among spins.

It must be stressed here that the interaction described in Eq.A.11 can spread through space or chemical bonds [154]. In the former case, the overall interaction can be treated as a simple dipole-dipole one, scaling as the third power of the distance between the spins. In the latter case, the interaction type depends strictly on the electronic properties and the orbital' overlap of metals and ligands.

A.2 Magnetometry

In the previous section, we presented the spin Hamiltonian as a fundamental tool to unveil the microscopic origin of the magnetic properties of a sample. At the same time, when we need to characterize the magnetic response of a compound with respect to the intensity of the magnetic field applied or to the temperature, we use two principal quantities, namely the magnetization ($\vec{M}$) and the magnetic susceptibility (χ). Here, a summary of the basic theoretical knowledge and experimental techniques is presented. For a more detailed explanation of them, we address the reader to more specialized literature [228−230].

Let us take as an example a two-level system such as that of a $S = 1/2$. The magnetic moment associated to a single electron as a function of the field $\vec{H}$ will be given by the relation: $\vec{\mu}_j = \left(-\frac{\partial E}{\partial H_j}\right)\hat{e}_j$, where j is a generic component. Because the magnetization is given by the sum over the whole set of magnetic moments present within the sample, for a statistic ensemble of spins the mean value of $\vec{M}$ expressed in cm^3 mol^{-1} G is given by the relation [228]:

$$\langle M \rangle = N_A \frac{\sum_{n=1}^{N} -\frac{\partial E_n}{\partial H} e^{-\frac{E_n}{k_B T}}}{\sum_{n=1}^{N} e^{-\frac{E_n}{k_B T}}} \tag{A.12}$$

where N_A is the Avogadro’s number, *n* is the *n*-th state of the system, and k_B is the Boltzmann constant.

For the sake of clarity, a magnetic sample may behave differently when exposed to a magnetic field, depending on its chemical/physical properties. For instance, the application of a magnetic field along with the *x* molecular direction (in the molecular reference frame) could affect the magnetic properties differently from what can be observed when applied along with the *z* molecular axis (see the previous section). If we consider one mole of a sample experiencing a magnetic field of strength *H*, the relation between $\vec{M}$ and $\vec{H}$ is given by the magnetic susceptibility tensor (Eq.A.13):

$$\chi_{ij} = \frac{\partial M_i}{\partial H_j} \tag{A.13}$$

Which strictly depends on the nature of the sample. For instance, the magnetic susceptibility of a coordination compound may depend on the electronic configuration of the metal ion, the nature of the ligand, and the coordination geometry. However, the anisotropy of χ can be probed only on oriented crystals. In this thesis, we always refer to powder samples, for which the magnetic susceptibility collected is a mean value mediated over the statistical orientation of crystallites within the sample. We can hence refer to a simple constant value χ hereafter.

Because the susceptibility is always given by the sum of two contributions: $\chi = \chi^D + \chi^P$, i.e., the diamagnetic and paramagnetic susceptibilities. We will refer to a paramagnetic or diamagnetic material depending on which of these quantities predominates. Furthermore, the magnetic susceptibility of a system can be conveniently rewritten (under opportune considerations) by employing the well-known Curie's equation (Eq.A.14).

$$\chi = \frac{N_A g_e^2 \mu_N^2}{3k_B T} S(S+1) \tag{A.14}$$

Such an equation resembles the behavior of an ideal paramagnet and is only valid in the limit of $H/k_B T << 1$. It follows that, in this limit, any paramagnetic material should be characterized by a characteristic value of the product χT (e.g., for a $S = 1/2$, the ideal χT value is of 0.375 $\mathrm{cm^3\ mol^{-1}\ K}$). Any deviation from this ideal behavior may arise from a different microscopic origin. As an example, strong deviations from this law are usually observed for ferromagnetic and antiferromagnetic materials [228].

During this work, we use to refer to two main techniques aimed at investigating these quantities, i.e., the direct current (dc) magnetometry or the alternate current (ac) susceptometry. These two techniques share a crucial working principle, i.e., they are both inductive methods (or flowmetry-based methods). In this respect, the working procedure requires a sample to be introduced within a cryogenic apparatus capable of reaching $1.8 - 1.9$ K thanks to a He cryostat. Thus, a static magnetic field can be applied to the sample by employing a superconductive magnet flooded by liquid helium in a chamber external to sample one. The sample is made sliding within the sample space along the axis of pick-up coils (first- or second-order gradiometers, depending on the instrumental setup). According to Faraday's law, the signal is generated by the induction of a current within the coils. Therefore, it is collected and converted to the relative magnetization value.

In modern apparatus, these pick-up coils are made of superconductive materials, and they may be coupled to an auxiliary device, external to the sample-space, known as SQUID (Superconductive Quantum Interference Device). This setup has been employed during this work to perform dc magnetization measurements. In particular, we adopted a *Quantum Design Magnetic Properties Measurement System* (MPMS).

While dc magnetometry works as described above, ac susceptometry requires a quite different apparatus to be employed. A secondary oscillating field (ac field) is generated by a secondary set of coils coaxial to the pick-up coils, while the sample is held in position. The general expression accounting for the time evolution of this field can be expressed as: $h(t) = hcos(2\pi\nu t) = hcos(\omega t)$, where h is the amplitude of the oscillating field, ν is the operational frequency, and $\omega = 2\pi\nu$.

This ac field has the primary role of inducing of producing the magnetic flux changes detected by the pick-up coils. Moreover, it properly serves as a modulating field to probe the dynamical equilibrium existing among the spin populations of magnetic states. Therefore, it is possible to collect the true susceptibility of a sample directly as the derivative of $\vec{M}$ with respect to the field $\vec{H}$ (Eq.A.13). A representative graph showing the difference between the susceptibility values extracted with dc and ac techniques is reported in Fig.A.2.

The employed oscillating field can span a wide frequency range, typically from 0.1 Hz to 10 kHz. Its amplitude is usually smaller than that of the static magnetic field. In the measurement apparatus mainly employed during this work, a Quantum Design PPMS, the value of h can reach a maximum of 10 Oe.

When the oscillating field is applied to the sample, a time-dependent term accounting for the oscillation sums to the total magnetization relying on the equation [229]:

$$\begin{aligned} M(t) &= M_0 + Re\{[(\chi' - i\chi'')He^{i\omega t}]\} \\ &= M_0 + H(\chi' \cos(\omega t) + i\chi'' \sin(\omega t)) \end{aligned} \tag{A.15}$$

Where χ' and χ'' are the susceptibility's real and imaginary components, respectively. When the χ'' value is maximum, the ac susceptibility is maximally

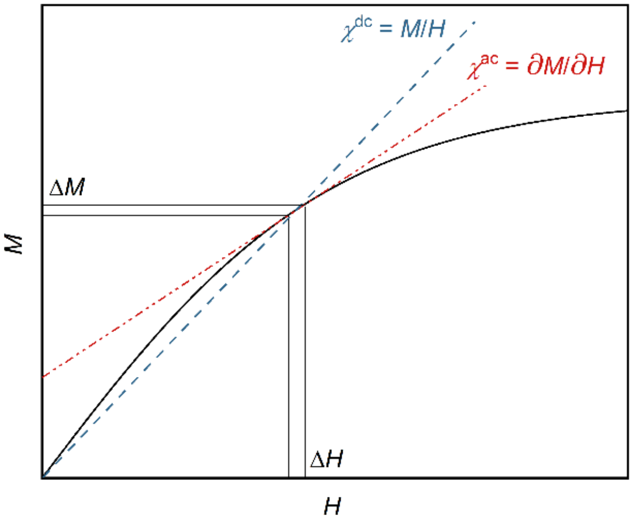

Figure A.2. Plot of *M* vs *H* reporting a representative illustration of the difference between the magnetic susceptibility extracted from ac measurements (χ^{ac}) and that one extracted from dc magnetometry (χ^{dc}).

out of phase with respect to the oscillating field, and we can observe the relaxation of the magnetization. Otherwise, when $\chi'' = 0$ we are probing the isothermal (χ_T) and adiabatic (χ_S) susceptibility regimes of our system.

The obtained experimental data for χ' nd χ'' can be fitted by adopting the phenomenological model [231, 232]:

$$\chi'(\omega) = \chi_S + (\chi_T - \chi_S)\frac{1 + (\omega\tau)^{1-\alpha}\sin\left(\frac{\pi\alpha}{2}\right)}{1 + 2(\omega\tau)^{1-\alpha}\sin\left(\frac{\pi\alpha}{2}\right) + (\omega\tau)^{2-2\alpha}} \tag{A.16}$$

$$\chi''(\omega) = (\chi_T - \chi_S)\frac{1 + (\omega\tau)^{1-\alpha}\cos\left(\frac{\pi\alpha}{2}\right)}{1 + 2(\omega\tau)^{1-\alpha}\sin\left(\frac{\pi\alpha}{2}\right) + (\omega\tau)^{2-2\alpha}} \tag{A.17}$$

In the equations above, α is a parameter limited between 0 and 1, which can be taken as the full width at half maximum of the χ'' distributions. The maximum of the imaginary component and the flex-point of the real component coincides with the center of the distribution at ω_{max}. This coordinate is thus directly correlated to a characteristic relaxation time for the magnetization (τ), according to the relation: $\omega_{max} = 2\pi/\tau$.

A.3 Electron Paramagnetic Resonance

The electron paramagnetic resonance (EPR) spectroscopy detects electromagnetic radiation absorption when an external magnetic field is applied. Radiation absorption emerges when the energy of an external electromagnetic field matches that of the splitting between the electronic levels. For instance, let us consider a $S = 1/2$ with an isotropic value of the g-tensor reported as g_{eff}. It is sensible to observe the splitting of the M_S levels due to the Zeeman interaction (Eq.A.1). In this case, a spin transition will be observed when the energy of the applied radiation matches ΔE among the fundamental and excited states, so that:

$$h\nu = \mu_B g_{eff} B_0 \tag{A.18}$$

Therefore, the characteristic absorption spectrum of a given compound is strictly correlated to the composition of the energy states and to the microscopic magnetic properties of the system. The importance of this technique in obtaining information on the spin Hamiltonian parameters and spin relaxation properties is remarkable.

Two main setups can be adopted to investigate the static and dynamic properties of a spin system. In the first case, we refer to continuous-wave EPR (cw-EPR) when the experimental setup causes a sample to undergo a spin transition when microwave radiation is applied continuously in time. In the second case, we refer to pulsed EPR when the microwave radiation is applied for a very short time. While the former is more indicated to investigate the static magnetic property of a magnetic system, the latter provides a more powerful tool to investigate dynamic properties and electron-electron or electron-nuclear correlations within the sample.

A.3.1 Continuous Wave EPR Spectroscopy

In the series of presented works, cw-EPR spectroscopy has been widely employed to investigate potential qubit static magnetic properties. Indeed, the extrapolation of spin Hamiltonian parameters was possible thanks to simulations of experimental spectra with the Easyspin software [146]. Furthermore, the technique was also employed as a powerful tool to get information on the coordination geometry of investigated compounds.

The EPR measurement can be performed on solid (powders or crystals) and liquid samples containing magnetic species. The probed sample undergoes a spin transition due to the application of an oscillating magnetic field of microwave radiation ($\vec{B}_1$) when a static magnetic field ($\vec{B}_0$) is applied. Commonly, the direction of application of $\vec{B}_1$ is perpendicular to that of $\vec{B}_0$. In this case, the observed spin transitions due to the absorption of a quantum wave-packet are those following the selection rules $\Delta M_S = \pm 1$ and $\Delta M_I = 0$. Depending on the application geometry of B_1, i.e., parallel or perpendicular with respect to the direction of B_0, we may observe different transitions such as those fulfilling $\Delta M_S = \pm 1$ and $\Delta M_I = \pm 1$. The complexity of the spectrum is then related to several factors, such as the anisotropy of $\mathbf{g}$, the presence of a hyperfine coupling interaction, the spin multiplicity, and the presence of dipolar or exchange coupling interaction.

The experimental setup mainly employed in the presented works operates by sweeping the static field while an electromagnetic field working at a fixed microwave frequency is continuously applied to the sample. For instance, the main employed frequencies were the X-Band (9.4 GHz) and the Q-Band (33.4 GHz). Furthermore, because the relaxation properties of potential qubits strictly depend on the working temperature (see Chap.3), measurements were performed adopting a cryostat working at the liquid helium temperatures (down to 5 K). The lowering of temperature also allows getting a frozen solution of paramagnetic species, whose signals are exactly mediated on the molecular orientation distribution as for powder samples. A representative sketch of the instrumental setup is reported in Fig.A.3.

The oscillating field $\vec{B}_1$ is generated by a Gunn diode and then attenuated by an electronic attenuator. The microwave frequency is split and sent to i) a reference arm and ii) to the cavity (where the sample resides) through waveguides. The output signal thus goes back through the waveguides and is collected by the phase-sensitive detector (PSD). Additionally, a smaller oscillating field (100 kHz) is employed as modulating field to collect the signal directly as the derivative (1st Harmonic) of the absorption one (0 Harmonic).

The intensity of the EPR signal is thus proportional to the transition probability among spin states due to the radiation absorption. If considering a simple two-level system with a total $S = 1/2$, the transition probability among the $M_S = \pm 1/2$ states (W) depends on the square module of the perturbation matrix (following the Fermi's golden rule), and it can be expressed through the general relation: $W \propto |\langle\alpha|\mu B_1|\beta\rangle|^2$.

Several examples of how spectra look or how they can be rationalized by employing the spin Hamiltonian formalism are reported in detail within the main chapters of this work.

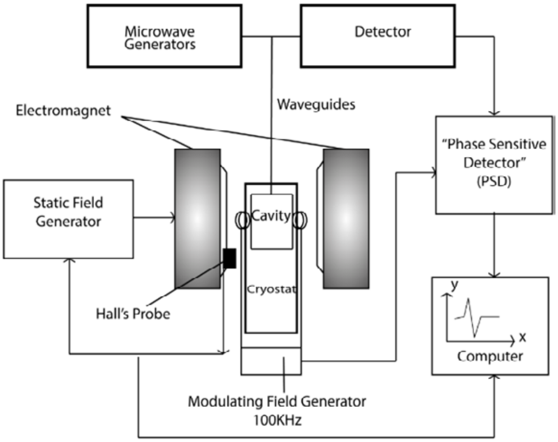

Figure A.3. Representative sketch of a cw-EPR experimental setup.

A.3.2 Pulsed EPR Spectroscopy

In the previous section dedicated to the cw-EPR technique, we outlined some basic concepts of EPR spectroscopy. Here, we will introduce some different basic concepts of pulsed EPR. Indeed, just as the cw-EPR, the pulsed EPR technique probe the absorption of microwave radiation by a magnetic sample when a static magnetic field is applied. Contrarily to the cw case, the spin transition is caused by applying a short electromagnetic pulse while the static magnetic field intensity (B_0) is kept constant. Employing a short pulse results in the application of a wide range of frequencies around a mean value [62].

In more convenient way of representing the overall process, let us consider a magnetic compound with a total $S = 1/2$ experiencing an external field B_0, that is conventionally applied along the z axis of the laboratory framework. The static magnetic field causes the M_S states splitting, as reported in Fig.A.1. The spin population will be distributed among the $|\alpha\rangle$ or $|\beta\rangle$ states depending on the system thermal energy at the given B_0. From the point of view of the single magnetic dipole associated with one of the M_S states, the Zeeman interaction causes it to precess around the z axis with a characteristic frequency known as the Larmor frequency: $\omega_L = \frac{\mu_B g_e}{h} S_z B_z^0$ (Fig.A.4). The resulting magnetization of the sample will be aligned with the z axis, and the major component is defined by the population difference between the two states.

When an oscillating and linearly polarized field $\vec{B}_1(\omega, t)$, with $\omega = \omega_L$, is applied on the xy plane of the reference framework, the magnetization $\vec{M}_z$ is tilted by an angle α depending by the application time as:

$$\alpha = \gamma B_1 t \tag{A.19}$$

Where γ is the characteristic gyromagnetic ratio of the spin system, B_1 is the amplitude of the oscillating field, and t is the application time of the electromagnetic pulse. In the simplest case, t is tuned to project $\vec{M}_z$ on the xy plane (i.e, $\alpha = \pi/2$), so that we are forcing the spin population of the low-lying state $M_S = -1/2$ to undergo a transition to the high-energy state $M_S = 1/2$, fulfilling the relation in Eq.1.11. In particular, when the direction of $\vec{B}_1(\omega, t)$ is set parallel x axes, $\vec{M}_z$ is projected onto the $\vec{M}_y$ component. From the point of view of magnetic dipoles, the process mentioned in Chap.1, Fig.1.4, well depicts the mentioned mechanism. Thus, after the excitation, the system returns to equilibrium through spin-lattice and spin-spin relaxation processes as explained in Chap.3.

From an instrumental point of view, the pick-up coils commonly lay on the xy plane, where the signal is detected. Because of the phase loss due to decoherence processes, the detected signal decays exponentially depending on the characteristic coherence time of the spin system T_2. At first instance, the obtained signal is a convolution of sine, cosine and exponential functions called *Free Induction Decay*, or FID.

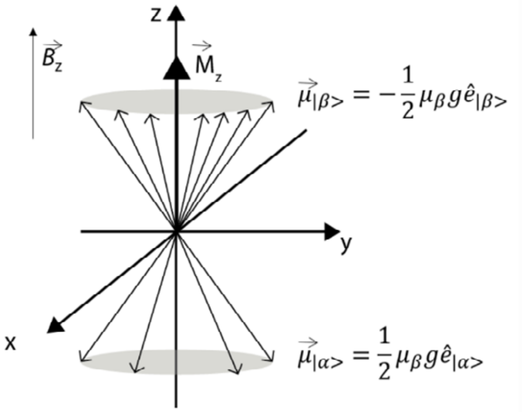

Figure A.4. Pictorial representation of precession motion of magnetic dipoles μ_α and μ_β along the quantization axis set by B_z. The resulting magnetization M_z is given by the sum of the single magnetic moments.

The complete scheme of the overall process is reported in Fig.A.5 adopting the Bloch sphere representation presented for qubits in Chap.1.

The pulsed EPR technique has been widely employed as a probe for the spin relaxation mechanism. Indeed, such a technique guarantees a large sensibility to the spin dynamics of the system. As an example, the value of T_2 can be, in principle, extracted from the line width magnitude of standard cw-EPR spectra but only if field inhomogeneity due to the sample or the instrument are avoided (*i.e.* an ideal case). The coherence time of a molecular sample can be more conveniently investigated by employing a series of pulses known as Hahn Echo, which probes the variation of the electron echo intensity as a function of the delay time between a first $\pi/2$ pulse and π pulse. Similarly, the spin-lattice relaxation time T_1 can be obtained from pulse sequences such as *inversion recovery* or *echo saturation by fast repetition experiments*. A more detailed explanation of these techniques can be found in [62], while a representative sketch of the mentioned pulse sequences is reported in Fig.A.6.

As mentioned before, the pulsed EPR technique is a useful tool for the investigation of the relaxation properties of a spin ensemble, but it could also outline several magnetic properties arising from the electron-electron or electron-nuclear correlations within a sample. Indeed, in this work of thesis, *ad-hoc* designed pulse-sequences were employed for this purpose. For instance, *HYSCORE* and *DEER* (Double Electron-Electron Resonance) experiments were employed to unveil hyperfine coupling interactions and electron-electron coupling interactions in the works reported in Chap.4 Sec.4.2 and Chap.6 Sec.6.2, respectively.

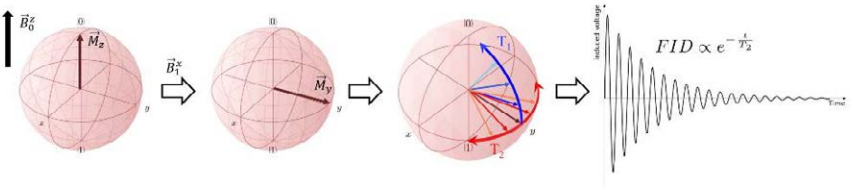

Figure A.5. Pictorial representation of the overall process described in the text for a S = 1/2 system. From left to the right i) the application of $\vec{B}_z^0$ gives rise to $\vec{M}_z$; ii) $\vec{M}_z$ is projected onto the *xy* plane by the application of $\vec{B}_x^1$; iii) free induction decay signal collected for a general spin ensemble. The Bloch sphere representation is obtained by adopting the QuTIP software [65].

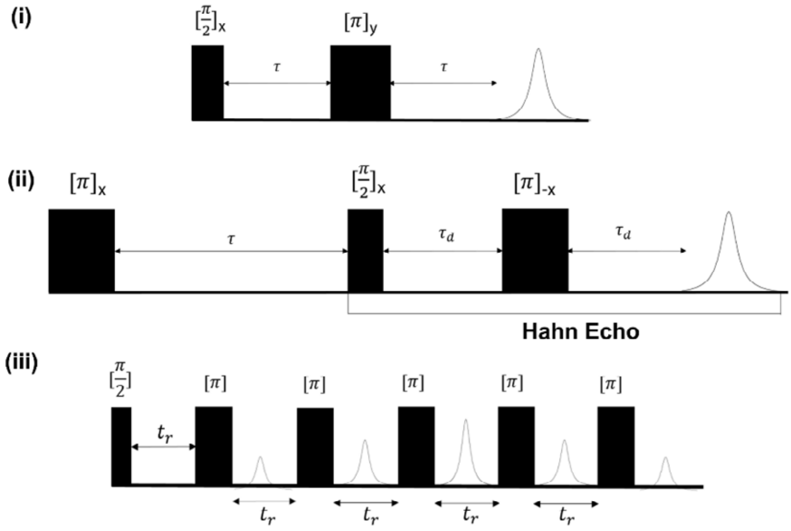

Figure A.6. Pictorial representation of pulse sequences mentioned in the text. From the top to the bottom: i) Hahn Echo experiment; ii) inversion recovery experiment; iii) echo saturation by fast repetition experiment. In the picture, all the pulses are represented as black rectangles of different widths depending on the pulse duration. The other parameters τ, τ_D, and t_r are the employed delay times.

Appendix B.
Supplementary material from published results

B.1 Section 4.1: [Cu(TTDPz)]

B.1.1 PXRD analysis

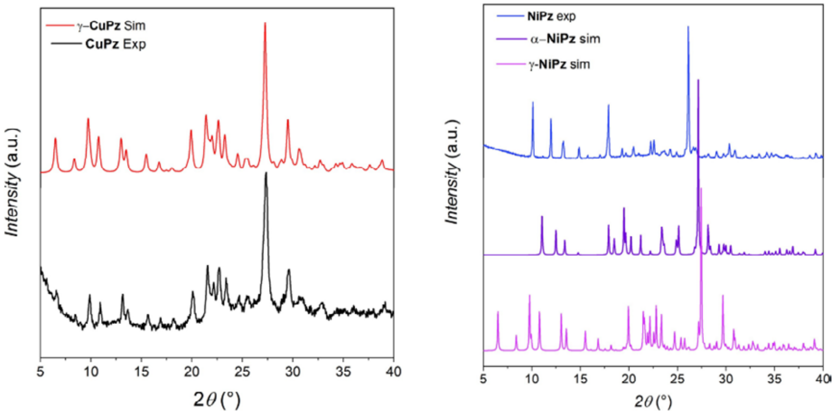

Figure B.1. On the left, experimental and simulated PXRD patterns of **CuPz**. The pattern of the polycrystalline sample resembles that simulated from the crystal structure of the γ polymorph [141]. On the right, experimental and simulated PXRD patterns of **NiPz**. The pattern of the polycrystalline sample is slightly different from that simulated from the crystal structure of the α polymorph [141].

Fabio Santanni, University of Florence, Italy, santannifabio@gmail.com, 0000-0002-0506-8333

Referee List (DOI 10.36253/fup_referee_list)
FUP Best Practice in Scholarly Publishing (DOI 10.36253/fup_best_practice)

Fabio Santanni, *Molecular approaches for quantum technologies. Optimization of electron spin-based quantum bits and quantum logic gates*, © 2025 Author(s), CC BY 4.0, published by Firenze University Press, ISBN 979-12-215-0670-9, DOI 10.36253/979-12-215-0670-9

B.1.2 DC magnetometry

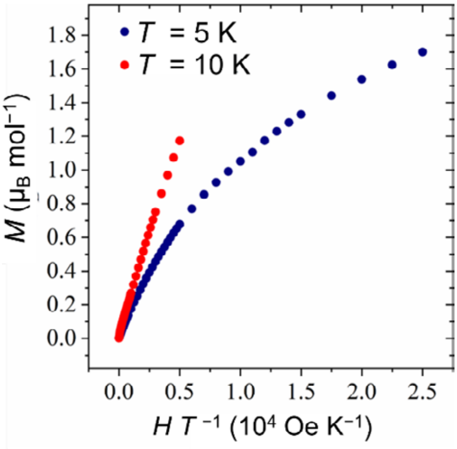

Figure B.2. Experimental magnetization curves M obtained at *T* = 2 K (blue circles) and *T* = 10 K (red circles) on a **NiPz** sample after treatment with CH_3SO_3H. The M values are reported as a function of B/T and rescaled to molar values by considering a concentration of *S* = 1 impurity of about 0.25%.

B.1.3 X-band CW-EPR

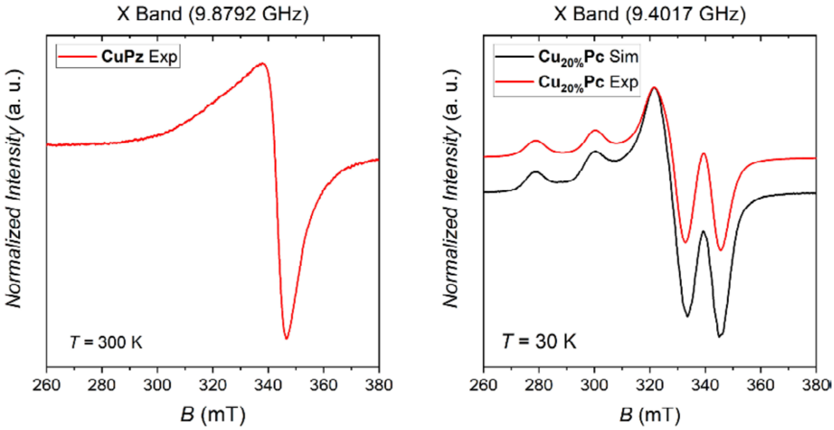

Figure B.3. Experimental CW-EPR spectra at the X-band frequency collected on **CuPz** and **Cu20%Pz** powders. The simulation of **Cu20%Pz** spectrum was implemented adopting the following parameters: $g_{\perp} = 2.050(1)$, $g_{\parallel} = 2.175(1)$, $A_{\perp} = 75(4)$ MHz, $A_{\parallel} = 624(2)$ MHz.

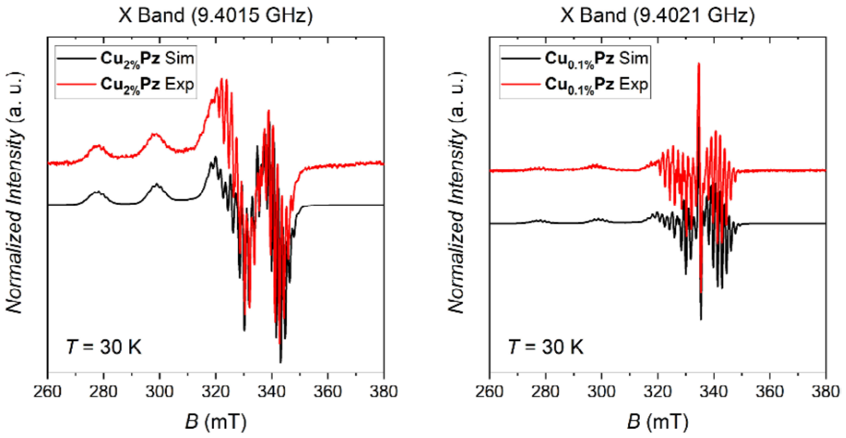

Figure B.4. Experimental CW-EPR spectra at the X-band frequency collected on **$Cu_{2\%}$Pz** and **$Cu_{0.1\%}$Pz** powders. Simulated curves obtained by employing the SH parameters of Table 4.1 (see Sec.4.1) are reported within the same plots.

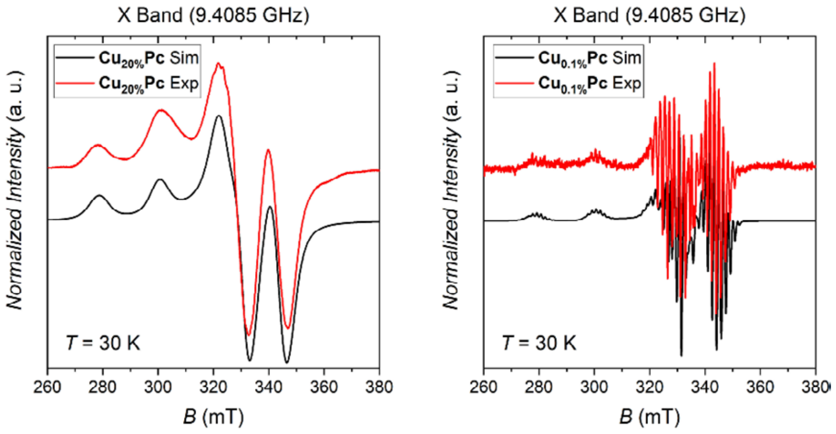

Figure B.5. Experimental CW-EPR spectra at the X-band frequency collected on **$Cu_{20\%}$Pc** and **$Cu_{0.1\%}$Pc** powders. Simulated curves obtained by employing the SH parameters of Table 4.1 (see Sec.4.1 and [147]) are reported within the same plots.

B.1.4 Q-band EDFS in D_2SO_4 solution

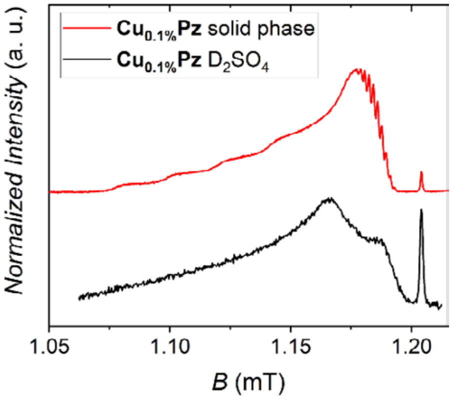

Figure B.6. Comparison between EDFS spectra obtained on a powder sample of **Cu$_{0.1\%}$Pz** and on a frozen solution of **CuPz** in D_2SO_4 at the same concentration. The major differences consist of a higher concentration of the radical fraction and a shift of the perpendicular component in D_2SO_4. Both highlight a possible degradation of the sample undergoing in this medium. The two spectra were collected at different frequencies and rescaled before plotting using the radical signal as an internal reference ($\nu^{Froz} = 33.68$ GHz; $\nu^{pwd} = 33.75$ GHz).

B.1.5 Fitting of T_1 and analysis of optical modes' contributions

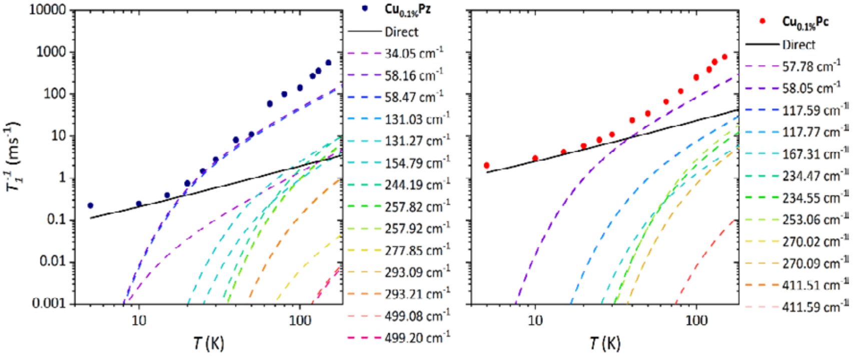

Figure B.7. Plots of experimental T_1^{-1} data of **Cu$_{0.1\%}$Pz** (left) and **Cu$_{0.1\%}$Pc** (right) reported together with the simulated curves of direct and Raman contributions to the spin-lattice relaxation. The curves are obtained by considering the a_{dir} and a_{Ram} values reported in Table 4.2. Each Raman contribution is simulated by employing the energy of one of the most active modes which are reported in legends.

B.2 Section 4.3: Dyacac

B.2.1 AC susceptometry

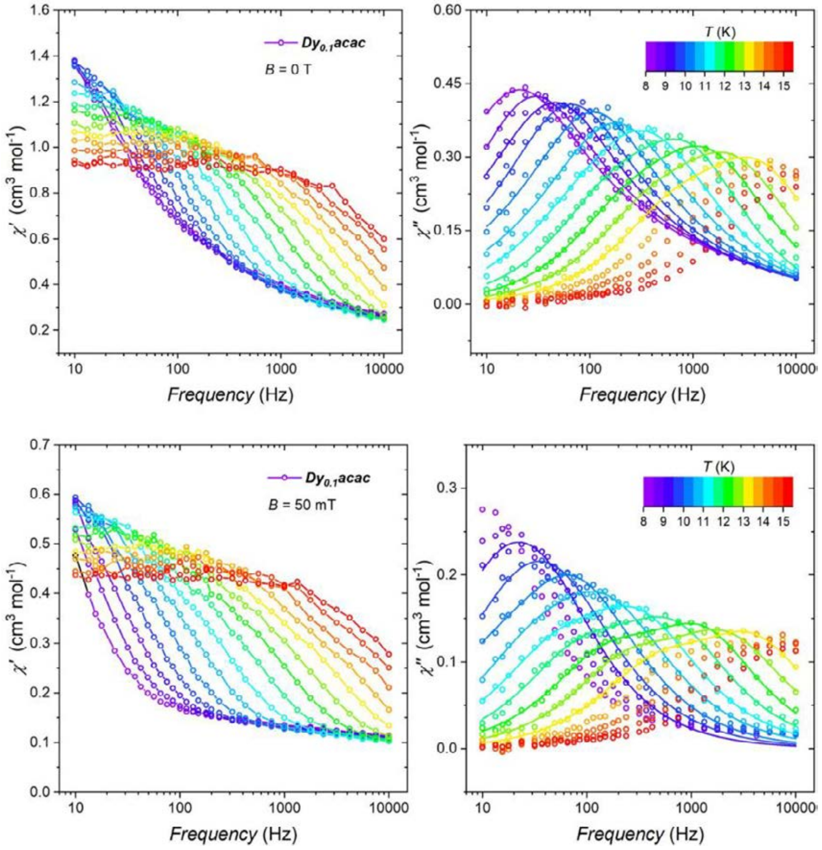

Figure B.8. Plots of χ' and χ'' components of AC susceptibility as a function of the frequency of the AC field. The values of the two components were extracted from measurements at B = 0T (top) and B = 50 mT (bottom). The fits obtained by employing Eq.A.17 extended for two contributions are reported as solid lines on the plot of χ''.

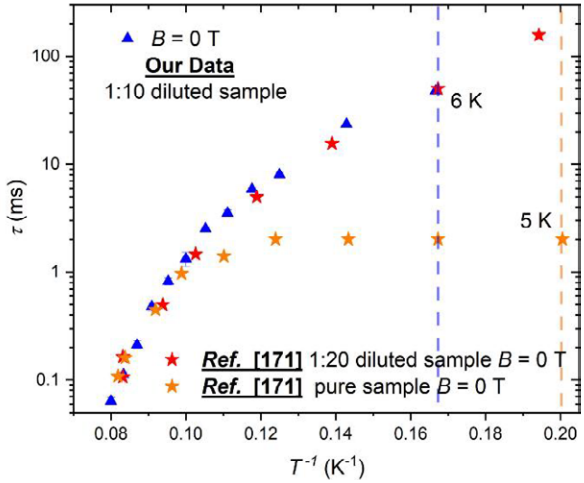

Figure B.9. Comparison between our experimental τ values and those extracted from [171].

B.2.2 Computed Raman transition rates

The following treatment is extracted from the paper. The Raman rate for the transition among two spin levels a and b is modelled with the expression:

$$W_{ba}^{2-ph} = \frac{2\pi}{\hbar^2} \sum_{\alpha\beta} \left| \sum_{c} \frac{\langle b|\hat{V}_\alpha|c\rangle\langle c|\hat{V}_\beta|b\rangle}{E_c - E_a \pm \hbar\omega_\beta} \right|^2 G_{\pm}^{2-ph}(\omega_{ba}, \omega_\alpha, \omega_\beta) \qquad \text{(B.1)}$$

Where, $\hat{V}_\alpha = \sum_{lm}(\partial B_m^l/\partial q_\alpha)\hat{O}_m^l$ describes the effects of the adsorbed or emitted α lattice vibration on $\hat{\mathcal{H}}_{CF}$, and $\hat{V}_\beta$ accounts for the same effect of the second adsorbed or emitted phonon; c is a generic excited spin state contributing to the Raman relaxation process; $G_{\pm}^{2-ph}$ accounts for the thermal populations of phonons and imposes the conservation of energy. For instance, the emission of a phonon q_α and the absorption of a phonon q_β contribute to $2G_{\pm}^{2-ph}$ as:

$$G_{\pm}^{2-ph}(\omega_{ba}, \omega_\alpha, \omega_\beta) = \delta(\omega_{ba} - \omega_\alpha + \omega_\beta)\bar{n}_\beta(\bar{n}_\alpha + 1) \qquad \text{(B.2)}$$

Where $\bar{\bar{n}}_\beta = [\exp{(\hbar\omega_\beta/k_B T)}$ (the analogue expression can be written for $\bar{n}_\alpha$) is the Bose-Einstein distribution of thermal population.

B.2.3 Computed SPC coefficients and electric dipoles resolved by atomic site.

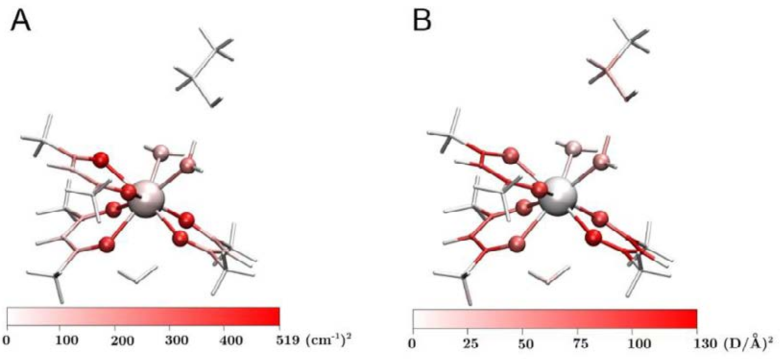

Figure B.10. a) Magnitude of the spin-phonon coupling coefficients resolved by atomic site. b) Magnitude of the first derivative of electric dipole resolved by atomic site. The module of the derivative for Dy has been set to zero.

B.3 Section 5.1: [VO(TPP)] on Coplanar Resonator

B.3.1 Experimental Setup

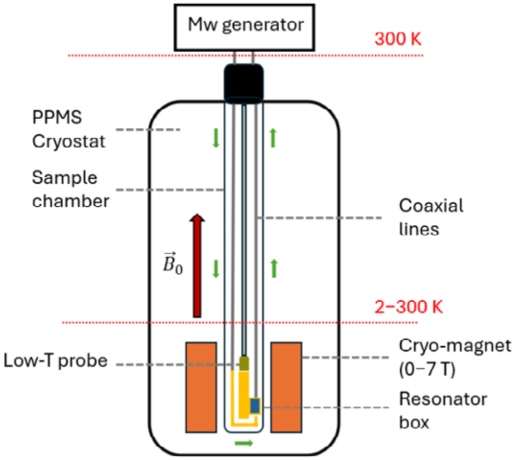

Figure B.11. Sketch of the setup developed in [233] and used for measurements in this work. Green arrows represent microwave paths along the waveguides. Then, microwaves are sent to the sample on the superconductive resonator (resonator box), thanks to antennas.

B.3.2 CW- and pulsed EPR on polycrystalline sample

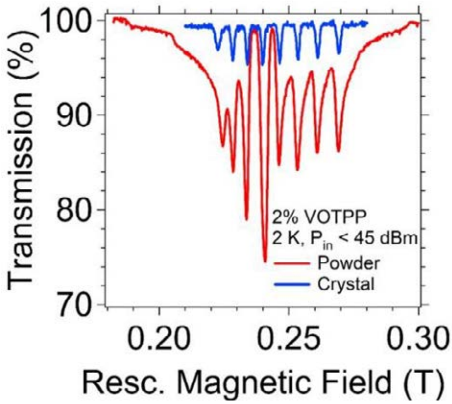

Figure B.12. Comparison between the CW transmission spectra of the **VO2%TPP** polycrystalline and crystal samples at 2 K.

The simulation of the experimental spectrum was performed considering a phenomenological Voigtian broadening composed of Gaussian and Lorentzian line shapes. In particular, the best simulation is obtained by setting a G-FWHM of 1.6 mT and an L-FWHM of 0.3 mT. Furthermore, we considered a distribution probability of the orientation $P(\phi) = exp(-U(\phi))$ with $U(\phi) = (3cos(2\phi) - 1)/2$, where ϕ is the angle between the molecular z axis and the static magnetic field. We had to introduce such a model for considering an incomplete powder averaging suggested by the anomalous intensity of perpendicular type transitions.

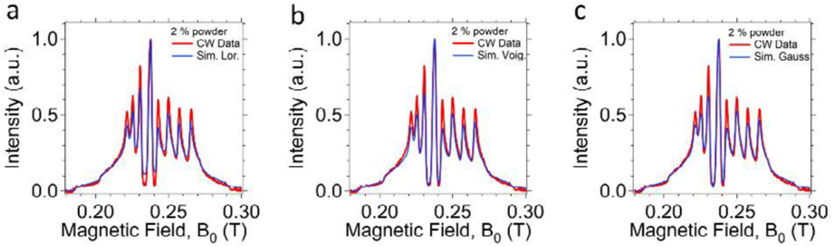

Figure B.13. The three plots report the comparison between the simulations for experimental CW transmission intensity of the **VO2%TPP** polycrystalline sample obtained by considering: a) only Lorentzian line shape only; b) Voigtian line shape; c) Gaussian line shape only. The FWHM set is that reported in the text.

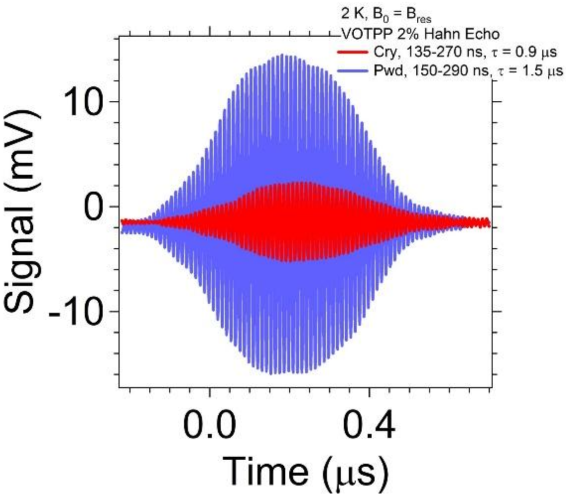

Figure B.14. Comparison between the echo signals obtained from the powder and the crystal samples of **VO2%TPP**.

Appendix C
Additional synthetic procedures and experimental results

C.1 Section 4.2: [Cu(dttt)$_2$]

C.1.1 Experimental TBAdttt

All the employed chemicals were of reagent grade. Anhydrous CH_2Cl_2 was purchased from ACROS organics^{TM} (99.9%, Extra Dry, AcroSeal^{TM}). Acetone was dried on molecular sieves (4 Å, preactivated in an oven at 300 °C under N_2) and distilled before use. SO_2Cl_2 was distilled before using to remove yellowish impurities. NEt_3 was dried on KOH, decanted, and distilled from Zn dust. All the other chemicals were employed without further purification. All the operations, except those involving the isolation of TBAdttt, were conducted under an inert atmosphere of N_2 by employing standard Schlenk techniques.

Synthesis of S,S'-ethane-1,2-diyl-diethanethioate (**a**). The synthetic procedure was adapted from [151]. Potassium thioacetate (40 g, 350 mmol) is added under N_2 to a stirred solution of 1,2-dibromoethane (33 g, 175 mmol) in freshly distilled acetone (800 mL). The solution is left to stir 24 h and kept at room temperature under N_2. As the reaction proceeds, a white precipitate forms out from the solution, and the color turns yellow/orange. The reaction mixture is thus poured onto 1.2 L of deionized H_2O, and the target compound is repetitively extracted with CH_2Cl_2 (1.5 L). All the fractions were collected and dried over $MgSO_4$. After the solvent was removed under reduced pressure, a brownish solid was obtained. The crude product was purified by flash column chromatography on SiO_2 adopting a mixture

Fabio Santanni, University of Florence, Italy, santannifabio@gmail.com, 0000-0002-0506-8333

Referee List (DOI 10.36253/fup_referee_list)
FUP Best Practice in Scholarly Publishing (DOI 10.36253/fup_best_practice)
Fabio Santanni, *Molecular approaches for quantum technologies. Optimization of electron spin-based quantum bits and quantum logic gates*, © 2025 Author(s), CC BY 4.0, published by Firenze University Press, ISBN 979-12-215-0670-9, DOI 10.36253/979-12-215-0670-9

of CH_2Cl_2/Hex 1:1. The whole process yielded 40 g of pure product as a pale yellow crystalline solid upon solvent removal. Yield: 65 %. ^{1}H-NMR (400 MHz, $CDCl_3$): δ (ppm) = 2.35 (s, 6H), 3.05 (s, 4H).

Synthesis of ethane-1,2-disulfenyl chloride (**b**). The synthesis of this compound has been extracted from [152]. Compound **a** (11 g, 62 mmol) was added to 100 mL of CH_2Cl_2 kept under nitrogen in a Schlenk flask. Some previously distilled SO_2Cl_2 (10 mL, 123 mmol) was thus added dropwise to the stirred solution. The reaction mixture was left to stir for 2 hours at RT, under N_2, and in the dark. The reaction was checked via ^{1}H-NMR until signals at 2.35 ppm have disappeared. The product was not isolated, and the solution was adopted as such for the next synthesis. ^{1}H-NMR (400 MHz, $CDCl_3$): δ (ppm) = 3.57 (s, 4H)

Synthesis of 1,3,2-dithiazolium chloride (**c**). The synthesis was adapted from [150]. Some more CH_2Cl_2 (20 mL) was added to the stirred solution of **b** obtained in the previous step. Trimethylsilylazide (TMSA, 8.6 mL, 65 mmol) was thus cautiously added by adopting a syringe. N_2 forms upon the addition of TMSA, and a yellow solid precipitated from the solution. The mixture was left to stir overnight. The yellow powder was thus filtered, washed abundantly with dichloromethane, and dried in vacuum over KOH. According to [150], the yellow precipitate contains the target compound 1,3,2-dithiazolium chloride and some minor impurities. However, we decided to adopt the obtained powder (8.7 g) as such without further purification.

Synthesis of TBAdttt. The synthesis of TBAdttt was conducted by slightly modifying what has been reported in [148]. Compound **c** (8.7 g, 62 mmol) was introduced into a Schlenk flask and pumped in vacuum for 2 h before the addition of N_2. Anhydrous CH_2Cl_2 (160 mL) was added to the flask, and the mixture was stirred for 15 minutes. Some freshly distilled NEt_3 (17.5 mL, 124 mmol) was slowly added to the solution for 1 h while kept in the dark. The violet mixture was left to react overnight under N_2. The solvent was thus removed under vacuum at RT, and the residual NEt_3 was removed by blowing N_2 overnight. The solid residue was extracted with H_2O (250 mL), filtered, and kept stirring. Tetrabutylammonium bromide (TBABr, 10 g) was then added in portions to the solution until the target product TBAdttt stopped precipitating. Upon filtration and washing with water (10 mL), the overall process yielded 1.68 g of TBAdttt (4.1 mmol) as a pure microcrystalline solid. Total Yield: 13 %. X-ray quality crystals were obtained by slow evaporation of an acetone/toluene solution kept in the dark (Fig.C.1). ^{1}H-NMR (400 MHz, $CDCl_3$): δ (ppm) = 0.99 (t, 12H), 1.40 (m, 8 H), 1.59 (m, 8H), 3.28 (m 8H) EA found (calcd. for $C_{18}H_{36}N_3S_4$): C, 52.65 (52.88); H, 9.49 (8.88); N, 6.94 (6.85) ATR-IR (cm^{-1}): 2960 (m), 2935 (m), 2869 (w), 1486 (m), 1462 (m), 1453 (w), 1422 (vw), 1382 (w), 1195 (s), 1176 (s), 1145 (m), 1107 (vw), 1038 (vs), 926 (s), 880 (s), 809 (w), 736 (vs), 451 (w) (Fig.C.2). UV-Vis (MeOH): λ_{max} = 315 nm, 420 nm, 576 nm (Fig.C.2). PXRD: See Fig.C.1. Unit cell parameters found (extracted from [148]): T = 100 K; a = 8.56 (8.57) Å; b = 12.90 (12.93) Å; c = 20.48 (21.22) Å; α = 90° (90); β = 97° (106); γ = 90° (90); V = 2243 (2259) Å^3; space group: $P2_1$.

C.1.2 Experimental [M(dttt)$_2$]

All the employed chemicals were of reagent grade and used as such without further purification.

Synthesis of [Cu(dttt)$_2$] (**Cudttt**). Compound TBAdttt (200 mg, 0.49 mmol) was added to 10 mL of MeOH and left to stir in the dark. A solution of $CuCl_2 \cdot H_2O$ (42 mg, 0.24 mmol) in MeOH (10 mL) was added dropwise to the ligand solution over 1 h. As soon as the copper(II) salt was added, a black precipitate formed out from the solution. The mixture was left to stir 6 h and then filtered. The precipitate was washed abundantly with H_2O, MeOH, Acetone, DCM, and diethyl ether. The powder was dispersed in a minimum amount of solvent at each washing cycle, sonicated, and centrifuged. Then, washed powders were dried in vacuum until constant weight. The process yielded 70 mg of a polycrystalline powder (Fig.C.1). Yield: 75% EA found (calcd. for $CuC_4N_2S_8$): C, 12.78 (12.13); H, 0.03 (0.00); N, 7.00 (7.07). ATR-IR (cm^{-1}): 1700 (vw), 1518 (vw), 1418 (vw), 1453 (w), 1237 (vs), 1120 (w), 1057 (m), 963 (s), 925 (w), 817 (vw), 756 (vs), 556 (m), 416 (w) (Fig.C.2).

Synthesis of [Ni(dttt)$_2$] (**Nidttt**). Compound TBAdttt (205 mg, 0.50 mmol) was added to 10 mL of MeOH and left to stir in the dark. A solution of $NiCl_2 \cdot 6H_2O$ (59 mg, 0.25 mmol) in MeOH (10 mL) was added dropwise to the ligand solution over 2 h. As soon as the nickel(II) salt is added, a dark green precipitate forms out from the solution. The mixture was left to stir 6 h and then centrifuged. The precipitate was washed abundantly with H_2O, MeOH, Acetone, DCM, and diethyl ether. The powder was dispersed in a minimum amount of solvent at each washing cycle, sonicated, and centrifuged. Then, washed powders were dried in vacuum until constant weight. The process yielded 80 mg of a polycrystalline powder (Fig.C.1). Yield: 82 % EA found (calcd. for $NiC_4N_2S_8$): C, 12.85 (12.28); H, 0.02 (0.00); N, 7.13 (7.16). ATR-IR (cm^{-}1): 1740 (vw), 1611 (vw), 1434 (w), 1375 (w), 1268 (vs), 1105 (vw), 1065 (m), 975 (s), 918 (m), 809 (w), 740 (vs), 555 (m), 451 (m) (Fig.C.2).

Synthesis of [Cu$_{0.2\%}$Ni(dttt)$_2$] (**Cu$_{0.2\%}$dttt**). Compound TBAdttt (500 mg, 1.223 mmol) was added to 35 mL of MeOH and left to stir in the dark. In another flask, a MeOH solution (50 mL) of $CuCl_2 \cdot H_2O$ (2 mg) and $NiCl_2 \cdot 6H_2O$ (1.452 g) was prepared. Thus, 5 mL of the stock solution were added dropwise to the ligand, and the resulting mixture was left to stir for 6 h before centrifugation. The precipitate was washed abundantly with H_2O, MeOH, Acetone, DCM, and diethyl ether. The powder was dispersed in a minimum amount of solvent at each washing cycle, sonicated, and centrifuged. Then, washed powders were dried in vacuum until constant weight. The process yielded 220 mg of a polycrystalline dark green powder (Figure S1). Yield: 89%. Relative concentrations of Cu^{2+} and Ni^{2+} species were verified by ICP-MS (Cu^{2+} = 0.2 %). The homogeneity of the sample was checked both by PXRD analysis (Fig.C.1) and X-band CW-EPR (Fig.C.6).

C.1.3 PXRD analysis

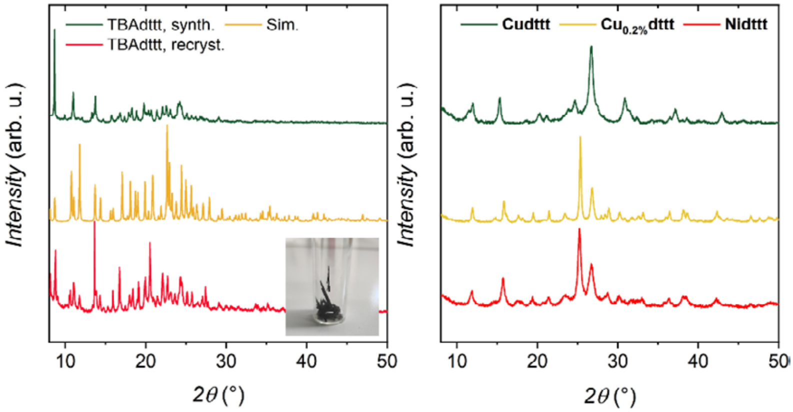

Figure C.1. On the left, experimental PXRD patterns of TBAdttt obtained before (green) and after recrystallization (red). The simulated spectrum (yellow) is reported for comparison [148]. A photograph of the obtained crystals is reported in the inset (bottom right corner). On the right, experimental PXRD patterns of **Cudttt**, **Cu$_{0.2\%}$dttt**, and **Nidttt**.

C.1.4 UV-Vis and IR analysis

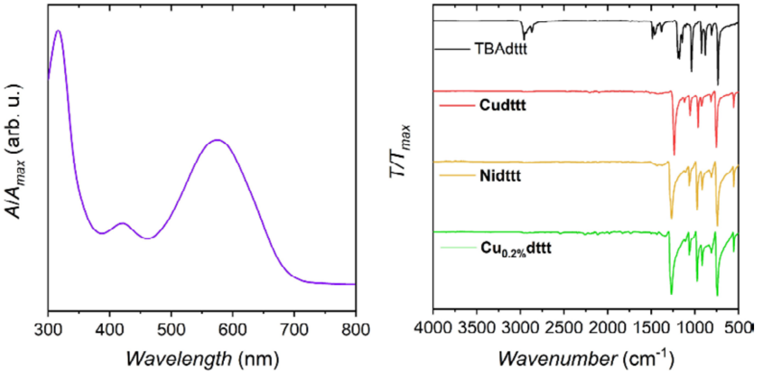

Figure C.2. On the left, UV-Vis characterization of compound TBAdttt. On the right, IR characterization of compounds TBAdttt, **Cudttt**, **Nidttt**, and **Cu$_{0.2\%}$dttt**.

C.1.5 Thermogravimetric analysis

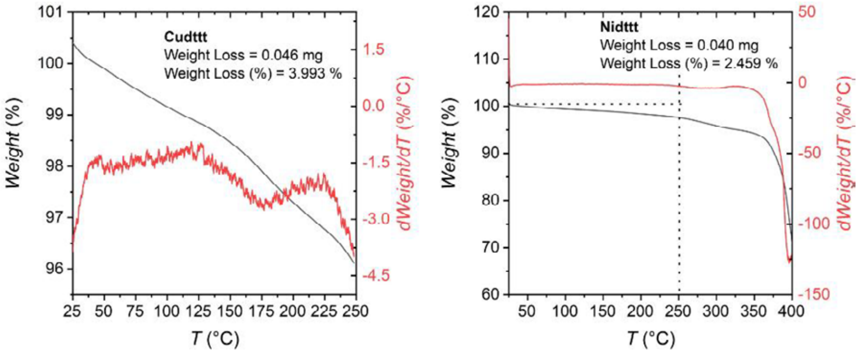

Figure C.3. Experimental results of thermogravimetric analyses (TGA) conducted on **Cudttt** and **Nidttt**.

C.1.6 XPS analysis of bulk samples

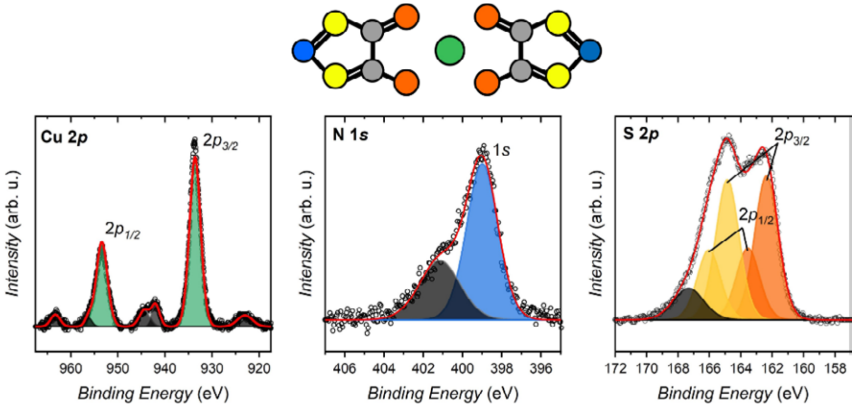

Figure C.4. Experimental core-level XPS spectra of a bulk sample of **Cudttt** molecules deposited by scratching on the Al substrate. For a clear attribution of the XPS components, each fitted component follows the atom color code of the reproduced **Cudttt** molecule. Gray components in the XPS spectra are ascribed to satellite or shake-up signals.

C.1.7 DC magnetometry

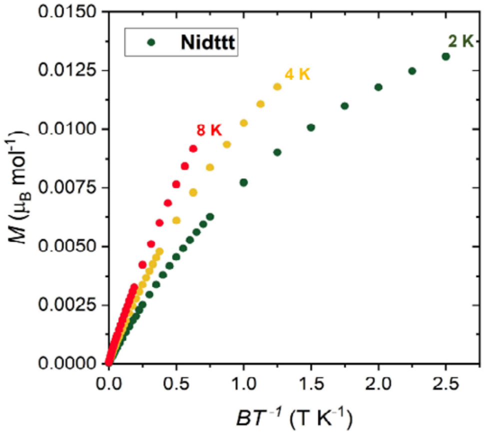

Figure C.5. Plot of M vs HT^{-1} for the **Nidttt** powdered sample after several washing cycles (sonication - centrifugation from different solvents). The saturation value of M at 2 K well agree with a $S = 1$ concentration of about 0.7 % of the total weight.

C.1.8 X-band CW-EPR

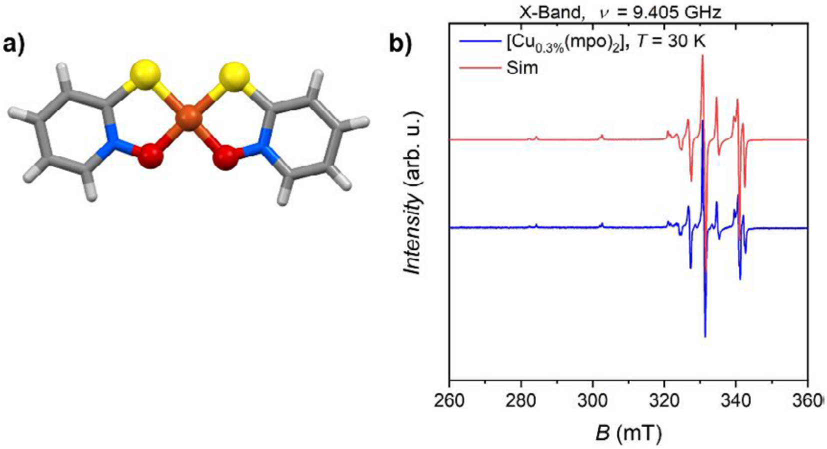

Figure C.6. a) Molecular structure of [Cu(mpo)$_2$] extracted from [234]. b) Experimental X-band CW-EPR spectra of [Cu$_{0.3\%}$(mpo)$_2$]. The simulated curve obtained by employing the SH in Eq.4.3 is reported in the same plot. Best simulation parameters: g_x = 2.036(1), g_y = 2.039(1), g_z = 2.156(1), A_x^{Cu} = 93(2) MHz, A_y^{Cu} = 99(2) MHz, A_z^{Cu} = 555(2) MHz

C.1.9 X-band HYSCORE measurements

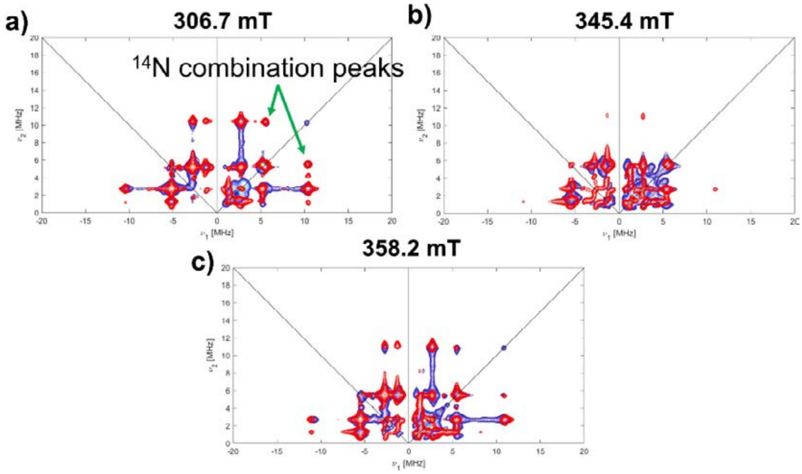

Figure C.7. Experimental (2D blue map) and simulated (2D red map) X-band HYSCORE data plot obtained from pulsed EPR experiments on **Cu$_{0.2\%}$dttt**. The measurements were conducted by pulsing on the three field positions: a) 306.7 mT; b) 345.4 mT; c) 358.2 mT.

C.2 Section 6.1: {[VO(TPyP)][Cr$_7$Ni]$_4$}

C.2.1 Synthetic procedures

All the employed chemicals were of reagent grade and adopted without further purification, except for [VO(acac)$_2$] that was purified by sublimation (60 °C, 10^{-5} mbar). Porphyrin H$_2$TPyP was purchased from Sigma-Aldrich, while H$_2$TrPPyP from PorphyChem Sas. All the operations involving inert atmosphere were conducted under N$_2$ by employing standard Schlenk techniques.

Synthesis of [VO(TPyP)] (VOTPyP). The synthesis was performed by adapting the procedure from [214]. H$_2$TPyP (1.1 g, 1.8 mmol) and [VO(acac)$_2$] (650 mg, 2.45 mmol) were added to a DMF/CH$_3$COOH (1:1) mixture (160 mL) and refluxed under N$_2$ for 24 h. After a TLC check (a red spot must be formed below the purple one of the ligand), the reaction was stopped, and the solution was brought to RT. The solution was then poured into 500 mL of water and ice and kept under stirring for 30 mins. The resulting mixture was filtered on a glass frit, and the collected purple powder (identified as residual ligand from TLC check) was washed several times with water, acetone (4 mL), and Et$_2$O. The filtrated collected, dried over MgSO$_4$, filtered, and pumped in vacuum at 70 °C until a microcrystalline reddish powder was obtained. The crude product was purified by column chromatography on flash silica gel adopting a CH$_2$Cl$_2$/MeOH (96:4) mixture. The overall process yielded 653 mg of [VO(TPyP)]·$2H_2O$ (≈ 50%). The presence of water was confirmed by elemental analysis. X-ray quality crystals were obtained by slow evaporation of a DCM/ACN solution over two weeks and adopted for structure determination. EA found (calcd. for $VC_{40}H_{28}N_8O_3$): V, 6.64 (7.08); C, 67.12 (66.76); H, 4.14 (3.92); N, 14.80 (15.57). UV-Vis (DCM): λ_{max} = 421 nm, 544 nm, 580 nm. In FigC.8a, it is reported the comparison between Q bands region of VOTPyP and H_2TPyP. ATR-IR (cm^{-1}) = 3111(vw), 3015(vw), 1592(s), 1547(w), 1408(m), 1333(m), 1201(w), 1068(w), 1000(vs, V=O stretching), 892(w), 852(vw), 802(s), 727 (s), 658 (s) (see Fig.C.8b). MALDI-MS (m/z): 684.6 ([$M+H^+$]), 619.7 ([$M-VO+H^+$]). Synthesis of [VO(TPyP)]{Cr_7Ni}$_4$ (VO{Cr_7Ni}$_4$). The synthesis was performed by adopting the procedure extracted from [57]. VOTPyP (160 mg, 0.23 mmol) was added to 50 mL of a DCM solution containing {$Cr_7NiF_3(Piv)_{15}$ (Etglu)(H_2O)} (2.2 g, 0.99 mmol). The solution was left to stir at RT for 72 h. After that, the solution was dried in vacuum, and the resulting purple powder left to stir with acetone (50 mL) for 24 h. After filtration, the solid residue was extracted three times with 15 mL of n-pentane, and the resulting solution was diluted with 45 mL of acetone. A crystalline red/purple solid (2.2 g) was collected upon the evaporation of n-pentane. X-ray quality crystals were obtained by slow diffusion of acetone into a hexane solution of VO{Cr_7Ni}$_4$. EA found (calcd. for $C_{372}H_{648}N_{12}O_{145}VCr_{28}Ni_4$): V, 0.47 (0.53); Ni, 2.75 (2.53); C, 46.87 (46.65); H, 6.55 (6.48); N, 1.77 (1.75).

Synthesis of [VO(TrPPyP)]. In a Schlenk flask, H_2TrPPyP (50 mg, 0.08 mmol) was added of PhOH (2 g), and the temperature was slowly increased up to 80 °C. [VO(acac)$_2$] (Purified by sublimation, 33 mg, 0.12 mmol) was thus added to the stirred solution, and the temperature increased up to 165 °C. The reaction was left stirring under nitrogen for 13 hours. The product formation was checked via UV-Vis spectroscopy (Fig.C.9). Once reacted, PhOH was completely removed by blowing nitrogen on the solution kept at 150 °C. The solid product obtained is dissolved in a minimum amount of EtOAc and purified by flash column chromatography on silica adopting a mixture EtOAc/MeOH 95:5 as eluent. Yield: 22 mg, 40%. X-ray quality crystals have been obtained by the slow evaporation of a solution in CH_2Cl_2/ACN. A preliminary structure is reported in Fig.C.10. EA found (calcd. for$VC_{40}H_{24}N_5O$): C, 74.12 (75.88); H, 3.64 (4.00); N, 11.03 (10.29). UV-Vis (DCM): λ_{max} = 424 nm, 546 nm, 582 nm. In FigC.9a, it is reported the comparison between Q bands region of ligand and [VO(TrPPyP)]. FT-IR (KBr, cm^{-1}) = 3113(vw), 3018(vw), 1591(s), 1544(w), 1487(vw), 1440(w), 1412(m), 1327(m), 1261(w), 1205(m), 1165(vw), 1073(m), 1000(vs, V=O stretching), 874(vw), 809(s), 724(m, s), 658(s),583(m) (see Fig.C.9b). MALDI-MS (m/z): 682 ([$M+H^+$]).

C.2.2 UV-Vis and FT-IR spectroscopy

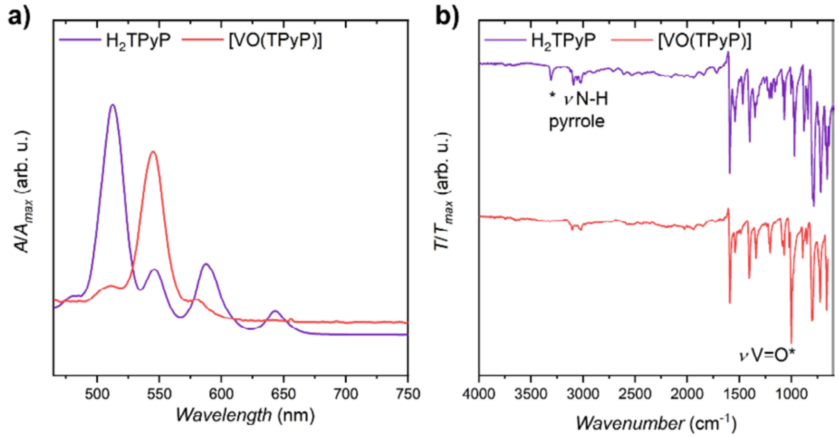

Figure C.8. a) Comparative plot of experimental UV-Vis spectra collected on H_2TPyP and **VOTPyP**. b) Comparative plot of experimental ATR-IR spectra collected on H_2TPyP and **VOTPyP**. The most indicative bands are highlighted with an asterisk.

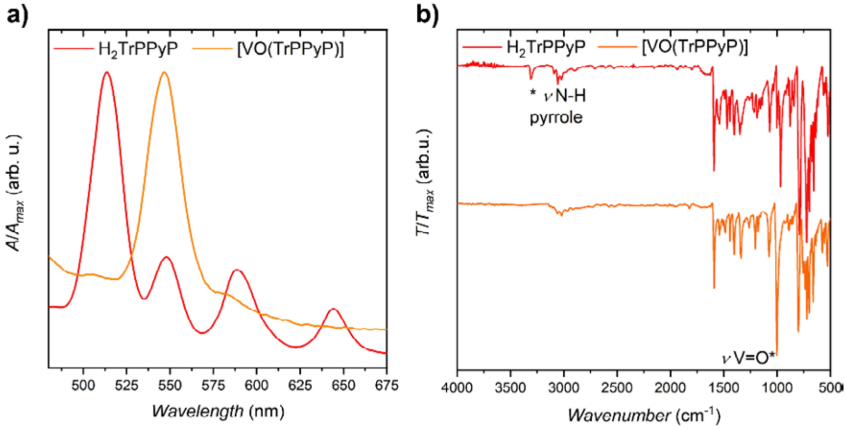

Figure C.9. a) Comparative plot of experimental UV-Vis spectra collected on H_2TrPPyP and [VO(TrPPyP)]. b) Comparative plot of experimental ATR-IR spectra collected on H_2TrPPyP and [VO(TrPPyP)]. The most indicative bands are highlighted with an asterisk.

C.2.3 Q-band CW-EPR spectroscopy on [VO(TPyP)]

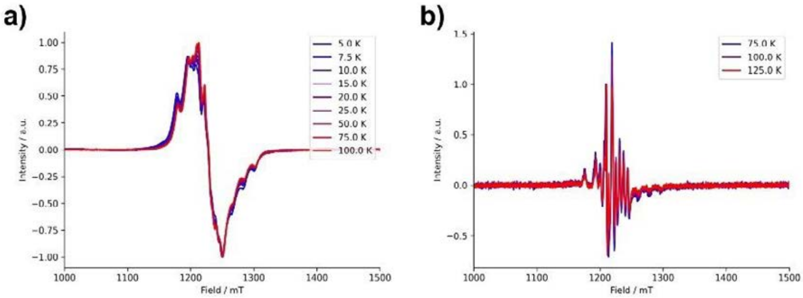

Figure C.10. a) Experimental CW-EPR spectra at the Q-band frequency collected on a polycrystalline sample of **VOTPyP** at different temperatures. b) Experimental CW-EPR spectra at the Q-band frequency collected at different temperatures on a frozen toluene solution (1 mM) of **VOTPyP**.

C.2.4 Q-band Hahn echo experiments on [VO(TPyP)]

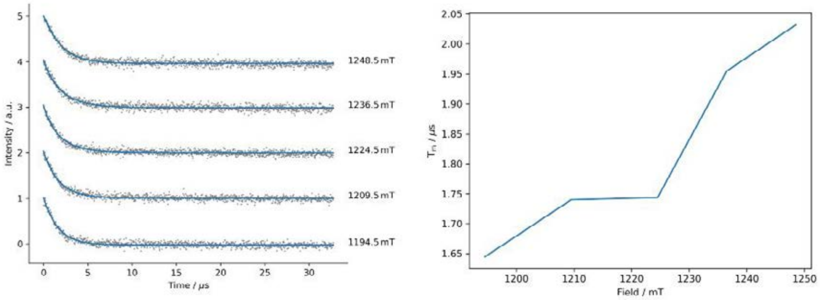

Figure C.11. On the left, experimental echo traces collected at different intensities of the magnetic field on a 1 mM toluene frozen solution of **VOTPyP** at 5 K. The fitted curves obtained with a stretched exponential law are reported on the plot as solid blue lines. The T_m values extracted are reported in the plot on the right side.

C.2.5 Structure and Q-band CW-EPR characterization of Cu{Cr_7Ni}

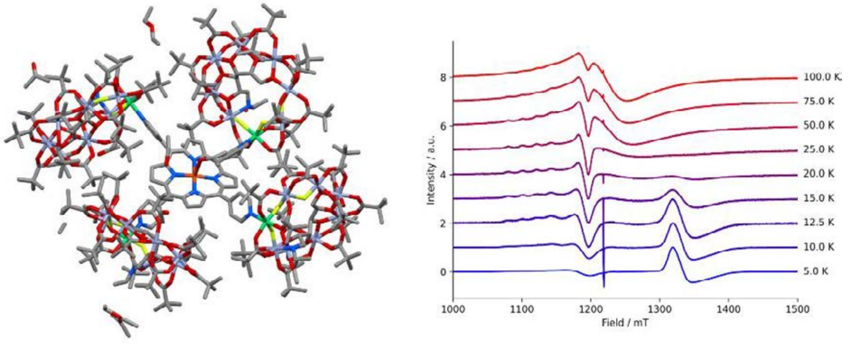

Figure C.12. On the left, preliminary molecular structure of compound **Cu{Cr_7Ni}$_4$**. In this case the central copper ion is penta-coordinated by the four nitrogen atoms of the porphyrin core and by an acetone molecule. However, no evidence of such a coordination geometry is observed within the EPR spectra reported on the right. On the right, Q-band CW-EPR spectra collected at different temperatures on a toluene/DCM (1:1) solution (1 mM) of **Cu{Cr_7Ni}$_4$**.

C.2.6 X-band CW-EPR spectroscopy on VO{Cr_7Ni}

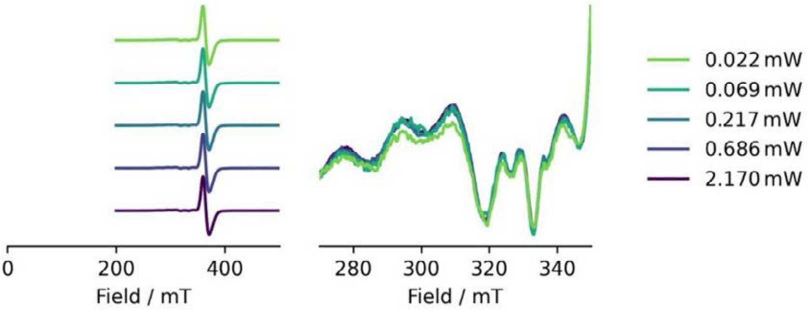

Figure C.13. Experimental X-band CW-EPR spectra collected on a 1 mM toluene/DCM (1:1) frozen solution of **VO{Cr_7Ni}$_4$** at different attenuation values of the mw radiation and at 5 K. As can be observed in the right panel, no variations of the signal's intensity were detected in the region of vanadyl. It follows that no saturation phenomena occur within the experimental limits.

C.2.7 Q-band pulsed EPR spectroscopy on VO{Cr_7Ni}

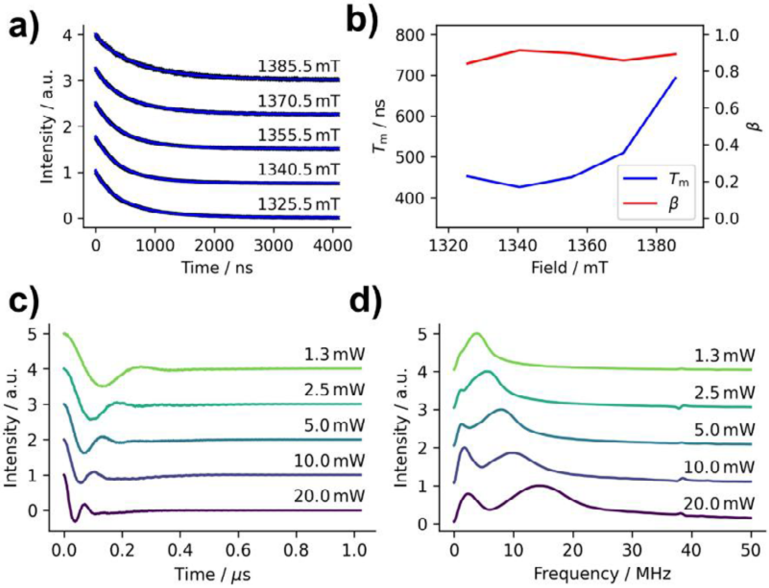

Figure C.14. In order: a) echo traces of {Cr_7Ni} rings within the **VO{Cr_7Ni}$_4$** sample (same as Fig.C.13)) collected at 5 K for different field intensities; b) experimental T_m values extracted from the fit of echo decays with a stretched exponential law (the value of stretching parameter, β, is reported in the same plot as a solid red line); c) Rabi oscillations as a function of the time collected at different values of mw power; d) Fourier's transform of Rabi oscillations in the previous plot. The color code follows the same map.

C.3 Section 6.2: [VO(TrPP)]$_2$

C.3.1 Synthetic procedures

All the employed chemicals were of reagent grade and adopted without further purification. Porphyrin H_2TrPP was purchased from PorphyChem Sas. All the operations involving an inert atmosphere were conducted under N_2 by employing standard Schlenk techniques.

Synthesis of [VO(TrPP)] (VOTrPP). The synthesis was performed by adapting the procedure from [77]. H_2TrPP (80 mg, 0.149 mmol) and VOacac2 (40 mg, 0.149 mmol) were added to Phenol (2 g) and heated to 80 °C. After a few vacuum/N_2 cycles, the reaction mixture was left to reflux under N_2 for 24 h. After TLC (DCM/Pet. ether 1:1, R_f = 74%) and UV-Vis checks, PhOH was firstly removed under reduced pressure and then by blowing N_2 on the crude product while kept at 140 °C – 150 °C. The crude product was then dissolved in 200 mL of DCM, filtered, and purified by column chromatography (flash silica gel, DCM/Pet. ether 1:1). UV-Vis (DCM): λ_{max} = 417 nm, 541 nm, 576 nm. FT-IR (KBr, cm^{-1}) = 3101 (w), 3052 (w), 3029 (w), 2921 (vw), 2852 (vw), 2363 (w), 2332(w), 1588 (w), 1492(w), 1442 (m), 1376 (w), 1324(m), 1075 (m), 1000 (vs, V=O stretching), 952(vs), 853 (m), 801 (s), 756 (s), 721 (s), 697 (s), 659 (w). MALDI-MS (m/z): 603.13 ($M^{\cdot+}$).

Synthesis of [VO(TrPP)]$_2$ ({VO}$_2$). The synthesis was performed by modifying the procedure from [224]. In a pre-dried 50 mL Schlenk flask, [VO(TrPP)] (15 mg, 0.025 mmol, 2 eq) was dissolved in 6 mL of dry CH_2Cl_2 under N_2 flow. The solution was cooled down to −78 °C with an acetone/N_2 bath. Thus, a PIFA solution in 4 mL of dry DCM (5 mg, 0.0125 mmol, 1 eq) was cautiously added to the **VOTrPP** solution. Once the addition was completed, the acetone/N_2 bath was removed, and the reaction mixture was stirred at RT for about 30 min. The TLC check confirmed that there was still unreacted **VOTrPP**. However, the reaction was quenched with a MeOH solution of $NaBH_4$ (5 mg in 3 mL), since longer exposure of **VOTrPP** to these harsh conditions promoted adverse reactions. The solution was stirred for another 15 minutes. After that, deionized H_2O (5 mL) was added to the reaction mixture to quench unreacted $NaBH_4$. The organic phase was separated from the water phase and washed twice with sat. $NaHCO_3$ solution (10 mL x 2). After drying with anhydrous $NaSO_4$, CH_2Cl_2 was removed under reduced pressure. The crude product was purified with column chromatography (flash silica gel, toluene). The unreacted **VOTrPP** was recovered and treated again with PIFA (same procedure). The overall procedure yielded 8 mg of pure **{VO}$_2$** (final yield = 53 %). UV-Vis (DCM): λ_{max} = 417 nm, 541 nm, 576 nm.

C.3.2 PXRD analysis

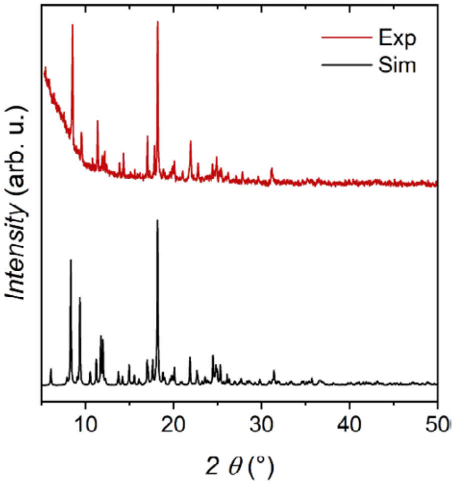

Figure C.15. Plot of experimental (red line) and simulated (black line, from structure in Fig.6.16) PXRD patterns of **{VO}₂**.

C.3.3 Nutation experiments

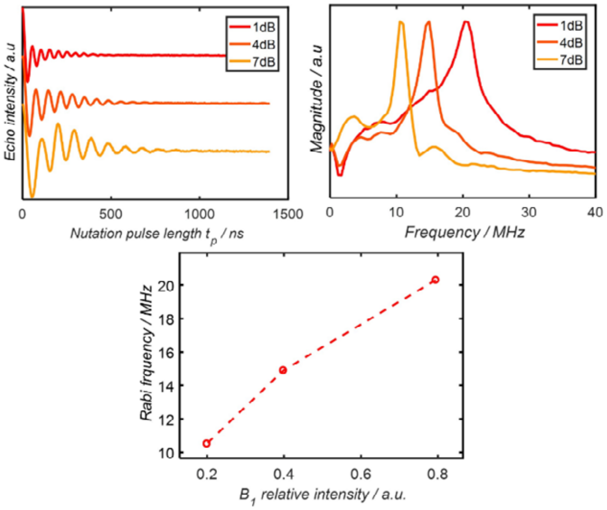

Figure C.16. Plot of experimental (red line) and simulated (black line, from structure in Fig.6.16) PXRD patterns of **{VO}₂**.

C.3.4 Zeeman plots

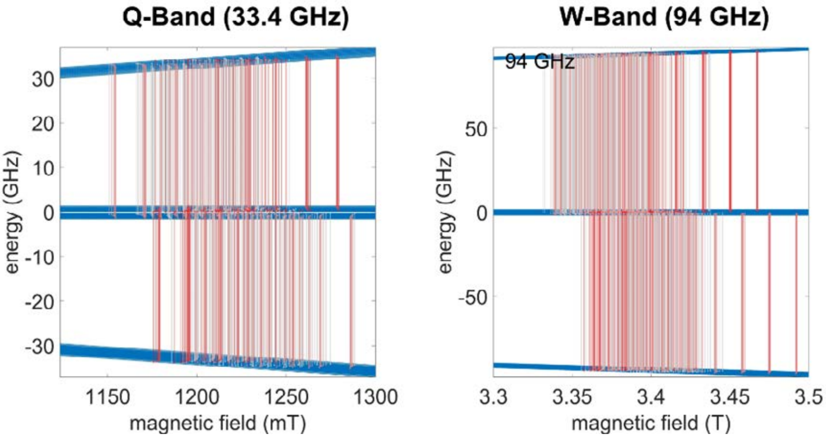

Figure C.17. Comparison between the Zeeman plots at Q-bands (left) and W-band (right) for compound **{VO}**$_2$ simulated by adopting the SH parameters of Table 6.2. Simulations were thus implemented on an oriented crystal for which the external static field B_0 direction coincides with that of the z axis.

References

[1] Nielsen, M. A. and Chuang, I. L. (2010). *Quantum Computation and Quantum Information*. Cambridge: Cambridge University Press.

[2] Le Bellac, M. (2006). *A Short Introduction to Quantum Information and Quantum Computation*. Cambridge: Cambridge University Press.

[3] Holevo, A. S. (2019). *Quantum Systems, Channels, Information*. Berlin/Boston: De Gruyter.

[4] Hardy, Y. and Steeb, W. (2001). *Classical and Quantum Computing*. Basel: Birkhäuser Basel.

[5] Grover, L. K. (1997). Quantum Computers Can Search Arbitrarily Large Databases by a Single Query. *Physical Review Letters*, 79, 4709–4712.

[6] Adedoyin, J. A., Ambrosiano, J., Anisimov, P., Bärtschi, A., Casper, W., Chennupati, G., Coffrin, C.,Djidjev, H., Gunter, D., Karra, S., Lemons, N., Lin, S., Malyzhenkov, A., Mascarenas, D., Mniszewski, S., … , and Lokhov, A. (2022). Quantum Algorithm Implementations for Beginners. *ACM Transactions on Quantum Computing*, 3, 1–92.

[7] Deutsch, D.E. (1989). Quantum computational networks. *Proceedings of the Royal Society of London. A. Mathematical and Physical Sciences*, 425, 73–90.

[8] Lloyd, S. (1995). Almost Any Quantum Logic Gate is Universal. *Physical Review Letters*, 75, 346–349.

[9] Sleator, T. and Weinfurter, H. (1995). Realizable Universal Quantum Logic Gates. *Physical Review Letters*, 74, 4087–4090.

[10] Aleksandrowickz, G., Alexander, T., Panagiotis, B., Bello, L., Ben-Haim, Y., Bucher, D., Cabrera-Hernández, F. J., Carballo-Franquis, J., Chen, A., Chen, C.-F., Chow, J., M., … ,Zoufal, C. (2019). Qiskit: An open-source framework for quantum computing (0.7.2). Zenodo. 10.5281/zenodo.8190968

FUP Best Practice in Scholarly Publishing (DOI 10.36253/fup_best_practice)

Fabio Santanni, *Molecular approaches for quantum technologies. Optimization of electron spin-based quantum bits and quantum logic gates*, published by Firenze University Press, ISBN 979-12-215-0670-9, DOI 10.36253/979-12-215-0670-9

[11] Westfall, L. and Leider, A. (2020). *Superdense coding step by step*. in *Advances in Information and Communication* (Arai, K. and Bhatia, R. eds.), pp. 357–372. Springer Nature Switzerland AG.

[12] Nielsen, M. A. (2010). Superdense Coding: How to Send Two Bits Using One Qubit. Nielsen, M. A. (2010). https://youtu.be/w5rCn593Dig

[13] Barreiro, J. T., Wei, T.-C., and Kwiat, P. G. (2008). Beating the channel capacity limit for linear photonic superdense coding. *Nature Physics*, 4, 282–286.

[14] Haroche, S. and Raimond, J.-M. (2006). *Exploring the Quantum: Atoms, Cavities, and Photons*. Oxford Graduate Texts, Oxford: Oxford University Press.

[15] Werninghaus, M., Egger, D. J., Roy, F., Machnes, S., Wilhelm, F. K., and Filipp, S. (2021). Leakage reduction in fast superconducting qubit gates via optimal control. *Nature Physics Journal Quantum Information*, 7, 14.

[16 Devoret, M. H. and Schoelkopf, R. J. (2013). Superconducting Circuits for Quantum Information: An Outlook. *Science*, 339, 1169–1174.

[17] Clarke, J. and Wilhelm, F. K. (2008). Superconducting quantum bits. *Nature*, 453, 1031–1042.

[18] Arute, F., Arya, K., Babbush, R., Bacon, D., Bardin, J. C., Barends, R., Biswas, R., Boixo, S., Brandao, L., Buell, D. A., Burkett, B., Chen, Y., Chen, Z.,Chiaro, B., Collins, R., …, and Martinis, J. M. (2019). Quantum supremacy using a programmable superconducting processor. *Nature*, 574, 505–510.

[19] Bradley, C. E., Randall, J., Abobeih, M. H., Berrevoets, R. C., Degen, M. J., Bakker, M. A., Markham, M., Twitchen, D. J., and Taminiau, T. H. (2019). A Ten-Qubit Solid-State Spin Register with Quantum Memory up to One Minute. *Physical Review X*, 9, 031045.

[20] Wu, Y., Wang, Y., Qin, X., Rong, X., and Du, J. (2019). A programmable two-qubit solid-state quantum processor under ambient conditions. *Nature Physics Journal Quantum Information*, 5, 9.

[21] Smith, J. M., Meynell, S. Bleszynski Jayich, A. C., and Meijer, J. (2019). Colour centre generation in diamond for quantum technologies. *Nanophotonics*, 8, 1889–1906.

[22] Eichhorn, T. R., McLellan, C. A., and Bleszynski Jayich, A. C., (2019). Optimizing the formation of depth-confined nitrogen vacancy center spin ensembles in diamond for quantum sensing. *Physical Review Materials*, 3, 113802.

[23] Carter, S. G., Sweeney, T. M., Kim, M., Kim, C. S., Solenov, D., Economou, S. E., Reinecke, T. R., Yang, L., Bracker, A. S., Gammon, D. (2013). Quantum control of a spin qubit coupled to a photonic crystal cavity. *Nature Photonics*, 7, 329–334.

[24] Friis, N., Marty, O., Maier, C., Hempel, C., Holzäpfel, M., Jurcevic, P., Plenio, M. B., Huber, M., Roos, C., Blatt, R., and Lanyon, B. (2018). Observation of Entangled States of a Fully Controlled 20-Qubit System. *Physical Review X*, 8, 021012.

[25] Manousakis, J., Altland, A., Bagrets, D., Egger, R., and Ando, Y. (2017). Majorana qubits in a topological insulator nanoribbon architecture. *Physical Review B*, 95, 165424.

[26] Ferreira, G. J. and Loss, D. (2013). Magnetically Defined Qubits on 3D Topological Insulators. *Physical Review Letters*, 111, 106802.

[27] Chatterjee, A., Stevenson, P., De Franceschi, S., Morello, A., de Leon, N. P., and Kuemmeth, F. (2021), Semiconductor qubits in practice. *Nature Reviews Physics,* 3, 157–177.

[28] Pla, J. J., Tan, K. Y., Dehollain, J. P., Lim, W. H., Morton, J. J. L., Jamieson, D. N., Dzurak, A. S., and Morello, A. (2012). A single-atom electron spin qubit in silicon. *Nature*, 489, 541–545.

[29] Veldhorst, M., Yang, C. H., Hwang, J. C. C., Huang, W., Dehollain, J. P., Muhonen, J. T., Simmons, S., Laucht, A., Hudson, F. E., Itoh, K. M., Morello, A., and Dzurak, A. S., (2015). A two-qubit logic gate in silicon. *Nature*, 526, 410–414, 2015.

[30] Atzori, M. and Sessoli, R. (2019). The Second Quantum Revolution: Role and Challenges of Molecular Chemistry. *Journal of the American Chemical Society*, 141, 11339–11352.

[31] Gaita-Ariño, Luis, F., Hill, S., and Coronado, E. (2019). Molecular spins for quantum computation. *Nature Chemistry*, 11, 301–309.

[32] Wasielewski, M. R., Forbes, M. D. E., Frank, N. L., Kowalski, K., Scholes, G. D., Yuen-Zhou, J., Baldo, M. A., Freedman, D. E., Goldsmith, R. H., Goodson, T., Kirk, M. L., McCusker, J. K., Ogilvie, J. P., Shultz, D. A., Stoll, S. and Whaley, K. B. (2020). Exploiting chemistry and molecular systems for quantum information science. *Nature Reviews Chemistry*, 4, 490–504, 2020.

[33] Carretta, S., Zueco, D., Chiesa, A., Gómez-Léon, Á., and Luis, F. (2021). A perspective on scaling up´ quantum computation with molecular spins. *Applied Physics Letters*, 118, 240501.

[34] Trauzettel, B., Bulaev, D. V., Loss, D., and Burkard, G. (2007). Spin qubits in graphene quantum dots. *Nature Physics*, 3, 192–196.

[35] Bermudez, A., Xu, X., Nigmatullin, R., O'Gorman, J., Negnevitsky, V., Schindler, P., Monz, T., Poschinger, U. G., Hempel, C., Home, J., Schmidt-Kaler, F., Biercuk, B., Blatt, R., Benjamin, S. and Müller, M. (2017). Assessing the Progress of Trapped-Ion Processors Towards Fault-Tolerant Quantum¨ Computation. *Physical Review X*, 7, 041061.

[36] Diamond, S., Fatemi, V., Hays, M., Nho, H., Kurilovic, P., Connolly, T., Joshi, V. R., Serniak, R., Frunzio, L., Glazman, L. I., and Devoret, M. H. (2022). Distinguishing Parity-Switching Mechanisms in a Superconducting Qubit. *PRX Quantum*, 3, 040304.

[37] Johnson, M. A. I., Madzik, M. T., Hudson, F. E., Itoh, K. M.., Jakob, A. M., Jamieson, D. N., Dzurak, A., and Morello, A. (2022). Beating the Thermal Limit of Qubit Initialization with a Bayesian Maxwell's Demon. *Physical Review X*, 12, 041008.

[38] Atzori, M., Tesi, L., Morra, E., Chiesa, M., Sorace, L., and Sessoli, R. (2016). Room-Temperature Quantum Coherence and Rabi Oscillations in Vanadyl

Phthalocyanine: Toward Multifunctional Molecular Spin Qubits. *Journal of the American Chemical Society*, 138, 2154–2157.

[39] DiVincenzo, D. P. (2000). The Physical Implementation of Quantum Computation. *Fortschritte der Physik*, v48, 771–783.

[40] Volkov, M. Y. and Salikhov, K. M. (2011). Pulse Protocols for Quantum Computing with Electron Spins as Qubits. *Applied Magnetic Resonance*, 41, 145–154.

[41] Chuang, I. L., Vandersypen, L. M. K., Zhou, X., Leung, D. W., and Lloyd, S., Experimental realization of a quantum algorithm. *Nature*, 393, 143–146.

[42] DiVincenzo, D. P. (1998). Real and realistic quantum computers. *Nature*, 393, 113–114.

[43] Kane, B. E. (1998). A silicon-based nuclear spin quantum computer. *Nature*, 393, 133–137.

[44] Pla, J. J., Tan, K. Y., Dehollain, J. P., Lim, W. H., Morton, J. J. L., Zwanenburg, F. A., Jamieson, D. N., Dzurak, A. S., and Morello, A. (2013). High-fidelity readout and control of a nuclear spin qubit in silicon. *Nature*, 496, 334–338.

[45] Atzori, M., Garlatti, E., Allodi, G., Chicco, S., Chiesa, A., Albino, A., De Renzi, R., Salvadori, E., Chiesa, M., Carretta, S., and Sorace, L. (2021). Radiofrequency to Microwave Coherent Manipulation of an Organometallic Electronic Spin Qubit Coupled to a Nuclear Qudit. *Inorganic Chemistry*, 11273–11286.

[46] Chicco, S., Chiesa, A., Allodi, G., Garlatti, E., Atzori, M., Sorace, L., De Renzi, R., Sessoli, S., and Carretta, S. (2021). Controlled coherent dynamics of [VO(TPP)], a prototype molecular nuclear qudit with an electronic ancilla. *Chemical Science*, 12, 12046–12055.

[47] Waldherr, G., Wang, Y., Zaiser, S., Jamali, M., Schulte-Herbrüggen, T., Abe, H., Ohshima, T., Isoya, J., Du, J. F., Neumann, P., and Wrachtrup, J. (2014). Quantum error correction in a solid-state hybrid spin register. *Nature*, 506, 204–207.

[48] Mądzik, M. T., Asaad, S., Youssry, A., Joecker, B., Rudinger, K. M., Nielsen, E., Young, K. C., Proctor, J. T., Baczewski, A. D., Laucht, A., Schmitt, V., Hudson, F. E., Itoh, K. M., Jakob, A. M., Johnson, B. J., Jamieson, D. N., Dzurak, A. S., Ferrie, C., Blume-Kohout, R., and Morello, A. (2022). Precision tomography of a three-qubit electron-nuclear quantum processor in silicon *Nature*, 601, 348–353.

[49] Edmonds, A. M., D'Haenens-Johansson, U. F. S., Cruddace, R. J., Newton, M. E., Fu, K.-M. C., Santori, C., Beausoleil, R. G., Twitchen, D. J., and Markham, M. L. (2012). Production of oriented nitrogen-vacancy color centers in synthetic diamond. *Physical Review B*, 86,035201.

[50] Rembold, P., Oshnik, N., Müller, M. M., Montangero, S., Calarco, T., and Neu, E. (2020). Introduction to quantum optimal control for quantum sensing with nitrogen-vacancy centers in diamond. *AVS Quantum Science*, 2, 024701.

[51] Pla, J. J., Tan, K. Y., Dehollain, J. P., Lim, W. H., Morton, J. J. L., Jamieson, D. N., Dzurak, A. S., and Morello, A. (2012). A single-atom electron spin qubit in silicon. *Nature*, 489, 541–545.

[52] Santini, P., Carretta, S., and Amoretti, G. (2016). *Magnetic Molecules as Spin Qubits*. in *Molecular Magnetic Materials* (Sieklucka, B. and Pinkowicz, D. edts.), pp. 103–129. Weinheim: Wiley-VCH Verlag GmbH and Co. KGaA.

[53] Troiani, F. and Affronte, M. (2011). Molecular spins for quantum information technologies. *Chemical Society Reviews*, 40, 3119.

[54] Atzori, M., Chiesa, A., Morra, E., Chiesa, M., Sorace, L., Carretta, S., and Sessoli, R. (2018). A two-qubit molecular architecture for electron-mediated nuclear quantum simulation. *Chemical Science*, 9, 6183–6192.

[55] Wedge, C. J., Timco, G. A., Spielberg, E. T., George, R. E., Tuna, F., Rigby, S., McInnes, E. J. L., Winpenny, R. E. P., Blundell, S. J., and Ardavan, A. (2012). Chemical Engineering of Molecular Qubits. *Physical Review Letters*, 108, 107204.

[56] Timco, G. A., Carretta, S., Troiani, F., Tuna, F., Pritchard, R. J., Muryn, C. A., McInnes, E. J. L., Ghirri, A., Candini, A., Santini, P., Amoretti, G., Affronte, M., and Winpenny, R. E. P. (2009). Engineering the coupling between molecular spin qubits by coordination chemistry. *Nature Nanotechnology*, 4, 173–178.

[57] Timco, G. A., Faust, T. B., Tuna, F., and Winpenny, R. E. P. (2011). Linking heterometallic rings for quantum information processing and amusement. *Chemical Society Reviews*, 40, 3067.

[58] Sato, K., Nakazawa, S., Rahimi, R., Ise, T., Nishida, S., Yoshino, T., Mori, N., Toyota, K., Shiomi, D., Yakiyama, Y., Morita, Y., Kitagawa, M., Nakasuji, K., Nakahara, M., Hara, H., Carl, P., Höfer, P., and Takui, T. (2009). Molecular electron-spin quantum computers and quantum information processing: pulse-based electron magnetic resonance spin technology applied to matter spin-qubits. *Journal of Materials Chemistry*, 19, 3739.

[59] Nelson, J. N., Zhang, J., Zhou, J., Rugg, B. K., Krzyaniak, M. D., and Wasielewski, M. R. (2020). NOT gate operation on a photogenerated molecular electron spin-qubit pair. *The Journal of Chemical Physics*, 152, 014503.

[60] Chiesa, A., Petiziol, F., Macaluso, E., Wimberger, S., Santini, P., and Carretta, S. (2021). Embedded quantum-error correction and controlled-phase gate for molecular spin qubits. *AIP Advances*, 11, 025134.

[61] Zadrozny, J. M., Niklas, J., Poluektov, O. G., and Freedman, D. E (2015). Millisecond Coherence Time in a Tunable Molecular Electronic Spin Qubit. *ACS Central Science*, 1, 488–492.

[62] Schweiger, A. and Jeschke, G. (2001). *Principles of pulse electron paramagnetic resonance*. Oxford: Oxford University Press.

[63] Aravena, D. and Ruiz, E. (2020). Spin dynamics in single-molecule magnets and molecular qubits. *Dalton Transactions*, 49, 9916–9928.

[64] Escalera-Moreno, L., Baldoví, J. J., Gaita-Ariño, A., and Coronado, E. (2018). Spin states, vibrations and spin relaxation in molecular nanomagnets and spin qubits: a critical perspective. *Chemical Science*, 9, 3265–3275.

[65] Johansson, J., Nation, P., and Nori, F. (2012). QuTiP: An open-source Python framework for the dynamics of open quantum systems. *Computer Physics Communications*, 183, 1760–1772.

[66] Warner, M., Din, S., Tupitsyn, I. S., Morley, G. W., Stoneham, A. M., Gardener, J. A., Wu, Z., Fisher, A. J., Heutz, S., Kay, C. W. M., and Aeppli, G. (2013). Potential for spin-based information processing in a thin-film molecular semiconductor. *Nature*, 503, 504–508.

[67] Bader, K., Dengler, D., Lenz, S., Endeward, B., Jiang, S.-D., Neugebauer, P., and van Slageren, J. (2014). Room temperature quantum coherence in a potential molecular qubit. *Nature Communications*, 5,5304.

[68] Gatteschi, D., Sessoli, R., and Villain, J. (2006). *Molecular Nanomagnets*. Oxford: Oxford University Press.

[69] Albino, A., Benci, S., Tesi, L., Atzori, M., Torre, R., Sanvito, S., Sessoli, R., and Lunghi, A. (2019). First-Principles Investigation of Spin–Phonon Coupling in Vanadium-Based Molecular Spin Quantum Bits. *Inorganic Chemistry*, 58, 10260–10268.

[70] Lunghi, A. and Sanvito, S. (2020). The Limit of Spin Lifetime in Solid-State Electronic Spins. *The Journal of Physical Chemistry Letters*, 11, 6273–6278.

[71] Garlatti, E., Tesi, L., Lunghi, A., Atzori, M., Voneshen, D. J., Santini, P., Sanvito, S., Guidi, T., Sessoli, R., and Carretta, S. (2020). Unveiling phonons in a molecular qubit with four-dimensional inelastic neutron scattering and density functional theory. *Nature Communications*, 11, 1751.

[72] Orbach, R. (1961). Spin-lattice relaxation in rare-earth salts. *Proceedings of the Royal Society of London. Series A. Mathematical and Physical Sciences*, 264, 458–484.

[73] Standley, K. J. and Vaughan, R. A. (1969). *Electron Spin Relaxation Phenomena in Solids*. Boston: Springer US.

[74] Abragam, A. and Bleaney, B. (1970). *Electron Paramagnetic Resonance of Transition Ions*. Oxford: Clarendon Press.

[75] De Vroomen, A., Lijphart, E., Prins, D., Marks, J., and Poulis, N. (1972). Electron spin-lattice relaxation of the Zeeman and interaction systems in $CuCs_2(SO_4)_2 \cdot 6H_2O$. *Physica*, 61, 241–249.

[76] Soeteman, J., Bevaart, L., and van Duyneveldt, A. (1974). The direct and Raman spin-lattice relaxation process in $YbCl_3 \cdot 6H_2O$. *Physica*, 74, 126–134.

[77] Yamabayashi, T., Atzori, M., Tesi, L., Cosquer, G., Santanni, F., Boulon, M.-E., Morra, E., Benci, S., Torre, R., Chiesa, M., Sorace, L., Sessoli, R., and Yamashita, M. (2018). Scaling Up Electronic Spin Qubits into a Three-Dimensional Metal–Organic Framework. *Journal of the American Chemical Society*, 140, 12090–12101.

[78] Tesi, L., Lunghi, A., Atzori, M., Lucaccini, E., Sorace, L., Totti, F., and Sessoli, R. (2016). Giant spin–phonon bottleneck effects in evaporable vanadyl-based molecules with long spin coherence. *Dalton Transactions*, 45, 16635–16643.

[79] Van Vleck, J. H. (1940). Paramagnetic Relaxation Times for Titanium and Chrome Alum. *Physical Review*, 57, 426–447.

[80] Atzori, M., Tesi, L., Benci, S., Lunghi, A., Righini, R., Taschin, A., Torre, R., Sorace, L., and Sessoli, R. (2017). Spin Dynamics and Low Energy Vibrations: Insights from Vanadyl-Based Potential Molecular Qubits. *Journal of the American Chemical Society*, 139, 4338–4341.

[81] Briganti, M., Santanni, F., Tesi, L., Totti, F., Sessoli, R., and Lunghi, A. A complete ab initio view of Orbach and Raman spin-lattice relaxation in a Dysprosium coordination compound. *Journal of the American Chemical Society*, 143, 13633–13645.

[82] Liddle, S. T. and van Slageren, J. (2015). Improving f-element single molecule magnets. *Chemical Society Reviews*, 44, 6655–6669.

[83] Atzori, M., Morra, E., Tesi, L., Albino, A., Chiesa, M., Sorace, L., and Sessoli, R. (2016). Quantum Coherence Times Enhancement in Vanadium(IV)-based Potential Molecular Qubits: the Key Role of the Vanadyl Moiety. *Journal of the American Chemical Society*, 138, 11234– 11244.

[84] Santanni, F., Albino, A., Atzori, M., Ranieri, D., Salvadori, E., Chiesa, M., Lunghi, A., Bencini, A., Sorace, L., Totti, F., and Sessoli, R. (2021). Probing Vibrational Symmetry Effects and Nuclear Spin Economy Principles in Molecular Spin Qubits. *Inorganic Chemistry*, 60,140–151.

[85] Lunghi, A. and Sanvito, S. (2019). How do phonons relax molecular spins? *Science Advances*, 5, eaax7163.

[86] Lunghi, A. and Sanvito, S. (2020). Multiple spin–phonon relaxation pathways in a Kramer single-ion magnet. *The Journal of Chemical Physics*, 153, 174113.

[87] Reta, D., Kragskow, J. G. C., and Chilton, N. F. (2021). Ab Initio Prediction of High-Temperature Magnetic Relaxation Rates in Single-Molecule Magnets. *Journal of the American Chemical Society*, 143, 5943–5950.

[88] Eaton, S. S. and Eaton, G. R. (2002). *Relaxation Times of Organic Radicals and Transition Metal Ions*, in *Distance Measurements in Biological Systems by EPR* (Berliner, L. J., Eaton, G. R., and Eaton, S. S., eds.), 29–154. New York: Springer New York.

[89] Graham, M. J., Zadrozny, J. M., Fataftah, M. S., and Freedman, D. E. (2017). Forging Solid-State Qubit Design Principles in a Molecular Furnace. *Chemistry of Materials*, 29, 1885–1897.

[90] Escalera-Moreno, L., Gaita-Ariño, A., and Coronado, E. (2019). Decoherence from dipolar interspin interactions in molecular spin qubits. *Physical Review B*, 100, 064405.

[91] Graham, M. J., Yu, C.-J., Krzyaniak, M. D., Wasielewski, M. R., and Freedman, D. E. (2017). Synthetic Approach to Determine the Effect of Nuclear Spin Distance on Electronic Spin Decoherence. *Journal of the American Chemical Society*, 139, 3196–3201.

[92] Camargo, L. C., Briganti, M., Santana, F. S., Stinghen, D., Ribeiro, R. R., Nunes, G. G., Soares, J. F., Salvadori, E., Chiesa, M., Benci, S., Torre, R., Sorace, L., Totti, F., and Sessoli, R. (2021). Exploring the Organometallic Route to Molecular Spin Qubits: The [CpTi(cot)] Case. *Angewandte Chemie International Edition*, 60, 2588–2593.

[93] Georgeot, B. and Mila, F. (2010). Chirality of Triangular Antiferromagnetic Clusters as a Qubit. *Physical Review Letters*, 104, 200502.

[94] Liu, J., Mrozek, J., Ullah, A., Duan, Y., Baldoví, J. J., Coronado, E., Gaita-Ariño, A., and Ardavan, A. (2021). Quantum coherent spin-electric control in a molecular nanomagnet at clock transitions. *Nature Physics*, 17, 1205–1209.

[95] Wojnar, M. K., Laorenza, D. W., Schaller, R. D., and Freedman, D. E. (2020). Nickel(II) Metal Complexes as Optically Addressable Qubit Candidates. *Journal of the American Chemical Society*, 142, 14826–14830.

[96] Fataftah, M. S., Bayliss, S. L., Laorenza, D. W., Wang, X., Phelan, B. T., Wilson, C. B., Mintun, P. J., Kovos, B. D., Wasielewski, M. R., Han, S., Sherwin, M. S., Awschalom, D. D., and Freedman, D. E. (2020). Trigonal Bipyramidal V^{3+} Complex as an Optically Addressable Molecular Qubit Candidate. *Journal of the American Chemical Society*, 142, 20400–20408.

[97] Malavolti, L., Briganti, M., Hänze, M., Serrano, G., Cimatti, I., McMurtrie, C., Otero, E., Ohresser, P., Totti, F., Mannini, M., Sessoli, R., and Loth, S. (2018). Tunable Spin–Superconductor Coupling of Spin 1/2 Vanadyl Phthalocyanine Molecules. *Nano Letters*, 18, 7955–7961.

[98] Willke, P., Paul, W., Natterer, F. D., Yang, K., Bae, Y., Choi, T., Fernández-Rossier, J., Heinrich, A. J., and Lutz, C. P. (2018). Probing quantum coherence in single-atom electron spin resonance. *Science Advances*, 4, eaaq1543.

[99] Zhang, X., Wolf, C., Wang, Y., Aubin, H., Bilgeri, T., Willke, P., Heinrich, A., and Choi, T. (2022). Electron spin resonance of single iron phthalocyanine molecules and role of their non-localized spins in magnetic interactions. *Nature Chemistry*, 14, 59–65.

[100] Yang, K., Phark, S.-H., Bae, Y., Esat, T., Willke, P., Ardavan, A., Heinrich, A. J., and Lutz, C. P. (2021). Probing resonating valence bond states in artificial quantum magnets. *Nature Communications*, 12, 993.

[101] Sessoli, R., Gatteschi, D., Caneschi, A., and Novak, M. A. (1993). Magnetic bistability in a metal-ion cluster. *Nature*, 365, 141–143.

[102] Delfs, C., Gatteschi, D., Pardi, L., Sessoli, R., Wieghardt, K., and Hanke, D. (1993). Magnetic properties of an octanuclear iron(III) cation. *Inorganic Chemistry*, 32, 3099–3103.

[103] Leuenberger, M. N. and Loss, D. (2001). Quantum computing in molecular magnets. *Nature*, 410, 789–793.

[104] Bal, M., Friedman, J. R., Suzuki, Y., Mertes, K. M., Rumberger, E. M., Hendrickson, D. N., Myasoedov, Y., Shtrikman, H., Avraham, N., and Zeldov, E. (2004). Photon-induced magnetization reversal in the Fe_8 single-molecule magnet. *Physical Review B*, 70, 100408.

[105] Troiani, F., Ghirri, A., Affronte, M., Carretta, S., Santini, P., Amoretti, G., Piligkos, S., Timco, G. A., and Winpenny, R. E. P. (2005). Molecular Engineering of Antiferromagnetic Rings for Quantum Computation. *Physical Review Letters*, 94, 207208.

[106] Ardavan, A., Rival, O., Morton, J. J. L., Blundell, S. J., Tyryshkin, A. M., Timco, G. A., and Winpenny, R. E. P. (2007). Will Spin-Relaxation Times in Molecular Magnets Permit Quantum Information Processing? *Physical Review Letters*, 98, 057201.

[107] Larsen, F. K., McInnes, E. J. L., Mkami, H. E., Overgaard, J., Piligkos, S., Rajaraman, G., Rentschler, E., Smith, A. A., Smith, G. M., Boote, V., Jennings, M., Timco, G. A., and Winpenny, R. E. P. (2003). Synthesis and Characterization of Heterometallic $\{Cr_7M\}$ Wheels. *Angewandte Chemie International Edition*, 42, 101–105.

[108] Ferrando-Soria, J., Moreno Pineda, E., Chiesa, A., Fernandez, A., Magee, A. A., Carretta, S., Santini, P., Vitorica-Yrezabal, I. J., Tuna, F., Timco, G. A., McInnes, E. J. L., and Winpenny, R. E. P. (2016). A modular design of molecular qubits to implement universal quantum gates. *Nature Communications*, 7, 11377.

[109] Candini, A., Lorusso, G., Troiani, F., Ghirri, A., Carretta, S., Santini, P., Amoretti, G., Muryn, C., Tuna, F., Timco, G., McInnes, E. J. L., Winpenny, R. E. P., Wernsdorfer, W., and Affronte, M. (2010). Entanglement in Supramolecular Spin Systems of Two Weakly Coupled Antiferromagnetic Rings (Purple-Cr_7Ni). *Physical Review Letters*, 104, 037203.

[110] Lockyer, S. J., Chiesa, A., Timco, G. A., McInnes, E. J. L., Bennett, T. S., Vitorica-Yrezebal, I. J., Carretta, S., and Winpenny, R. E. P. (2021). Targeting molecular quantum memory with embedded error correction. *Chemical Science*, 12, 9104–9113.

[111] Urtizberea, A., Natividad, E., Alonso, P. J., Andrés, M. A., Gascón, I., Goldmann, M., and Roubeau, O. (2018). A Porphyrin Spin Qubit and Its 2D Framework Nanosheets. *Advanced Functional Materials*, 28, 1801695.

[112] Yu, C.-J., Krzyaniak, M. D., Fataftah, M. S., Wasielewski, M. R., and Freedman, D. E. (2019). A concentrated array of copper porphyrin candidate qubits. *Chemical Science*, 10, 1702– 1708.

[113] Cimatti, I., Bondí, L., Serrano, G., Malavolti, L., Cortigiani, B., Velez-Fort, E., Betto, D., Ouerghi, A., Brookes, N. B., Loth, S., Mannini, M., Totti, F., and Sessoli, R. (2019). Vanadyl phthalocyanines on graphene/SiC(0001): toward a hybrid architecture for molecular spin qubits. *Nanoscale Horizons*, 4, 1202–1210.

[114] Atzori, M., Benci, S., Morra, E., Tesi, L., Chiesa, M., Torre, R., Sorace, L., and Sessoli, R. (2018). Structural Effects on the Spin Dynamics of Potential Molecular Qubits. *Inorganic Chemistry*, 57, 731–740.

[115] Ariciu, A.-M., Woen, D. H., Huh, D. N., Nodaraki, L. E., Kostopoulos, E. K., Goodwin, C. A. P., Chilton, N. F., McInnes, E. J. L., Winpenny, R. E. P., Evans, W. J., and Tuna, F. (2019). Engineering electronic structure to prolong relaxation times in molecular qubits by minimising orbital angular momentum. *Nature Communications*, 10, 3330.

[116] Du, J.-L., Eaton, G. R., and Eaton, S. S. (1995). Temperature and Orientation Dependence of ElectronSpin Relaxation Rates for Bis(diethyldithiocarbamato)copper(II). *Journal of Magnetic Resonance, Series A*, 117, 67–72.

[117] Canarie, E. R., Jahn, S. M., and Stoll, S. (2020). Quantitative Structure-Based Prediction of Electron Spin Decoherence in Organic Radicals. *The Journal of Physical Chemistry Letters*, 11, 3396–3400.

[118] Graham, M. J., Yu, C.-J., Krzyaniak, M. D., Wasielewski, M. R., Freedman, D. E. (2017). Synthetic Approach to Determine the Effect of Nuclear Spin Distance on Electronic Spin Decoherence. *Journal of the American Chemical Society*, 139, 3196–3201.

[119] Jain, S. K., Yu, C.-J., Wilson, C. B., Tabassum, T., Freedman, D. E., and Han, S. (2021). Dynamic Nuclear Polarization with Vanadium(IV) Metal Centers. *Chem*, 7, 421–435.

[120] Jackson, C. E., Lin, C.-Y., Johnson, S. H., van Tol, J., and Zadrozny, J. M. (2019). Nuclear-spin-pattern control of electron-spin dynamics in a series of V(IV) complexes. *Chemical Science*, 10, 8447–8454.

[121] Macaluso, E., Rubín, M., Aguilà, D., Chiesa, A., Barrios, L. A., Martínez, J. I., Alonso, P. J., Roubeau, O., Luis, F., Aromí, G., and Carretta, S. (2020). A heterometallic [LnLn'Ln] lanthanide complex as a qubit with embedded quantum error correction. *Chemical Science*, 11, 10337–10343.

[122] Tacchino, F., Chiesa, A., Sessoli, R., Tavernelli, I., and Carretta, S. (2021). A proposal for using molecular spin qudits as quantum simulator of light-matter interactions. *Chemical Science*, 9, 10266–10275.

[123] Godfrin, W., Ferhat, A., Ballou, R., Klyatskaya, S., Ruben, M., Wernsdorfer, W., and Balestro, F (2017). Operating Quantum States in Single Magnetic Molecules: Implementation of Grover's Quantum Algorithm. *Physical Review Letters*, 119, 187702.

[124] Giménez-Santamarina, S., Cardona-Serra, S., Clemente-Juan, J. M., Gaita-Ariño, A., and Coronado, E. (2020). Exploiting clock transitions for the chemical design of resilient molecular spin qubits. *Chemical Science*, 11, 10718–10728.

[125] Collett, C. A., Santini, P., Carretta, S., and Friedman, J. R. (2020). Constructing clock-transition-based two-qubit gates from dimers of molecular nanomagnets. *Physical Review Research*, 2, 032037.

[126] Aguilà, D., Barrios, L. A., Velasco, V., Roubeau, O., Repollés, A., Alonso, P. J., Sesé, J., Teat, S. J., Luis, F., and G. Aromí, G. (2014). Heterodimetallic [LnLn'] Lanthanide Complexes: Toward a Chemical Design of Two-Qubit Molecular Spin Quantum Gates. *Journal of the American Chemical Society*, 136, 14215–14222.

[127] Luis, F., Repollés, A., Martínez-Pérez, M. J., Aguilà, D., Roubeau, O., Zueco, D., Alonso, P.J., Evangelisti, M., Camón, A., Sesé, J., Barrios, L. A., and Aromí, G. (2011). Molecular Prototypes for Spin-Based CNOT and SWAP Quantum Gates. *Physical Review Letters*, 107, 117203.

[128] Borilovic, I., Alonso, P. J., Roubeau, O., and Aromí, G. (2020). A bis-vanadyl coordination complex as a 2-qubit quantum gate. *Chemical Communications*, 56, 3139–3142.

[129] Timco, G. A., Carretta, S., Troiani, F., Tuna, F., Pritchard, R. J., Muryn, C. A., McInnes, E. J. L., Ghirri, A., Candini, A., Santini, P., Amoretti, G., Affronte, M., and Winpenny, R. E. P. (2009). Engineering the coupling between molecular spin qubits by coordination chemistry. *Nature Nanotechnology*, 4, 173–178.

[130] von Kugelgen, S., Krzyaniak, M. D., Gu, M., Puggioni, D., Rondinelli, J. M., Wasielewski, M. R., and Freedman, D. E. (2021). Spectral Addressability in a Modular Two Qubit System. *Journal of the American Chemical Society*, 143, 8069–8077.

[131] Bader, K, Winkler, M., and van Slageren, J. (2016). Tuning of molecular qubits: very long coherence and spin–lattice relaxation times. *Chemical Communications*, 52, 3623–3626.

[132] Briganti, M., Lucaccini, E., Chelazzi, L., Ciattini, S., Sorace, L., Sessoli, R., Totti, F., and Perfetti, M. (2021). Magnetic Anisotropy Trends along a Full 4f-Series: The f^{n+7} Effect. *Journal of the American Chemical Society*, 143, 8108–8115.

[133] Jenkins, M. D., Zueco, D., Roubeau, O., Aromí G., Majer, J., and Luis, F. (2016). A scalable architecture for quantum computation with molecular nanomagnets. Dalton Transactions, 45, 16682–16693.

[134] Bonizzoni, C., Ghirri, A., Atzori, M., Sorace. L., Sessoli, R., and Affronte, M. (2017). Coherent coupling between Vanadyl Phthalocyanine spin ensemble and microwave photons: towards integration of molecular spin qubits into quantum circuits. *Scientific Reports*, 7, 13096.

[135] Thiele, S., Balestro, F., Ballou, R., Klyatskaya, S., Ruben, M., and Wernsdorfer, W. (2014). Electrically driven nuclear spin resonance in single-molecule magnets. *Science*, 344, 1135–1138.

[136] Perlovich, G. L., Golubchikov, O. A., and Klueva, M. E. (2000). Thermodynamics of porphyrin sublimation. *Journal of Porphyrins and Phthalocyanines*, 4, 699–706.

[137] Auwärter, W., Écija, D., Klappenberger, F., and Barth, J. V. (2015). Porphyrins at interfaces. *Nature Chemistry*, 7, 105–120.

[138] Wang, Y., Hou, J., Eguchi, K., Nanjo, C., Takaoka, T., Sainoo, Y., Awaga, K., and Komeda, T. (2020). Structural, Electronic, and Magnetic Properties of Cobalt Tetrakis (Thiadiazole) Porphyrazine Molecule Films on Au(111). *ACS Omega*, 5, 6676–6683.

[139] Hou, J., Wang, Y., Eguchi, K., Nanjo, C., Takaoka, T., Sainoo, T., Arafune, R., Awaga, K., and Komeda, T. (2020). Enhanced magnetic spin–spin interactions observed between porphyrazine derivatives on Au(111). *Communications Chemistry*, 3, 36.

[140] Miyoshi, Y., Kubo, M., Fujinawa, T., Suzuki, Y., Yoshikawa, H., and Awaga, K. (2007). Electrochromism and Stable n-Type Doping of Highly Oriented Thin Films of Tetrakis(thiadiazole)porphyrazine. *Angewandte Chemie International Edition*, 46, 5532–5536.

[141] Suzuki, Y., Fujimori, M.,Yoshikawa, H., and Awaga, K. (2004). Packing Motifs and Magneto-Structural Correlations in Crystal Structures of Metallo-Tetrakis(1,2,5-thiadiazole)porphyrazine Series, MTTDPz (M = H_2, Fe, Co, Ni, Cu, Zn). *Chemistry - A European Journal*, 10, 5158– 5164.

[142] Hoshino, A., Takenaka, Y., and Miyaji, H. (2003). Redetermination of the crystal structure of α-copper phthalocyanine grown on KCl. *Acta Crystallographica Section B Structural Science*, 59, 393–403.

[143] Stuzhin, P. A., Bauer, E. M., and Ercolani, C. (1998). Tetrakis(thiadiazole)porphyrazines. 1. Syntheses and Properties of Tetrakis(thiadiazole)porphyrazine and Its Magnesium and Copper Derivatives. *Inorganic Chemistry*, 37, 1533–1539.

[144] Linstead, R. P. (1934). 212. Phthalocyanines. Part I. A new type of synthetic colouring matters. *Journal of the Chemical Society*, 1016–1017.

[145] Mørkved, E. H., Neset, S. M., Kjøsen, H., Hvistendahl, G., Mo, F., Balzarini, J., Fransson, B., Ragnarsson, U., and Francis, G. W. (1994). Template Assisted Cyclotetramerisations of 1,2,5-Thiadiazole-3,4dicarbonitrile. *Acta Chemica Scandinavica*, 48, 912–916.

[146] Stoll, S. and Schweiger, A. (2006). EasySpin, a comprehensive software package for spectral simulation and analysis in EPR. *Journal of Magnetic Resonance*, 178, 42–55.

[147] Finazzo, C., Calle, C., Stoll, S., Van Doorslaer, S., and Schweiger, A. (2006). Matrix effects on copper(ii)phthalocyanine complexes. A combined continuous wave and pulse EPR and DFT study. *Physical Chemistry Chemical Physics*, 8, 1942, 2006.

[148] Nakamura, T., Sasamori, K., Kodama, T., Kikuchi, K., and Fujita, W. (2013). Preparation, Crystal Structure, and Magnetic Properties of a New Dithiolene Ligand, 1,3,2-Dithiazole-4-thione-5thiolate, and its Metal Complex. *Chemistry - An Asian Journal*, 8, 348–350.

[149] Morris J. L., and Rees, C. W. (1987). Organic heterocyclothiazenes. Part 3. Synthesis and structure of 1,3,5,2,4-trithiadiazepines. *Journal of the Chemical Society, Perkin Transactions 1*, 211.

[150] Johann, R. and Wolmershäuser, G. (1997). 1,3,2-Dithiazolylium Cations with Various Anions; Syntheses and Solid-State Structures. *Phosphorus, Sulfur, and Silicon and the Related Elements*, 124, 233–242.

[151] Zheng, T.-C., Burkart, M., and Richardson, D. E. (1999). A general and mild synthesis of thioesters and thiols from halides. *Tetrahedron Letters*, 40, 603–606.

[152] Mueller, W. H., and Dines, M. (1969). Dithioheterocycles from ethane-1,2-disulfenyl chloride. *Journal of Heterocyclic Chemistry*, 6, 627–630.

[153] Morris, J. L., Rees, C. W., and Rigg, D. J. (1985). 1,3,5,2,4-Trithiadiazepine. *Journal of the Chemical Society*, *Chemical Communications*, 7, 396.

[154] Bencini, A., and Gatteschi, D. (2012). *EPR of Exchange Coupled Systems*. Mineola, New York: Dover Publications, Inc.

[155] Henfling, S., Kultaeva, A., Pöppl, A., Klose, J., Kersting, B., Domasevitch, K. V., and Krautscheid, H. (2021). Proton and Electron Transfer in the Formation of a Copper Dithiolene-Based Coordination Polymer. *Inorganic Chemistry*, 60, 9008–9018.

[156] Jacobsen H., and Donahue, J. P. (2008). Computational Study of Iron Bis(dithiolene) Complexes: Redox Non-Innocent Ligands and Antiferromagnetic Coupling. *Inorganic Chemistry*, 47, 10037–10045.

[157] Hoffmann, S. K., Goslar, J., Lijewski, S., and Zalewska, A. (2013). EPR and ESE of CuS_4 complex in $Cu(dmit)_2$: g-Factor and hyperfine splitting correlation in tetrahedral Cu–sulfur complexes. *Journal of Magnetic Resonance*, 236, 7–14.

[158] Peisach, J., and Blumberg, W. (1974). Structural implications derived from the analysis of electron paramagnetic resonance spectra of natural and artificial copper proteins. *Archives of Biochemistry and Biophysics*, 165, 691–708.

[159] Colston, K. J., Dille, S. A., Mogesa, B., Astashkin, A. V.,. Brant, J. A., Zeller, M., and Basu, P. (2019). Design, Synthesis, and Structure of Copper Dithione Complexes: Redox-Dependent Charge Transfer. *European Journal of Inorganic Chemistry*, 2019, 4939–4948.

[160] Vance, C. T., Welch, J. H., and Bereman, R. D. (1989). Syntheses, characterization and structural studies of copper complexes of the 1,2-dithiolene ligand, 5,6-dihydro-1,4-dithiin-2,3-dithiolate. *Inorganica Chimica Acta*, 164, 191–200.

[161] Amri, A., Hasan, K., Taha, H., Rahman, M. M., Herman, S., Andrizal, Awaltanova, E., Wantono, I., Kabir, H., Yin, C.-Y., Ibrahim, K., Bahri, S., Frimayanti, N., Hossain, M. A., and Jiang, Z.-T. (2019). Surface structural features and optical analysis of nanostructured Cu-oxide thin film coatings coated via the sol-gel dip coating method. *Ceramics International*, 45, 12888–12894.

[162] Biesinger, M. C., Lau, L. W., Gerson, A. R., and Smart, R. S. (2010). Resolving surface chemical states in XPS analysis of first row transition metals, oxides and hydroxides: Sc, Ti, V, Cu and Zn. *Applied Surface Science*, 257, 887–898.

[163] Jin, Z., Liu, C., Qi, K., and Cui, X. (2017). Photo-reduced Cu/CuO nanoclusters on TiO_2 nanotube arrays as highly efficient and reusable catalyst. *Scientific Reports*, 7, 39695.

[164] Zou, X., Fan, H., Tian, Y., Zhang, M., and Yan, X. Chemical bath deposition of Cu_2O quantum dots onto ZnO nanorod arrays for application in photovoltaic devices. *RSC Advances*, 5, 30, 23401–23409.

[165] Briggs, D. (1981). Book Review: Wanger, C. D., Riggs, W. M., Davis, L. E., Moulder, J. F., and Muilenberg, G. E. (1979). *Handbook of X-ray Photoelectron Spectroscopy.* Perkin-Elmer Corp., Physical Electronics Division, Eden Prairie, Minnesota, USA. *Surface and Interface Analysis*.

[166] Chandra Deb Nath, N., Yoo, K., and Lee, J.-J. (2018). Halogen-free guanidinium-based perovskite solar cell with enhanced stability. *RSC Advances*, 8, 17365–17372.

[167] Schild, D. (2008). *X-ray Photoelectron Spectroscopy* in *Hydrogen Technology*: *Mobile and Portable Applications* (Léon, A., ed), pp. 575–601. Berlin, Heidelberg: Springer Berlin Heidelberg.

[168] Chiesa, A., Cugini, F., Hussain, R., Macaluso, E., Allodi, G., Garlatti, E., Giansiracusa, M., Goodwin, C. A. P., Ortu, F., Reta, D., Skelton, J. M., Guidi, T., Santini, P., Solzi, M., De Renzi, R., Mills, D. P., Chilton, N. F., and Carretta, S. (2020). Understanding magnetic relaxation in single-ion magnets with high blocking temperature. *Physical Review B*, 101, 174402.

[169] Goodwin, C. A. P., Ortu, F., Reta, D., Chilton, N. F., and Mills, D. P. (2017). Molecular magnetic hysteresis at 60 kelvin in dysprosocenium. *Nature*, 548, 439–442.

[170] Ullah, A., Cerdá, J., Baldoví, J. J., Varganov, S. A., Aragó, J., and Gaita-Ariño, G. (2019). In Silico Molecular Engineering of Dysprosocenium-Based Complexes to Decouple Spin Energy Levels from Molecular Vibrations. *The Journal of Physical Chemistry Letters*, 10, 7678–7683.

[171] Jiang, S.-D., Wang, B.-W., Su, G., Wang, Z.-M., and Gao, S. (2010). A Mononuclear Dysprosium Complex Featuring Single-Molecule-Magnet Behavior. *Angewandte Chemie International Edition*, 49, 7448–7451.

[172] Chilton, N. F., Collison, F., McInnes, E. J. L., Winpenny, R. E. P., and Soncini, A. (2013). An electrostatic model for the determination of magnetic anisotropy in dysprosium complexes. *Nature Communications*, 4, 2551.

[173] Rigamonti, L., Cornia, A., Nava, A., Perfetti, M., Boulon, M.-E., Barra, A.-L., Zhong, X., Park, K., and Sessoli, R. (2014). Mapping of single-site magnetic anisotropy tensors in weakly coupled spin clusters by torque magnetometry. *Physical Chemistry Chemical Physics*, 16, 17220.

[174] Perfetti, M., Lucaccini, E., Sorace, L., Costes, J. P., and Sessoli, R. (2015). Determination of Magnetic Anisotropy in the LnTRENSAL Complexes (Ln = Tb, Dy, Er) by Torque Magnetometry. *Inorganic Chemistry*, 54, 3090–3092.

[175] Perfetti, M. (2017). Cantilever torque magnetometry on coordination compounds: from theory to experiments. *Coordination Chemistry Reviews*, 348, 171–186.

[176] Tennant, W. C., Walsby, C. J., Claridge, R. F. C., and McGavin, D. G. (2000). Rotation matrix elements and further decomposition functions of two-vector tesseral spherical tensor operators; their uses in electron paramagnetic resonance spectroscopy. *Journal of Physics: Condensed Matter*, 12, 9481–9495.

[177] Lunghi, A., Totti, F., Sanvito, S., and Sessoli, R. (2017). Intra-molecular origin of the spin-phonon coupling in slow-relaxing molecular magnets. *Chemical Science*, 8, 6051–6059.

[178] Moseley, D.H., Stavretis, S. E., Thirunavukkuarasu, K., Ozerov, M., Cheng, Y., Daemen, L. L., Ludwig, J., Lu, Z., Smirnov, D., Brown, C. M., Pandey, A., Ramirez-Cuesta, A. J., Lamb, A. C., Atanasov, M., Bill, E., Neese, F., and, Xue, Z.-L. (2018). Spin–phonon couplings in transition metal complexes with slow magnetic relaxation. *Nature Communications*, 9, 2572.

[179] Grezes, C., Kubo, Y., Julsgaard, B., Umeda, T., Isoya, J., Sumiya, H., Abe, H., Onoda, S., Ohshima, T., Nakamura, K., Diniz, I., Auffeves, A., Jacques, V., Roch, J.-F., Vion, D., Esteve, D., Moelmer, K., and Bertet, P. (2016). Towards a spin-ensemble quantum memory for superconducting qubits. *Comptes Rendus Physique*, 17, 693–704.

[180] Morton, J. J. L., Tyryshkin, A. M., Brown, R. M., Shankar, S., Lovett, B. W., Ardavan, A., Schenkel, T., Haller, E. E., Ager, J. W., and Lyon, S. A. (2008). Solid-state quantum memory using the ^{31}P nuclear spin. *Nature*, 455, 1085–1088.

[181] Kurizki, G., Bertet, P., Kubo, Y., Mølmer, K., Petrosyan, D., Rabl, P., and, Schmiedmayer, J. (2015). Quantum technologies with hybrid systems. *Proceedings of the National Academy of Sciences*, 112, 3866–3873.

[183] Bonizzoni, C., Ghirri, A., Santanni, F., Atzori, M., Sorace, L., Sessoli, R., and Affronte, M. (2020). Storage and retrieval of microwave pulses with molecular spin ensambles. *Nature Physics Journal Quantum Information*, 6.

[183] Ghirri, A., Bonizzoni, C., Gerace, D., Sanna, S., Cassinese, A., and Affronte, M. (2015). $YBa_2Cu_3O_7$ microwave resonators for strong collective coupling with spin ensembles. *Applied Physics Letters*, 106, 184101.

[184] Eaton, G. R. and Eaton, S. S. (2011). *Multifrequency Electron Spin-Relaxation Times*, in *Multifrequency Electron Paramagnetic Resonance* (Misra, S. K., eds.), pp. 719–753, Weinheim: Wiley-VCH Verlag GmbH and Co. KGaA.

[185] Uhrig, G. S. (2007). Keeping a Quantum Bit Alive by Optimized π-Pulse Sequences. *Physical Review Letters*, 98, 100504.

[186] Souza, A. M., Álvarez, G. A., and Suter, D. (2012). Robust dynamical decoupling. *Philosophical Transactions of the Royal Society A: Mathematical, Physical and Engineering Sciences*, 370, 4748–4769.

[187] Wu, H., George, R. E., Wesenberg, J. H., Mølmer, K., Schuster, D. I., Schoelkopf, R. J., Itoh, K. M., Ardavan, A., Morton, J. J. L., and Briggs, G. A. D. (2010). Storage of Multiple Coherent Microwave Excitations in an Electron Spin Ensemble. *Physical Review Letters*, 105, 140503.

[188] Grezes,C., Julsgaard, B., Kubo, Y., Stern, M., Umeda, T., Isoya, J., Sumiya, H., Abe, H., Onoda, S., Ohshima, T., Jacques, V., Esteve, J., Vion, D., Esteve, D., Mølmer, K., and Bertet , P. (2014). Multimode Storage and Retrieval of Microwave Fields in a Spin Ensemble. *Physical Review X*, 4, 021049.

[189] Bollinger, J. J., Prestage, J. D., Itano, W. M., and Wineland, D. J. (1985). Laser-Cooled-Atomic Frequency Standard. *Physical Review Letters*, 54, 1000–1003.

[190] Haljan, P. C., Lee, P. J., Brickman, K.-A., Acton, M., Deslauriers, L., and Monroe, C. (2005). Entanglement of trapped-ion clock states. *Physical Review A*, 72, 062316.

[191] McAuslan, D. L., Bartholomew, J. G., Sellars, M. J., and Longdell, J. J. (2012). Reducing decoherence in optical and spin transitions in rare-earth-metal-ion–doped materials. *Physical Review A*, 85, 032339.

[192] Wolfowicz, G., Tyryshkin, A. M., George, R. E., Riemann, H., Abrosimov, N. V., Becker, P., Pohl, H. J., Thewalt, M. L. W., Lyon, S. A., and Morton, J. J. L. (2013). Atomic clock transitions in silicon-based spin qubits. *Nature Nanotechnology*, 8, 561–564.

[193] Shiddiq, M., Komijani, D., Duan, Y., Gaita-Ariño, A., Coronado, E., and Hill, S. (2016). Enhancing coherence in molecular spin qubits via atomic clock transitions. *Nature*, 531, 348–351.

[194] Rubín-Osanz, M., Lambert, F., Shao, F., Rivìere, E., Guillot, R., Suaud, N., Guihéry, N., Zueco, D., Barra, A.-L., Mallah, T., and Luis, F. (2021). Chemical tuning of spin clock transitions in molecular monomers based on nuclear spin-free Ni(II). *Chemical Science*, 12, 5123–5133.

[195] Collett, C., Ellers, K.-I., Russo, N., Kittilstved, K., Timco, G. A., Winpenny, R. E. P. and Friedman, J. R. (2019). A Clock Transition in the Cr_7Mn Molecular Nanomagnet. *Magnetochemistry*, 5, 4.

[196] Joshi, G., Kubasek, J., Nikolov, I., Sheehan, B., Costa, T. A., Allão Cassaro, R. A., and Friedman, J. R. (2020). Adjustable coupling and in situ variable

frequency electron paramagnetic resonance probe with loop-gap resonators for spectroscopy up to X-band. *Review of Scientific Instruments*, 91, 023104.

[197] Shevchenko, O. A., Melnikov, A. R., Tararyshkin, S. V., Getmanov, Y. V., Serednyakov, S. S., Bykov, E. V., Kubarev, V. V., Fedin, M. V., and Veber, S. L. (2019). Electronic Modulation of THz Radiation at NovoFEL: Technical Aspects and Possible Applications. *Materials*, 12, 3063.

[198] Vasyukov, V. N. (2011). Manifestation of non-centrality effect in the EPR spectrum of Fe^{3+} ion in the polycrystalline materials. *Journal of Physics: Conference Series*, 324, 012024.

[199] Das, P. K., Chatterjee, S., Samanta, S., and Dey, A. (2012). EPR, Resonance Raman, and DFT Calculations on Thiolate- and Imidazole-Bound Iron(III) Porphyrin Complexes: Role of the Axial Ligand in Tuning the Electronic Structure. *Inorganic Chemistry*, 51, 10704–10714.

[200] Christoforidis, K. C., Louloudi, M., Milaeva, E. R., Sanakis, Y., and Deligiannakis, Y. (2007). EPR study of a novel [Fe–porphyrin] catalyst. *Molecular Physics*, 105, 2185–2194.

[201] Collison, D. and Powell, A. K. (1990). Electron spin resonance studies of ”FeO6”tris chelate complexes: models for the effects of zero-field splitting in distorted S = 5/2 spin systems. *Inorganic Chemistry*, 29, 4735–4746.

[202] Barra, A. L., Caneschi, A., Cornia, A., Fabrizi de Biani, F., Gatteschi, D., Sangregorio, C., Sessoli, R., and Sorace, L. (1999). Single-Molecule Magnet Behavior of a Tetranuclear Iron(III) Complex. The Origin of Slow Magnetic Relaxation in Iron(III) Clusters. *Journal of the American Chemical Society*, 121, 5302–5310.

[203] Hiroto, S., Miyake, Y., and Shinokubo, H. (2017). Synthesis and Functionalization of Porphyrins through Organometallic Methodologies. *Chemical Reviews*,117,2910–3043.

[204] Li, W.-S. and Aida, T. (2009). Dendrimer Porphyrins and Phthalocyanines. *Chemical Reviews*, 109, 6047–6076.

[205] Koo, J., Kim, I., Kim, Y., Cho, D., Hwang, I.-C., Mukhopadhyay, R. D., Song, H., Ko, Y. H., Dhamija, A., Lee, H., Hwang, W., Kim, S., Baik, M.-H., and Kim, K. (2020). Gigantic Porphyrinic Cages. *Chem*, 6, 3374–3384.

[206] Goldberg, I. (2005). Crystal engineering of porphyrin framework solids. *Chemical Communications*, 10, 1243.

[207] Jaquinod, L., Siri, O., and Khoury, R. G. (2001). Linear fused oligoporphyrins: potential molecular wires with enhanced electronic communication between bridged metal ions. *Chemical Communications*, 12, 1261–1262.

[208] Tsuda, A. and Osuka, A. (2001). Fully Conjugated Porphyrin Tapes with Electronic Absorption Bands That Reach into Infrared. *Science*, 293, 79–82.

[209] Kim, D. and Osuka, A. (2003). Photophysical Properties of Directly Linked Linear Porphyrin Arrays. *The Journal of Physical Chemistry A*, 107, 8791–8816.

[210] Kato, K., Furukawa, K., Mori, T., and Osuka, A. (2018). Porphyrin-Based Air-Stable Helical Radicals. *Chemistry - A European Journal*, 24, 572–575.

[211] Fukui, N., Kim, T., Kim, D., and Osuka, A. (2017). Porphyrin Arch-Tapes: Synthesis, Contorted Structures, and Full Conjugation. *Journal of the American Chemical Society*, 139, 9075– 9088.

[212] Shimizu, D. and Osuka, A. (2018). A Benzene-1,3,5-Triaminyl Radical Fused with Zn^{II}-Porphyrins: Remarkable Stability and a High-Spin Quartet Ground State. *Angewandte Chemie International Edition*, 57, 3733–3736.

[213] Schissler, C., Schneider, E. K., Felker, B., Weis, P., Nieger, M., Kappes, M. M., and Bräse, S. (2021). A Synthetic Strategy for Cofacial Porphyrin-Based Homo- and Heterobimetallic Complexes. *Chemistry – A European Journal*, 27, 3047–3054.

[214] Kadish, K. M., Sazou, D., Araullo, C., Liu, Y. M., Saoiabi, A., Ferhat, M., and Guilard, R. (1998). Electrochemistry of vanadyl porphyrins in dimethylformamide. *Inorganic Chemistry*, 27, 2313– 2320.

[215] Timco, G. A., McInnes, E. J. L., Pritchard, R. G., Tuna, F., and Winpenny, R. E. P. (2008). Heterometallic Rings Made from Chromium Stick Together Easily. *Angewandte Chemie International Edition*, 47, 9681–9684.

[216] Carretta, S., Santini, P., Amoretti, G., Affronte, M., Ghirri, A., Sheikin, I., Piligkos, S., Timco, G. A., and Winpenny, R. E. P. (2005). Topology and spin dynamics in magnetic molecules. *Physical Review B*, 72, 060403.

[217] Fábregas Ibáñez, L., Jeschke, G., and Stoll, S. (2020). DeerLab: a comprehensive software package for analyzing dipolar electron paramagnetic resonance spectroscopy data. *Magnetic Resonance*, 1, 209–224.

[218] Osuka, A. and Shimidzu, H. (1997). meso, meso-Linked Porphyrin Arrays. *Angewandte Chemie International Edition*, 36, 135–137.

[219] Wili, N., Richert, S., Limburg, B., Clarke, S. J., Anderson, H. L., Timmel, C. R., and Jeschke, G. (2019). ELDOR-detected NMR beyond hyperfine couplings: a case study with Cu(II)-porphyrin dimers. *Physical Chemistry Chemical Physics*, 21, 11676–11688.

[220] Giovannetti, R. (2012). *The Use of Spectrophotometry UV-Vis for the Study of Porphyrins*, in *Macro to Nano Spectroscopy* (Uddin J., eds), 87–108. InTech.

[221] Zhang, Y.-H., Ruan, W.-J., Li, Z.-Y., Wu, Y., and Zheng, J.-Y. (2005). DFT study on the influence of meso-phenyl substitution on the geometric, electronic structure and vibrational spectra of free base porphyrin. *Chemical Physics*, 315, 201–213.

[222] Ryan, A. A. and Senge, M. O. (2013). Synthesis and Functionalization of Triply Fused Porphyrin Dimers. *European Journal of Organic Chemistry*, 2013, 3700–3711.

[223] Jin, L.-M., Chen, L., Yin, J.-J., Guo, C.-C., and Chen, Q.-Y. (2005). A Facile and Potent Synthesis of meso, meso-Linked Porphyrin Arrays Using Iodine(III) Reagents. *European Journal of Organic Chemistry*, 2005, 3994–4001.

[224] Ouyang, Q., Zhu, Y.-Z., Zhang, C.-H., Yan, K.-Q., Li, Y.-C., and Zheng, J.-Y. (2009). An Efficient PIFA Mediated Synthesis of Fused Diporphyrin and Triply/Singly Interlacedly Linked Porphyrin Array. *Organic Letters*, 11, 5266–5269.

[225] Bencini, A. and Totti, F. (2009). A Few Comments on the Application of Density Functional Theory to the Calculation of the Magnetic Structure of

Oligo-Nuclear Transition Metal Clusters. *Journal of Chemical Theory and Computation*, 5, 144–154.

[226] Grimme, S. (2012). Supramolecular Binding Thermodynamics by Dispersion-Corrected Density Functional Theory. *Chemistry - A European Journal*, 18, 9955–9964.

[227] Brustolon, M. and Giamello, E. (2009). *Electron Paramagnetic Resonance*: *A Practitioner's Toolkit.* Hoboken: John Wiley and Sons, Inc.

[228] Kahn, O. (1993). *Molecular Magnetism*. Orsay: VCH Publishers, Inc.

[229] Morrish, A. H. (1965). *The Physical Principles of Magnetism*. New York: Wiley-IEEE Press.

[230] Drago, R. S. (1992). *Physical Methods for Chemists*. Gainesville: Saunders College Publishing.

[231] Casimir, H., and du Pré, F. (1938). Note on the thermodynamic interpretation of paramagnetic relaxation phenomena. *Physica*, 5, 507–511.

[232] Cole, K. S., and Cole, R. H. (1941). Dispersion and Absorption in Dielectrics I. Alternating Current Characteristics. *The Journal of Chemical Physics*, 9, 341–351.

[233] Bonizzoni, C., Ghirri, A., and Affronte, M. (2018). Coherent coupling of molecular spins with microwave photons in planar superconducting resonators. *Advances in Physics: X*, 3, 1435305.

[234] Niu, D. -Z., Yao, L., Min, X., and Zou, H. (2011). Crystal structure of cis-bis[1-hydroxypyridine-2(1H)thionato-S,O]copper(II),Cu($C_5H_4NOS_2$)$_2$, *Zeitschrift für Kristallographie - New Crystal Structures*, 226.

Index

FUP Best Practice in Scholarly Publishing (DOI 10.36253/fup_best_practice)

Fabio Santanni, *Molecular approaches for quantum technologies. Optimization of electron spin-based quantum bits and quantum logic gates*,, published by Firenze University Press, ISBN 979-12-215-0670-9, DOI 10.36253/979-12-215-0670-9

Acknowledgements

This thesis is the result of three years of work supported by all the people involved in the series of works presented in the text. I want to acknowledge all of them and those who shared with me this experience.

In particular, I want to thank my mentor, Roberta, who made this possible and shared her passion for science and knowledge with me. I am so grateful for all your trust and teaching.

I also want to acknowledge Lorenzo S. and Mauro P. for their kind help and moral/scientific support. Thank you for everything.

These years were not just characterized by the work but also by funny and pleasant times. I want to thank all the LAMM group, you are fantastic people, and I am glad to have spent most of my time with you during this period. A special acknowledgement goes to Andrea S., Niccolò G., and Andrea A. We shared science and funny (and not) moments. You indeed are three great friends more than colleagues.

I want to thank my parents, Stefano and Valeria, for all the love I have received. If I am here, it is because you believed in me and allowed me to study and grow. I also acknowledge my family and friends. Without your support, it would have been hard to reach this objective.

At last, but not the least, I want to thank the woman who shared nine years of her life with me, Camilla, my sweet lover. As Hemingway said" *I love you for all that you are, all that you have been, all that you're yet to be*."

FUP Best Practice in Scholarly Publishing (DOI 10.36253/fup_best_practice)

Fabio Santanni, *Molecular approaches for quantum technologies. Optimization of electron spin-based quantum bits and quantum logic gates*, © 2025 Author(s), CC BY 4.0, published by Firenze University Press, ISBN 979-12-215-0670-9, DOI 10.36253/979-12-215-0670-9

PREMIO TESI DI DOTTORATO CITTÀ DI FIRENZE

TITOLI PUBBLICATI

ANNO 2023

Catani Andrea, *L'indipendenza e l'*accountability *democratica delle banche centrali. Profili comparatistici*

Cinnella Della Porta Silvia, *Traduttori e mercanti. La scoperta inglese del Nuovo Mondo*

Ciravegna Gabriele, *On the Two fold Role of Logic Constraints in Deep Learning*

Colucci Clementina, *Tra ottimizzazione della funzione comando e prospettive di un suo superamento. I nuovi scenari della normatività penale*

Di Gesto Cristian, *Influenze socioculturali, immagine corporea e chirurgia estetica*

Santanni Fabio, *Molecular approaches for quantum technologies. Optimization of electron spin-based quantum bits and quantum logic gates*

Premio Tesi di Dottorato
Città di Firenze 2023

Quantum computers provide a powerful resource to push the boundaries of current knowledge. At the core of their logical architecture are quantum bits and quantum logic gates. Electron spin can be used as a resource to encode logical operators, and, as such, magnetic molecules have proven to be a versatile platform for the realization of fundamental logical units. They offer the possibility of finely tuning desired quantum properties by exploiting targeted chemical approaches. This thesis book provides fundamental knowledge about quantum logical units, with a focus on magnetic molecules and electron spin dynamics. It reports on the various chemical approaches employed to advance beyond the current state-of-the-art in electron spin-based molecular quantum technologies.

FABIO SANTANNI was born in Prato, Italy, in 1994. In 2022, he obtained the PhD title from the University of Florence, under the supervision of Prof. Roberta Sessoli, defending the dissertation that forms the basis of this thesis book. He is currently a research fellow at Trinity College Dublin, Ireland.

ISBN 979-12-215-0669-3 (Print)
ISBN 979-12-215-0670-9 (PDF)
ISBN 979-12-215-0671-6 (XML)
DOI 10.36253/979-12-215-0670-9
www.fupress.com